SOURCE APPORTIONMENT OF $PM_{2.5}$ SHIP EMISSIONS IN HALIFAX, NOVA SCOTIA, CANADA

by

Dilyara Toganassova

Submitted in partial fulfilment of the requirements
for the degree of Master of Applied Science

at

Dalhousie University
Halifax, Nova Scotia
March 2013

DALHOUSIE UNIVERSITY

DEPARTMENT OF ENVIRONMENTAL ENGINEERING

The undersigned hereby certify that they have read and recommend to the Faculty of Graduate Studies for acceptance a thesis entitled "SOURCE APPORTIONMENT OF $PM_{2.5}$ SHIP EMISSIONS IN HALIFAX, NOVA SCOTIA, CANADA" by Dilyara Toganassova in partial fulfilment of the requirements for the degree of Master of Applied Science.

Dated: 21 March, 2013

Supervisor: _____

Readers: _____

_____

DALHOUSIE UNIVERSITY

DATE: 21 March, 2013

AUTHOR: Dilyara Toganassova

TITLE: SOURCE APPORTIONMENT OF $PM_{2.5}$ SHIP EMISSIONS IN HALIFAX, NOVA SCOTIA, CANADA

DEPARTMENT OR SCHOOL: Department of Environmental Engineering

DEGREE: MASc CONVOCATION: May YEAR: 2013

_____

Signature of Author

TABLE OF CONTENTS

LIST OF TABLES

LIST OF FIGURES

ABSTRACT

This study investigated the source attribution of ship emissions to atmospheric particulate matter with a median aerodynamic diameter less than, or equal to 2.5 micron ($PM_{2.5}$) in the port city of Halifax, Nova Scotia, Canada. $PM_{2.5}$ continues to be of concern because of its acute and chronic adverse health effects.

The incentive for the study was that new International Maritime Organization (IMO) regulation in August 1, 2012 caused a reduction in the sulfur content of ship fuel from 3.5% to 1%, which is postulated to lead to an associated reduction in exposure to ship emissions in port cities around North America.

To determine if there was a significant reduction in $PM_{2.5}$ emissions from ships due to the new IMO regulations coming into force, Health Canada funded this 12-month study. Continuous and filter based measurements of $PM_{2.5}$ mass concentration and chemical species were made between August 20, 2011 and August 20, 2012. $PM_{2.5}$ chemical species collected on the filters were analyzed both within the Department and at a number of external laboratories contracted by Health Canada. The USEPA (Positive Matrix Factorization) PMF model was applied to the $PM_{2.5}$ chemical species data to determine the source apportionment of ship emissions (and other sources) to the total $PM_{2.5}$ concentration observed over the 12-month sampling period.

The PMF model successfully determined the following sources with the average mass (percentage) contribution: Sea salt 0.147 $\mu g\ m^{-3}$ (5.3%), Surface dust 0.23 $\mu g\ m^{-3}$ (8.3%), LRT Secondary (ammonium sulfate) 0.085 $\mu g\ m^{-3}$ (3.1%), LRT Secondary (nitrate and sulfate) 0.107 $\mu g\ m^{-3}$ (3.9%), Ship emissions 0.182 $\mu g\ m^{-3}$ (6.6%), and Vehicles and re-suspended gypsum 2.015 $\mu g\ m^{-3}$ (72.8%). A good correlation was achieved between $PM_{2.5}$ total mass predicted and observed with $R^2 = 0.83$, bias = -0.23, and RMSE = 0.09 $\mu g\ m^{-3}$. In addition, a 2.5 times (60%) reduction in sulfate was estimated, when compared to 2006-2008 Government data in Halifax. Air mass back trajectories, pollution roses, wind rose, and meteorological parameters were used as supplementary tools in identifying the sources.

This thesis provides baseline information of air quality in Halifax before Emission Control Area was adopted by IMO in August 2012. This study also represents a foundation data set and modelling results for further analysis to be conducted internally by Health Canada.

LIST OF ABBREVIATIONS USED

ANOVA	Analysis of variance
APCS	Absolute principal component scores
BAM	Beta attenuation monitor
BORTAS	Boreal forest fires on Tropospheric oxidants over the Atlantic using Aircraft and Satellites
CMB	Chemical Mass Balance
EC	Elemental carbon
ED-XRF	Energy dispersive X-ray fluorescence
ICP-MS	Inductively coupled plasma mass spectrometry
IMO	International Maritime Organization
LRT	Long-range transport
NAPS	National air pollution surveillance
OC	Organic carbon
PAH	Polynuclear aromatic hydrocarbons
PCA	Principal component analysis
PEAS	Process Engineering and Applied Science
PM	Particulate matter
$PM_{1.0}$	Particulate matter with an aerodynamic diameter less than 1 micron
$PM_{2.5}$	Particulate matter with aerodynamic diameter less than 2.5 micron
PM_{10}	Particulate matter with aerodynamic diameter less than 10 micron
PMF	Positive Matrix Factorization
POPs	Persistent organic pollutants
Std	Standard deviation
TEOM	Tapered element oscillating microbalance
TSP	Total suspended particles
USEPA	United States Environmental Protection Agency

ACKNOWLEDGEMENTS

First of all, I would like to say my special gratitude to my supervisor, Dr. Mark Gibson, for his invaluable help, encouragement and support over the last two years.
I would like to acknowledge my thesis committee, Dr. Rob Jamieson and Dr. Jan Haelssig for their useful comments and guidance.
I am also very grateful to Gavin King, James Kuchta, and my fellow AFRG (Atmospheric Forensics Research Group) group members for their kind support and considerable assistance with this thesis.
I would also like to say a special thanks to my family and friends for their patience, encouragement, and support while working through this study.

CHAPTER 1 INTRODUCTION

1.1 STRUCTURE OF THE THESIS

This study provides details of the sampling, analysis, and modelling of ambient airborne fine particulate matter less than, or equal to, a median aerodynamic diameter of 2.5 microns ($PM_{2.5}$) in Halifax, Nova Scotia, Canada. Receptor modelling of the sampled $PM_{2.5}$ was used to determine the seasonal source contribution of ship emissions to the total $PM_{2.5}$ mass concentration in Halifax and will be presented and discussed. The aim and objectives of the study are given in detail in Chapter 1. Chapter 2 provides a literature review of ship emissions, the health, and environmental effects of $PM_{2.5}$ and the main methods of measuring, analyzing, and modelling $PM_{2.5}$. Chapter 3 gives information of the methods and materials used during the research. The annual and seasonal receptor modelling results will be presented in Chapter 4. The discussion and conclusion are included in Chapter 5 and Chapter 6, respectively. Supplemental material will be presented in the Appendix.

1.2 RATIONALE FOR CONDUCTING THE STUDY

In 2005, the International Maritime Organization (IMO) introduced a global cap on the sulfur (S) content of fuel (S_F) of 4.5%, reducing to 3.5% in 2012 and 0.5% by 2020 (Lack et al., 2011; Lack and Corbett, 2012). A reduction in S has been shown to have a significant reduction in ship emissions (Lack et al., 2011) with anticipated improvements in the air quality of port cities around the world. Because of the knowledge gap related to the anticipated improvements in air quality in Canadian ports after the low S_F is introduced, the Fuels Group at Health Canada (Ottawa) comissioned this 12-month intensive air monitoring study. Therefore, the aim of the study was to determine the source contribution of ship emissions prior to the new regulations coming into force on August 1, 2012 that reduced S_F from 3.5% to 1%. It is expected that Health Canada will repeat the study in 2014 to determine if there has been a reduction in ship $PM_{2.5}$ emissions as a result of sulfur reduction in fuel from 3.5% to 1% S_F. For that reason, this thesis

represents an important baseline study to inform future research into the improvements in airborne particulate air quality in Canadian port cities.

1.3 AIM AND OBJECTIVES OF THE THESIS

The aim and objectives of the research are to quantify the temporal variation in the source contribution of ship emissions (and other sources, e.g., vehicles) to the total mass concentration of $PM_{2.5}$ in Halifax, Nova Scotia, Canada.

CHAPTER 2 LITERATURE REVIEW

2.1 AIRBORNE PARTICULATE MATTER

Airborne particulate matter is a heterogeneous mixture of many different chemical species and phases (liquid droplets and solid material) that are conventionally divided into three main size classifications, e.g. median aerodynamic diameter ≤ 10, 2.5 and 0.1 micron (PM_{10}, $PM_{2.5}$ and ultrafine/nanoparticles) (Harrison et al., 1997; Gibson et al., 2009; Wallace and Ott, 2011). The size fraction chosen for the Canadian National Air Quality Standard is $PM_{2.5}$. The Canada Wide Standard for $PM_{2.5}$ is 30 $\mu g/m^3$ (Dabek-Zlotorzynska et al., 2011). Therefore, for this thesis, we follow the Canadian air quality standard for assessing particulate air quality by measuring and modelling $PM_{2.5}$.

In terms of their origin, $PM_{2.5}$ can be considered as either primary or secondary air pollutants (Gibson et al., 2009). For example, many 1000's of primary emitted volatile organic compounds (VOCs) and oxides of nitrogen (NO_x) can undergo complex photochemical reactions to form ozone, which then reacts further with other VOCs, e.g. isoprene, to form secondary organic aerosols, e.g. oxalate and formate (Querol et al., 2004; Harrison and Yin, 2008; Carlton et al., 2009; Gibson et al., 2009; Nguyen et al., 2010). One example of the formation of secondary inorganic $PM_{2.5}$ is the reaction between ammonia (NH_3), water vapour and NO_x to form ammonium nitrate (NH_4NO_3) (Gibson et al., 2009b). Another important secondary $PM_{2.5}$ component is ammonium sulfate ($(NH_4)_2SO_4$) which is formed during reactions of NH_3 with SO_2 over time scales of hours to days and, thus, is usually associated with long-range transport (LRT). Together, NH_4NO_3 and $(NH_4)_2SO_4$ alone can often make up 75% of the $PM_{2.5}$ mass observed in Halifax (Gibson et al., 2013b).

Primary PM are released directly to the ambient air (Harrison et al., 2011). There are many sources of primary $PM_{2.5}$, e.g. elemental carbon (soot) and particles emitted directly from the combustion of fossil and biomass fuels for heating, power, and transport (Wardoyo, 2007; Jeong et al., 2008; Yin and Harrison, 2008; Allen et al., 2009; Katzman et al., 2010). Primary particles also include windblown and mechanical re-suspension of surface material (soil, road dust, and sand) (Brewer & Belzer, 2001; Ward, 2007; Gibson et al., 2009b; Khodeir et al., 2012;

Gibson et al., 2013b). A more detailed overview of $PM_{2.5}$ sources will be presented in Section 2.2.

2.2 SOURCES

It is known from previous studies and evident by land-use that the main sources of $PM_{2.5}$ in Halifax include vehicle emissions (diesel and gasoline), residential home heating, sea salt, marine vessel emissions, re-suspended surficial material, refinery emissions, and LRT (Phinney et al., 2006; Waugh, 2006; Dabek-Zlotorzynska et al., 2011; Jeong et al., 2011; Gibson et al., 2013b). Clearly there are natural and anthropogenic, local and long-range contributions to $PM_{2.5}$ in Halifax.

2.2.1 NATURAL SOURCES

The major natural sources of $PM_{2.5}$ are sea spray, forest wildfires, terrestrial dust, volcanic eruptions, and chemical reactions between gaseous pollutants (Pierce, 2006; La Spina et al., 2010; Parrington et al., 2011; Gibson et al., 2013b). It is estimated that the Sahara is one of the major contributors of dust, 100 Mt (megatonne) each year (Khodeir et al., 2012). The median diameter of these particles varies between 50 μm and 2 μm depending on the distance from the source. Sea water is another main source of airborne particles with median diameter about 8 μm (Gibson et al., 2009; Tiwary & Colls, 2010). Table 1 illustrates composition, sources, formation, and other characteristics of fine and coarse particles (Tiwary & Colls, 2010). Nonindustrial fugitive sources are formed during windblown and mechanical suspension of agricultural dust and dust from roads (Harrison et al., 2004; Yin and Harrison, 2008; Gibson et al., 2013b). Forest wildfires are a major nonindustrial source according to the Boreal forest fires on Tropospheric oxidants over the Atlantic using Aircraft and Satellites (BORTAS) study (Palmer et al., 2013). The BORTAS study identified that in summer of 2011 the number of forest fires in North America was 4,012 while the 10-year average was 5,062 per year. The highest number of fires was observed in Ontario, Alberta, and British Columbia (Palmer et al., 2013).

2.2.2 MAN-MADE SOURCES

All anthropogenic activities (e.g., combustion of fossil fuel for transport, heat and power) produce airborne particulate matter that is suspended in the air. Heating, cooking, and hot water generation is responsible for 95% of all biomass combustion during the last decade (Dohoo et al., 2013). Biomass burning emits sulfates, nitrates, soot, and hydrocarbons. Another major contributor is road transport followed by industrial processes, both which are major sources of air pollution (Tiwary & Colls, 2010).

A study in Vancouver identified the main anthropogenic sources of $PM_{2.5}$ as fossil fuel combustion, industrial processes, and fugitive emissions (Brewer & Belzer, 2001). Process fugitive $PM_{2.5}$ originates from wind erosion of unpaved roads, storage piles, and loading activities. Another source is transport that can be divided into emissions from vehicles and particles from tire and break wear. The sources of SO_2 in port cities are the oil and gas sector, metal smelting, and the marine ships. During dry wind conditions, coupled with vehicle movement, surficial $PM_{2.5}$ dust can become suspended and re-suspended to the detriment of air quality (Gibson et al., 2013a). Residential wood burning is a major contributor in the winter in rural areas, e.g. the average woodsmoke contribution to total $PM_{2.5}$ is 56.2% (Bergauff et al., 2008; Gibson et al., 2010). However, as the price of fossil fuels increase it has captured a larger share of the market in urban Halifax over the past number of years (Wheeler et al., 2011). From Table 1 (see below), it can be seen that the majority of coarse ($PM_{2.5\text{-}10}$) mass composition is associated with natural sources, e.g. wind re-suspended and mechanical suspended surficial material, sea salt, and wildfire black smoke (Harrison et al., 2011; Gibson et al., 2013b). The fine particulate ($<PM_{2.5}$) is a combination of anthropogenic (e.g., combustion of fossil fuels) and natural sources (secondary organic aerosol and condensation nuclei) plus the smaller size fraction associated with natural coarse particles (sea salt particles) (Leaitch et al., 1996; Finlayson-Pitts and Pitts, 1999; Pierce and Adams, 2009).

Table 1 Comparison of fine and coarse particles (adapted from Seinfeld & Pandis, 2006).

	Fine particles	Coarse particles
Formation pathways	Chemical reaction, nucleation, condensation, coagulation, cloud/fog processing	Mechanical disruption, suspension of dust
Composition	Sulfate, nitrate, ammonium, hydrogen ion, EC, OC, metals, water	Re-suspended dust, coal and oil fly ash, crustal element (Ti, Si, Al, Fe) oxides, $CaCO_3$, NaCl, pollen, animal and plant debris, tire wear debris
Sources	Combustion (coal, oil, diesel, gasoline, wood) Gas-to-particle conversion of NO_x, SO_3 and VOCs Smelters, mills	Re-suspension of industrial dust and soil, suspension of soil (unpaved roads), biological sources, ocean spray, construction

2.2.3 SECONDARY PARTICLES

Secondary particles usually include ammonium sulfate ($(NH_4)_2SO_4$), ammonium nitrate (NH_4NO_3), ammonium chloride (NH_4Cl), sodium nitrate ($NaNO_3$), and sulfuric acid (H_2SO_4). For instance, NH_4NO_3 and NH_4Cl are formed during reactions of ammonia (NH_3) with HNO_3 or HCl, respectively (Gibson et al., 2009b). One of the dominant sources of secondary particles is the atmospheric reactions of the hydroxyl radical ($\cdot OH$) with SO_2 to form H_2SO_4 (Gibson, 2003). Another source is NH_3, which derives from animal urine, wastes (e.g., landfills), and nitrogenous fertilisers (e.g., urea $CO(NH_2)_2$). The formation of NH_3 from urea follows the hydrolysis reaction (Finlayson-Pitts and Pitts, 1999):

$$CO(NH_2)_2 + H_2O = CO_2 + 2NH_3$$

The released NH_3 reacts with H_2SO_4 droplets and forms $(NH_4)_2SO_4$ or ammonium bisulfate (NH_4HSO_4) (Finlayson-Pitts and Pitts, 1999).

2.3 COMPOSITION

Particulate matter consists of primary components, such as organic compounds from burning and fuel combustion, and secondary particulates, e.g. condensation nuclei, secondary organic aerosols, and gas-to-particle conversion reactions. The latter also includes products from photochemical reactions (Finlayson-Pitts and Pitts, 1999). Also particles that are hygroscopic readily attract water and grow rapidly in size, especially in humid environments, e.g. H_2SO_4, particles in coastal cities (Finlayson-Pitts and Pitts, 1999).

2.3.1 BIOGENIC AND ANTHROPOGENIC COMPOUNDS

The ratio of biogenic and anthropogenic contributions to $PM_{2.5}$ mass can change both seasonally and daily. The biogenic components are formed from precursor gases, e.g. terpenes (e.g., isoprene), carbonyls (e.g., dimethylsulphide), and halocarbons (e.g., iodomethane), with the following nucleation and condensation processes (Shaw et al., 2010).

Studies (O'Dowd et al., 2004; Vaattovaara et al., 2006; O'Dowd & De Leeuw, 2007; Facchini et al., 2008) show that biogenic secondary marine aerosols consist mainly of sulfur compounds, iodine oxides, and isoprene emitted by marine algae. For example, phytoplankton releases dimethylsulfide (DMS) which oxidizes in the presence of ·OH radical and produces SO_2 with subsequent reaction that forms H_2SO_4 (O'Dowd & De Leeuw, 2007). According to Facchini et al. (2008), dialkylamines, released by marine algae, react with ammonia by producing dialkylamonium salts, and thus are a main component of secondary marine aerosols (Facchini et al., 2008).

The major anthropogenic contributors of metals are industry, traffic, and power stations (Jeong et al., 2011). Table 2 illustrates that secondary sulfate contributes significantly (19-37%) to the total $PM_{2.5}$ concentration in Canadian cities. However, nitrate in Halifax has a smaller input of approximately 9-26% (Jeong et al., 2011a).

Table 2 Average contributions of PMF-resolved sources at five sites (Jeong et al., 2011).

	Windsor, %	Toronto, %	Montreal, %	Halifax, %	Edmonton, %
Sec. sulfate	37.1	33.4	33.7	37.3	19.0
Sec. nitrate	24.0	26.4	13.5	9.3	21.9
Traffic	13.9	10.4	13.9	14.2	12.4
EC-rich	6.1	15.6	14.9		
Biomass burning		1.1	6.4		12.0
Salt	2.3	1.8	4.4	18.3	2.5
Road dust		3.2	3.9		7.0
Soil dust	5.3	1.9	3.8	3.8	
Metallurgy	7.6	6.2			4.9
Oil combustion	3.7		5.5	4.5	
Oil refinery				3.5	
Ship emission				9.1	
Cement kiln					2.6
Biogenic SOA					17.7

2.3.1.1 SEA SALT

In maritime regions, $PM_{2.5}$ can contain significant quantities of sea salt. Sea salt is composed of 86% sodium chloride (NaCl) by mass (Gibson, 2004; Gibson et al., 2009b). Because of this, NaCl is used as a good chemical marker of sea salt (together with SO_4, Ca and Mg) (Gibson et al., 2009; Gibson et al., 2013b). The sea salt associated $PM_{2.5}$ forms through the evaporation of ocean sea spray (Gibson et al., 2009). In cases when road salt re-suspends from highways during the winter, the concentration of NaCl is often observed to increase (Gibson et al., 2009). This makes it difficult to distinguish between the marine sea salt and road salt component of $PM_{2.5}$ (Gibson et al., 2009). Studies done by Jeong et al. (2011) for identifying the contribution of sea salt to $PM_{2.5}$ in 5 Canadian cities indicate the highest concentration was found

at the coast in Halifax (18.3% $PM_{2.5}$ mass contribution), whereas the lowest concentration was found inland in Toronto (1.8% $PM_{2.5}$ mass contribution).

2.3.1.2 CARBONACEOUS COMPONENT OF $PM_{2.5}$

Carbonaceous components consist of carbonate, organic carbon (OC), and elemental carbon (EC) also commonly referred to as black carbon or graphitic carbon (soot). Carbonate usually exists in the coarse particle size range and contributes less than 5% to the total mass of $PM_{2.5}$ (Gibson, 2004). Organic carbon and EC originate mainly from vehicles and industrial emissions, but also from biomass wild fires and biomass combustion for space heating and cooking (Jones and Harrison, 2005; Naeher et al., 2007). Gibson (2004) found that 80% of PM_{10} in the city of Glasgow, UK consisted of carbonaceous material. The mean contribution of OC to the total $PM_{2.5}$ mass at urban and rural areas varies between 26% and 42% (Jeong et al., 2011). OC consists of primary fossil fuel combustion products, such as aromatic hydrocarbons, aliphatic hydrocarbons, and carcinogenic polynuclear aromatic hydrocarbons (PAH) (Sun et al., 1998). Gibson et al. (1997) estimated the concentration of PAH in the city of Glasgow, UK during rush hour to be 363 ng m^{-3}.

Organic carbon also consists of secondary components that originate from oxidation reactions in the atmosphere and a process of conversion of gas to particles (Gibson et al., 1997; Gibson et al., 2013a). The amount of secondary organic $PM_{2.5}$ depends on the chemistry and morphology of particles, solar intensity, and meteorological conditions (Gantt et al., 2010; George and Abbatt, 2010).

Elemental carbon is produced by incomplete combustion of carbonaceous fuels (e.g., gasoline, diesel, organic wastes). The contribution of EC to total $PM_{2.5}$ mass in 5 Canadian cities was 6-19% (Jeong et al., 2011a).

To identify the content of OC and EC thermal/optical techniques can be applied. Currently the Thermal Optical Transmission (TOT) method is used. The principle of TOT analysis is that samples are heated to 820^0C and oxidized to carbon dioxide which is measured by a flame ionization detector (FID). The transmission of laser light through the filter determines the difference between OC and EC (Lonati et al., 2005).

2.3.1.3 METALS

Metals can be found in terrestrial water (Na, Mg, Ca) and crustal material (Fe and Al). They exist in the form of soluble ions in water and salts/oxides in the crust (Brewer & Belzer, 2001). Natural sources will emit large particles, while anthropogenic sources emit $<PM_{2.5}$ associated metals. A summary of typical metal concentrations in Halifax and other Canadian cities is presented in Table 3. It shows the differences in metal and other species concentrations between five cities as well as the relation of concentrations and various sources. As an example, the concentration of Ni and V in Halifax was significantly higher than in other cities because of the oil-refinery plant and marine vessel emissions (Jeong et al., 2011). Moreover, Na contributes significantly to $PM_{2.5}$ because of the vicinity to the sea. In comparison, Windsor has high concentration of Zn which indicates the influence of the galvanizing metal industry. Metals can be used as excellent chemical markers to aid in the identification of $PM_{2.5}$ sources (Querol et al., 2004).

Table 3 Average concentrations of $PM_{2.5}$ chemical species at five cities (Jeong et al., 2011)**.**

	Windsor $\mu g\ m^{-3}$	Toronto $\mu g\ m^{-3}$	Montreal $\mu g\ m^{-3}$	Halifax $\mu g\ m^{-3}$	Edmonton $\mu g\ m^{-3}$
Al	2.60×10^{-2}	3.11×10^{-2}	4.50×10^{-2}	n/a	n/a
As	1.00×10^{-3}	n/a	n/a	1.81×10^{-4}	2.30×10^{-4}
Ba	2.20×10^{-3}	4.66×10^{-3}	1.36×10^{-2}	1.03×10^{-3}	2.12×10^{-3}
Br	n/a	1.32×10^{-3}	2.59×10^{-3}	n/a	n/a
Ca	7.20×10^{-2}	5.80×10^{-2}	6.84×10^{-2}	1.47×10^{-2}	4.09×10^{-3}
Cl	1.00×10^{-1}	3.99×10^{-2}	1.01×10^{-1}	1.72×10^{-1}	6.92×10^{-2}
Cr	3.50×10^{-4}	n/a	n/a	1.65×10^{-4}	4.84×10^{-4}
Cu	3.60×10^{-3}	n/a	n/a	9.15×10^{-4}	1.94×10^{-3}
Fe	1.20×10^{-1}	6.61×10^{-2}	5.69×10^{-2}	8.10×10^{-3}	1.62×10^{-2}
K	6.50×10^{-2}	4.42×10^{-2}	4.20×10^{-2}	2.99×10^{-2}	4.10×10^{-2}
Mg	1.80×10^{-2}	1.14×10^{-2}	9.08×10^{-3}	1.57×10^{-2}	6.31×10^{-3}
Mn	4.20×10^{-3}	6.25×10^{-3}	4.70×10^{-3}	7.96×10^{-4}	3.37×10^{-3}
Na	5.50×10^{-2}	4.97×10^{-2}	8.27×10^{-2}	1.45×10^{-1}	5.41×10^{-2}
Ni	5.30×10^{-4}	2.32×10^{-3}	3.82×10^{-3}	3.33×10^{-3}	6.59×10^{-4}
Pb	3.80×10^{-3}	2.86×10^{-3}	3.99×10^{-3}	1.85×10^{-3}	6.22×10^{-4}
Si	7.60×10^{-2}	8.32×10^{-2}	1.01×10^{-1}	n/a	n/a
Ti	3.70×10^{-4}	1.25×10^{-2}	1.05×10^{-2}	1.74×10^{-4}	2.54×10^{-4}
V	1.30×10^{-3}	7.91×10^{-3}	8.56×10^{-3}	8.64×10^{-3}	2.81×10^{-4}
Zn	3.60×10^{-2}	1.09×10^{-2}	1.20×10^{-2}	7.78×10^{-3}	1.05×10^{-2}
Ammonium	1.70	1.36	8.98×10^{-1}	5.93×10^{-1}	6.05×10^{-1}
Nitrate	2.70	2.31	1.20	2.63×10^{-1}	1.47
Sulfate	3.60	2.88	2.23	2.27	8.88×10^{-1}
OC1	1.30×10^{-1}	1.12×10^{-1}	1.05×10^{-1}	9.31×10^{-2}	8.94×10^{-2}
EC1	1.20	1.02	1.03	6.61×10^{-1}	6.69×10^{-1}

2.3.1.4 POLYNUCLEAR AROMATIC HYDROCARBONS AND PESTICIDES

Particulate matter also consists of semi-volatile compounds, e.g. PAHs, that can be derived naturally (e.g., forest fires) and anthropogenically through incomplete combustion of organic materials (e.g., combustion of fossil fuels). Also, volatilization from soil and vegetation can be a significant source of PAHs in gas and particulate phases. However, PAHs are mostly produced by industry, power plants, residential heating, vehicles, and waste incinerators (Maliszewska-Kordybach, 1999). They are considered to be hazardous to human health and the environment for several reasons. Some PAHs are potent carcinogens, e.g. benzo(a)pyrene, which cause mutagenic transformations of DNA. Secondly, they are persistent organic pollutants (POPs) and are very resistant in the environment. For example, they can remain in ground water and sediments for several years (Nielsen et al., 1996; Armstrong et al., 2004). Other hazardous substances that can be found in the particulate phase are pesticides produced in agriculture, industry, and residential use. They are widely used to protect crops from damage and thus can be found in products that have been treated. Also, pesticides are used in homes to control pests and as personal insect repellents (Whyatt et al., 2002; "Pesticides and health," 2007).

2.3.2 SECONDARY COMPONENTS

The main secondary $PM_{2.5}$ components are SO_4, NO_3, and NH_4. During oxidation reactions of SO_2 to SO_3 and further chemical reactions in the presence of water, H_2SO_4 forms. The reaction mechanism for the formation of SO_4 is described below:

$$SO_2 + {}^{\cdot}OH + M \longrightarrow HOSO_2 + M$$
$$HOSO_2 + O_2 \longrightarrow HO_2 + SO_3$$
$$SO_3 + H_2O \longrightarrow H_2SO_4$$

where M is a chaperone molecule, either atmospheric nitrogen or oxygen (Gibson, 2003). H_2SO_4 then reacts rapidly to form $(NH_4)_2SO_4$ which is non-volatile and stable. H_2SO_4 crystals are highly hygroscopic and attract water readily which results in them growing in size extremely quickly.

Sulfuric acid particulate is also twice as dense as water and careful consideration has to be giving to the aerodynamic properties of these acidic $PM_{2.5}$ (Hinds, 1999).

The formation of NO_3 is quite complicated because of diurnal and seasonal variations. For instance, during day-time the reaction mechanism is the following:

$$NO_2 + \cdot OH + M \longrightarrow HNO_3 + M$$

However, during night-time the concentration of $\cdot OH$ is low, so the reaction is:

$$NO_2 + O_3 \longrightarrow NO_3 + O_2$$

$$NO_3 + NO_2 + M \longrightarrow N_2O_5 + M$$

$$N_2O_5 + H_2O \longrightarrow 2HNO_3$$

The highest nitrate concentrations are observed during the winter period when nitric acid transforms to the particulate phase by reaction with NH_3. Moreover, the concentration of NO_3 is usually at a peak during low temperatures (before sunrise). During the summer NH_4NO_3 is unstable so nitric acid usually reacts with calcium carbonate or sea salt forming coarser particles (Tiwary & Colls, 2010).

The NH_4^+ (NH_4) ion is an important component of the continental tropospheric aerosol. It is formed by the reactions between acid gases and ammonia. The reaction proceeds as follows:

$$NH_3 + H_2SO_4 \longrightarrow NH_4HSO_4$$

$$NH_3 + NH_4HSO_4 \longrightarrow (NH_4)_2SO_4$$

$$NH_3 + HNO_3 \longrightarrow NH_4NO_3$$

In warm seasons the concentration of NH_4NO_3 decreases due to sublimation into the gas phase (Gibson, 2003).

2.4 BACKGROUND

According to the Canadian Council of Ministers of the Environment, the Federal, Canada-Wide Standard (CWS) for $PM_{2.5}$ is 30 μg m^{-3} for a 24-hr average time based on three year averaging of the 98th percentile. The daily standard for the USA is 35 μg m^{-3} (U.S. Environmental Protection Agency, 1997). A new annual threshold of 25 μg m^{-3} based on 3-year averaging to be attained by 2015 for $PM_{2.5}$ was established by the European Union (Dabek-Zlotorzynska et al., 2011).

Estimation and comparison of $PM_{2.5}$ at different cities across Canada was done by the National Air Pollution Surveillance (NAPS) program over a six year period (2003-2008). To measure $PM_{2.5}$ concentrations and associated chemical components Thermo Scientific Partisol-Plus Model 2025-D sequential dichotomous particle samplers and Thermo Scientific Partisol 2300 Chemical Speciation samplers equipped with ChemComb 3500 cartridges were used. Their study showed the average concentration of $PM_{2.5}$ in Halifax ranged between 6 and 11 μg m^{-3} (Figure 1). Contribution of nitrates to $PM_{2.5}$ was 1-4%, sodium chloride 5%, and particle-bound water 8-12% (Dabek-Zlotorzynska et al., 2011). Another study by Jeong et al. (2011) found that the major contributor to $PM_{2.5}$ in Halifax was nitrate. The second strongest source was sea salt with an 18% contribution to $PM_{2.5}$. In comparison with other cities Halifax had negligible amounts of OC and EC, while the contribution of Ni and V was more significant than in Windsor and Edmonton due to ship emissions and oil combustion plants (Jeong et al., 2011). There was a slight seasonality change in $PM_{2.5}$ in Halifax (see Figure 1). Concentrations during summer period are higher than during other seasons mainly due to high sulfate level in summer.

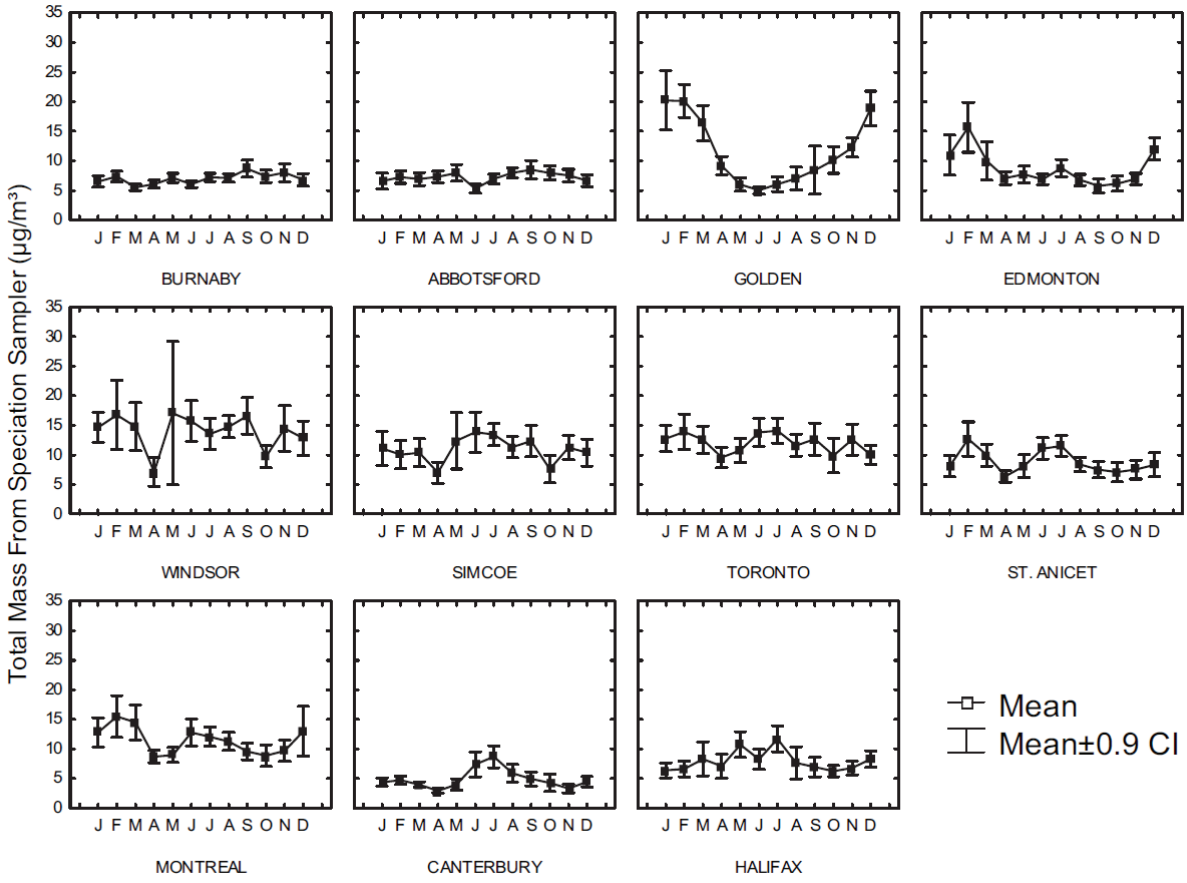

Figure 1 Monthly mean $PM_{2.5}$ mass in Canadian cities (Dabek-Zlotorzynska et al., 2011).

2.5 SHIP EMISSIONS

It is common to think that ship emissions are a minor contributor to air pollution in comparison with other sources, e.g. vehicles. However, many studies have demonstrated the significant impact of ship emissions on coastal and inland areas (Lonati et al., 2010). For instance, the research done by Tzannatos (2010) indicates a twofold increase in primary pollutants (SO_2, NO_x and $PM_{2.5}$) and greenhouse gases (GHG) due to ship emissions. Carbon monoxide (CO), volatile organic compounds (VOCs), nitrogen oxides (NO_x), PM, sulfur dioxide (SO_2), heavy metals, and GHG's such as carbon dioxide (CO_2) and ground-level ozone (O_3) are the main contaminants from marine vessels.

According to a report on the "Feasibility of Extending the Contribution of Marine Activities to Ambient Air Chemistry Study to Saint John, NB, and St John's, NL", the

contribution of ship emissions to the annual emissions of SO_2 and NO_x was approximately 10% for the Halifax region in 2002 (Phinney, 2008).

One reason for the increased pollution is that ship engines burn a heavy residue from oil refinery processing, otherwise known as bunker fuel oil (BFO). Current research indicates that ocean shipping activities consumed 289 million tonnes of fuel in 2001, emitting 7×10^{12} g of NO_x and 5 Tg of SO_2 into the marine atmosphere (S.-K. Song et al., 2010). In terms of $PM_{2.5}$ emissions resulting from marine vessels activity, the increase was up to 5 $\mu g\ m^{-3}$ when ships were in port on weekend days according to a study conducted in Victoria, BC, Canada (Poplawski et al., 2011). Other research indicates that the contribution of ships to the total Mediterranean $PM_{2.5}$ emissions is 0.10% in the port of Piraeus, Greece (Tzannatos, 2010, p.406). According to the studies mentioned above, ship emissions contribute significantly to air pollution in coastal areas. A study by Gibson et al. (2013b) showed that ship emissions during the summer of 2011 contributed 3.4% to the total $PM_{2.5}$ mass in Halifax.

2.6 HEALTH EFFECTS

PM has garnered increased attention from researchers not only because it was legally declared by European directive EU/1999/30 that it must be carefully monitored and assessed, but also because PM has a severe and adverse effect on human health. Research conducted by Corbett et al. (2007) demonstrated that marine shipping emissions increase the global death rate by 60,000 people annually. Moreover, this trend is anticipated to increase by 40% in the following years because of the expansion of vessel traffic (Corbett et al., 2007, p. 8517). In addition, marine vessel emissions affect not only the coastal area but also inland areas (S.-K. Song et al., 2010). Tiwary & Colls (2010) reported that according to a WHO analysis the death rate was approximately 2.4 million people per year due to inhaling $PM_{2.5}$. As illustrated in Figure 2, the increase in $PM_{2.5}$ concentration causes a gradual rise in mortality. Health effects depend not only on the size of particles but also on morphology and chemistry (Healy et al., 2012). Particles with fuzzy and fluffy morphology, e.g. asbestos and diesel, can adhere in the lungs more readily than spherical particles and have more adverse effects. Moreover, various PM sources have different negative impacts on human health. For instance, combustion constituents are strongly correlated with the enhanced mortality rate as indicated in the study by Jantunen et

al. (2002). A correlation of death rate and traffic-generated particles was also robust, while crustal elements have weak correlation (Jantunen et al., 2002).

Short-term and long-term exposure to PM has been observed by numerous studies (Dockery et al., 1993; Samet et al., 2000; Stieb et al., 2000; Pope III et al., 2002; Stieb et al., 2002; Pope III et al., 2006; Burnett et al., 2010*).* According to research by Stieb et al. (2000) and Pope III et al. (2006), short-term exposure causes acute ischemic disease, increased plasma viscosity, and atherosclerosis, while long-term it contributes to pulmonary and inflammatory diseases, progression of atherosclerosis, and mortality. A study by Pope III et al. (2006) showed that a short-term exposure to fine particles leads to coronary artery disease, which means the buildup of plaque in the arteries. They found that a 10 times rise in $PM_{2.5}$ leads to a 4.5% increase in risk of acute coronary diseases. The risk was better correlated with $PM_{2.5}$ than with PM_{10}. Their findings state that short-term exposure contributes to plaque buildup, thrombosis, and ischemic diseases. However, the contribution to the development of these disorders is high when individuals have existing coronary events (Pope III et al., 2006).

The first fundamental study on long-term health exposure by $PM_{2.5}$ was The Harvard Six City Study conducted by Dockery et al. (1993). It indicates a strong positive correlation of mortality with the levels of fine, inhalable, and sulfate particles. For example, death rate due to exposure to particles was associated mainly with cardiopulmonary diseases (with 53.1% contribution) and lung cancer (with 8.4% contribution). The study took into account gender, smoking status, body-mass index, and occupation. It indicates high correlation of air pollution with occupational exposure to dust, fumes, and gases. However, the study found that air pollution exposure among smokers and different genders also had positive associations with death rate. The research determined that high levels of airborne pollutants affect the respiratory and cardiovascular system. The major finding of the 6-City study was that mortality rose by 1% with every increase in PM_{10} of 10 $\mu g\ m^{-3}$ (Dockery et al., 1993). A lower mortality rate (0.5%) was estimated by Samet et al. (2000) due to refined statistical modelling applied to the study. Moreover, Dockery et al. (1993) evaluated that the level of pollution contributes to increased death rates at average annual PM_{10} concentrations lower than 18 $\mu g\ m^{-3}$, while the US ambient standard is 50 $\mu g\ m^{-3}$ (Dockery et al., 1993). Figure 3 demonstrates a gradual decrease in survival rate with an increasing rate of follow-up years. According to the studies mentioned above there is no safe exposure threshold for $PM_{2.5}$.

Burnett et al. (2010) investigated the association between $PM_{2.5}$, PM_{10}, and gaseous species and cardiorespiratory hospitalization for a 15-year period in Toronto, Canada. A 10 µg m^{-3} rise in $PM_{2.5}$ and PM_{10} caused 3.3% and 1.9% increase in respiratory and cardiac hospital admissions.

A larger study was conducted by Pope III et al. (2002) involving 1.2 million American adults within a 16-year period. They found that a 10 µg m^{-3} increase in $PM_{2.5}$ caused a 6% rise in cardiopulmonary and 8% rise in lung cancer deaths. The study also compared the risk mortality by different factors, such as body mass, smoking rates, and exposure to fine particles. The results indicated that the cigarette smoking and obesity (grade 3 overweight) factors have more influence than exposure to $PM_{2.5}$ (Pope III et al., 2002).

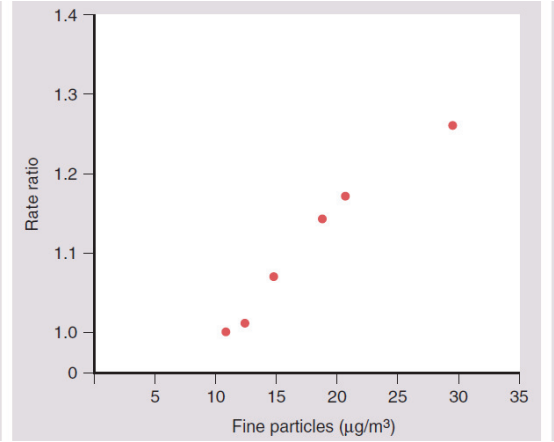

Figure 2 Correlation of fine particulate concentration and mortality rate in six US cities (Carlsten & Kaufman, n.d.).

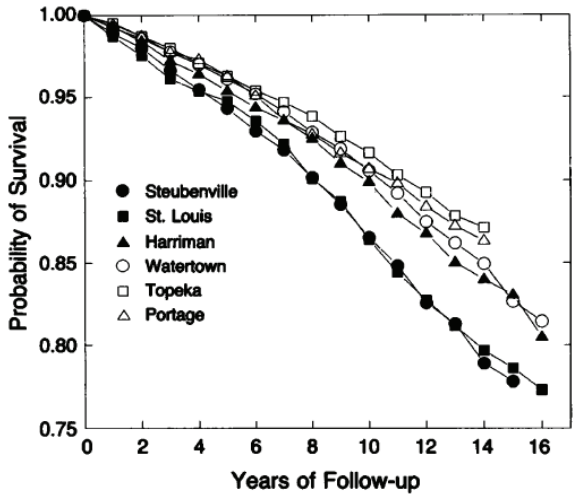

Figure 3 Crude probability of survival in six cities, according to years of follow-up (Dockery, 1993).

2.7 EFFECTS ON CLIMATE AND ECOSYSTEM

Particulate matter has an adverse effect on ecosystems, vegetation and construction materials (acidic particulate damage to limestone) (Brook et al., 1997). For instance, PM can deposit directly on leaves causing slow photosynthesis and gas exchange. In addition, particles may contain high acid concentrations generated from vehicles and oil refinery plants. High levels of acidity damage the leaves of plants and destroy the nutrients in the soil (Gibson et al., 2013a). Therefore, plants are becoming more vulnerable to disease. Moreover, PM that contains heavy metals can accumulate in soil and decrease the nutrient exchange of plants, which in turn inhibits the growth of plants and reduces yields. In terms of its effect on construction, increased concentrations of $PM_{2.5}$ adhering to the fabric of buildings requires high cleaning and maintenance expenses to remove. For example, particulate dust, e.g. smoke from coal-fired heating industries, deposits on building materials causing dark discoloration which is also known as soiling. Building soiling from airborne particulates has been known to have impacted historic buildings in London, Glasgow, Paris, and Bath. PM reduces the durability of painted materials causing erosion, chalking, and loss of gloss (Watt et al., 2009). Another problem with PM deposition on buildings is corrosion, caused by hygroscopic PM that reacts with water. Particles may contain ammonium salts (e.g., NH_4NO_3) or NaCl which accelerate corrosion. The reason is

that ions increase the lifespan of wetness, while chloride is a very corrosive element which in combination with high humidity and temperature becomes ever more corrosive. Increased PM pollution can also cause haze, reducing safety and visibility (Godish, 2004).

In terms of its impact on climate, an increased concentration of PM leads to cooling-heating effects due to the scattering or absorption of solar radiation. As an example $(NH_4)_2SO_4$ scatters radiation and thus has a cooling effect on climate whereas the presence of soot causes heating due to its good absorption characteristics (Bond et al., 2013). Therefore, the temperature of the atmosphere depends on the mixture of those particles as well as the chemistry of PM (Seinfeld & Pandis, 2006).

2.8 METHODS OF $PM_{2.5}$ MEASUREMENT

2.8.1 IMPACTORS AND CYCLONES

There are two main methods of measuring the concentration of PM, collectors and counters. Collectors use an integrated sampler with a substrate (e.g., a filter/foam) on which particles are deposited, while the counter detects particles continuously, using light scattering or light obscuration (Hinds, 1999). The collector substrate can be analyzed gravimetrically, biologically, and/or chemically.

The two main techniques for PM size selection used in both collectors and counters are impactors and cyclones. They separate particles into the desired size fraction for direct measurement or collection on a substrate, e.g. filter, foam or grease. Typical size selective impactors and cyclones provide size cuts for TSP, PM_{10}, $PM_{2.5}$ and $PM_{1.0}$ (Harrison & Yin, 2008; Gibson et al., 2009; Tiwary & Colls, 2010).

The cascade impactor is a multistage device that divides the sample air by particle size. The minimum size depends on the jet diameter, the stream velocity, and the pressure of process operation (Harrison & Yin, 2008). The sampled air passes all collection plates and is deposited on the back-up filter. Large particles accumulate on the first collection plates, while the smaller ones continue passing the rest of stages. If the smallest particles do not deposit on the final stage, they will be collected on the back-up filter. The particle-stopping distance on the plate depends on the Stokes number, so the impaction efficiency is larger with a higher Stokes number (Cyrys et al., 2001).

In terms of flow rate, impactors are divided into large and low. Hi-volume samplers use a large flow rate (1000 l/min), while low flow rate impactors (from 2 l/min to 16.7 l/min) are designed for personal and ambient sampling. The air in the high-volume sampler goes through the eaves of a protective roof and through a large quartz-fibre filter. The flow rate is controlled before and after sampling, because the flow fluctuates due to particle build-up and changes in temperature and pressure. Sharp cut impactors have become popular because of mechanical and theoretical simplicity, but they have some drawbacks. For instance, if the impactor has a large number of stages this can reduce the pressure, so more power is required. Another issue with sharp cut impactors is that due to high speeds at the last stage, large particles can be split into small particles, causing a corruption of the particle size resolution. In addition, impactors are only designed to measure particles larger than 0.3μm, because during high air speed (required for deposition of ultrafine particles) the pressure reduces rapidly (Tiwary & Colls, 2010).

The main advantage of cyclones is that they provide a low cost method of separating particles. Particles in the cyclone are drawn into the inlet where the swirling gas causes a vortex. Due to their high momentum the large particles are not able to turn so they fall out of the air stream and are deposited in a grit pot below the body of the cyclone. At the bottom of the device the air stream changes from descending to ascending to aid in the separation of larger particles. The range of particle sizes varies with the diameter of the cyclone. The efficiency of the device depends on its dimensions. If the inlet is small, the velocity will be high which increases the efficiency; however, the pressure drop rises as well. The main parameters that describe a cyclone's performance are cut diameter (size of particles collected with 50% efficiency), pressure drop, and overall collection efficiency (Theodore, 2008).

2.8.2 Tapered Element Oscillating Microbalance

Sample air is drawn through a series of size-selective inlets (PM_{10} and then $PM_{2.5}$ or $PM_{1.0}$ depending on the application), before passing through a flow splitter, where the 3 l/min air stream passes to the tapered element and the remaining air flow is directed to exhaust (Cyrys et al., 2001). Particles deposited on the oscillating filter cause a change in the oscillating frequency. The tapered element is fixed at the base, but the platform holding a small filter on the top of the tapered tube vibrates. The computer estimates those changes (vibration) and converts the

frequency into mass (Harrison et al., 1997). According to the following Equation 1, the change in frequency (Δf) is proportional to the change in mass (Δm) (Tiwary & Colls, 2010).

$$\Delta m = K\left(\frac{1}{f^2} - \frac{1}{f_0^2}\right), \text{or } \Delta m \cong \frac{2}{f_0^3}\Delta f \quad (1)$$

The main advantage of Tapered element oscillating microbalance (TEOM) is that it provides a continuous near-real time measurement (1-min average) of $PM_{2.5}$. The instrument was widely used for measuring PM_{10} in the 1990's, because it can work with 1-hour time resolution. The major drawback is that instruments do not differentiate between water and PM. If we heat the PM sample, for example, up to 50 ^{0}C this will lead to evaporation of volatile compounds (e.g., NH_4NO_3). Consequently, over the long-term $PM_{2.5}$ mass will be gradually lost. For instance, due to this problem the daily underestimation of TEOM is approximately 30% in a typical urban environment. Thus relative humidity and temperature changes are the main distortions in $PM_{2.5}$ data when using the TEOM. To fix this issue a pre-treatment method Sample Equilibrium System (SES) based on diffusion drier was designed. It helped to reduce the temperature to 30 ^{0}C and thus improve the instruments bias due to volatilisation (Tiwary & Colls, 2010).

The final stage of the TEOM's re-design is the Filter Dynamic Measurement System (FDMS) that eliminates the loss of volatile compounds due to the presence of permeation dryer working at 30 ^{0}C (Teom FDMS Equipment, 2008). A study by Grover et al. (2005) reported that FDMS showed robust results during measuring semi-volatile and non-volatile species. They found that the concentration measured by FDMS was two times higher than by conventional TEOM due to the loss of NH_4NO_3 at 50 ^{0}C (Grover et al., 2005).

2.8.3 Beta Attenuation Monitor

Beta attenuation monitors (BAM) operate by drawing air through the same size selective inlet as mentioned in section 2.8.2, to provide $PM_{2.5}$ that are then collected onto a quartz filter reel that advances every 24-hr, or when the sample spot is overloaded (Hauck et al., 2004). A carbon-14 (60 μCi) radioactive source emits beta-rays every hour. First, beta-ray transmission is

measured on a clean portion of the filter to provide a zero measurement. Then the filter tape is moved to the particle inlet where a beam passes the filter and causes attenuation due to accumulation of particles. The dirty tape, caused by a build-up of $PM_{2.5}$, attenuates more beta rays than a clean tape. The difference between the two measurements is associated with the concentration using Beer-Lambert's law (Tiwary & Colls, 2010). The BAM works in real time and provides repeatable measurements. The results are automatically reported and can be displayed on the internet in real-time. Continuous sampling of $PM_{2.5}$ can be measured by TEOM and BAM. BAM's perform better than a TEOM as the heated inlet is set to 25 ^{0}C and not 50 ^{0}C. BAM's have now replaced TEOM's in Canada. A BAM at the US Embassy in Beijing reported $PM_{2.5}$ concentrations as high as 800 μg m^{-3} in the city in January 2013 (http://www.democratandchronicle.com/usatoday/article/1828451). By way of comparison, typical mean ambient $PM_{2.5}$ concentrations in Halifax are 5 μg m^{-3}.

2.8.4 INTEGRATED FILTER BASED $PM_{2.5}$ SPECIATION MONITORS

The most commonly used instruments for determining the chemical composition of $PM_{2.5}$ are integrated filter based samplers (e.g., Ward et al., 2004; Yin et al., 2005; Dabek-Zlotorzynska et al., 2011; Jeong et al., 2011). Typical instruments that are used in the Canadian NAPS network, indeed world-wide are the Federal Reference Method (FRM) Thermo Partisol 2025 sampler, the Thermo Partisol 2025 dichotomous sampler (Federal Equivalent Method), and Thermo Partisol 2300 Chemical Speciation Sampler that contains 12x Thermo Partisol ChemComb samplers (Gibson et al., 2009; Dabek-Zlotorzynska et al., 2011; Gibson et al., 2013b).

2.8.4.1 CHEMCOMB SAMPLERS

The Thermo Partisol ChemComb is a flexible active sampling module used for measurements of $PM_{2.5}$, elemental carbon, organic carbon, metals, and ions. It contains a $PM_{2.5}$ or PM_{10} impactor size-selective inlet, two honeycomb denuders for the collection or removal of selected gases, and a four-stage filter pack for the collection of particles. The flow rate for $PM_{2.5}$ and PM_{10} is 10 (16.7) l/min and 10 l/min, respectively. The filter pack is made of Teflon material to prevent interferences and may contain a 2.0 μm pore-size Teflon, nylon or quartz filter (Gibson et al., 2013b). The first type is designed to collect metals, the second to collect

anions/cations, and the last to collect OC/EC. Honeycomb denuders coated with sodium carbonate/glycerol collect acidic gases (e.g., SO_2, HNO_3), while citric acid coated denuders collect basic gases (e.g., NH_3) (Jeong et al., 2011). Moreover, after the filter pack additional polyurethane foam (PUF) can be installed to collect PAHs and pesticides. It is convenient that the sampler can work without honeycomb denuders. Another advantage is that it can be used for long-term field measurements; moreover, they are easy to use and maintain. Finally, honeycomb denuders are small, have a large internal surface area and are made from glass, which reduces gas losses (Dabek-Zlotorzynska et al., 2011).

2.8.4.2 PARTISOL 2025- DICHOTOMOUS SAMPLER

The Thermo Partisol 2025 dichotomous sampler works continuously and is designed to be installed outdoors. The Partisol 2025 dichotomous sampler is contained in a weather proof environmental enclosure. The system consists of 16 filter cassettes. Each cassette holds a 46.2 mm diameter ring-supported, 0.2 μm pore size Teflon filter. The 16 filter cassettes allow for two weeks of unattended daily sampling of PM. Filter exchange is based on a pneumatic mechanism providing high reliability. The 2025-dichot is designed to measure simultaneously the fine and coarse components of PM (Dabek-Zlotorzynska et al., 2011).

2.8.4.3 FILTERS

The collection of $PM_{2.5}$ chemical species needed to conduct source apportionment requires a variety of specially treated filters.

One of the least expensive filter medium is quartz fibre. However, quartz filters are known to contain inorganic contamination. Another disadvantage is that they are fragile and hygroscopic; therefore, they are seldom used for mass and inorganic determination of $PM_{2.5}$. However, because they are thermal resistant they can be pre-sample "fired" at 900°C to remove any carbon contamination, for this reason these filters are primarily used for collecting OC and EC. Quartz filters are known to absorb organic pollutants, even when not in use, so care in transport and storage is critical for conducting $PM_{2.5}$ associated OC and EC sampling and post-sample analysis.

Another common filter type is nylon. Nylon filters are used for collecting $PM_{2.5}$ for the determination of anions and cations. Teflon filters have virtually no chemical contamination and

have a Teflon ring to support the filter membrane. Because Teflon filters are very stable, robust, and virtually free of chemical contaminants, they are often used for the determination of $PM_{2.5}$ associated elements, ions, and for the determination of $PM_{2.5}$ mass. Teflon filters are expensive ($5/filter) and not applicable for collecting and analyzing OC and EC substances by thermal methods. However, one advantage of the Teflon filter is that a smoke stain reflectometer can be used as a non-destructive method to determine the EC component of $PM_{2.5}$ (Kothai et al., 2008). A significant feature of this study was the proper selection of filters. According to Jantunen et al. (2002), a good filter should be low flow resistant, chemically inert and stable, robust, hygroscopic, and all without generating a static electrical charge.

2.8.4.4 PROBLEMS ASSOCIATED WITH FILTER SAMPLING

One of the problems associated with $PM_{2.5}$ filter sampling is their storage before and after weighing. According to 1997 EPA requirements, the room temperature should be between 20 °C and 23°C with humidity between 30% - 40%. In addition, light can destroy or alter $PM_{2.5}$ chemical species, so filters should be stored in the dark. The main problems using gravimetric sampling are the evaporation of water droplets, or other semi-volatile components and the formation of bacteria, which may change physical and chemical composition of samples. Moreover, filter sampling is a time consuming process that requires time between the sample being taken, its transport back to the lab and then storage at the correct temperature and humidity before the filter can be re-weighed. Typically, it can take 3 months to receive the $PM_{2.5}$ filter mass results from the external laboratory.

Due to variations in meteorological conditions the air density, and as a consequence buoyancy force, may change causing changes in filter mass. For example, the research by Hanninen et al. (2002) shows an error of approximately 10 µg during such changes. These problems can be decreased if all the parameters (e.g., relative humidity, temperature) are noted and applied to the ideal gas law. Furthermore, to minimize errors it is better to decrease the time between weighing filters, to keep filters cool, and to conduct thermal pre-treatment (Jantunen et al., 2002). To regulate meteorological variables (i.e., temperature and relative humidity) in the laboratory, air conditioning and heating system can be applied. According to the study of Jantunen et al. (2002), to improve climate control, non-hygroscopic and stable filters as well as air conditioning in conjunction with dehumidifiers can be used. Other problems are related to

instruments, such as filters "sticking" during the pneumatic filter change process, rain ingress and loss of power (Gibson, 2003). To counter the issues of differences associated with systematic and environmental conditions, 6 control filters are weighed with the batch of sample filters three times, pre and post weight (Gibson et al., 2009).

2.8.5 NEPHELOMETERS

The most commonly used particle counters are such nephelometers as the TSI DustTrak, Turnkey Osiris, and Aurora 1000 Integrating Nephelometers. The TSI DustTrak continuously identifies outdoor, indoor, and workplace aerosols exposure. Sample aerosols driven by the pump go through an optics chamber and are measured there. It has many advantages: 1) quite cheap and portable; 2) real-time data and automated sampling; 3) high time resolution (1 hour or better); 4) a new DustTrak provides data for $PM_{2.5,}$ $PM_{10,}$ PM_1 fractions simultaneously, while the old one – only one at a time; 5) can work in unattended operation. The disadvantage is that it over-reads during high relative humidity level events.

Turnkey Osiris determines the concentration of dust, PM (TSP, PM_{10}, $PM_{2.5}$, and $PM_{1.0}$), and some meteorological parameters using anemometers. The principle of its work is based on light scattering technique. A pump draws the particles and passes them to a nephelometer where each particle goes through a laser beam. After that they are deposited on a reference filter. Turnkey Osiris measures concentrations of different particles continuously and simultaneously. In addition, the instrument is portable, small, and compact. Aurora 1000 Integrating Nephelometer identifies PM_{10}, $PM_{2.5}$, and $PM_{1.0}$ depending on the specified wavelength. The instrument is reliable in determining local atmospheric visibility (http://www.ecotech.com/).

Some technical characteristics of the main instruments for measuring $PM_{2.5}$ are presented in Table 4 and Table 5 (adapted from Gibson, 2004).

Table 4 Examples of direct-reading monitors for $PM_{2.5}$.

Name	Measurement technique	Flow rate l min^{-1}	Particle fraction	Concentration range µg m^{-3}	Precision (1h) µg m^{-3}	Comments
TEOM Series 1400a Ambient Particle Monitor	Tapered element oscillating microbalance	6.7 inlet	PM_{10}, $PM_{2.5}$ or $PM_{1.0}$	0.06-1500	1.5	Direct-reading monitor in which output directly related to mass
Beta Attenuation Monitor FH621	Attenuation of beta rays by particles collected on a filter	6.7	PM_{10}, $PM_{2.5}$	$6\text{-}10^4$	10	Measurement cycle every 6 min
Thermo Sharp 5030	Combination of beta attenuation and light-scattering photometer	16.67	PM_{10}, $PM_{2.5}$ or $PM_{1.0}$	$0\text{-}10^4$	0.5	Digital filtering for continuous calibration update and the intelligent moisture reduction regulate humidity
Thermo DataRAM 2000 Aerosol Monitor	Light-scattering photometer	1.7-2.3	PM_{10} or $PM_{2.5}$	0.1- 400	1.0	Optical/electronic real-time instrument
Airborne particle monitor APM1	Attenuation of beta rays by particles collected on a filter	15-30	PM_{10}	$2\text{-}10^7$	56	Cassette system with 30 filters in sequential loader
TSI DustTrak	Photometer	1.7	PM_{10}, $PM_{2.5}$ or $PM_{1.0}$	0.001-100 mg m^{-3}	1.0	Aerosols driven by the pump go through an optics chamber and are measured there
Turnkey Osiris	Light-scattering photometer	0.6	TSP, PM_{10}, $PM_{2.5}$, and $PM_{1.0}$	0-6000	-	Portable, small, and compact
EcoTech Aurora 1000	Light-scattering photometer	5	PM_{10}, $PM_{2.5}$, and $PM_{1.0}$	-	-	Single wavelength for visibility measurements

Table 5 Examples of gravimetric $PM_{2.5}$ samplers.

Name	Flow rate l min^{-1}	Particle fraction	Filter diameter (mm)	Comments
PQ100 Portable $PM_{2.5}$ sampling unit	16.7	PM_{10}, $PM_{2.5}$ or PM_1	47	Microprocessor control, mass flow control, so flow corrections are not needed
Partisol Model 2000 Air Sampler	16.7	TSP, PM_{10}, $PM_{2.5}$ or PM_1	47	Uses validated $PM_{2.5}$ inlet connected to microprocessor with internal data storage. Operate as a single-filter system, or as a sequential sampler.
Partisol 2025-dichot	5-18	PM_{10} and $PM_{2.5}$	47	Sequential with 16-filter capacity, pneumatic filter exchange
Partisol 2300 Chemical Speciation Sampler	Up to 18	PM_{10} and $PM_{2.5}$	47	Sequential 4-channel and 12-channel speciation configurations
MiniVol TAS	5	TSP, PM_{10}, or $PM_{2.5}$	47	Equipped with low flow and low battery shut-offs
MicroVol 1100	1.0-4.5	TSP, PM_{10}, or $PM_{2.5}$	47	Contains constant volumetric flow rate

2.9 SOURCE APPORTIONMENT OF $PM_{2.5}$

Source apportionment is the process where individual sources contributing mass to the total $PM_{2.5}$ concentration are first identified and then quantified (Gibson et al., 2009; Jeong et al., 2011). There are a number of methodologies employed to accomplish this. The catchall technical term for the variety of approaches used in source apportionment is receptor modelling, e.g. the determination of the source contribution to $PM_{2.5}$ mass at a receptor. The receptor could be a person, an indoor environment, an ambient monitoring station or the northern hemisphere (Watson and Chow, 2007).

2.9.1 RECEPTOR MODELLING

There are a number of commonly used receptor models for the source apportionment of $PM_{2.5}$ which include US EPA Chemical Mass Balance (CMB), US EPA Positive Matrix Factorization (PMF), US EPA UNMIX, and Absolute Principal Component Scores (APCS) (Thurston and Spengler, 1985; Ward, 2007; Watson and Chow, 2007; Wagstrom and Pandis, 2011; Ward et al., 2012; Gibson et al., 2013b). Receptor models use multivariate least squares regression on the sample chemical species matrix to identify "factors" of covarying chemical species and $PM_{2.5}$ mass. These factors are interpreted by the user as the source of $PM_{2.5}$. The receptor model then quantifies the source contribution to the total $PM_{2.5}$ mass. In the case of the CMB model the sample source factors are compared with known source profile factors removing the model user from the source identification process. Other supplemental models such as Principal Components Analysis (PCA) can be used to help identify the source factors within receptor models by incorporating weather variables and gaseous air pollutants. Dispersion modelling, air mass back trajectory analysis, wind roses, pollution roses, and satellite imagery can all be used to help interpret the source factors observed in the receptor model(s) (Watson and Chow, 2007; Wagstrom and Pandis, 2011).

2.9.2 EVOLUTION OF RECEPTOR MODELLING

The first mathematical approach of a receptor model was described by Spearman in 1927. Then it was developed for multiple factor analysis by Thurston in 1947 (Cooper, 2011). However, the first environmental application of the model for statistical weather predictions was conducted by Lorenz in 1956 (Cooper, 2011). Following that Blifford, Meeker, Prinz, and Stratman applied receptor models for aerosol source apportionment (Cooper, 2011). The first formula for CMB modeling was established in 1972 by Miller, Friedlander, and Hidy (Cooper, 2011). An important step towards the development of receptor models occurred in 1980 when the Quail Roost Conference Center acknowledged it as a distinct discipline. Since 1980 receptor modeling has been used as a validation technique for dispersion models (Cooper, 2011).

2.9.3 PRINCIPAL COMPONENT ANALYSIS

Principal component analysis is applied to a set of sample $PM_{2.5}$ mass and chemical components to identify sources in each sample. PCA determines factors that elucidate the pattern of covariance within a group of observed variables. After that it rotates the initial factor matrix into one that is easier to explain (Thurston and Spengler, 1985; Guo et al., 2004; Viana et al., 2006).

PCA is an exploratory method of determining sources that has been used since 1979 by Henry and Hidy (1979; 1982). They estimated sources of particulate sulfate in four American cities. Thurston and Spengler identified sources of inhalable particles in Boston in 1985 (Thurston and Spengler, 1985). The study by Harrison et al. (1996) estimated the major sources of PAH in England. Currently, the model has been used for identifying sources of various pollutants. For example, sources of VOCs, NO_x, CO, and carbonyls were studied by Bruno et al. (2001) and Miller et al. (2002). Another study by Viana et al. (2006) reports that PCA successfully identified seven sources of coarse and fine particles in industrialised city in Spain (Viana et al., 2006).

2.9.4 ABSOLUTE PRINCIPAL COMPONENT SCORES

Absolute principal component scores (APCS) is usually used for identifying the contributions of all sources to a specific pollutant. APCS was firstly proposed and applied to $PM_{2.5}$ and PM_{10} by Thurston and Spengler (1985). It was used by Bruno et al. (2001) to measure the contribution of sources to CO, VOCs, and NO_x (Guo et al., 2004).

Guo et al. (2004) conducted source apportionment of non-methane hydrocarbons (NMHCs) in Hong Kong using PCA and APCS models. The study found that these models are appropriate for evaluating source contributions to NMHCs due to good agreement of measured and predicted concentrations. The model needs minimum input information and does not require detailed source profiles like some receptor models, e.g. CMB. However, the APCS algorithm occasionally produces negative source contributions which are physically impossible. Therefore, a new model was developed by Paatero (1997) called Positive Matrix Factorization that forces the model to only produce positive source contributions to the $PM_{2.5}$ mass (Hopke, 1991; Paatero, 1997; Watson and Chow, 2007; Norris and Vedantham, 2008) .

2.9.5 POSITIVE MATRIX FACTORIZATION

A data set in the PMF model is represented by a matrix *X (i×j)*, with *i* indicating the number of samples and *j* the number of chemical species. The model decomposes the matrix into two matrices *G (i×p)* and *F (p×j),* where *p* is the number of sources. The task of PMF is to identify a *p* value, source contributions, and the chemical profiles as well as reduce the object function (*Q*) based on the uncertainties (*u*). The object function is shown in equation 2.

$$Q = \sum_{i=1}^{n} \sum_{j=1}^{m} \left[\frac{x_{ij} - \sum_{k=1}^{p} g_{ik} f_{kj}}{u_{ij}} \right]^2 , \quad (2)$$

where g_{ik} - source contributions over time, the f_{kj} - the chemical profiles

PMF receptor-oriented source apportionment modelling does not require source profiles of emissions. It works with "factors" by arranging 2 matrices (factor contributions and factor profiles), where an expert can then identify the source types with the help of meteorology and marker elements. PMF generates "factors" based on the correlations of species. A mass balance is used in order to calculate the mass contribution of a "factor". By analyzing an analyst can determine the sources associated with each "factor". It is important to mention that in order to satisfy statistical requirements of the model you must provide PMF with data containing at least 30 days of samples, whereas CMB works with 1 day data only (Norris and Vedantham, 2008). Thus, seasonal source apportionment can be conducted using PMF, but not daily source apportionment of $PM_{2.5}$. However, when PMF is conducted on a sample (n>30) the daily $PM_{2.5}$ source apportionment can be predicted by the model.

2.9.6 CHEMICAL MASS BALANCE

The CMB model consists of a solution to linear equations that expresses each receptor chemical concentration as a linear sum of products of source fingerprint abundances. Equation 3 describes the multilinear least square engine found within the CMB model (Ward et al., 2006).

$$C_i = \sum_{j=1}^{p} F_{ij}\, S_j \qquad (3)$$

where C_i is the ambient concentration of specie i, F_{ij} is the fractional concentration of specie i in the emissions from source j, S_j is the total mass concentration contributed by the source (Gibson et al., 2010).

The CMB model requires *a priori* knowledge of sources and emission characteristics. It works by matching profile "fingerprints" in the measured pollutants to those pollutants which come from potential sources. The inputs of the model require the receptor concentrations and source profiles, which are the fractional quantity of the species from each source. The contribution of each source-type to each chemical species serves as the output of CMB. One of the assumptions of the model is that species from the source and receptor do not react with each other; hence, the most reactive compounds are not used as fitting species. The statistical parameters, described by the model, are R-square (R^2), chi-square (χ^2), percent mass (mass%), the ratio of calculated/measured (C/M), and the ratio of residual/uncertainty (R/U) (Ward et al., 2007).

The major difference between factor analytical (FA) techniques and CMB is that FA models identify the source composition from $PM_{2.5}$ mass and chemical species data, while CMB uses detailed emission source profiles to determine source apportionment of the $PM_{2.5}$ at the receptor (Marmur et al., 2006).

2.9.7 Pragmatic Mass Closure

Pragmatic Mass Closure (PMC) uses mole fraction conversion factors to reconstruct the mass of chemical compounds estimated to have been in the original $PM_{2.5}$ sampled. It is simple and does not require factorization and detailed source profiles. According to Harrison et al. (2003), it also accurately identifies sulfate and nitrate which are major contributors to $PM_{2.5}$ mass (Ward et al., 2007; Jeong et al., 2011). One limitation is the lack of identified source trace elements which leads to the limited source estimation. For example, carbonaceous compounds originate from different combustion processes, but due to the insufficient data all those combustion sources cannot be identified (Harrison et al., 2003). The PMC model has been shown

to produce robust results in identifying $(NH_4)_2SO_4$, NH_4NO_3, EC, OC, NaCl, and crustal matter in a study by Harrison et al. (2003). The same conversion factors were applied for a study by Yin & Harrison (2008). Pragmatic Mass closure was used for $PM_{1.0}$, $PM_{2.5}$, and PM_{10} at urban background, roadside, and rural locations (Harrison et al., 2003; Yin et al., 2005; Yin & Harrison, 2008; Gibson et al., 2009; Dabek-Zlotorzynska et al., 2011). It was expected that conversion factors would vary for different site locations, timeframe, and particles. However, the model showed good results with the same coefficients (Yin & Harrison, 2008). Gibson et al. (2009) used PMC for identifying the chemical sources contributing to PM_{10} in Glasgow, Scotland and showed that it can be applied along with meteorological parameters to accurately determine sources (Gibson et al., 2009).

2.9.8 EMISSION INVENTORIES

One of the methods used to help identify sources of $PM_{2.5}$ are emission inventories. They represent databases of pollution sources for a specific area, such as a region, a province, or the country. Stationary emission sources are broken down into point (e.g., smelters, power plants) and area sources (e.g., small businesses). Information of emissions on large sources usually come from monitoring or stack sampling, whereas for small facilities emissions are estimated. Emission inventories can be used as input for dispersion models to give detailed description of pollutants. Moreover, information from emission inventories can help determine the sources that should focus on minimizing their emissions. However, it has spatial limitations; for example, data of emissions within the province may not apply for a local area. Source inventories are available through the National Pollutant Release Inventory (NPRI) that collects data on more than 300 pollutants from a variety of sources. Inventories are updated every year. Information about main air pollutant emissions, such as criteria air contaminants (CAC), is available from the 1990s. However, natural and open (e.g., agriculture, forest fires, construction) sources are not included.

In Table 6 it can be seen that the total national annual emissions of CAC in Canada dropped by approximately 50% (from 1,284,918 to 660,667 tonnes) between 1985 and 2010. Industrial emissions have been reduced by about half, mainly due to switching from coal to oil and natural gas. However, oil and gas production and emissions are increasing from year to year. Emissions from non-industrial sources have decreased sharply by almost 65% over the period

(from 395,196 to 141,526 tonnes). The reason is that people switched from coal to natural gas for electricity and heat generation. Emissions from mobile sources have decreased during the 25-year period by 30% due to changing vehicles to new Canadian Vehicle Emissions Regulations and manufacturing more fuel efficient vehicles.

Table 6 Emissions for Canada (adapted from NPRI, 2012).

	Emissions (tonnes)			
Sources	**1985**	**1995**	**2005**	**2010**
Industrial	780,060	600,655	437,523	440,447
Non- Industrial	395,196	245,267	228,412	141,526
Mobile	96,894	97,137	75,196	68,834
Total CAC (without natural and open)	1,284,918	956,399	679,687	660,667

2.10 METEOROLOGICAL FACTORS

In order to understand why air quality can vary from day to day, we must measure meteorological variables that include: wind direction, wind speed, temperature, precipitation, cloud cover, solar radiation, and air pressure. It is also desirable to know the ceiling height of the boundary layer, which is measured using balloon radio sondes. For, Nova Scotia, balloon sondes are released twice daily at Yarmouth. It is important to know this data because it has a significant effect on the concentration of air pollution. Wrobel et al. (1999) says that precipitation along with wind speed and wind direction are the most significant parameters influencing the concentration of $PM_{2.5}$. If the precipitation rate is known, we can predict the "wash out rate" of PM (Gibson, 2004). For instance, a study conducted by Hien et al. (2002) indicated that rainfall and relative humidity explain the day-to-day variations of coarse particles. However, wind speed and temperature largely control the concentration of $PM_{2.5}$ (Hien et al., 2002). Unfavourable meteorological conditions, such as fog, zero or light wind fields, and high temperatures increase the concentration of contaminants by up to 2-3 times. Wind direction is fundamentally important in determining the impact at a ground receptor from an upwind source of $PM_{2.5}$ (Perry et al., 2005). According to a study by Wrobel et al. (1999), high wind speed helps to decrease the concentration of fine and coarse particles via dispersion. Strong winds and unstable air enhance

the rate of dispersion of air pollutants, while weak winds and stable air suppress it. A temperature inversion also inhibits the dispersal of air pollutants. Using both wind roses and pollution roses we can identify the nearby sources of upwind $PM_{2.5}$ (Lakes Environmental, 2010). It is important to take into account the atmospheric stability by comparing the environmental and dry adiabatic lapse rates. For instance, if the air is stable, we can predict reduced dispersion and higher concentrations of PM (Kesarkar et al., 2007).

2.11 AIR MASS BACK TRAJECTORY

In order to assess receptor models in identifying LRT sources, air mass back trajectories can be applied. Using meteorological parameters the model can be used to identify the forward and backward trajectories of each air parcel (Air Resources Laboratory, 2012). One of the most commonly used models is HYbrid-Single Particle Lagrangian Integrated Trajectory (HYSPLIT) designed by the National Oceanic and Atmospheric Administration's (NOAA) Air Resources Laboratory (ARL). HYSPLIT was successfully applied all over the world (Yin et al., 2005; Davis et al., 2009; Gibson et al., 2009; Davy et al., 2011; Gibson et al., 2013b) to explain the history of an air mass, its transportation, dispersion, and deposition. However, Stohl (1998) reports that the model may have a 20% error of the travel distance; therefore, uncertainties of trajectories should be measured carefully (Stohl, 1998). Air mass back trajectories in conjunction with pollution roses are useful to explain PMF results and identify potential upwind sources of $PM_{2.5}$ and $PM_{2.5}$ species.

CHAPTER 3 MATERIALS AND METHODS

3.1 SITE DESCRIPTION

Halifax, the target receptor of this study, is one of the biggest port cities located on the eastern seaboard of North America. The port handles over 1,500 marine vessel berthings and the entry of approximately 2 million passengers over the year ("Port of Halifax," 2012). Regular visitors to the Halifax harbour include cruise, passenger and cargo ships, as well as the Canadian East Coast Navy, and NATO fleets ("Port of Halifax," 2012).

The $PM_{2.5}$ filter based and continuous sampling campaign was conducted over a 12-month period between August 20, 2011 and August 20, 2012. The sampling site was located at a latitude and longitude of 44°38'17.46" N and 63°35'37.52" W, respectively and at a height of 15 m on the roof of the Sir James Dunn Building of Dalhousie University. This site is in the South End region of the Halifax peninsula located in a mixed institutional and residential area. The $PM_{2.5}$ sampling site in Halifax is shown in Figure 4.

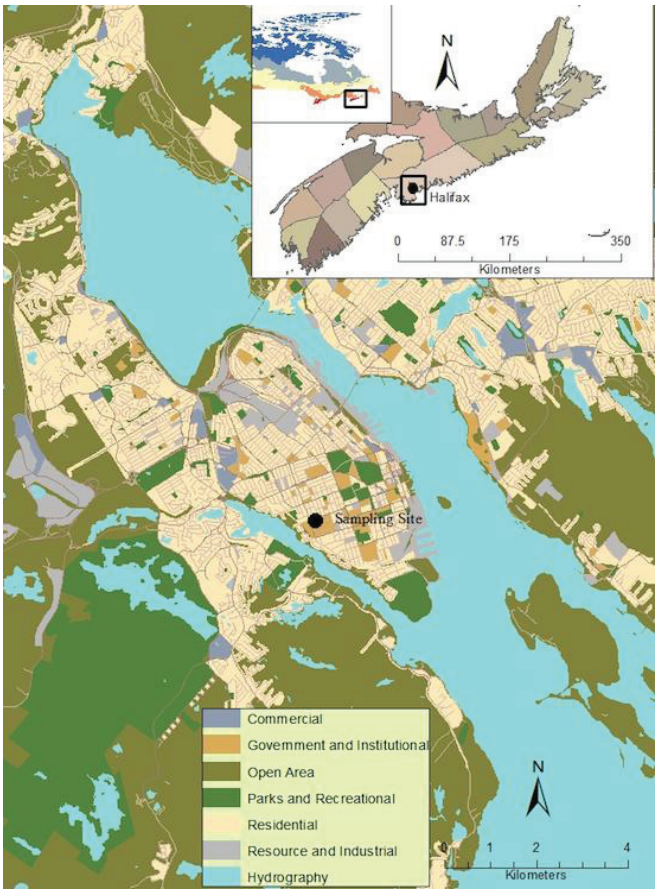

Figure 4 $PM_{2.5}$ sampling location in Halifax, Nova Scotia, Canada.

3.2 SAMPLING EQUIPMENT

In order to accomplish source apportionment it was necessary to determine the total mass concentration and the chemical speciation of the collected $PM_{2.5}$. To do so, $PM_{2.5}$ samples were measured using both continuous instruments and filter based samplers for a 24-hr period (midnight to midnight) every 3rd day. $PM_{2.5}$ mass was collected using a Thermo Scientific 2025-dichotomous Partisol (2025-dichot). The filter from the 2025-dichot was used to determine the total mass concentration and the chemical speciation of 33 elements. Thermo 3500 ChemComb were used to collect anions and cations on nylon filters and a Magee Scientific AE42 aethalometer continuously measured BC with a 1 minute resolution. Figure 5 shows the placement of the instruments at the sampling site. Partisol 2025-dichot is shown on the left,

while the ChemComb nylon filter samplers are shown on the right under the metal weather shelters. The Magee AE42 is located inside the white box on the back right of the platform.

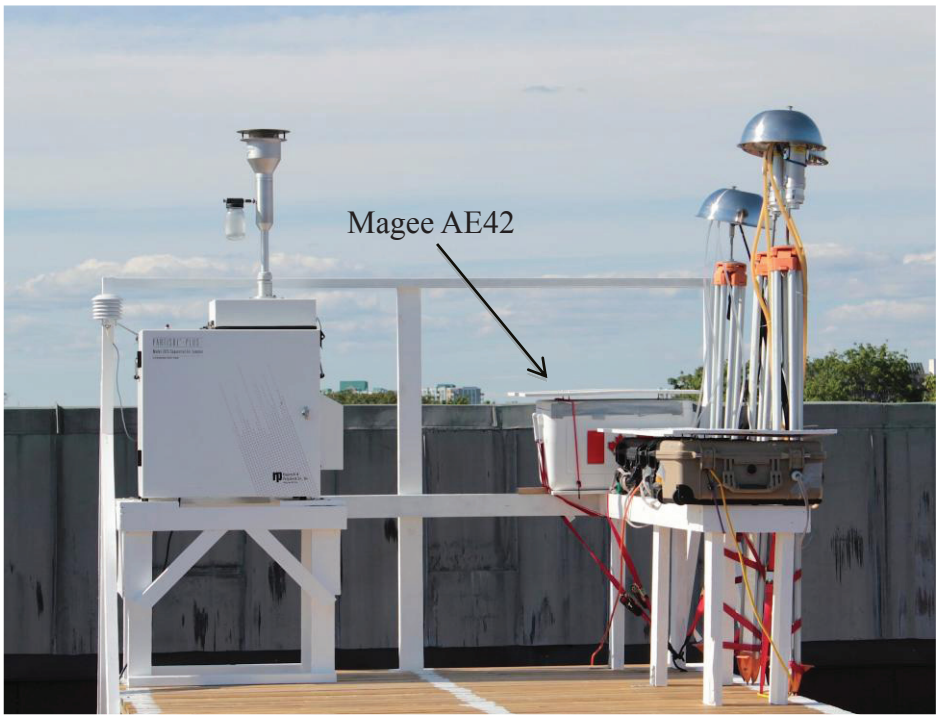

Figure 5 Photograph of the sampling equipment used at the sampling site.

3.2.1 FILTER BASED SAMPLING OF $PM_{2.5}$

As stated above, $PM_{2.5}$ samples were collected using a Thermo Scientific Partisol 2025-dichotomous sampler. This instrument uses two 47 mm diameter, ring supported Teflon filters to collect fine (< 2.5 μm) particles. The $PM_{2.5}$ instrument channel flow rate was 15.0 l/min and was checked weekly with a NIST traceable flow meter (Dry Cal Defender). In cases of flow deviation by more than ±10% the 2025-dichot would log the error and cease functioning. Monthly leak checks were performed on 2025-dichot as specified by the manufactures instructions (Harrison et al., 2003).

The Thermo-Fisher Scientific ChemComb (Model 3500) was used for chemical speciation. Four ChemComb cartridges with three 47 mm diameter, 0.2 μm pore size, ring-supported pre-fired quartz filters and one 47 mm diameter nylon filter with a sodium carbonate denuder were run simultaneously with the 2025-dichot. The denuder scrubbed SO_2 from the

sample stream to prevent an artificial enhancement of SO_4 particles on the filter caused by the SO_2. During analysis of the first batch of nylon filters it was found that the nylon filters had high background chloride concentrations. Therefore, they were exchanged for Teflon filters on February 24, 2012.

To separate fine particles ($PM_{2.5}$) from coarse ($PM_{2.5-10}$) each ChembComb was fitted with polyurethane foam (PUF) impactor. During each sampling period a new PUF was used. Medo vacuum pumps (MEDO USA, Inc., 46 Chancellor Drive, Roselle, IL, pump model: VP 0435A) were used with each ChemComb sampler. The instrument flow rate of 10 l/min was measured by using a Dry Cal Defender flow meter at the beginning and the end of each sampling period; ± 20% of the base flow rate was considered acceptable.

Both blank and duplicate filters were used during the sampling campaign, with each equal to 10% of the total number of active samples. The duplicates were used to check the repeatability of the sampling and the blanks were used to blank correct the active samples. Both the blanks and duplicates were stored, transported and analyzed with the active samples.

3.2.2 CONTINUOUS INSTRUMENTATION

A two wavelength Magee Scientific AE42 aethalometer (Magee Scientific Corp, 1916A M.L. King Jr. Way, Berkeley, CA, USA) was employed at the sampling site to continuously measure BC over the one-year period. The Magee determines the mass of BC at a wavelength of 880 nm. BC is collected on quartz fiber tape and due to optical transmission absorption the concentration of aerosols is estimated. The flow rate the instrument used was 4 l/min, it was calibrated using a TSI Series 4100 flow meter and tested each month and the data time resolution was 1 min. Data was obtained every month by AFRG staff and stored on the laboratory modelling computer with back-up copies stored off site. Detailed description of the $PM_{2.5}$ sampling instrumentation used at the sampling site is provided in Table 7.

Table 7 Sampling instrumentation and post sample chemical analysis employed in the study.

Metric	Instrument Manufacturer Model	Principle	Frequency
Black Carbon	Magee AE42 aethalometer	Reflectance (AFRG)	1 minute
$PM_{2.5}$ chemical speciation	ChemComb (47 mm diameter, nylon filters)	Ion Chromatography for anions/cations (AFRG)	24-hr integrated sample. Every 3rd Day
$PM_{2.5}$ mass & elements	Thermo Partisol 2025-dichot (Health Canada & AFRG)	Gravimetric > XRF analysis of 33 elements	24-hr integrated sample. Every 3rd Day
T, RH, Wind Direction, Wind speed, mb & Rain	Davis Vantage Pro II	Various Sensors (AFRG)	1-hr

During the sampling period some instrumentation issues with the sampling equipment were observed (see Table 8).

Table 8 Instrument malfunctions.

Date	Issues	Comments
24/11/2011	Partisol-2025 filter transition problem	Fixed the next day
12/11/2011	BC monitor tape clumped before the detector and stuck	Monitor did not detect the issue and continued working. Rectified on 12/02/12
24/02/2012	Nylon filters identified to have high level of chloride	Switched to un-weighed Teflon filter
27/02/2012	Partisol failed its Leak check, investigation is still continuing as to the cause	Several attempts to discern the leak have been unsuccessful. Though leak value has remained steady at 35 whereas the threshold for a pass is 20
06/06/2012	The black carbon monitor seemed to be having some electrical issues	Switched BC from Dunn with Site 3
01/07/2012	BC was off when arrived	Was restarted on 04/07/2012
04/08/2012	BC could not advance tape	It was done manually, restarted on the 06/08/2012
04/08/2012	Dichot malfunctioned, could not advance filter	Started again on the 10/08/2012
08/08/2012	BC tape stuck	Was advanced manually, started on 12/08/2012
14/08/2012	Dichot failed again this time with a major internal leak, could not advance a filter at all	
15/08/2012	BC monitor was getting more and more unreliable	Intermittent data until the 18/08/2012 when it stopped completely

3.3 EXPERIMENTAL METHODS

3.3.1 PRE SAMPLE CHEMICAL ANALYSIS

The pre and post gravimetric measurement of the filters from ChemComb and 2025-dichot was done in accordance to the USEPA quality assurance guidance for weighing Teflon filters (USEPA, 1998). Filters were stored in the refrigerator at 4 ^{0}C after sampling to prevent bacteria growth, chemical species degradation, and evaporation of semi-volatile compounds, e.g. NH_4NO_3 (USEPA, 1998). Assembly and disassembly of the ChemComb and 2025-dichot filter cassettes was conducted in Clean-Ceil, high efficiency particle air (HEPA) cleaner hood within the Department of Process engineering and Applied science (PEAS), Dalhousie University. The Clean Ceil was operated at a high flow setting to clear the air of $PM_{2.5}$ within the cleaner hood and after five minutes on the low flow setting while handling filters.

Teflon filters from 2025-dichot were triple bagged in Ziplock bags and shipped in cold airtight transport containers to Alberta Innovates (Vegreville, Alberta) for weighing to estimate the ambient $PM_{2.5}$ mass concentration. Following that, they were shipped to RTI International (Research Triangle Park, North Carolina, US) for the analysis of 33 elements (Ag, Al, As, Ba, Br, Ca, Cd, Ce, Cl, Co, Cr, Cs, Cu, Fe, In, K, Mg, Mn, Na, Ni, P, Pb, Rb, S, Sb, Se, Si, Sn, Sr, Ti, V, Zn and Zr) by a Thermo Fisher Scientific Quant'X ED-XRF.

The ED-XRF analytical method is non-destructive and quantifies the concentration of the $PM_{2.5}$ elemental composition by measuring the intensity of the wavelength of fluorescent emission specific to each element in the $PM_{2.5}$ samples. After ED-XRF analysis filters were sent back to PEAS for refrigerated storage.

In order to determine anions and cations, ion chromatography (IC) was used. Nylon (replaced by Teflon) filters from the ChemComb samplers were extracted and analyzed by the author in PEAS. The following anions were extracted and analyzed: chloride (Cl^-), nitrate (NO_3^-), bromide (Br^-), fluoride (F^-), nitrite (NO_2^-), phosphate (HPO_4^{3-}), and sulfate (SO_4^{2-}) as well as the following cations: ammonium (NH_4^+), sodium (Na^+), lithium (Li^+), potassium (K^+), magnesium (Mg^{2+}), and calcium (Ca^{2+}).

Black carbon was measured using a Magee Scientific AE42 aethalometer and the mass absorption conversion factor was 16.6 (Gibson et al., 2013b). In order to check the precision of

the aethalometer, it was compared with a second collocated Magee AE42. The precision was estimated as 18% . Since the frequency of the measurement was 1 minute, data was integrated to match the collocated 24-hr filter samples.

3.3.2 POST SAMPLE CHEMICAL ANALYSIS

Anions and cations in $PM_{2.5}$ were determined using a Thermo Fisher Scientific, Dionex ICS-1000 ion chromatography system with electronic suppressed conductivity detection with an attached AS40 auto sampler (Dionex Canada Ltd, PRO Maple Grove Village, Oakville, Ontario). The Analysis method is described in the following paragraphs.

To extract anions and cations from the nylon and Teflon filters, the filters were placed sample side down in clear straight-sided jars (Fisher Scientific) and wetted with 100 µl of isopropanol (ISA) and 3.9 ml of Type-1,18 MΩ water. Second, the extraction vials were put into an ultrasonic bath (Fisher Scientific, Branson 5510, 111 Scotia Court, Whitby, Ontario) for 15 min, removed and gently swirled and returned to the ultrasonic bath for a further 15 min. Following sonication, the solution was decanted into a 8 ml opaque vial (Nalgene Amber Narrow-Mouth Bottle) using a 12 mm syringe with a 0.45 µm pore size syringe filter (Fisher Scientific). Each sample was filtered using a clean syringe and filter. All vials were labeled and stored in the fridge at 4 ^{0}C until ready to be analyzed by IC. During analysis, the Dionex ICS-1000 was calibrated using an external mixed standard solution from Dionex (Dionex Canada Ltd, PRO Maple Grove Village, Oakville, Ontario).

After preparation, samples were loaded into the AS40 auto sampler where they were introduced into the IC in a batch method controlled by Dionex Chromeleon software. As each sample is introduced into the IC it is moved through the instrument using a carbonate eluent first to an inline guard column where a final filtering for particulate materials and contaminants occurs. Following which they pass through the separation column where multiple ion-exchange equilibria between the stationary phase (analytical column) and the mobile phase (eluent) provides separation of the ions of interest.

During the chromatographic separation, the column sample ions and eluent ions compete for ion-exchange sites which cause the anions or cations to separate gradually when passing through the analytical column**.** The sample anions and cations, based on their partitioning between the stationary and mobile phase, leave the column at different times, the retention time

(RT). Electrolytic suppression is applied to the chromatography in order to increase the detection sensitivity for the anions and cations. For anion analysis, an anion self-regenerating suppressor (ASRS® 300 4 mm) was used. For cations a cation self-regenerating suppressor (CSRS® 300 4 mm) was used. A conductivity cell was used to quantify the concentration of each anion and cation by measuring the increase in electrical conductance resulting from the anions or cations passing through the detector. Instrument control and data processing was achieved using the associated Dionex Chromeleon data acquisition software. After that Chromeleon determined the ions based on their RT. Finally, data obtained from a sample are compared with the standards (Fritz, 2000).

The analysis of cations was conducted using an IonPac CS12A-5 µm analytical column with 20 mM of the methanesulfonic (MSA) acid as the eluent. To prepare the eluent a 2000 ml volumetric flask was filled with 2.6 ml of MSA and topped with Type-1water. The flow rate of the eluent in the IC system was 0.5 ml min^{-1} with the sample run time 25 min. The injection loop used had a volume of 25 µl, the standards for cation analysis were prepared with the concentration of 0.05 mg/l, 0.1 mg/l, 0.5 mg/l, 0.75 mg/l, 1 mg/l, 3 mg/l, and 5 mg/l.

To analyze the anions, a 9 mM sodium carbonate eluent with a flow rate of 1 ml min^{-1} , run time of 30 min, and 25 µl inject loop was used. An IonPac®, AG9-HC, 4 x 50 mm guard and an IonPac®, AS9-HC, 4 x 250 mm, anion-exchange column both of which are designed for the fast separation of inorganic anions. The following standard concentrations were used 0.25 mg/l, 0.5 mg/l, 0.75 mg/l, 1 mg/l, 1.25 mg/l, 1.5 mg/l, and 2 mg/l.

A seven point standard curve was used to quantify cation and anion peaks, following which both lab and field blanks were used to correct the samples and control for any errors. After blank correction, the volume of the air that passed through the instrument within 24-hr, as well as the intercept and slope of the standard curve were used to calculate the concentration of each sample in µg m^{-3}.

3.4 METEOROLOGICAL MEASUREMENTS

A Davis Vantage Pro II weather station (Davis Instruments Corp. Hayward, California 94545 USA) provided meteorological data at the $PM_{2.5}$ sampling site at Dalhousie University. The meteorological variables included: wind speed, wind direction, temperature (T), pressure (mb), solar radiation (SR), UV radiation (UV), relative humidity (RH), and rainfall.

Meteorological data was collected every 15-min, therefore, it was integrated in order to match the 24-hr filter based sampling. IgorPro (v 6.2.2.2) was used to obtain daily averaged wind vectors. In order to better understand the wind directional dependence of the air pollution metrics and wind direction, pollution roses, wind roses, and PMF source contribution roses were generated for every species and source, and overlaid onto a Google earth map of Halifax. Wind speed and orientation data was analyzed using Igor Pro (v 6.2.2.2) by generating pollution roses and wind directional polar plots.

3.5 STATISTICAL ANALYSIS

All of the $PM_{2.5}$ sample chemical species and meteorological parameters were combined into a master spreadsheet. Statistical analysis of data was conducted using SigmaPlot (v 12.0) and SAS (v 4.3). In order to find the minimum detection limit (MDL) the standard deviation of the 10 replicates of the lowest measureable standard of each chemical species was multiplied by the Student critical t-value (one-tailed probability, α=0.01) (Gibson et al., 2013a). Data was carefully examined for the completeness in order to obtain robust results from PMF model. Species missing with a data completeness < 50% were removed from the data set. Thus, Li^+, F^-, NO_2^-, PO_4^{3-}, Br^-, As, Ce, Co, Cr, and Sr were omitted. If the data completeness for each chemical species was > 50%, any remaining negative values were replaced by half MDL which is a standard protocol used by Health Canada (Stieb et al., 2007; Wheeler et al., 2008; Wheeler et al., 2011).

Graphs were created using Excel (v 2010), SigmaPlot (v 12.0), IgorPro (v 6.2.2.2), and HYSPLIT (Air Resources Laboratory) model.

3.6 AIR MASS BACK TRAJECTORIES

In order to help identify the $PM_{2.5}$ chemical species that originated from certain upwind source regions over the course of the 12-month sampling campaign in Halifax, the three-dimensional HYbrid-Single Particle Lagrangian Integrated Trajectory (HYSPLIT) was used (Draxler and Rolph, 2012). HYSPLIT air mass back trajectory modelling was conducted online via the National Oceanic and Atmospheric Administration (NOAA) web portal (http://www.arl.noaa.gov/HYSPLIT_info.php). In all, 365, 5-day air mass back trajectories were plotted. The trajectories were modeled to arrive in Halifax at 16:00 UTC and 15:00 UTC

respectively (depending upon daylight saving time). The arrival time of 16:00/15:00 UTC corresponds to half way (12:00 AST) of the 24-hr sampling period in Halifax. The arrival height was set up as a default 500 m (950 hPa) to prevent the interaction of air mass with the ground (Gibson et al., 2013b).

3.7 POSITIVE MATRIX FACTORIZATION MODEL

After the $PM_{2.5}$ mass and chemical species components were compiled into the master spreadsheet the source apportionment was conducted. The USEPA PMF v 3.0.2.2 software was used for the source apportionment of the $PM_{2.5}$ samples (Paatero and Tapper, 1994; Harrison et al., 2011; Gibson et al., 2013b).

In order to conduct PMF modelling, two data files are required – concentrations and their corresponding uncertainties. These were generated using SAS (v 4.3). Only measured concentrations were analyzed to avoid values that could perturb model performance. For example, species with more than 90% of data below the detection limit were excluded from our data (Reff et al., 2007). In data that did not have concentration values, the median values of elements were applied and their uncertainties were calculated as four times the median value. Data below the detection limit were substituted with half of the detection limit of corresponding element and their uncertainties were 5 times the detection limit (Polissar et al.,1998). To obtain robust results using the PMF model, duplicate species were avoided. For example, both Na^+ (Na) and SO_4^{2-} (S) were analyzed by both IC and ED XRF; however, ED XRF results were used due to the better analytical precision when comparing the two analytical techniques. Moreover, by analyzing time series and scatter plots samples within the PMF model (Figure 26), extreme events were screened and assessed. Any outliers were omitted from the data set. For instance, Ca extreme event on May 3, 2012, Ni extreme event on March 28, 2012, S extreme event on July 14, 2012, and $PM_{2.5}$ extreme events on July 14 and 26, 2012 were removed from the data set. After which, species were assessed on their completeness and signal-to-noise (S/N) ratios. Based on S/N ratio we categorize chemicals as having a “strong”, “weak”, and “bad” influence on the model as directed by the model user guide (Paatero and Hopke, 2003). For example, if the S/N ratio is less than 0.2 the species were defined as “bad”, the ratio between 0.2 and 2 indicated that the species are “weak”, while higher than 2 were defined “strong”. Any sample species labelled as “bad” were not included in the model. For example, the following $PM_{2.5}$ components were

considered as “bad”: Ba, P, Pb, Se, and Ti. In addition, information about the number of missing or below detection limit values, the presence of the elements in the receptor area, and the issues occurred during the sampling was considered during categorization of species.

PMF is an iterative process where the user has to gain confidence in the models ability to first identify the $PM_{2.5}$ source via the chemical species present in the model “factors” and then finally to apportion the source mass contribution to the total $PM_{2.5}$ mass concentration (Hopke, 1991). In order to obtain the first PMF results, the base run was initiated using the following parameters. First, the number of base runs was chosen as 20. Each run started at a random point in the time series data set to make sure that it robustly accounts for elevated concentrations within the time series of data. After that, the model selected another random point and went through it again until it finished the 20 runs. The model tests itself to determine if each model run converged. Second, the number of factors was determined in an iterative process by identifying the $PM_{2.5}$ source from the chemical species present in each factor. According to the previous research (Jeong et al., 2011; Gibson et al., 2013b), the number of potential factors found in Halifax lay between 7 and 8. They are secondary sulfate, secondary nitrate, refinery, ship emissions, vehicles, sea salt, soil dust, and oil combustion. The initial number of factors was chosen as 5, because there are at least 5 sources in Halifax, e.g. LRT, ship emissions, vehicles, sea salt, and soil dust. The model “seed” was indicated as random, so the model could select any sample point as the starting point for each run. The summary gives information about Q, which is the object function and should be approximately equal to the degrees of freedom, Q (robust), Q (true), the number of converged runs, as well as the lowest Q value run which is boldfaced. Q (robust) is measured without outliers, while Q (true) includes all values. In case the solutions are non-converged, a user should check if appropriate uncertainties or input parameters were used.

The base run results are indicated through Residual Analysis, Observed/Predicted Scatter Plots, Observed/Predicted Time Series, Profiles/Contribs, Aggregate Contribs, G-Space Plot, Factor Pie Chart, and Diagnostics. Residual Analysis, Observed/Predicted Scatter Plots, and Observed/Predicted Time Series help to identify the robustness of the model. For instance, large scaled residuals (more than ±3) and a non-normal distribution of the histogram (Residual Analysis) show poor fit of the model. Dates by Species option and Absolute Scaled Residual as 3 were selected for plotting histograms. Observed/Predicted Scatter Plots tab demonstrates the correlation of the observed and predicted values as well as the distribution of residuals. The

factor resolved solution is presented in Profiles/Contribs screen. The first graph shows the contribution of each element to the factor, while the second graph illustrates the contribution of each factor to the total mass. To have a better understanding of the temporal variation (yearly, seasonal, and weekday/weekend) of the factors the user can analyze Aggregate Contribs tab. G-Space Plot tab is useful for comparison of factors against each other and identifying if the solution has a rotational ambiguity or not. At the end of the base run results, PMF generates a pie chart displaying the percentage and mass contribution of factors to each species (Norris and Vedantham, 2008).

In order to check the stability and uncertainty of the base run results, the PMF statistical bootstrap facility was applied to the model output. During bootstrapping the model randomly chooses a number of samples from the original dataset and replaces it with a new dataset. Thus, estimating bootstrapping source profiles and comparing them with a base factor source profiles. If a bootstrap factor has a high correlation with a base factor the PMF modelling is considered to be robust and the results can be accepted.

In addition to bootstrapping, another test can be applied to provide further verification of the model results. This is the Fpeak test and is used to evaluate any rotational ambiguity within the model results. Different Fpeak values during each run of the model are applied in order to determine whether the object function Q is stable and lie within the range found during the base run. Fpeak can be useful for some solutions but was found not to be needed for our data set and was therefore set to zero (Norris and Vedantham, 2008).

CHAPTER 4 RESULTS

This chapter will describe the $PM_{2.5}$ concentration, its composition, and meteorological parameters sampled during a one year period as well as receptor modelling results. The meteorological data are tabulated in Table 10 and Table 16 that integrate statistical analysis of weather and meteorological conditions during the sampling period. Also, a wind rose (see Appendix Figure 45) was plotted to show the average wind direction and speed frequencies for the one year sampling period. Descriptive statistics, box-whisker plots, and time series as well as pollution roses present $PM_{2.5}$ species composition, their seasonal variation, and distribution. Pollution roses demonstrate the average wind direction and associated concentration of $PM_{2.5}$ and other species. Three distinct wind vectors (SW, W, SE) were noticed that are associated with the air pollutants. The PMF model results are presented in Sections 4.4 and 4.5.

4.1 DESCRIPTIVE STATISTICS OF SPECIES

Descriptive statistics for the $PM_{2.5}$ and 24 other species that were collected every 3rd day from August 20, 2011 to August 20, 2012 can be found in Table 9. Generally, the air pollution concentrations are within the desirable limits. For instance, the mean $PM_{2.5}$ concentration is 3.8 $\mu g\ m^{-3}$ which is below the mean threshold for $PM_{2.5}$ (30 $\mu g\ m^{-3}$) for 24-hr average. Among the ions the highest mean concentration was observed to be at sulfate (0.916 $\mu g\ m^{-3}$), while potassium had the lowest (0.013 $\mu g\ m^{-3}$). The highest element concentration was found to be sulfur (0.322 $\mu g\ m^{-3}$), followed by sodium (0.142 $\mu g\ m^{-3}$).

Table 10 summarizes descriptive statistics for meteorological variables by season. The main parameters, such as wind speed and direction, T, RH, SR, and pressure that influence $PM_{2.5}$ concentration are presented here. Descriptive statistics for annual meteorological data is provided in Appendix (Table 15).

Table 9 Descriptive statistics of $PM_{2.5}$ mass (µg/m^3) and species mass (µg/m^3) concentration.

	n	Mean	Std	Min	25th Pctl	Median	75th Pctl	Max	LOD*
$PM_{2.5}$	148	3.8447	2.7525	0.0839	1.9413	3.34596	5.11286	13.73	0.04
BC	116	0.283	0.166	0.0545	0.178	0.236	0.314	0.974	0.01
Na^+	166	0.211	0.416	-0.0124	0.0659	0.142	0.217	4.919	0.0003
NH_4^+	166	0.303	0.231	-0.314	0.158	0.247	0.441	1.336	0.0010
K^+	166	0.0125	0.0243	-0.0062	0.0027	0.00851	0.0167	0.249	2.92E-05
Mg^{2+}	166	0.0166	0.0195	-0.0028	0.0065	0.0114	0.0186	0.143	6.63E-05
Ca^{2+}	166	0.0506	0.0391	-0.0135	0.012	0.0497	0.084	0.139	0.000671
NO_3^-	166	0.191	0.208	-0.127	0.0728	0.142	0.233	1.372	0.0030
SO_4^{2-}	166	0.916	1.231	-0.0434	0.3	0.567	1.092	9.503	0.070
Al	149	0.0197	0.0313	0.0089	0.0091	0.00998	0.01959	0.286	0.0182
Ba	150	0.0062	0.00169	0.0031	0.00561	0.00561	0.00561	0.018	0.0112
Br	149	0.0018	0.00100	0.001	0.000996	0.001417	0.00222	0.005	0.001992
Ca	148	0.0190	0.02999	0.0018	0.008372	0.013852	0.02081	0.301	0.00369
Cl	148	0.0964	0.17335	0.0019	0.004942	0.02879	0.11181	1.060	0.00372
Cu	148	0.0013	0.00078	0.0006	0.000858	0.001176	0.00151	0.006	0.00127
Fe	148	0.0219	0.03301	0.0008	0.009284	0.014765	0.02473	0.316	0.001584
K	148	0.0253	0.02055	0.0017	0.01333	0.021901	0.02992	0.140	0.00348
Mg	148	0.0213	0.02316	0.0039	0.006126	0.015647	0.02602	0.139	0.00774
Mn	150	0.0010	0.00058	0.0005	0.000843	0.000843	0.00097	0.007	0.001686
Na	148	0.1418	0.15726	0.0089	0.03802	0.105078	0.18086	0.926	0.01782
Ni	149	0.0010	0.00127	0.0004	0.000459	0.00059	0.00125	0.014	0.000918
S	148	0.3217	0.25425	0.0022	0.182877	0.276063	0.41024	1.813	0.00447
Si	148	0.0500	0.13568	0.0044	0.009687	0.023616	0.04238	1.240	0.00885
V	149	0.0027	0.00200	0.0016	0.001614	0.001902	0.00294	0.017	0.003228
Zn	148	0.0026	0.00194	0.0007	0.001199	0.002164	0.00332	0.010	0.001464

*LOD = Limit of detection

Table 10 Descriptive statistics for the meteorological variables by season.

	Sample Metrics	n	Mean	Std	Min	25th Pctl	Median	75th Pctl	Max
Winter	Wind direction (º)	29	203	66.947	59	135.5	225	238.75	323
	Wind Speed (m/sec)	29	8.351	4.438	2.143	4.97	7.495	12.06	16.423
	Temperature (ºC)	29	0.249	4.743	-9.12	-2.621	0.899	3.149	9.192
	Relative Humidity (%)	29	77.178	10.891	53.637	69.291	77.194	85.895	94.592
	Solar Radiation (W/m^2)	29	0.507	0.257	0.0305	0.326	0.467	0.687	1.07
	Pressure (kPa)	29	97.811	5.43	84.785	93.975	100.576	101.775	102.962
Spring	Wind direction (º)	30	199	105.211	7	139	239.5	277	317
	Wind Speed (m/sec)	30	9.016	3.594	3.919	6.484	7.975	10.435	18.151
	Temperature (ºC)	30	7.271	6.042	-6.284	3.64	7.907	10.694	21.753
	Relative Humidity (%)	30	70.366	14.791	49.204	56.324	70.625	83.706	96.017
	Solar Radiation (W/m^2)	30	1.736	0.994	0.37	0.801	1.52	2.642	3.247
	Pressure (kPa)	30	101.421	0.833	99.843	100.908	101.518	102.032	103.068
Summer	Wind direction (º)	27	224	108.17	9	149.25	264	307	359
	Wind Speed (m/sec)	27	6.248	3.222	1.89	3.893	5.629	8.303	12.695
	Temperature (ºC)	27	18.659	3.505	9.965	17.561	19.233	20.729	22.674
	Relative Humidity (%)	27	79.812	12.318	52.415	70.625	81.869	90.113	95.945
	Solar Radiation (W/m^2)	27	2.02	0.903	0.503	1.16	2.235	2.841	3.11
	Pressure (kPa)	27	70.453	45.256	3.955	4.01	100.678	101.112	102.35
Fall	Wind direction (º)	30	175	57.722	108	121	161	225	314
	Wind Speed (m/sec)	30	8.637	6.796	0	3.229	5.975	13.568	23.306
	Temperature (ºC)	30	12.595	5.869	-0.143	7.989	12.979	17.987	22.071
	Relative	30	81.556	9.411	59.952	76.176	82.356	89.183	97.377

	Sample Metrics	n	Mean	Std	Min	25th Pctl	Median	75th Pctl	Max
	Humidity (%)								
	Solar Radiation (W/m^2)	30	1.035	0.665	0.0181	0.444	1.112	1.578	2.319
	Pressure (kPa)	30	101.046	1.514	94.335	100.716	101.288	101.708	103.071

4.2 ANALYSIS OF $PM_{2.5}$ AND ITS COMPONENTS

Seasonal patterns of total $PM_{2.5}$ mass concentration were plotted in Figure 6. The box plots suggest a normal distribution (normally skewed), but this will be tested and shown in our table of descriptive statistics. Detailed information on seasonal variation can be found in the Appendix which was calculated using the Kruskal-Wallis ANOVA test. It reports that the highest median value is 3.85 µg m^{-3} (summer) and the lowest is 2.67 µg m^{-3} (winter). Moreover, the results show that there is no significant seasonal variation in Halifax with a high p-value (P = 0.659). The analysis was completed using the One Way ANOVA test in SigmaPlot (v 12.0).

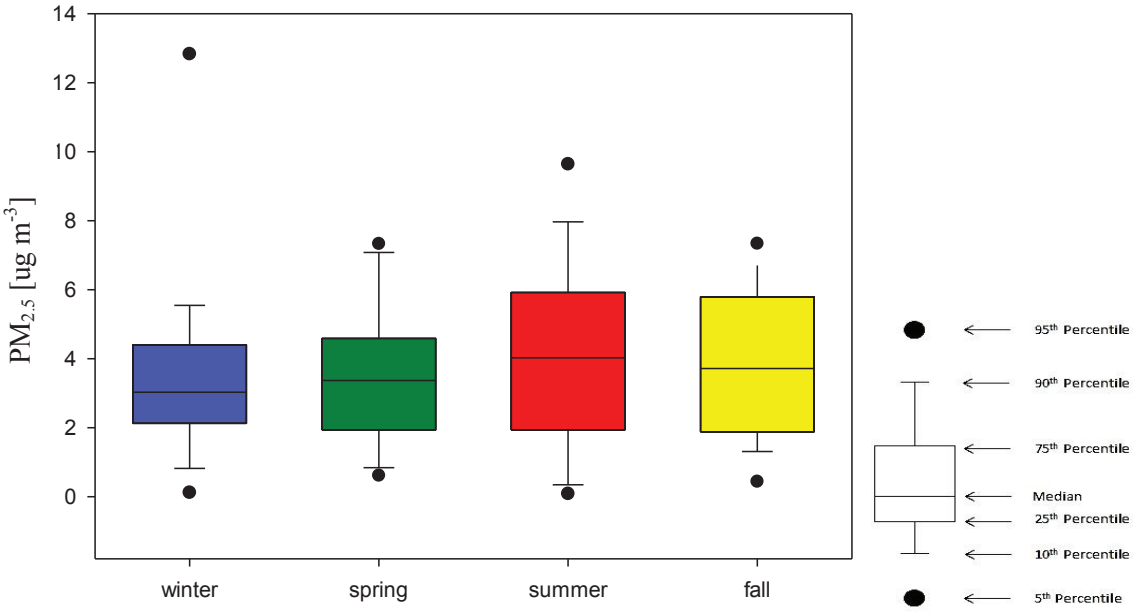

Figure 6 Box plot of total $PM_{2.5}$ mass values by season.

Figure 7 shows a box plot of monthly variability of $PM_{2.5}$ concentration with high median values during August (~5 µg m^{-3}) and November (~ 6 µg m^{-3}). We can notice a gradual increase in median $PM_{2.5}$ concentration while moving towards August and a slight decrease after. However, the median concentration rises in November followed by the extreme values in December. Mostly, the box plots represent low values in the winter period. The nature of the extreme events will be examined and discussed in the next chapter. Generally, there is no significant monthly variability in mean $PM_{2.5}$ concentrations in the small area of Halifax.

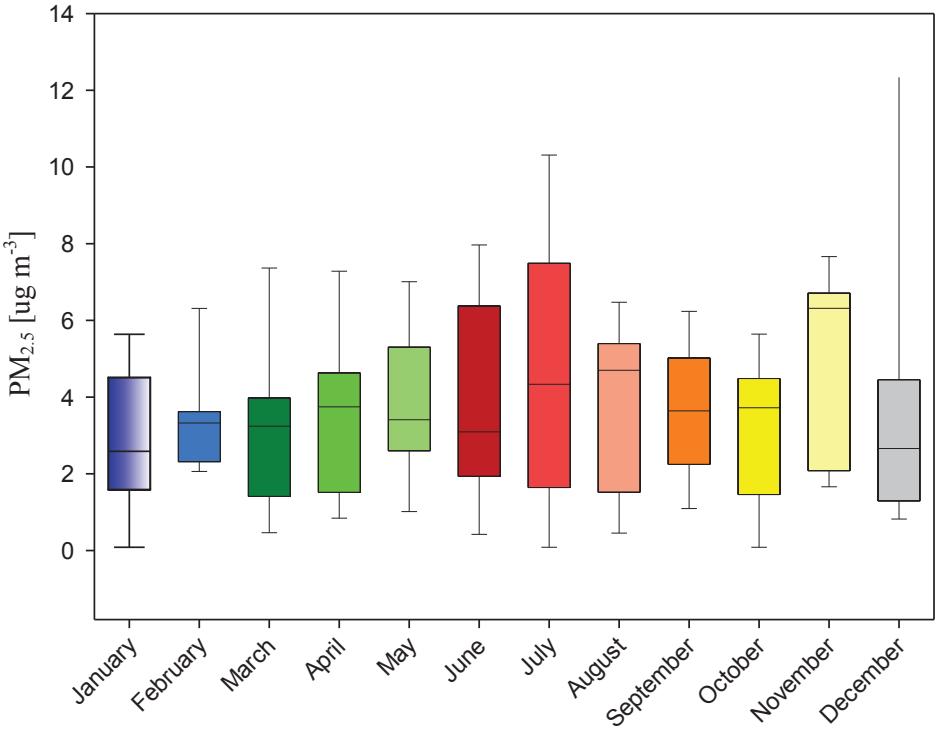

Figure 7 Box plot of monthly $PM_{2.5}$ concentration.

The box-whisker plots in Figures 8 through 12 represent concentrations of air pollutants measured at the sampling site during the one year sampling campaign. The figures show the major and minor components of $PM_{2.5}$. Box plots help to understand the spread of data and provide insight into the central tendency and the variance on the range of data by means of non-parametric visualization.

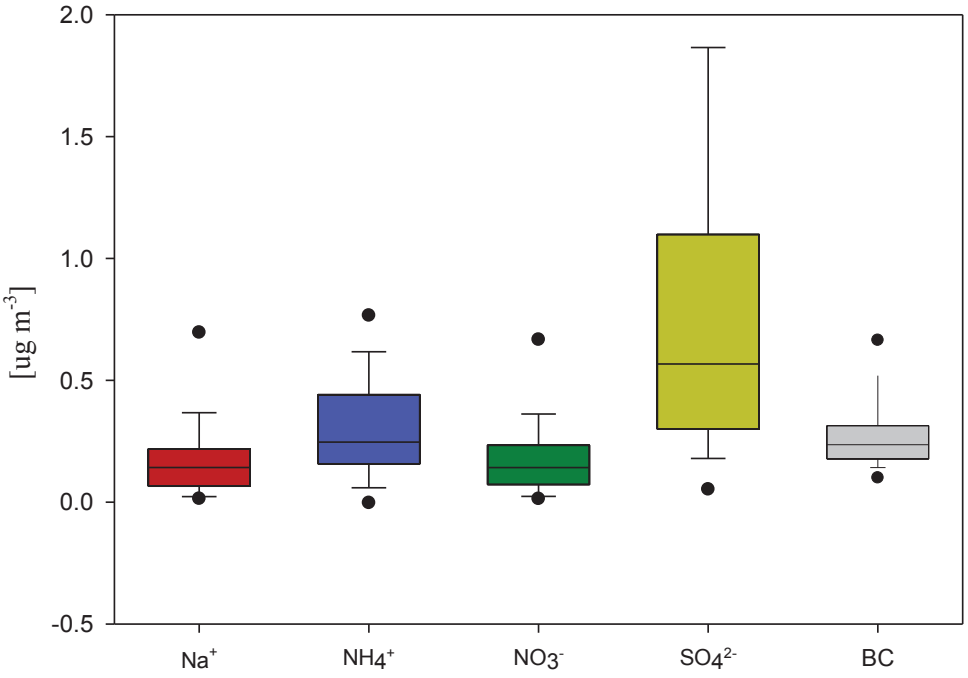

Figure 8 Box plot of anion, cation and BC species concentration.

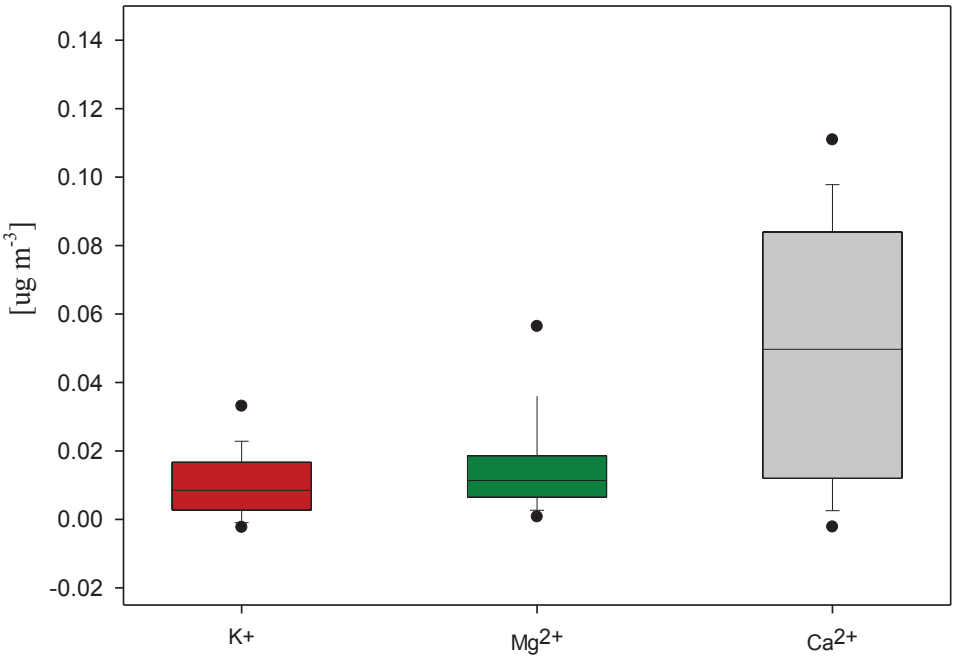

Figure 9 Box plot of cation components of $PM_{2.5}$.

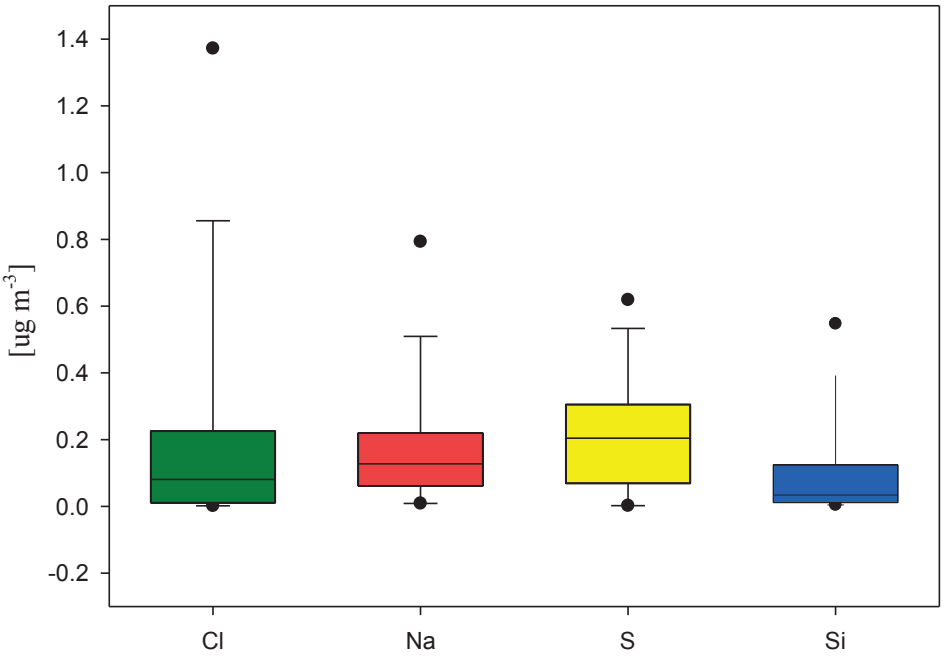

Figure 10 Box plot of Cl, Na, S and Si contribution to $PM_{2.5}$.

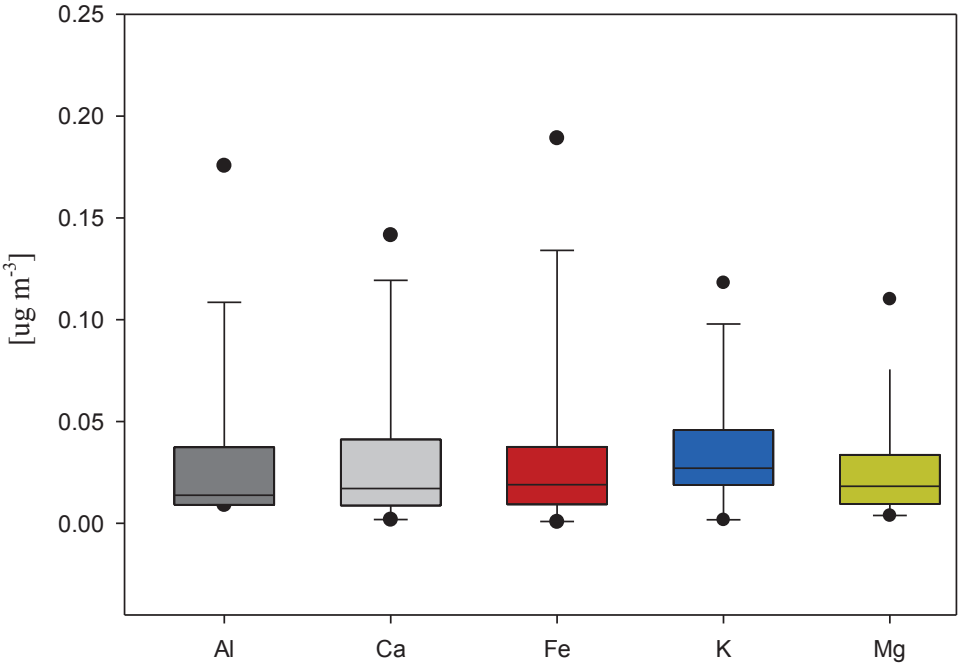

Figure 11 Box plot of Al, Ca, Fe, K and Mg contribution to $PM_{2.5}$.

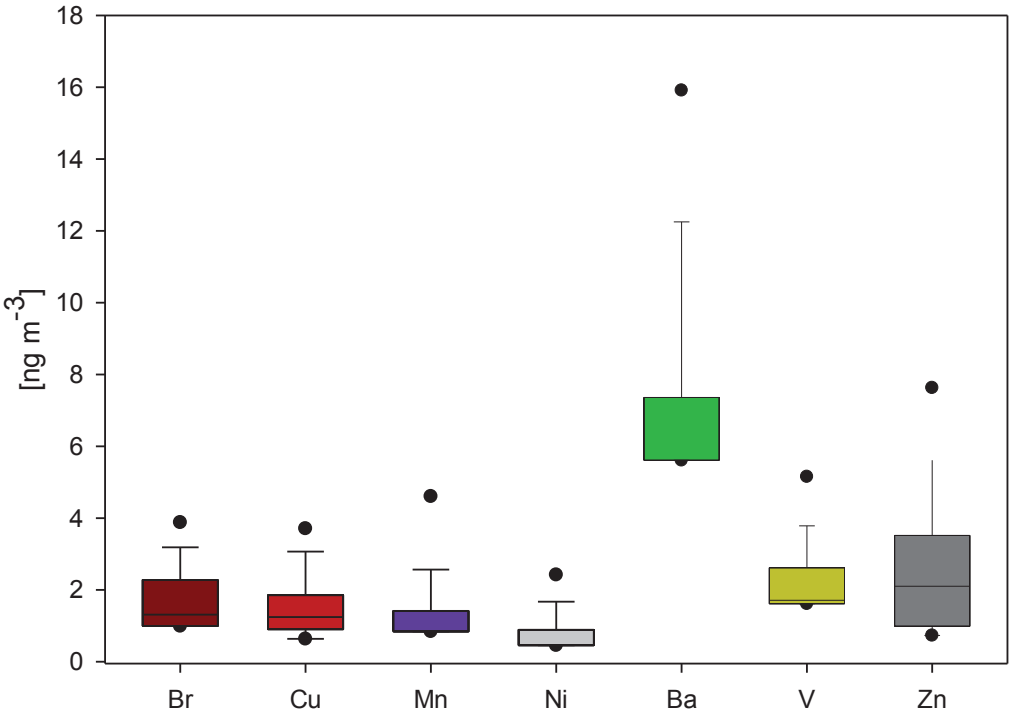

Figure 12 Box plot of Ba, Br, Cu, Mn, Ni, V and Zn contribution to $PM_{2.5}$.

Figure 13 through Figure 21 represent annual time series plot of $PM_{2.5}$ components that were sampled from August 20, 2011 to August 20, 2012. Plots clearly indicate extreme events within the one year sampling campaign. The reason for abnormal values will be discussed in the next chapter. Looking at the variation of several species, it can be noticed that some of them line up with each other indicating on a common source.

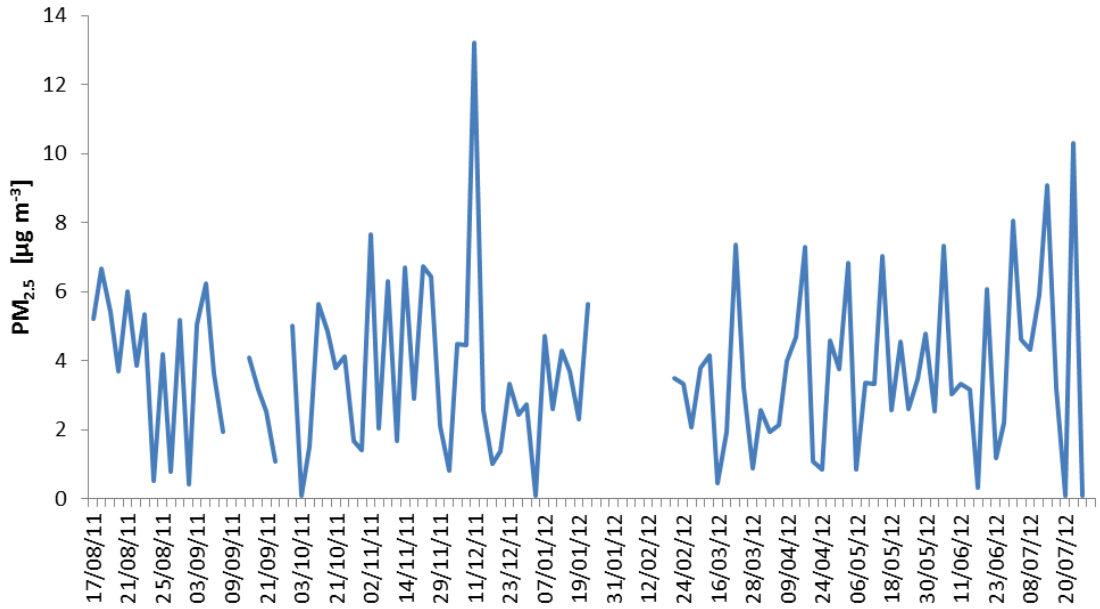

Figure 13 Time series plot of total $PM_{2.5}$ mass concentration.

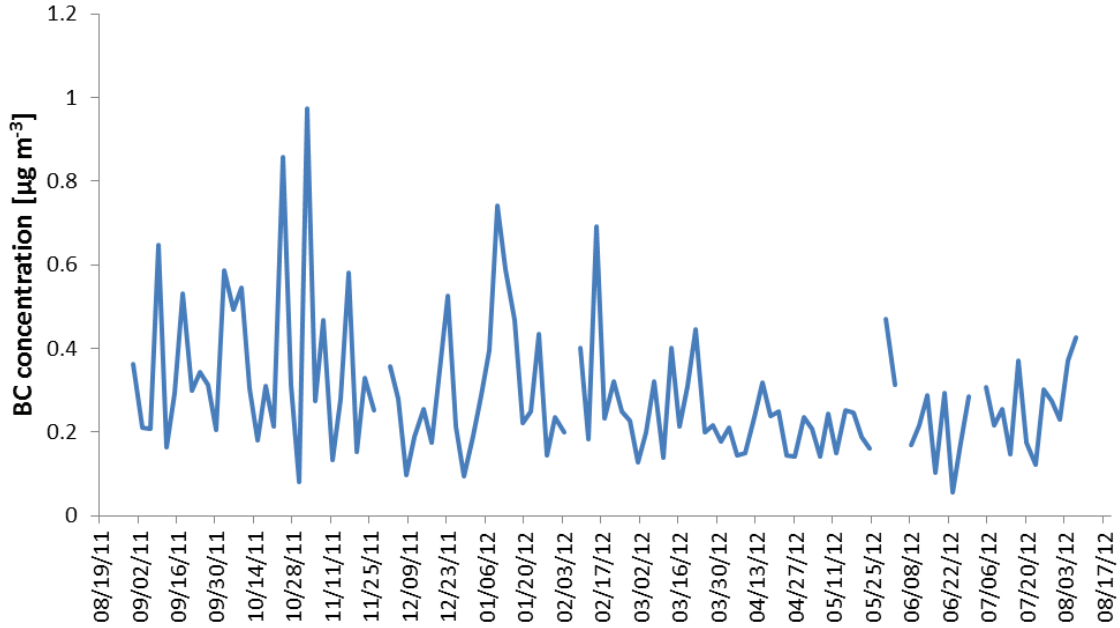

Figure 14 Time series plot of BC mass concentration.

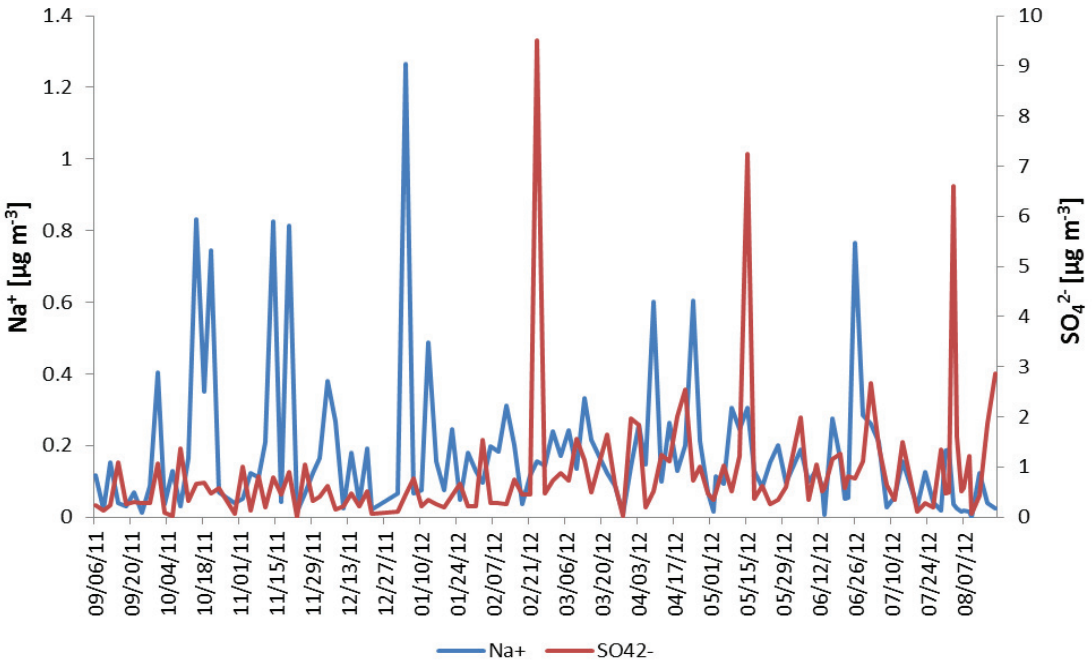

Figure 15 Time series plot of anions/cations mass concentration.

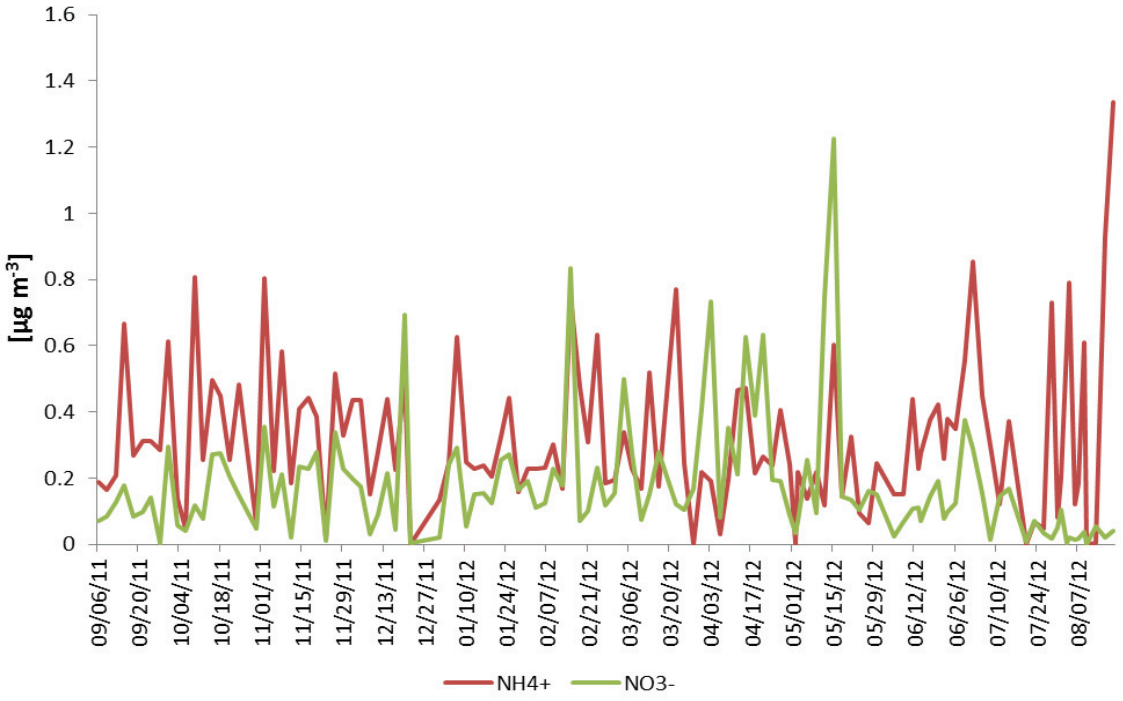

Figure 16 Time series plot of NH_4^+ and NO_3^- mass concentration.

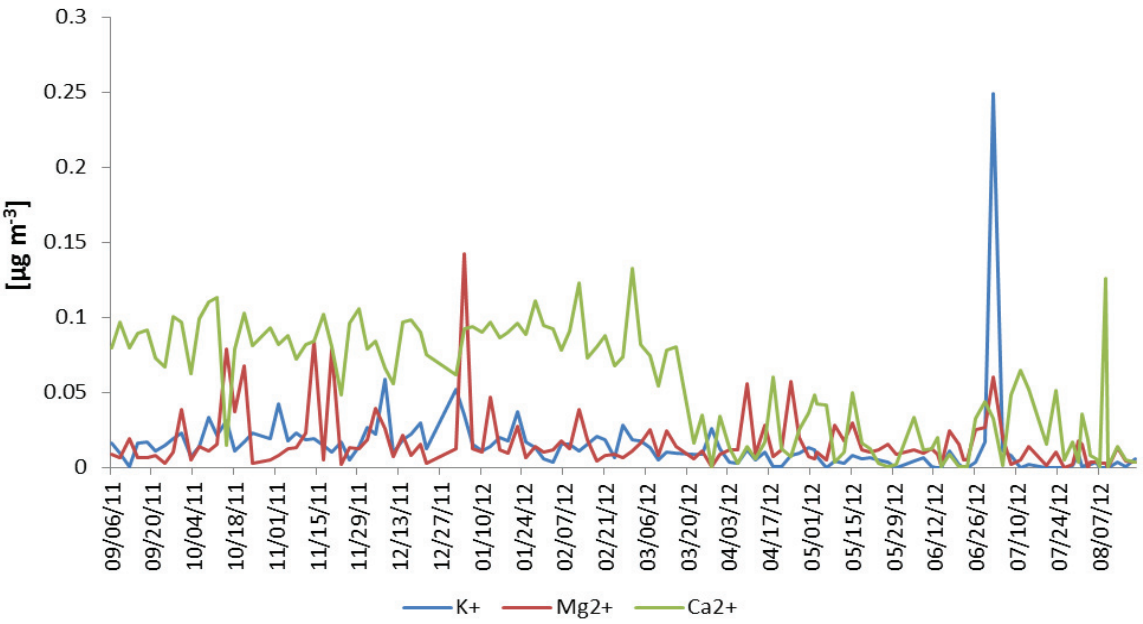

Figure 17 Time series plot of K^+, Mg^{2+} and Ca^{2+} mass concentration.

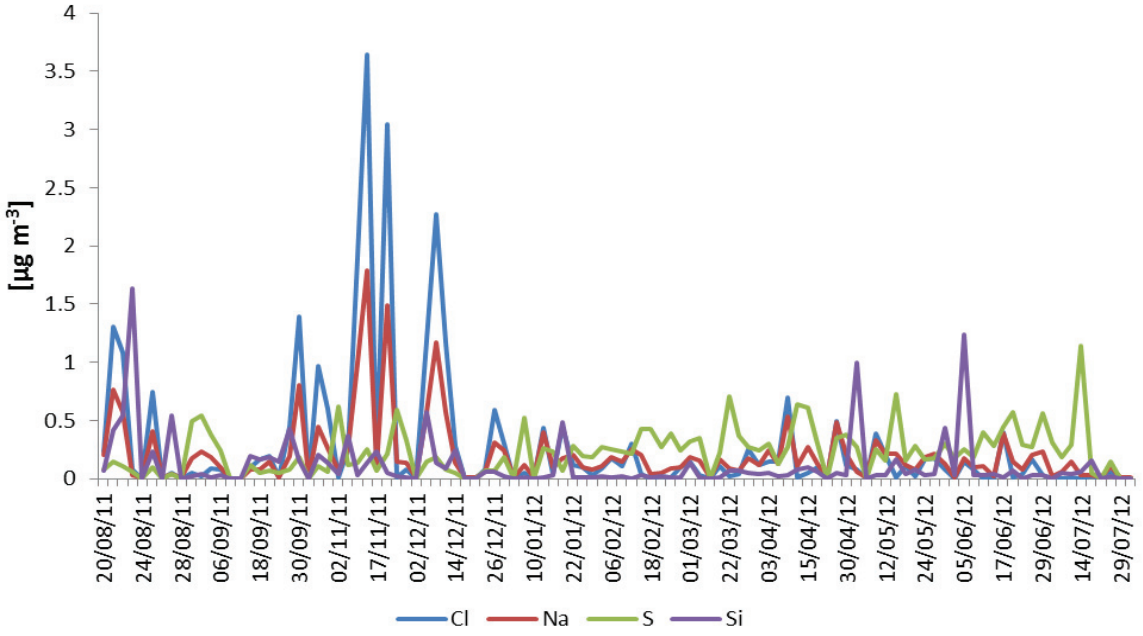

Figure 18 Time series plot of Cl, Na, S and Si mass concentration.

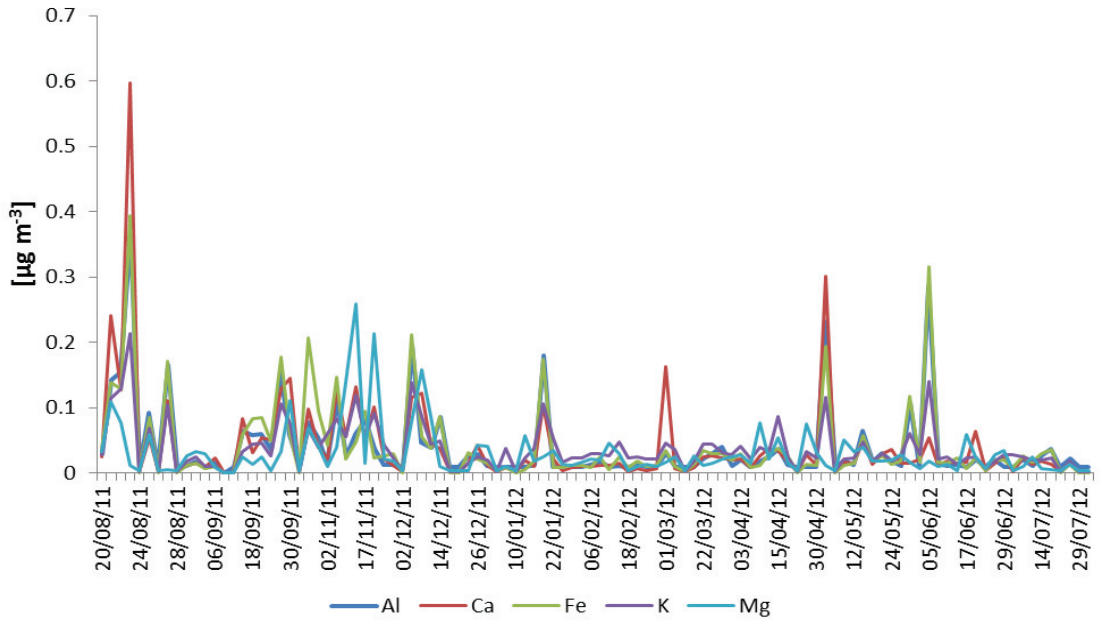

Figure 19 Time series plot of Al, Ca, Fe, K and Mg mass concentration.

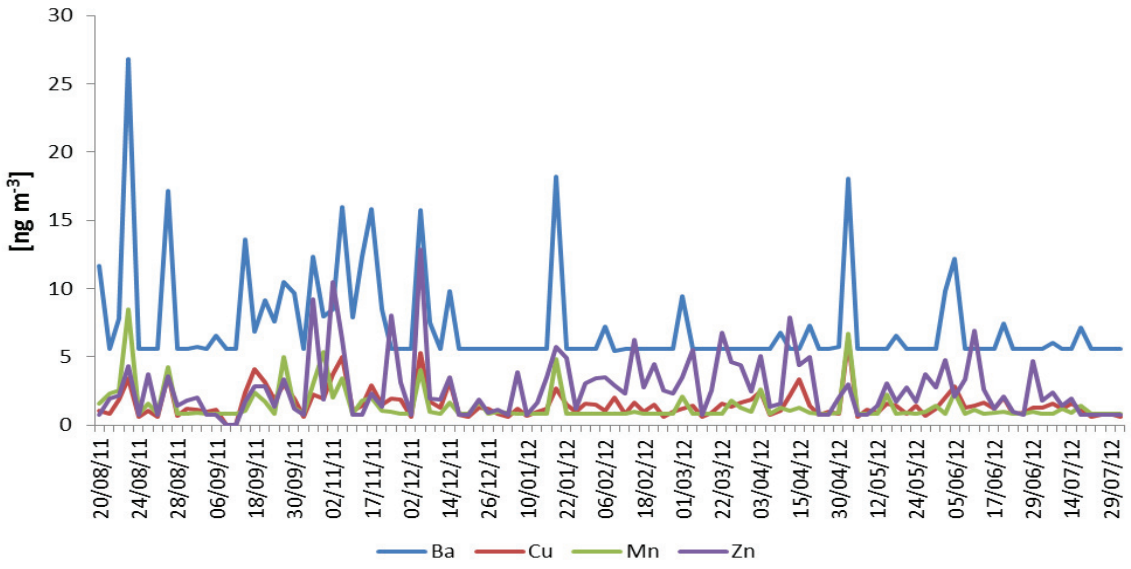

Figure 20 Time series plot of Ba, Cu, Mn and Zn mass concentration.

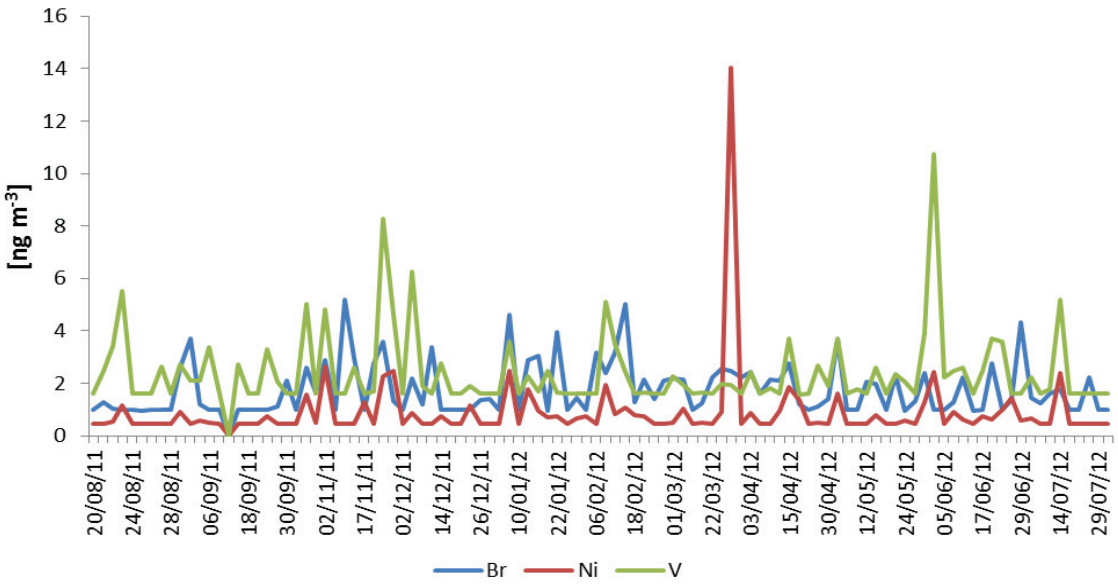

Figure 21 Time series plot of Br, Ni and V mass concentration.

4.3 SEASONAL DISTRIBUTION OF THE NUMBER OF SHIPS

Additional information to support PMF output was obtained from Marinetraffic.com. Figure 22 illustrates the total number of ships as well as the number of cargo ships, tankers, and cruise ships observed in Halifax port within a one year period of study (August 20, 2011 to August 20, 2012). Cargo ships were calculated by summing up general cargo, Ro-Ro cargo, and container cargo ships. Tankers represent products, chemical, and crude/oil products tankers. The bar chart is useful for validating the PMF model results of seasonal ship emissions contribution.

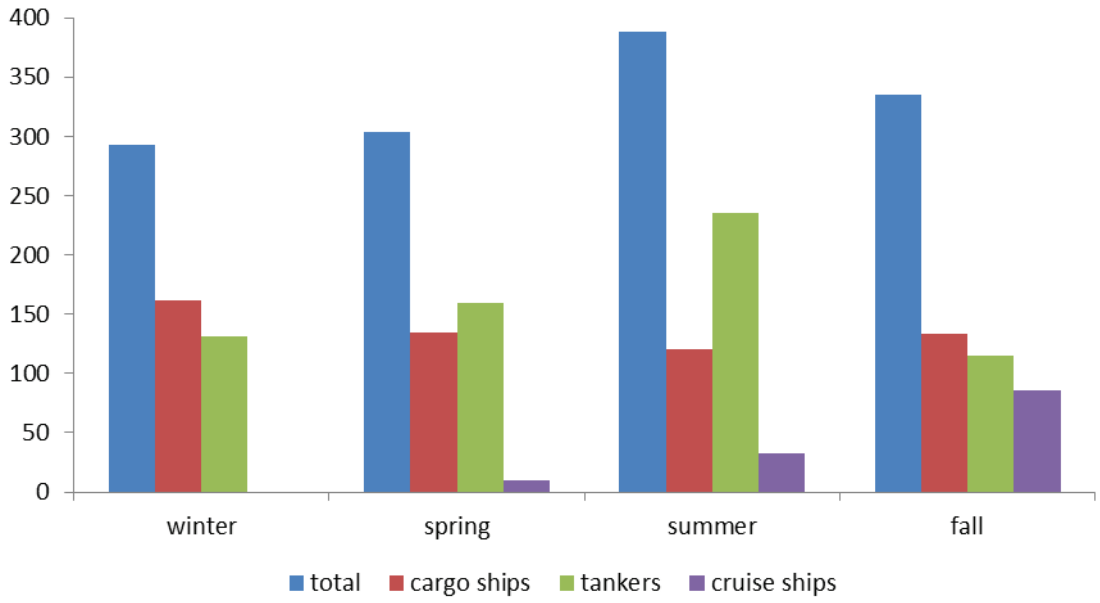

Figure 22 Number of cargo, cruise ships and tankers in Halifax port for the period of August 20, 2011 to August 20, 2012.

4.4 POSITIVE MATRIX FACTORIZATION MODEL EVALUATION

The base run model summary is presented in Table 11 with Q (robust) and Q (true) and shows that all runs were converged. Q (robust), which is the object function of the model without outliers, is almost at the same magnitude as Q (true) (with outliers) which means that extreme events proportionally influence the model. Observed versus PMF predicted time series for several species are illustrated in Figures 23 and 24. The time series variation as well as R^2 indicate a good correlation of predicted and observed concentrations. The histogram in Figure 25 demonstrates how well the model fit V within the scale +1 and -1 and the normal distribution of the residuals. Some extreme events were found during analyzing time series plots which were removed from the data set in order to improve the model output. An example of a peak event (shown as a pink point) is presented in Figure 26.

The bootstrap run model results that estimate the stability of the model are summarized in Table 12 and Figures 27 and 28. More detailed information on bootstrapping is described in Section 3.7. It can be seen that 96 bootstrap runs were matched to base runs in Factor 3 and 5, while other factors showed a perfect match (100). Figures 27 and 28 represent variability in percentage and concentration for Ship emissions and Vehicles and re-suspended gypsum factors. They were compared with factor profiles obtained from base run results for analyzing any deviations. Even though Fpeak runs, that estimate the stability of the rotational ambiguity, were set to zero as was discussed in Section 3.7, the results are displayed in Table 13 and Figures 29 and 30 indicating similarity with the base run output.

Table 11 Base model run summary.

Run number	Q(Robust)	Q(True)	Converged
1	1105.4	1127	Yes
2	1105.1	1126.6	Yes
3	1105.1	1126.6	Yes
4	1105.1	1126.6	Yes
5	1105.8	1127.7	Yes
6	1105.1	1126.6	Yes
7	1105.1	1126.6	Yes
8	1105.5	1127.4	Yes
9	1105.1	1126.6	Yes
10	1105.1	1126.6	Yes
11	1105.1	1126.6	Yes
12	1105.1	1126.6	Yes
13	1105.1	1126.6	Yes
14	1105.1	1126.6	Yes
15	1105.1	1126.6	Yes
16	1105.1	1126.6	Yes
17	1105.1	1126.6	Yes
18	1157.3	1225.8	Yes
19	1105.1	1126.6	Yes
20	1105.1	1126.6	Yes

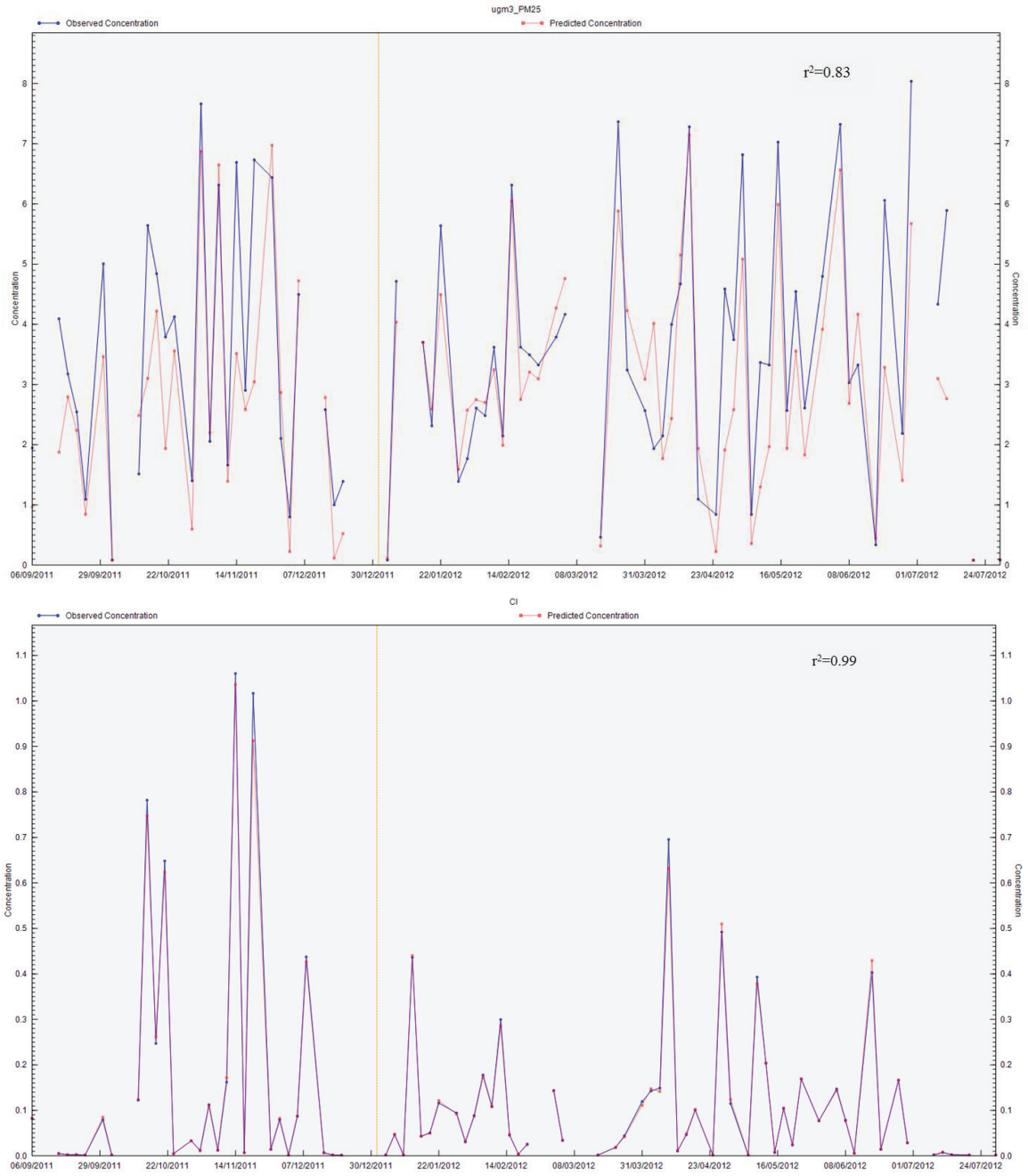

Figure 23 PMF observed versus predicted time series of $PM_{2.5}$ (top) and Cl (bottom).

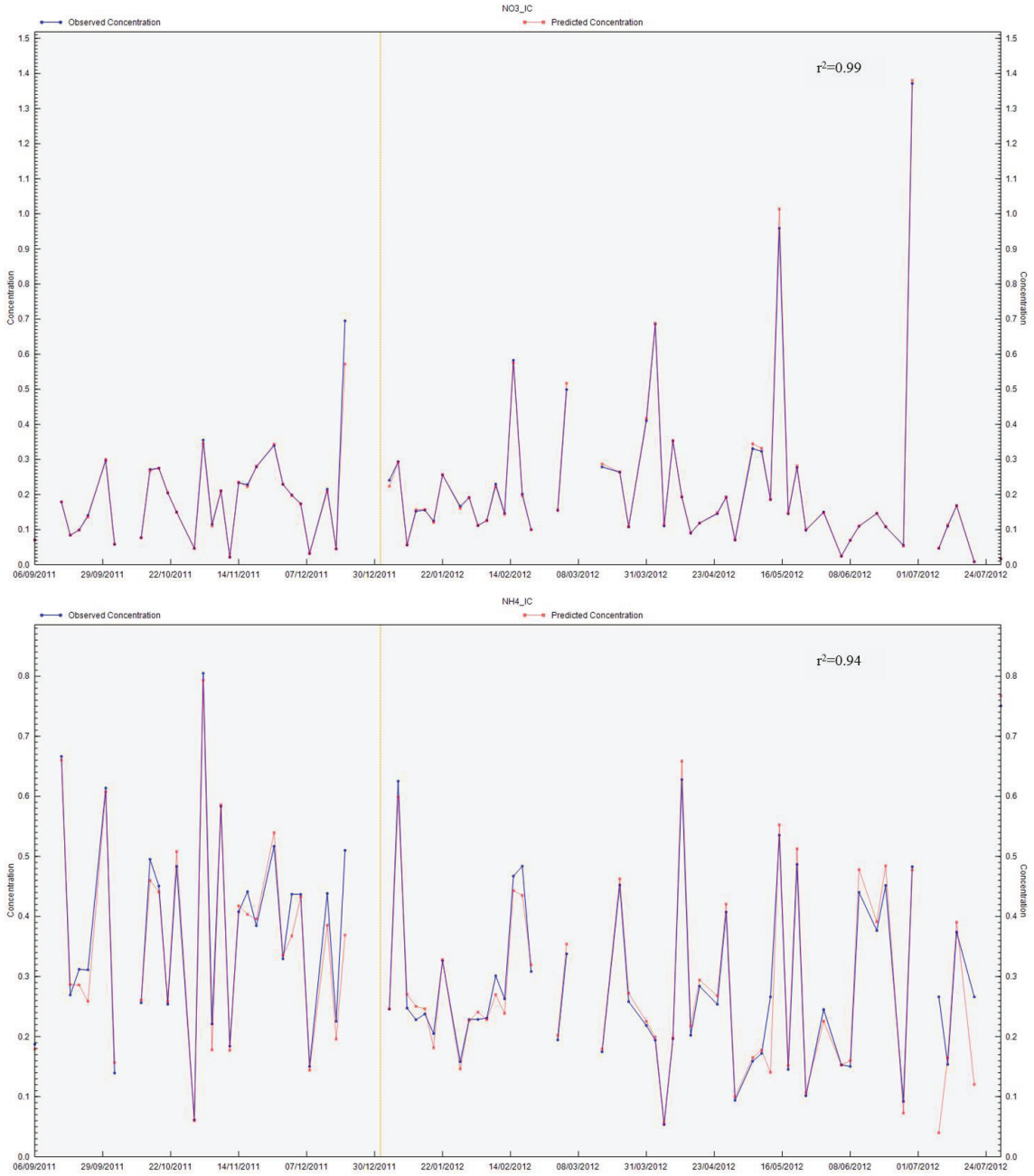

Figure 24 PMF observed versus predicted time series of NO_3 (top) and NH_4 (bottom).

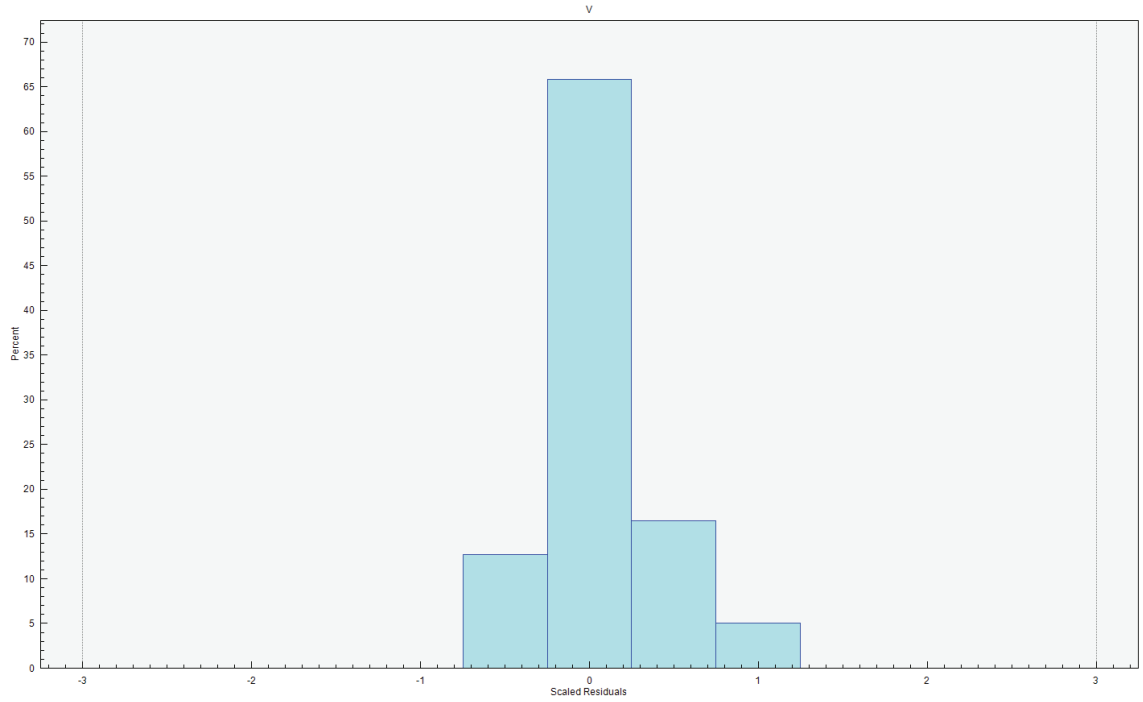

Figure 25 Scaled residuals for V.

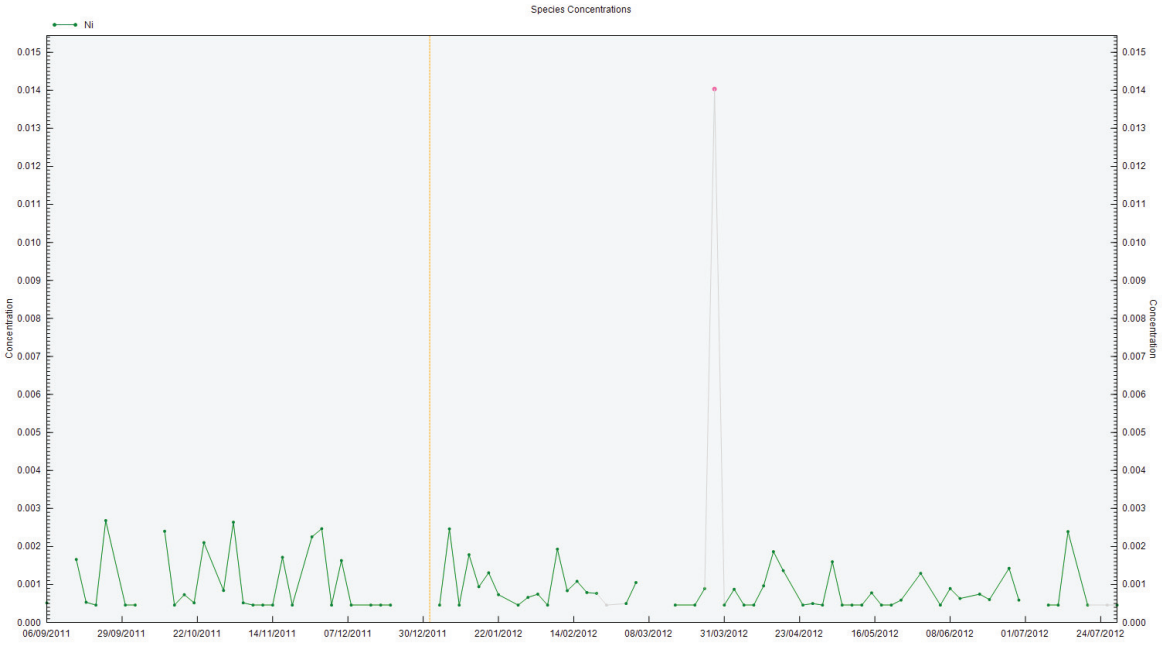

Figure 26 Ni time series plot indicating an extreme event (pink point).

Table 12 Mapping of bootstrap factors to base factors.

	Base Factor 1	Base Factor 2	Base Factor 3	Base Factor 4	Base Factor 5	Base Factor 6	Unmapped
Boot Factor 1	100	0	0	0	0	0	0
Boot Factor 2	0	100	0	0	0	0	0
Boot Factor 3	0	0	96	0	1	0	3
Boot Factor 4	0	0	0	100	0	0	0
Boot Factor 5	0	1	0	1	96	0	2
Boot Factor 6	0	0	0	0	1	99	0

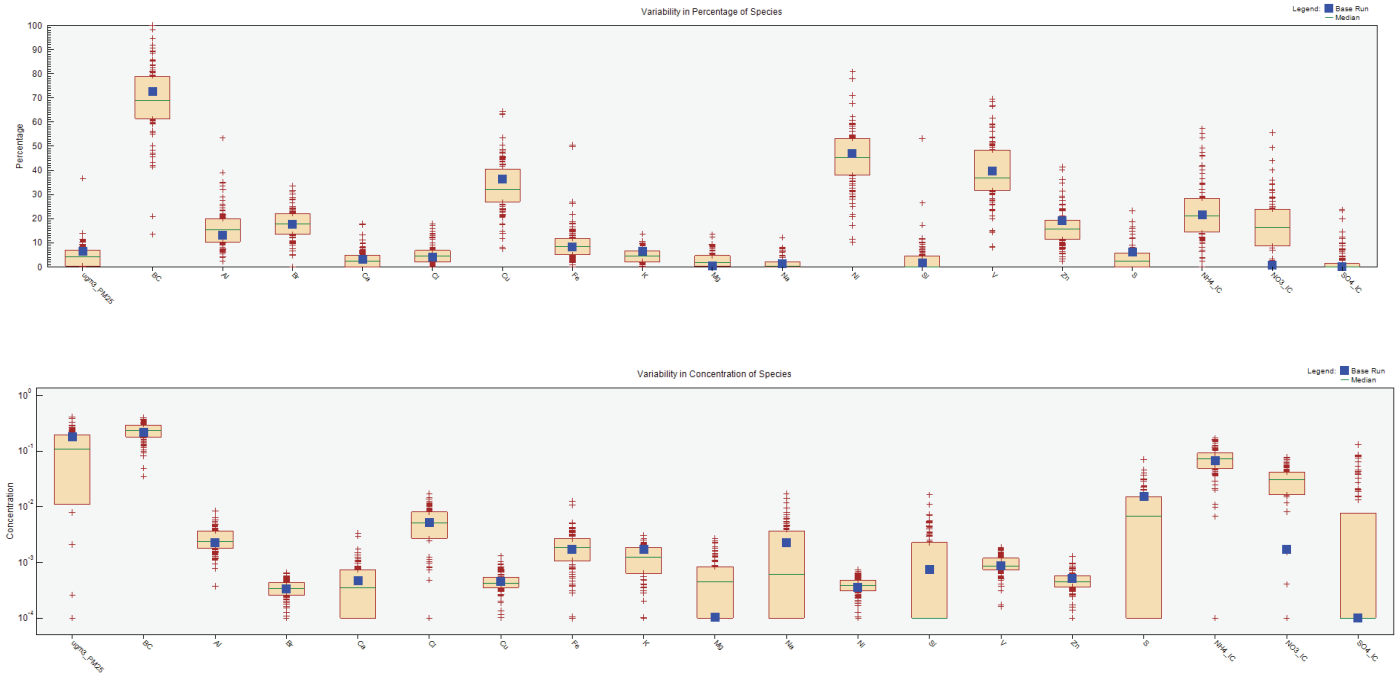

Figure 27 Ship emissions factor bootstrap box plots.

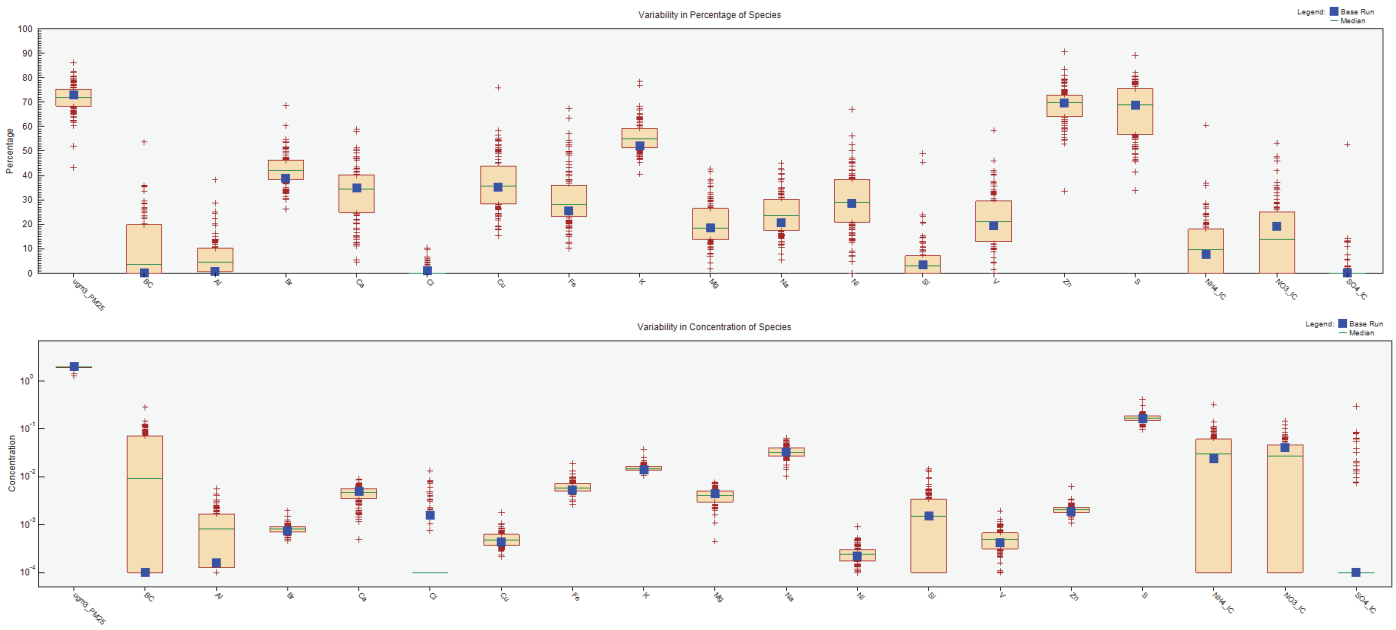

Figure 28 Vehicles and re-suspended gypsum factor bootstrap box plots.

Table 13 Fpeak model run summary.

Fpeak #	Strength	Q(Robust)	Q(True)	Converged
1	0.1	1112.9	1127	Yes
2	0.2	1136.6	1127.9	Yes
3	0.3	1177.3	1129.4	Yes
4	0.4	1239.3	1132.5	Yes
5	0.5	1316.2	1134.9	Yes

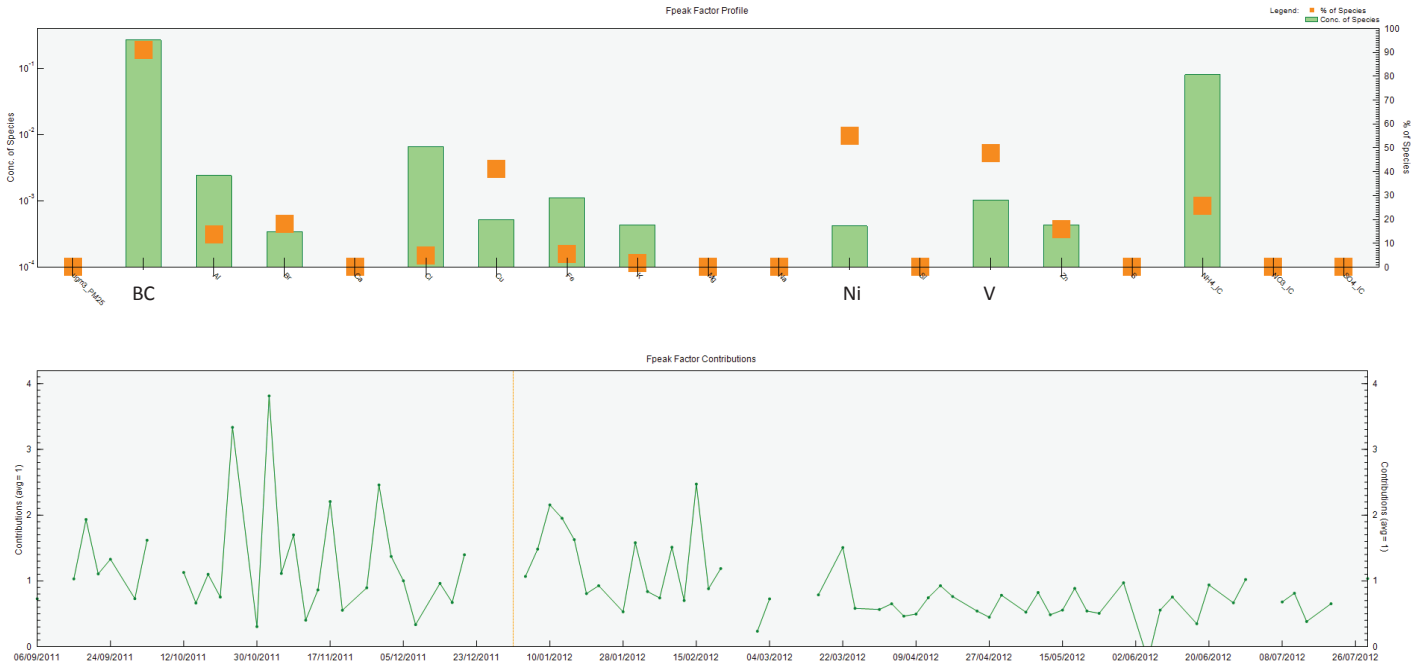

Figure 29 Ship emissions factor Fpeak profiles (top panel) and Fpeak factor contributions (bottom panel).

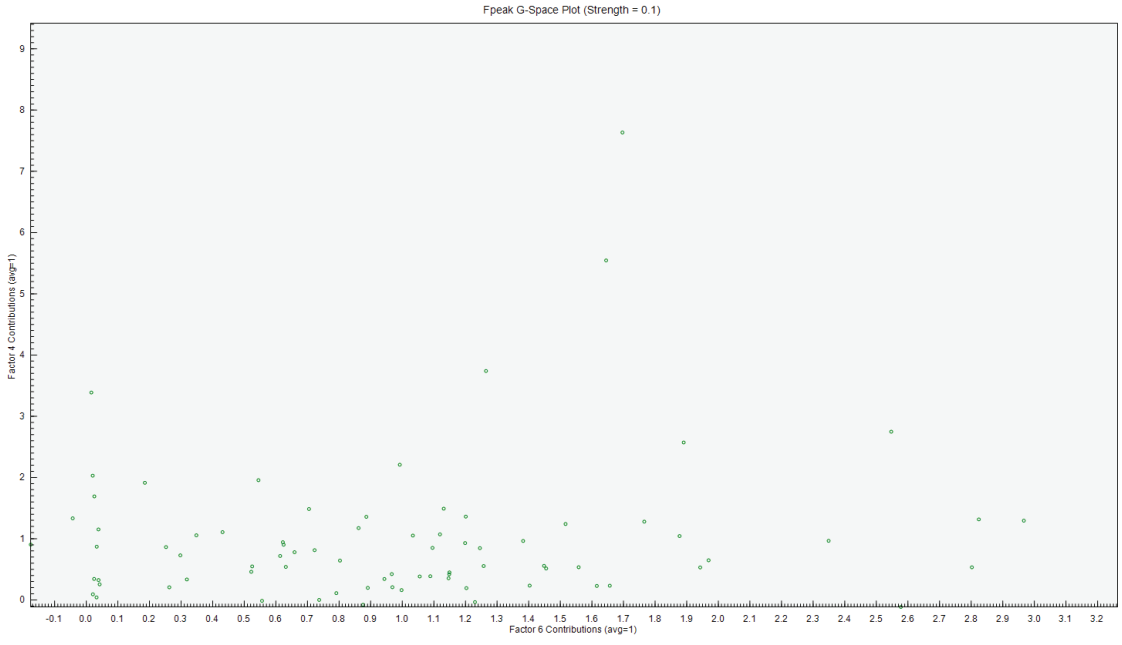

Figure 30 G-Space plot indicating independence between Factor 4 and Factor 6.

4.5 POSITIVE MATRIX FACTORIZATION MODEL RESULTS

Six factors (~ sources) resolved by PMF are presented in Figures 31-36. The top panel shows the factor profile with a red box denoting the percent of each species attributed to the factor and a blue bar denoting the mass of each species attributed to the factor. The bottom panel displays the contribution of the factor to the total mass. Yearly, seasonal, and weekday/weekend contribution of each source can be found in Figures 37-42. Descriptive statistics of seasonal Ship emission source contributions were generated by SigmaPlot (v 12.0) and presented in Table 14. The mass contributions of the six sources and their directional dependence are demonstrated in the source contribution rose (Figure 43). A pie chart in Figure 44 represents an average mass concentration of apportioned sources and percentage source contributions over the one year sampling campaign.

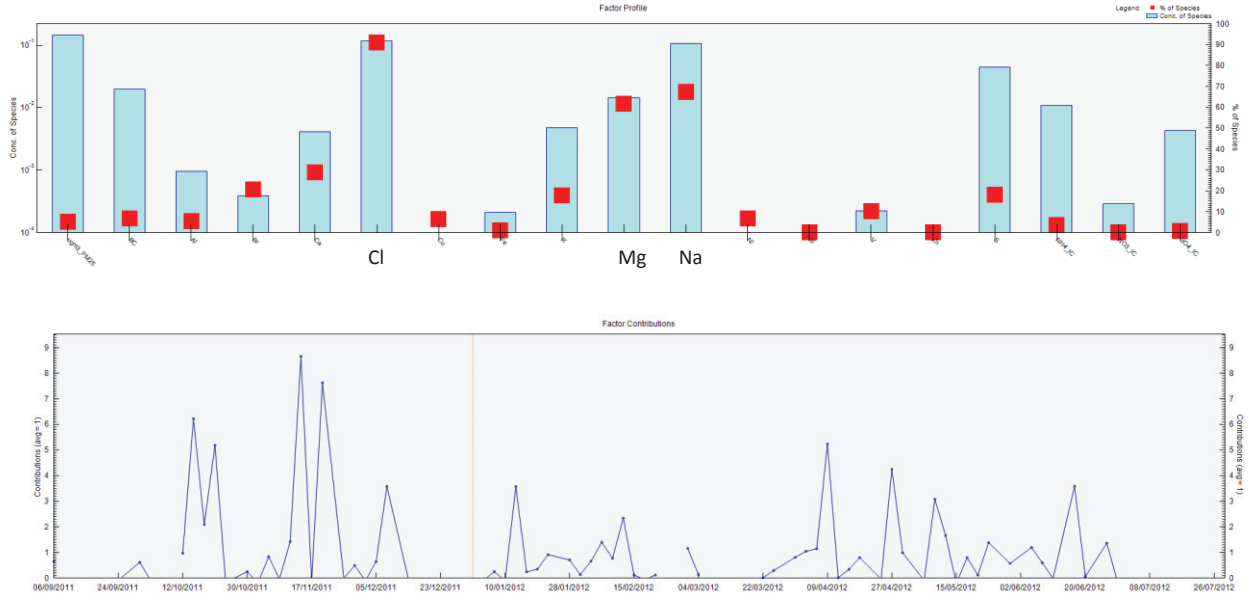

Figure 31 Sea salt factor profiles (top panel) and factor contributions (bottom panel).

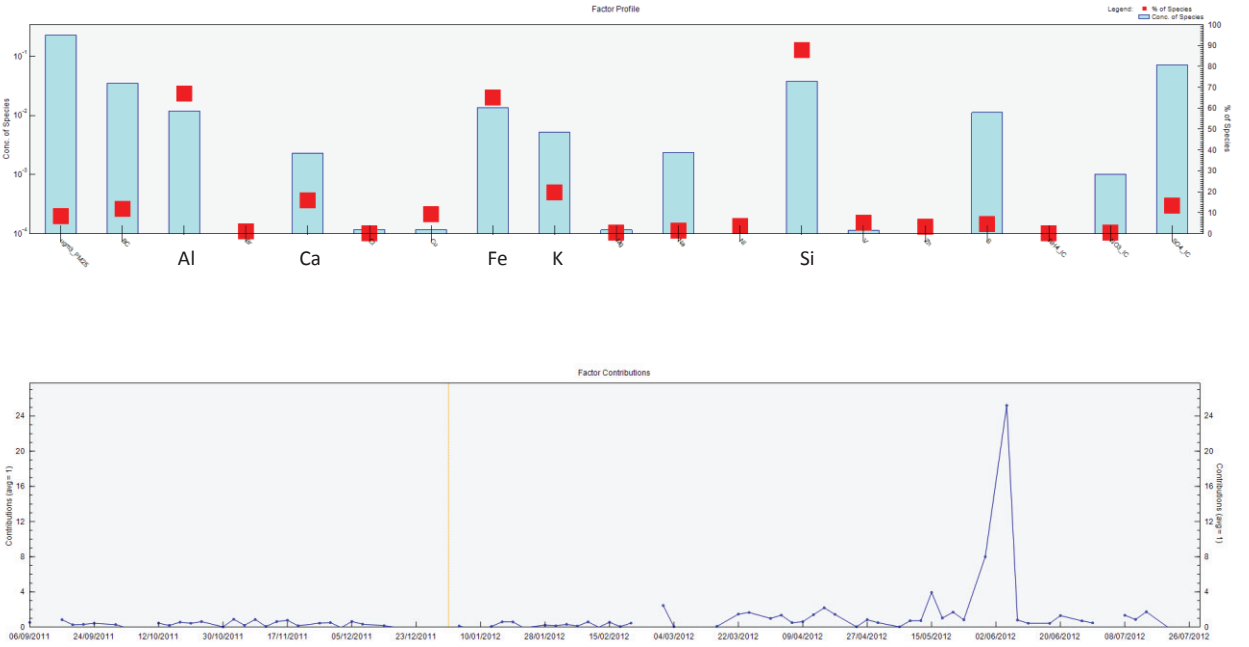

Figure 32 Surface dust factor profiles (top panel) and factor contributions (bottom panel).

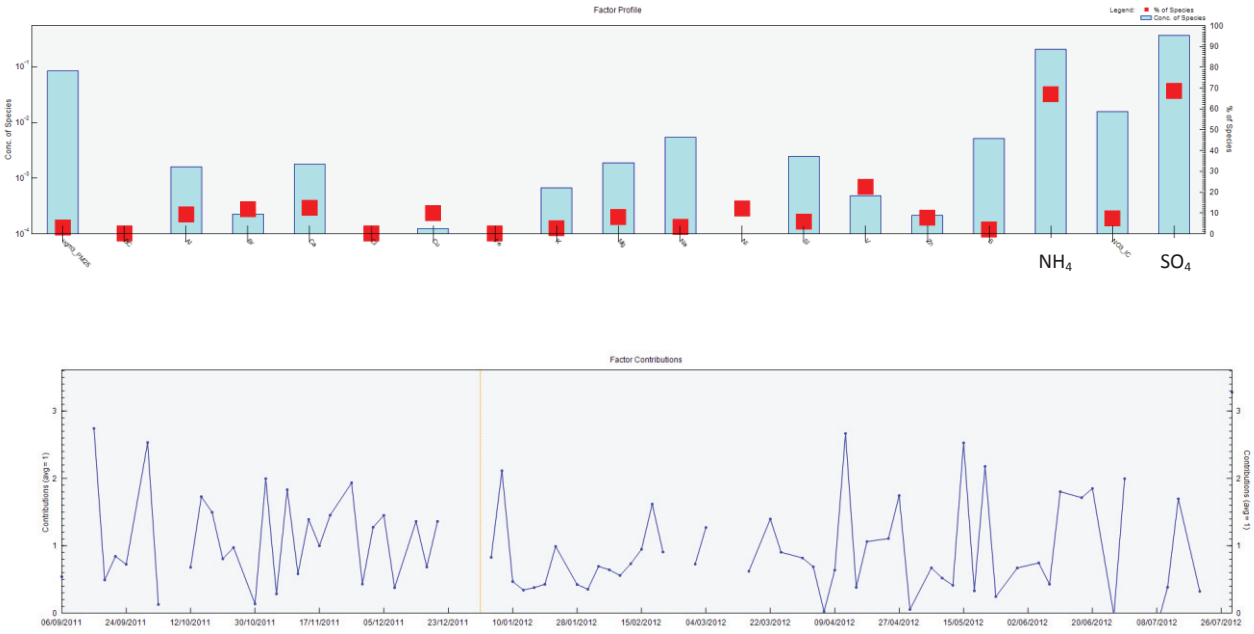

Figure 33 LRT Secondary (ammonium sulfate) factor profiles (top panel) and factor contributions (bottom panel).

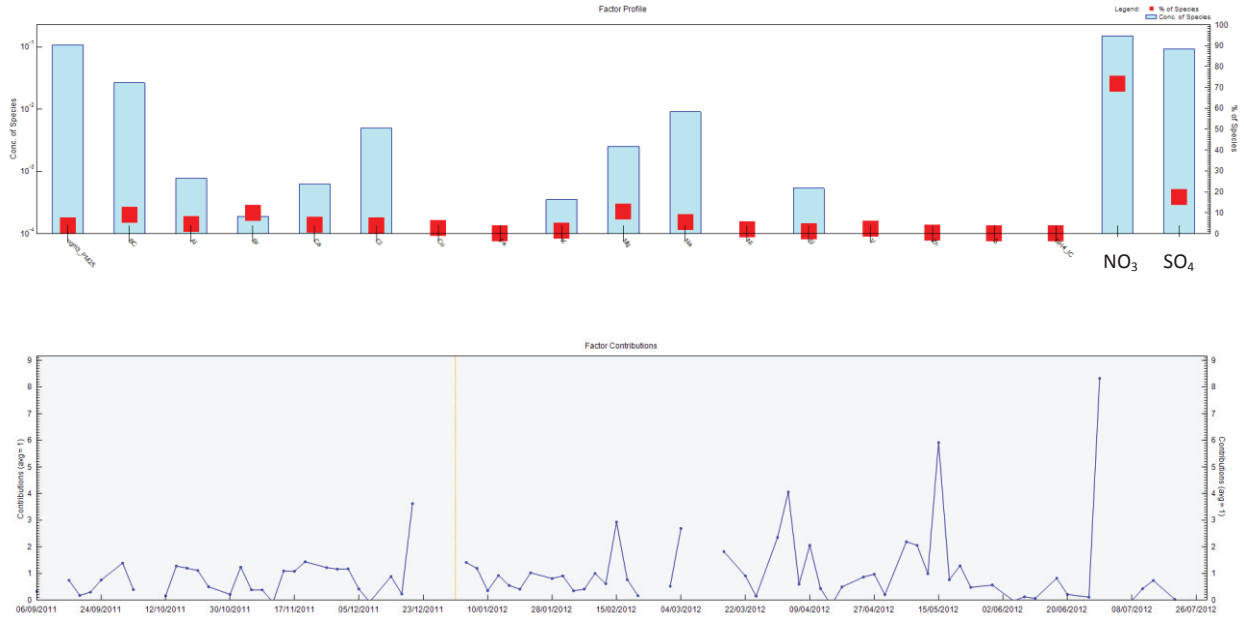

Figure 34 LRT Secondary (nitrate and sulfate) factor profiles (top panel) and factor contributions (bottom panel).

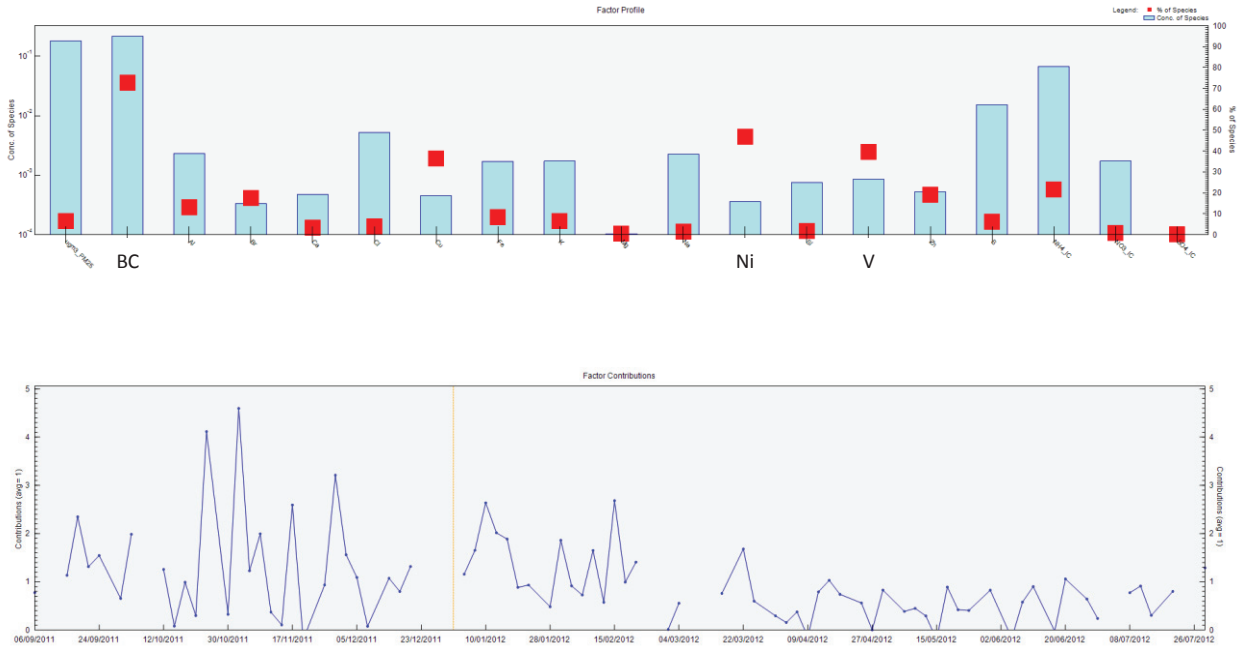

Figure 35 Ship emissions factor profiles (top panel) and factor contributions (bottom panel).

Figure 36 Vehicles and re-suspended gypsum factor profiles (top panel) and factor contributions (bottom panel).

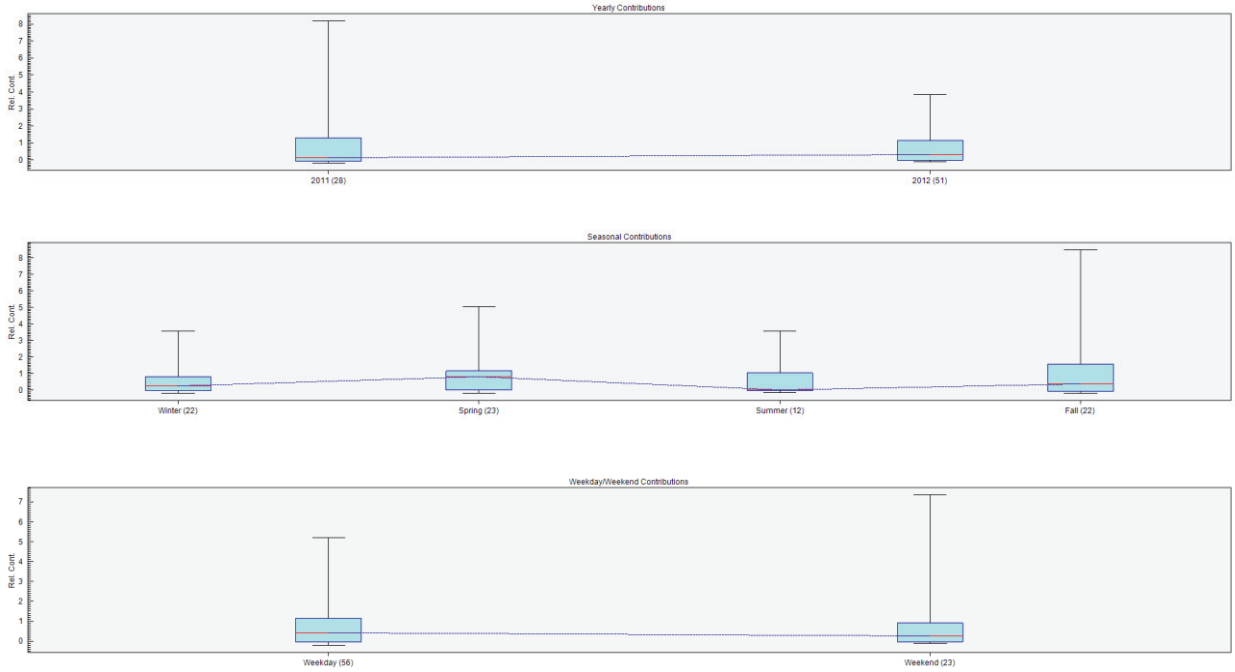

Figure 37 Yearly, seasonal and weekday/weekend Sea salt contributions.

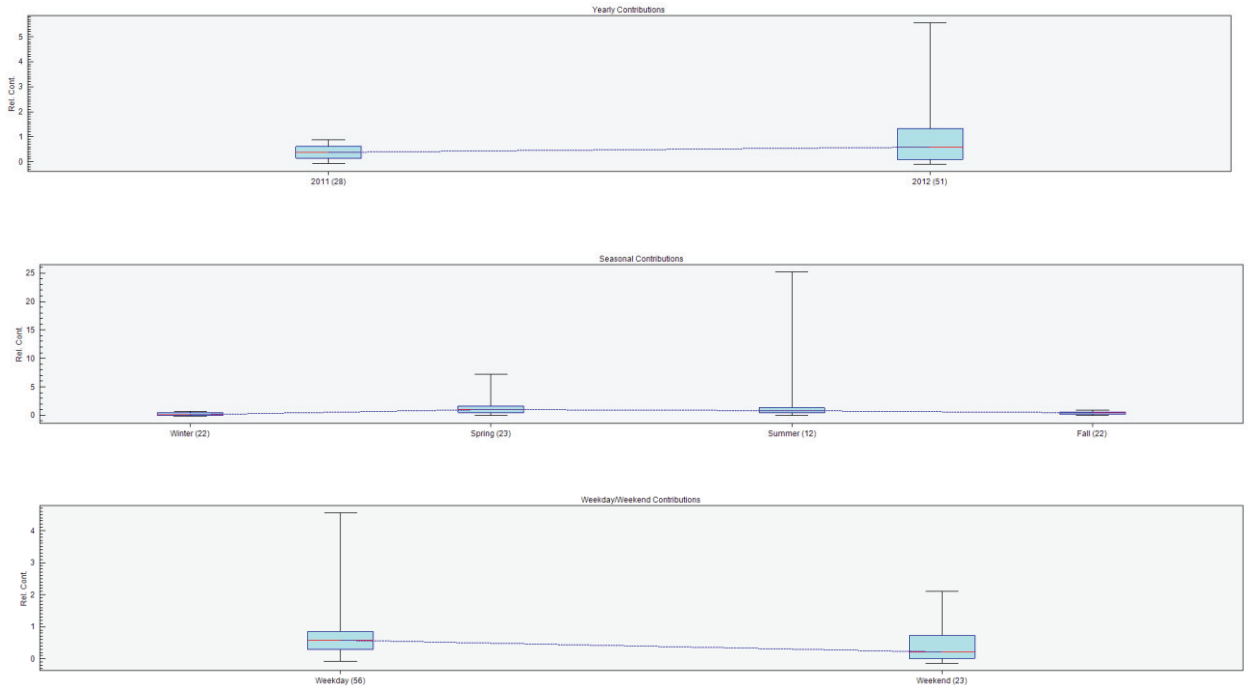

Figure 38 Yearly, seasonal and weekday/weekend Surface dust contributions.

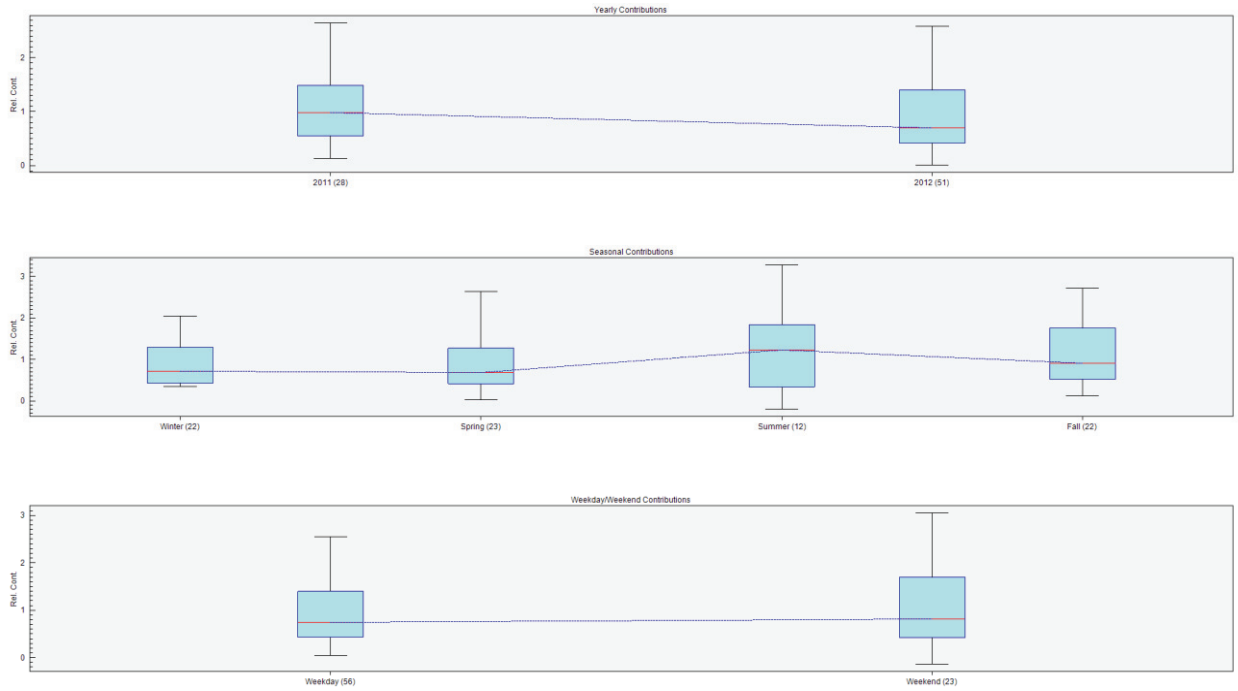

Figure 39 Yearly, seasonal and weekday/weekend LRT Secondary (ammonium sulfate) contributions.

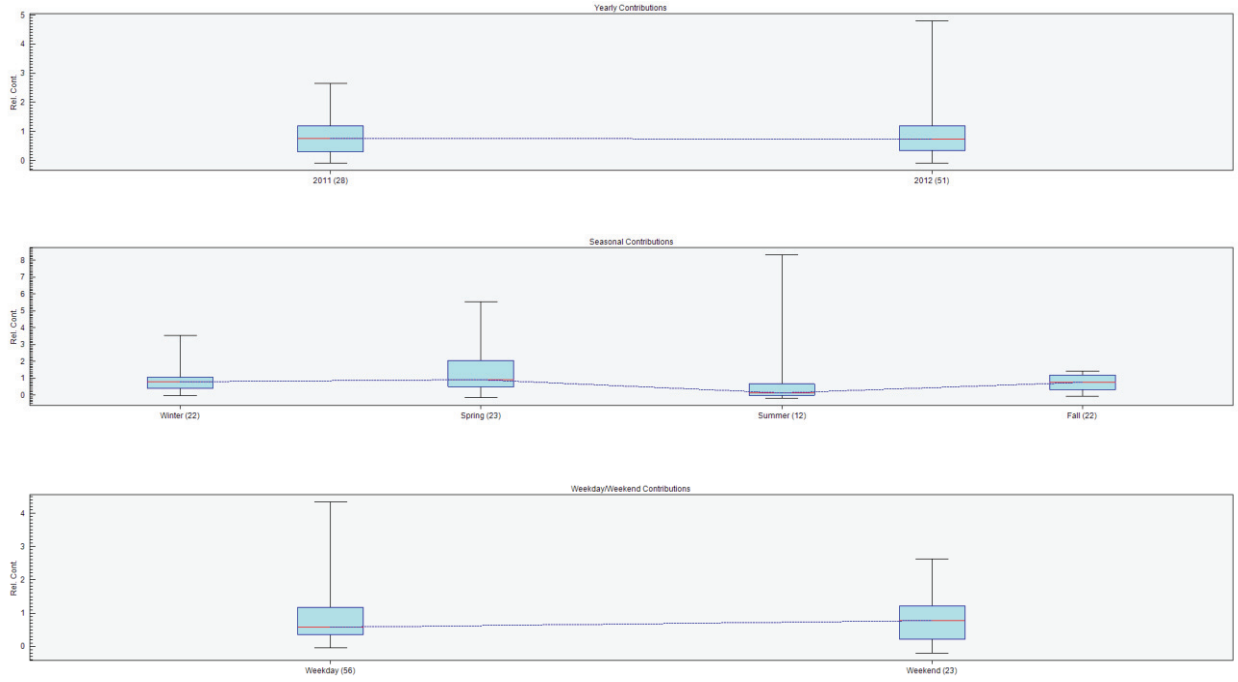

Figure 40 Yearly, seasonal and weekday/weekend LRT Secondary (nitrate and sulfate) contributions.

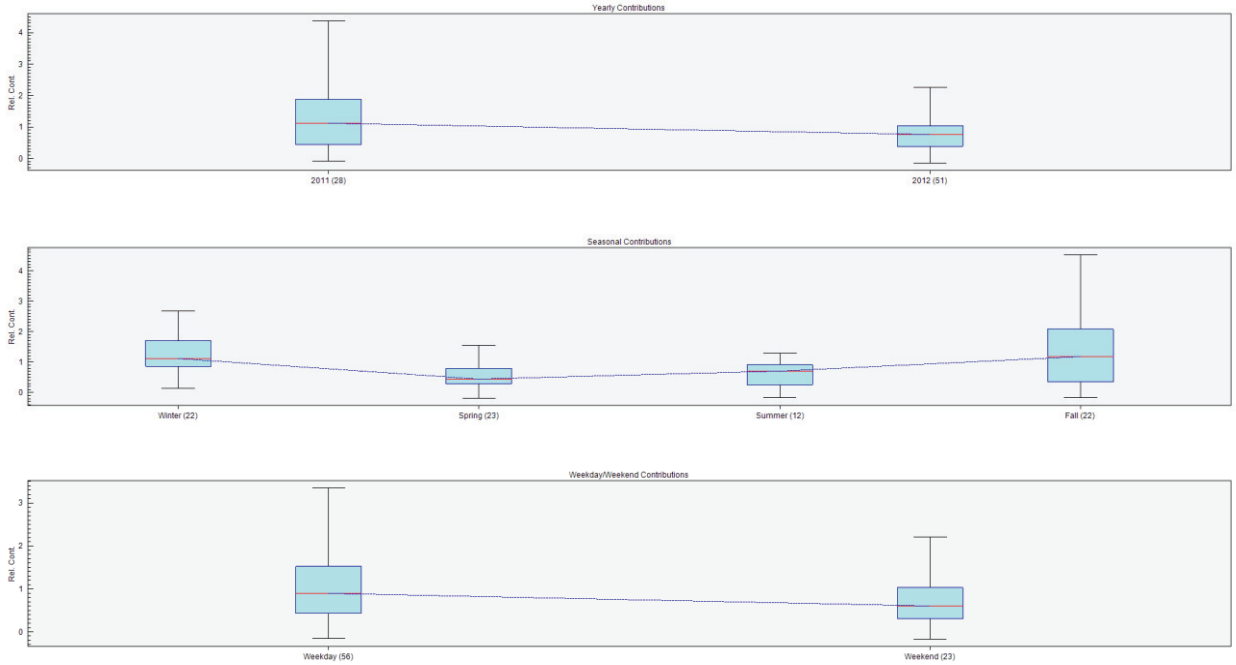

Figure 41 Yearly, seasonal and weekday/weekend Ship emissions contributions.

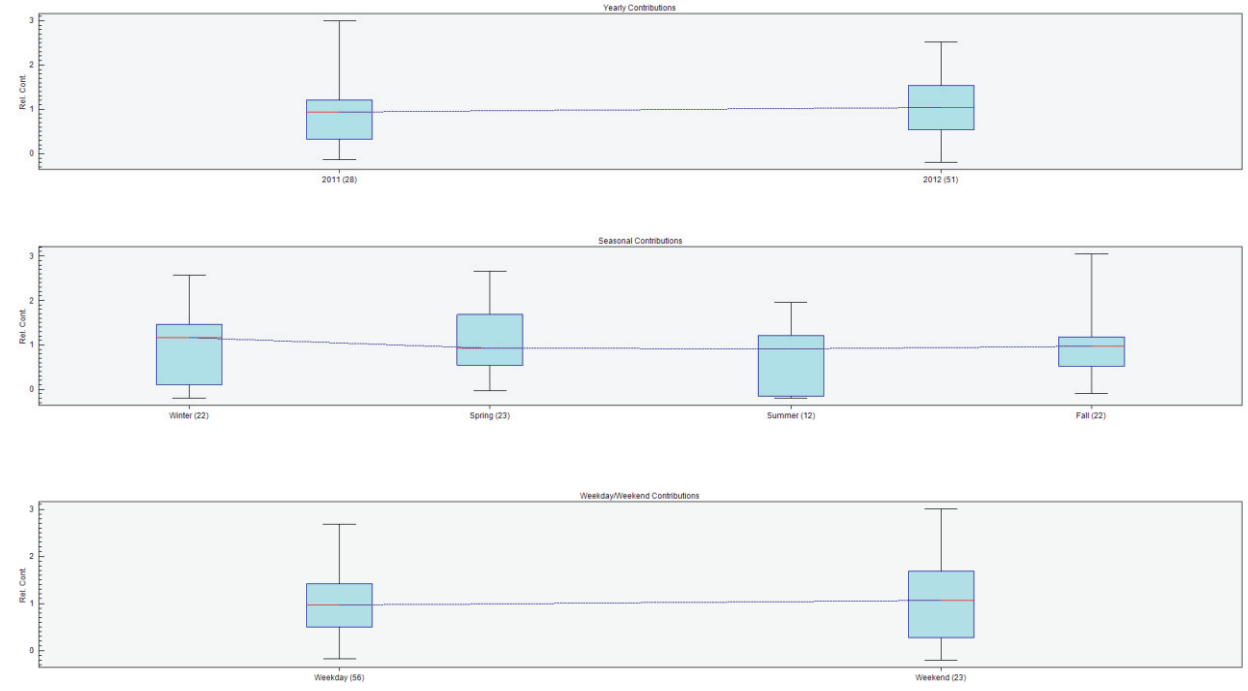

Figure 42 Yearly, seasonal and weekday/weekend Vehicles and re-suspended gypsum contributions.

Table 14 Seasonal Ship emissions source contribution to total $PM_{2.5}$ mass (µg m^{-3}).

Seasons	n	Mean	Std	Min	25th Pctl	Median	75th Pctl	Max
fall	22	1.434	1.22	0.033	0.416	1.047	1.982	4.35
winter	22	1.228	0.706	0.477	0.728	0.971	1.773	2.699
spring	24	0.552	0.541	0.02	0.167	0.47	0.94	2.083
summer	12	0.693	0.375	0.25	0.391	0.64	0.936	1.553

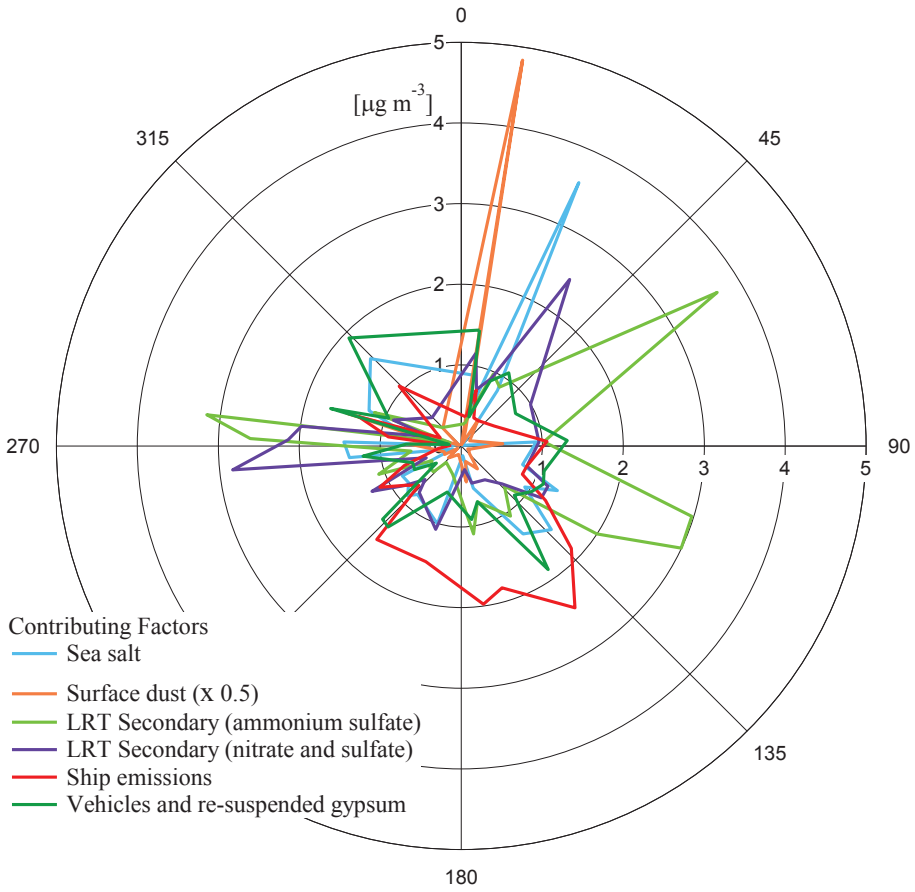

Figure 43 Source contribution rose.

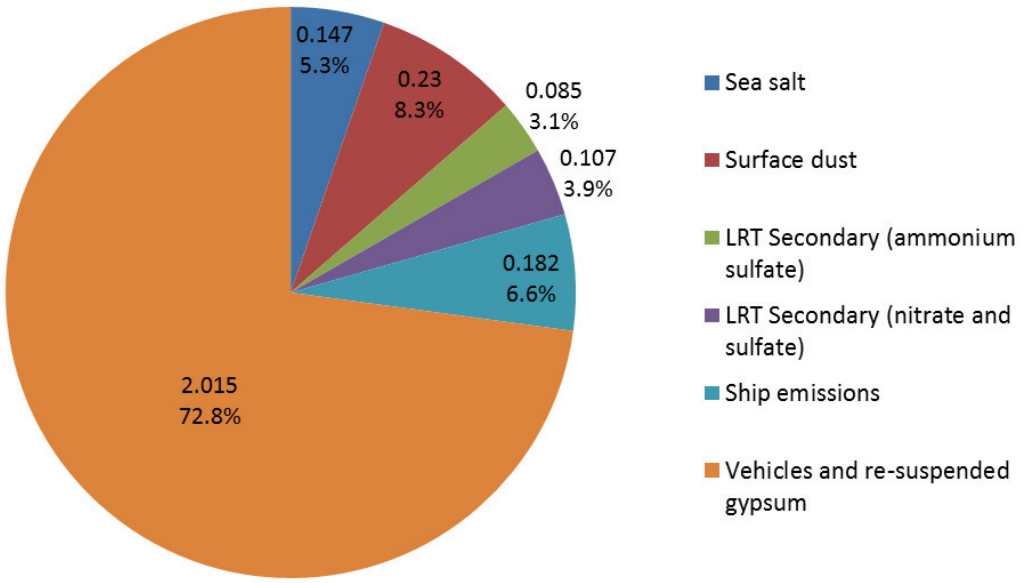

Figure 44 Average mass concentration (μg m^{-3}) of attributed sources and percentage source contributions over the one year sampling campaign.

CHAPTER 5 DISCUSSION

5.1 DESCRIPTIVE STATISTICS

With reference to Table 9, it can be seen that the annual mean $PM_{2.5}$ concentration = 3.8 μg m^{-3}, which is in agreement with the median $PM_{2.5}$ (3.9 μg m^{-3}) measured during the BORTAS study conducted in Halifax in 2011 45 days prior to this study (Gibson et al., 2013b). However, the median $PM_{2.5}$ concentration (9.0 μg m^{-3}), reported in a previous source apportionment study conducted by Jeong et al. (2011) between 2006-2008 in Halifax, is significantly different to this study. It is assumed that the reason for that difference is due to the location of the sites. This ship emissions study site is in a residential area, whereas the 2006-2008 sampling campaign was conducted in downtown area of Halifax with a higher vehicle density and closer to the harbour Cruise ship terminal and Naval base dock. A study by Dabek-Zlotorzynska et al. (2011) found that the mean nitrate concentration during the winter was 0.3 μg m^{-3}, while Jeong et al. (2011) reported 0.263 μg m^{-3} for 2-year sampling period (Dabek-Zlotorzynska et al., 2011; Jeong et al., 2011). BORTAS data estimated the mean concentration of nitrate over the summer to be 0.093 μg m^{-3}. This work shows that the mean value of nitrate is comparable with the previous results, 0.191 μg m^{-3}. Jeong et al. (2011) found that the mean sulfate concentration was 2.27 μg m^{-3} over a 2-year study. BORTAS data reported the mean concentration of sulfate during summer was 0.78 μg m^{-3}. Interestingly, this study indicates that a mean sulfate concentration was 0.916 μg m^{-3}. It can be clearly seen a 2.5 times (60%) reduction in sulfate content in our study in comparison with Jeong et al. (2011) conducted during 2006-2008 period. It is assumed that this is the result of IMO regulations which have resulted in a drop in the S_F in marine fuels as well as switching the Tufts Cove Power Plant from oil to natural gas. Concentrations of Na (0.142 μg m^{-3}) and Cl (0.096 μg m^{-3}) are also similar with the values found by Jeong et al. (2011) which were 0.145 μg m^{-3} and 0.172 μg m^{-3}, respectively. This was anticipated as the sea salt flux from the ocean has not undergone a dramatic change.

Descriptive statistics for weather data obtained from Davis Vantage Pro II weather station was done to support results of the research. From Table 10 the prevailing wind direction (and average wind speed) in summer, fall, winter, and spring was SW~224º (6 m s^{-1}), S~175º (8.6 m s^{-1}), SSW~203º (8 m s^{-1}), and SSW~199º (9 m s^{-1}), respectively. The lowest mean temperature was

0.2 ºC in winter, followed by 7 ºC in spring, 13 ºC in fall, and 19 ºC in summer. RH for summer, fall, winter, and spring was 80%, 82%, 77%, and 70%, respectively. SR showed high amount in summer (2 W m^{-2}), followed by spring (1.7 W m^{-2}), fall (1 W m^{-2}), and winter (0.5 W m^{-2}).

5.2 BOX PLOTS ANALYSIS

Figure 6 illustrates box plots of $PM_{2.5}$ concentration by season. It can be clearly seen that the highest median value is during summertime, while the winter period has the lowest $PM_{2.5}$ concentration. Interestingly, studies (Querol et al., 2004; Ward et al., 2004; Chen et al., 2007; Jeong et al., 2008; Dabek-Zlotorzynska et al., 2011) show that winter has the highest $PM_{2.5}$ concentration due to biomass combustion for residential heating, temperature inversion, and high amount of nitrate. However, we found that Halifax is defined as a region with low concentrations of nitrate and high amount of sulfate during summertime; hence, we can observe that winter is the least polluted season. Studies by Dabek-Zlotorzynska et al. (2011) and Jeong et al. (2011) also report that the lowest $PM_{2.5}$ concentration in Halifax was measured in winter.

Detailed information on $PM_{2.5}$ variability by month is presented in Figure 7. One of the reasons for the high concentrations of particles during November, August, and July is the prevailing meteorological conditions. Descriptive statistics (Table 10) show that the prevailing wind during these months was from SW transporting polluted air mass from NE seaboard of the US. High median $PM_{2.5}$ concentration in July can be explained by low precipitation amount (2 mm) and high solar radiation (5600 W m^{-2}) (obtained from Table 16). Another reason might be due to high summertime concentrations of surface dust which contributes 0.23 μg m^{-3} to the total $PM_{2.5}$ mass according to the PMF results. Therefore, elevated concentrations occurred during that period. Low concentrations during winter months are presumably due to meteorological conditions with high winds (8 m s^{-1}) and increased turbulence which increases the dispersion rate of pollutants.

Figures 8-12 demonstrate how well the species are distributed and extremes in the data by virtue of outliers. The salient features in Figure 8 are that SO_4^{2-} is clearly the dominant species contribution to total $PM_{2.5}$ mass (0.6 μg m^{-3}) with NH_4^- half the contribution of SO_4^{2-} (0.25 μg m^{-3}). It can be seen that the chemical composition is also dominated by NO_3^- (0.14 μg m^{-3}), Na^+ (0.14 μg m^{-3}), and BC (0.24 μg m^{-3}). This $PM_{2.5}$ composition is typical in any maritime urban centre, e.g. Glasgow, UK (Gibson et al., 2009), Halifax 2006-2008 (Jeong et al., 2011), Halifax

summer 2011 (Gibson et al., 2013b). These data might give preliminary information on abundant species and hence potential sources that significantly contribute to the ambient air. For instance, SO_4^{2-}, NH_4^-, NO_3^- indicate LRT while Na^+ is a marker element of marine sources, with NO_3^- and Na^+ in the absence of Cl^- being indicative of aged marine aerosol (Gibson et al., 2013b). Figure 9 indicates that the concentration of Ca^{2+} is roughly 5 times the concentration of such cations as K^+ and Mg^{2+}. The same pattern was found in Prestwick and Paisley, coastal cities of Scotland (Gibson et al., 2009). In terms of elements, the dominant constituents of total $PM_{2.5}$ mass are Cl (0.03 μg m^{-3}), Na (0.1 μg m^{-3}), S (0.3 μg m^{-3}), and Si (0.02 μg m^{-3}) indicating on sea salt (Cl and Na), soil (Si), and oil combustion (S) (see Figure 10). The main feature of Figure 11 is that Al:Fe ratio is almost 1:1 which is an indicator of surface/soil dust. Figure 12 shows box plots of Ba, Br, Cu, Mn, Ni, V, and Zn which are mainly markers of industrial, ships, and vehicles emissions. The element concentrations are in the same range as reported in the Jeong et al. (2011) 2006-2008 Halifax study.

5.3 TIME SERIES PLOTS ANALYSIS

It can be seen that some periods, e.g. December 11, 2011, have elevated $PM_{2.5}$ concentrations (Figure 13). Analysis of the meteorological data during these elevated $PM_{2.5}$ conditions coincided with the low wind speed and temperature inversion during winter time. Another reason of increased $PM_{2.5}$ concentrations is dry weather, slow wind speed (3 m s^{-1}), and clear skies with high levels of solar radiation (7206 W m^{-2} and 5186 W m^{-2}) which were prevalent on July 14 and 26, 2012. The low concentrations occurred during days with high precipitation amounts and winds from E and N which are known regions of low $PM_{2.5}$ emissions (Gibson et al., 2013b). The plot indicates that there is some missing data which occurred due to instrument malfunction.

Figures 14-21 illustrate annual variability of species measured during this study. Time series plots show that some species are strongly correlated with other species (which is a simple indicator that they share the same source). For instance, the trend in Na and Cl concentrations (Figure 18) closely follows each other which is indicative of these metals being related to ocean spray sea salt. Figure 19 also provides good covariance of species pointing on a common source, surface soil/dust. NH_4 and NO_3 are trending together (Figure 16) indicating a LRT.

It can be noticed from Figure 14 that high peaks of BC concentration are during the fall and winter, followed by the gradual decrease in spring and summer. The reason is that BC is a known chemical marker of biomass and fossil fuel combustion which increases in wintertime due to residential heating needs (Ward et al., 2006; Jeong et al., 2008; Gibson et al., 2013b). For instance, a study in Montana, USA reports that residential wood burning contributed 82% to the total $PM_{2.5}$ mass in winter (Ward et al., 2006). Research by Jeong et al. (2008) demonstrated a 74% contribution from wood burning to the total $PM_{2.5}$ mass in British Columbia during winter.

Studies (Lee et al., 2001; Ward et al., 2004; Song et al., 2010) report strong seasonal changes in nitrate concentrations with high values increasing in winter and gradually decreasing in summertime. However, there is no significant seasonal trend in nitrate, which agrees with the results found by Jeong et al. (2011). In contrast to nitrate, sulfate shows seasonal variability with high values and peaks in summertime. This is due to photochemical reactions and high ozone concentration that catalyzes the oxidation of SO_2 and hence the formation of sulfate (Khoder, 2002; Song et al., 2010; Jeong et al., 2011).

Although we plotted time series of Ca^{2+} (Figure 17) we are suspicious that there was an issue with the actual filter composition, i.e. high Ca^{2+} cation contamination. This time series plot likely confirms our assumption because of a sudden drop toward the end of March. We suspect that this is due to the change of filter batches and does not represent the real values. Therefore, it was decided not to use Ca^{2+} in the further analysis.

Variation of soil metals is presented in Figure 19 with elevated concentrations in summer and the beginning of fall. This is characterized by increased concentrations of the soil elements due to vehicle re-suspended street dust/wind blown soil. The same pattern was observed in several studies: Querol et al. (2004), Jaeckels et al. (2007), Jeong et al. (2008), Yin and Harrison (2008), and Rahman et al. (2011). A good relationship is observed in Figure 20 with chemical markers of vehicles such as Mn (antiknocking agent), Cu and Ba (brake wear), and Zn (tire wear). Figure 21 (V,Ni) demonstrates that V and Ni have a covarying temporal relationship. An extreme value of 14 ng m^{-3} was observed on March 28, 2012 with backward trajectories pointing on Québec region where Ni/Co smelter is located.

5.4 EXPLANATION OF THE ANNUAL VARIATION OF SPECIES MASS CONCENTRATION BY MEANS OF AIR MASS BACK TRAJECTORIES AND METEOROLOGY

HYbrid-Single Particle Lagrangian Integrated Trajectory was used to explain the variation of time series plots. Backward trajectories are presented in Appendix (Figure 73) for the whole year of sampling.

Figure 13 represents elevated $PM_{2.5}$ concentrations on December 11, 2011, March 22, 2012, April 15, 2012, May 15, 2012, June 29 2012, July 14 and 26, 2012 and other days. In order to explain this pattern back trajectories were analyzed and it was found that the air mass was coming from Central Canada, Windsor-Québec corridor, and Ohio Valley. Additional information on $PM_{2.5}$ concentration across the US was obtained from AIRNow website (http://airnow.gov/) that helped to validate the back trajectories results. On March 22, 2012 it can be seen from backward trajectory that the air flow was coming from the central part of the US through Windsor-Québec corridor, which is the main industrial region of Central Canada. Figure 71 shows that the area of Michigan-Indiana-Ohio is coloured in yellow, indicating that $PM_{2.5}$ Air Quality Index (AQI) was moderate (51-100) and this provides evidence of the high concentrations of upwind $PM_{2.5}$ that were evident before the air mass crossed Halifax which led to an increase in $PM_{2.5}$. Figure 72 is helpful to explain the elevated $PM_{2.5}$ concentration found on July 14, 2012 with a moderate AQI in the area of Windsor-Québec where the air mass was coming from. High values on November 2, 2011, May 15, 2012, June 29 2012, and July 14 and 26, 2012 can be explained by dry weather, slow wind speed (1-3 m s^{-1}), and clear skies with high levels of solar radiation, conditions favourable for photochemical smog formation and elevated concentrations of $PM_{2.5}$. Low values of $PM_{2.5}$ were observed on August 28, 2011, March 16 and June 17, 2012 when the wind direction was aligned with the ocean (E) and clean marine air. Another factor that influences the air pollution is the height of the boundary level where the air mass originated. For instance, on March 16, 2012 the air mass originated at free troposphere (5000 m) and remained elevated until it reached Halifax. In addition, due to high precipitation amount (6-43 mm) on August 28, 2011, October 30, 2011, and September 24, 2011 concentrations of $PM_{2.5}$ stayed comparably low.

We can see from Figure 14 high concentrations of BC on October 24, 2011 and November 2, 2011. The reason is that the air mass was coming from NW passing the Windsor-Québec corridor. A very low amount of BC (<0.1 μg m^{-3}) was observed on November 2, 2011 and December 29, 2011. Trajectories show the direction from North, an area of low anthropogenic emissions and thus an air with low $PM_{2.5}$ concentrations. In addition, air mass originated and remained at 3000 m (free troposphere) for a long period of time before making ground fall in Halifax, indicative of an air mass free from the influence by ground based $PM_{2.5}$ sources. On December 8, 2011 low BC concentrations coincided with air parcels originated from the North Atlantic, and as such relatively free of strong regional BC sources.

The highest peak (~10 μg m^{-3}) of SO_4^{2-} was observed on February 24, 2012 (Figure 15) due to the air mass flow from W and SW (US) and low boundary level (1500 m). On May 15, 2012 the air parcels were coming from SW (US) and NE seaboard of the US . Direction from NE coast of US was also prevalent on August 4, 2012. The elevated SO_4^{2-} observed on these days is a result of the combustion of sulfur containing fuel in these upwind source regions that then undergoes gas-to-particle transformation to secondary SO_4^{2-} associated $PM_{2.5}$. These secondary SO_4^{2-} are then advected to Halifax.

On December 20, 2011 back trajectory analysis indicates the presence of fast air mass from NW with a very low boundary level. Backward trajectories on February 15, 2012, April 15 and 21, 2012 represent the air parcels from NE coast of the US. Those air masses are enriched with sea salt that has undergone exchange of Cl for NO_3^-, known as aged sea salt (Gibson et al., 2009; Gibson et al., 2013). Low NO_3^- concentrations were recorded on January 1 and July 20, 2012 with the clean air mass flow from N (Figure 16).

It can be clearly seen that elevated concentrations of Na and Cl occurred during the imported marine air masses from E and NE seaboard of the US on November 14 and 20, 2011 and December 8, 2011. Trace elements of industrial production, e.g. V, Ni, Zn had high concentrations when the air mass passed over the Central US, Ohio valley, and Windsor-Québec corridor on November 2, 26 and 29, 2011, February 9, 2012, and July 14, 2012.

To summarise, the air masses arriving from W and SW are associated with elevated secondary anions and cations (SO_4^{2-}, NO_3^-, and NH_4^+) $PM_{2.5}$ pollutants imported air from the Windsor-Québec corridor, Ohio valley, and the interstate-95 corridor. Air masses from the E, SE, and N air flow are from clean marine and clean northern air masses.

5.5 WIND ROSE AND POLLUTION ROSES

Wind rose analysis was conducted in order to understand the variation in $PM_{2.5}$ mass and $PM_{2.5}$ species concentrations with wind direction. Annual wind rose is provided in Figure 45 (see Appendix). The average wind direction was from the SW (210º) and W (270º), while the highest wind speed was observed from the SE and E.

To help understand the wind directional dependence of the $PM_{2.5,}$ pollution roses were constructed for 25 species (Figures 46-70). These plots are useful for PMF model interpretation, especially with the identification of the local origin of the $PM_{2.5}$ and chemical components.

5.6 POSITIVE MATRIX FACTORIZATION

With reference to Table 11 it can be seen that all 20 of the randomly seeded base runs converged and Q values showed stable results, which indicates that the model predicted the input data with high model skill. Q (robust) deviates by only 2% from Q (true) which demonstrates that outliers do not significantly affect the Q value. The goodness-of-fit parameter, Q robust and Q true, were found to be within 50% of Q theoretical, again showing a parsimonious model.

Initially, 5 to 15 factors (~ sources) were explored with PMF. When the model was run with 8 factors, the Surface dust (Ca, Al, Fe, K, Si) source was split into two separate factors. Secondary sulfate also became two distinct factors, sulfate and ammonium, which is not physically representative of the reality of the chemical composition of the $PM_{2.5}$ sampled, e.g. the sulfate and ammonium must exist as $(NH_4)_2SO_4$ in the $PM_{2.5}$ (Gibson et al., 2009). The seven-factor solution split Ca from the Surface dust species Al, Fe, K and Si. Moreover, the calculated Q value was 3 times less than the Q theoretical indicating a poor model fit. Therefore, the optimum number of factor profiles chosen was six: Sea salt, Surface dust, LRT Secondary (ammonium sulfate), LRT Secondary (nitrate and sulfate), Ship emissions, and Vehicles and re-suspended gypsum. High factor loadings of chemical indicators, meteorological parameters, source profiles, air mass back trajectories, and our knowledge of source chemical markers (available in the literature) helped in identifying the factor solutions, i.e. the six major sources of $PM_{2.5}$ that impacted the sampling site in Halifax.

To check if the PMF results are robust, predicted versus observed time series plots were examined. Figures 23 and 24 demonstrate high correlations of $PM_{2.5}$, Cl, NO_3, and NH_4. In addition, scaled residuals were analyzed for each species and showed normal distribution within ±3 (Figure 25). Results from bootstrap runs support that the model successfully found six-factor solution. For example, the bootstrap summary showed that, out of a possible 600, the number of unmapped runs were only 5, indicating a very stable results. Also it can be seen from Figures 27 and 28 that the variabilities in Ship emissions and Vehicles and re-suspended gypsum factor profiles correspond the bootstrap variabilities in percentage and concentration. This can be concluded from the match of the blue box (base run) and the green line (median of bootstrap run). The final verification test, Fpeak test, was applied with results presented in Table 13 and Figures 29 and 30. We found that all five runs were converged and the Fpeak factor profile for Ship emissions did not deviate from the base run factor profile. In addition, G-space plot indicates the independence between two factors which agrees with the results obtained from base run (Figure 30). In summary, the Fpeak runs did not show any rotational ambiguity within the model results, for that reason it was set to zero.

5.6.1 Sea salt

The first factor is assigned to Sea Salt due to high factor loadings of Na and Cl with 70% and 95%, respectively as well as Mg and Ca (Jeong et al., 2008; Larson et al., 2004). The Cl:Na ratio is 1.4 which corresponds to the ratio in sea water (Gibson, 2004, p.149). To verify that the source was chosen correctly we checked the amount of Na which is more than 50%. This complies with the study results by Yatkin and Bayram (2008). Also this source is known as fresh sea salt (Song et al., 2001). However, sometimes the reduction of Cl can be noticed in sea salt spray. This occurs when marine aerosol comes into contact with strong acids, like H_2SO_4 and HNO_3, by replacing Cl^- with SO_4^{2-} and NO_3^- (Jeong et al., 2008; Gibson et al., 2013b). In this case it is considered as aged sea salt. Figure 37 represents seasonal contribution of the factor with high median values in spring, winter, and fall. As was mentioned by Jeong et al. (2011), the reason is that strong winds and storms with high ocean wave energy usually happen in fall, winter and, the beginning of spring. Sea water droplets are evaporated and advected by wind leaving behind salt crystals and tiny salt water droplets. Moreover, Na and Cl are unique tracers for road salt (Jeong et al., 2011). During dry conditions vehicles can cause the mechanical re-

suspension of salt in wintertime causing such a high seasonal pattern. Sea salt factor contribution plot (see Figure 31) illustrates two high events on 14 and 20 November, 2011 which might be caused by high winds (7 m s^{-1}) and as a result the increased formation of ocean spray sea-salt $PM_{2.5}$.

5.6.2 SURFACE DUST

Al, Ca, Fe, K, and Si are the key chemical markers of soil and re-suspended dust (Jeong et al., 2008; Jeong et al., 2011; Gibson et al., 2013b). Therefore, Factor 2 was chosen as Surface dust. This Factor originated mainly from construction sites and street landscaping. Time series plots (Figures 32) give a better understanding of seasonal variation of crustal elements with high values during summer and spring and low in wintertime. Pollution roses (Figures 55, 58, 61, 62 and 68) help to identify the direction of the highest concentrations and their frequency. It can be seen, that the wind direction was from SW where Highway 102 and major roads are located. The vicinity to the major and minor roads indicates that Surface dust factor is mainly due to the road dust. Factor contribution plot (see Figure 32) shows high peak on June 5, 2012 presumably due to high wind speed with 5 m s^{-1} causing re-suspension of surficial dust. Seasonal and weekday/weekend Surface dust contribution plots (see Figure 38) indicates high factor contributions in summer and spring as well as weekdays. This is due to increased traffic density on weekdays and as a result of re-suspended road dust.

5.6.3 LONG RANGE TRANSPORT

According to the studies by Lee et al., 1999 and Ward et al., 2006 the indicators of LRT are NH_4, NO_3 and SO_4. They are known as secondary inorganic aerosols and produced due to SO_2, NO_2 and NH_3 gas-to-particle transformations (Gibson et al., 2009a). Therefore, the third and fourth factors with the key chemical markers of SO_4, NH_4, and NO_3 were assigned as LRT. The source contribution rose, Figure 43, indicates that those species are aligned with ENE, ESE and W, Eastern Canada and the NE US, where it is known large emissions of sulfur occur.

LRT Secondary (ammonium sulfate) factor contribution plot illustrates peaks in the late spring and summer. This is the result of increased photochemical reactions that was discussed in Section 5.3. In addition, seasonal and weekday/weekend LRT Secondary (ammonium sulfate)

contribution plots also show high median values in summertime and a gradual decrease in winter.

The contribution of the fourth factor LRT Secondary (nitrate and sulfate) indicates a gradual increase in winter due to the fact that nitrate is sensitive to temperature. During warm weather (summertime) nitrate transforms to nitric acid gas causing the decrease of particulate NO_3 (Rattigan et al., 2006). Moreover, the increased NO_x and SO_2 emissions are formed from the combustion of biomass and fossil fuel for space heating, coupled with lower ceiling heights and low wind speed at night which result in higher surface concentrations of NO_3 and SO_4.

5.6.4 SHIP EMISSIONS

The Ship Emissions factor was characterized by the presence of V, Ni, and BC (Hobbs et al., 1997; Isakson et al., 2001; Jeong et al., 2011; Lack et al., 2011; Schembari et al., 2012; Kotchenruther, 2013; Gibson et al., 2013b). As reported by Zhao et al. (2013) ship emissions are characterized by V/Ni ratio, which is between 1.9 and 6.5. In this current study the ratio was 2.7, thus verifying that the factor was chosen correctly. Moreover, according to Pacyna et al. (1984) approximately 100% of V comes from oil combustion (Isakson et al., 2001) which indicates that it is a strong marker for ship emissions. We can see several peaks in factor contribution plot on October 24, 2011, November 2 and 29, 2011, and May 30, 2012 which can be explained using meteorological data, back trajectories, and pollution roses for that species. The local wind direction on November 2, 2011 and May 30, 2012 was from SE aligned with East coast of Nova Scotia. On the rest of the days the local wind direction was from N indicating on the Naval dockyard. The presence of key marker elements of ship emissions factor along with the wind direction lined up with the harbour support the theory that these emissions are related to ships. Figure 41 demonstrates seasonal patterns of the Factor with high levels during fall and winter followed by summer. With reference to Table 14 the median Ship emissions source contributions in fall, winter, spring, and summer are 1.047 $\mu g\ m^{-3}$, 0.971 $\mu g\ m^{-3}$, 0.47 $\mu g\ m^{-3}$, and 0.64 $\mu g\ m^{-3}$. The results are consistent with the data obtained from Marinetraffic.com. As we can see from Figure 22 the highest number of cargo ships is in wintertime and cruise ships in fall. Cruise ships are assumed to be the main contributors to ship emissions due to the fact that instead of using low auxiliary engine during hotelling, they employ high auxiliary engine in order to supply with electricity the hotel services throughout their stay at berth (Tzannatos, 2010). In addition, due to

photochemical processes generating secondary SO_4-$PM_{2.5}$ during warm weather, a rise in concentrations of ship emissions was observed. Also, it can be seen from Figure 41 that the contribution in 2011 demonstrates higher amount than in 2012 which can be explained by the new IMO regulations that came into force on August 1, 2012.

5.6.5 VEHICLES AND RE-SUSPENDED GYPSUM

Vehicles and re-suspended gypsum factor, with high loadings of Br, Ca, Cu, Fe, K, Zn, and S, was chosen as a combined factor where Ca and S represent gypsum (Larson et al., 2004; Gibson et al., 2009). During the sampling campaign there was building renovation, mainly repointing, of the Dunn building. Gypsum is known as a major constituent of asphalt, side-walk, and landscaping materials; therefore, PMF model showed high contribution (70% of S and 40% of Ca) from these species (Tiwary & Colls, 2010). Indicators of vehicle brake wear are Ba, Cu, and Fe, while Zn is a marker for tire wear (Chen et al., 2007; Kim et al., 2009; Harrison et al., 2011). According to Jeong et al. (2008), Zn and Fe can also be derived from lubricating oil (Jeong et al., 2008). It was difficult with the current data set to separate the traffic factor into gasoline, diesel, tire wear, and brakes factors. The current study did not include the major fingerprints of vehicle emissions, such as OC and EC, and for that reason we assume that PMF could not separate the vehicle factor. The factor profile and factor contributions (Figure 36) represent high peaks on November 2 and 26, 2011 and April 15, 2012. According to the weather data these days were characterized with clear skies and low wind speed (2-3 m s^{-1}) from WNW and N. Figure 42 illustrates that weekend contribution is higher than during weekday which agrees with the results reported by Jeong et al. (2011).

Factors determined in this study can be divided into local and regional sources. Studies (Pekney et al., 2006; Jeong et al., 2011; Gugamsetty et al., 2012) show that pollution roses help in the identification of local sources, while air mass back trajectories were used to identify regional upwind source regions/sources. According to the source contribution rose LRT Secondary (ammonium sulfate) and LRT Secondary (nitrate and sulfate) factors characterizing regional sources, while Sea salt, Ship Emissions, Surface dust, and Vehicles and re-suspended gypsum factors represent local sources.

5.6.6 SOURCE CONTRIBUTION ROSE

Source contribution rose (Figure 43) provides an opportunity to understand the local geographical location of sources estimated by PMF. According to the wind rose the prevailing wind direction was from the SW and W, indicating that the dominant direction contribution of source factors was from that vector. The potential source direction of Sea salt factor was from SE, E and NE which is aligned with the ocean. Generally, the main direction of Surface dust was from W (except one event lined up with NNE) which agrees with the results found by Gibson et al. (2013b). Ammonium sulfate factor is associated with ENE, ESE and W wind vectors indicating on Eastern Canada, New Brunswick, and the NE US, the largest sulfur sources. The similar pattern we observe for LRT Secondary (nitrate and sulfate). According to Jeong et al. (2011) the possible source regions of secondary nitrate were New Brunswick and Southern Québec. The ship emissions factor shows the directional dependency with NW, SE and E which aligns with the Bedford basin cargo terminal, cruise ship terminal, and Naval dockyard. Source contribution rose verifies that ship emissions were correctly attributed by PMF. Vehicles and re-suspended dust factor lined up with N, NW, W, SW and SE. N, NW and W wind vectors are coming from the main roads and highways, e.g. Highway 102.

5.6.7 SOURCE CONTRIBUTION

The average mass and percentage contribution from the six sources found by PMF model is presented as a pie chart in Figure 44. The contribution of Sea salt factor was estimated as 0.147 μg m^{-3} (5.3%) indicating a 3.5% decrease in comparison with Jeong et al. (2011). Surface dust contributed 0.23 μg m^{-3} (8.3%) to the total $PM_{2.5}$ mass concentration. Comparing these results with BORTAS study (0.23 μg m^{-3} or 6.3%) we can see the same magnitude for mass. However, Jeong et al. (2011) reports 0.3 μg m^{-3} (3.8%) dust contribution which is similar in mass concentration and two times less in % than in our study. The increased % contribution might be due to exterior building restoration taking place at the sampling site. LRT Secondary (ammonium sulfate) and LRT Secondary (nitrate and sulfate) contributions found by PMF showed similar mass (%) contributions with 0.085 μg m^{-3} (3.1%) and 0.107 μg m^{-3} (3.9%), respectively. The Ship emissions contribution = 0.182 μg m^{-3} (6.6%), which is less than the contribution estimated by Jeong et al. (2011) during 2006-2008 sampling period in Halifax with 0.6 μg m^{-3} (9.1%). A 3.3 times mass (1.4%) reduction might be due to IMO regulations on S_F.

The study by Zhao et al. (2013) showed that the average contribution from ships in Chinese port cities is 1.96 μg m^{-3} with the highest value in Shanghai Port (3.58 μg m^{-3}). The average ships contribution to $PM_{2.5}$ estimated near the Los Angeles-Long Beach harbor was 0.24 μg m^{-3} (Minguillon et al., 2008). Another study conducted in the strait of Gibraltar found that ships contribution varied between 1.2-2.3 μg m^{-3} (Pandolfi et al., 2011). Generally, these results indicate that ship emissions contribution in Halifax is not significant comparing to other port cities. In comparison between the current study and Jeong et al. (2011) the contribution of vehicles was 2.015 μg m^{-3} (72.8%) and 1.0 μg m^{-3} (14.2%), respectively. Such a significant increase might be due to combination of two factors, vehicles and re-suspended gypsum. In addition, as was mentioned before due to repointing works at the sampling site high concentrations of S and Ca was measured. This was also reported in Gibson et al. (2013b) which was 45-days prior to the start of this study and at the same site.

5.6.8 Root-mean-square-error and bias

The mass contribution from six sources resolved by the model was compared with the original $PM_{2.5}$ mass. In order to estimate the difference between predicted $PM_{2.5}$ mass by PMF and observed and calculate the accuracy of the model the root-mean-square-error (RMSE) was applied (see Equation 4). The bias of PMF was calculated as $(A\text{-}T)/T$, where A is predicted $PM_{2.5}$ mass concentration by PMF and is T observed (Gibson et al., 2013b).

$$\mathrm{RMSE} = \sqrt{\frac{1}{n}\sum_{i=1}^{n} (\hat{y}_i - y_i)^2} \qquad (4)$$

where $\hat{y}_i$ is total $PM_{2.5}$ mass concentration (μg m^{-3}) estimated by the PMF model and y_i is observed total $PM_{2.5}$ mass concentration (μg m^{-3}).

The slope of the linear regression of the predicted $PM_{2.5}$ mass concentration versus observed was 0.83, the intercept was 0.14, and $R^2 = 0.83$. The calculated PMF RMSE = 0.09 μg m^{-3} and the model bias = -0.23. On the basis of these calculations we may conclude that the PMF model showed accurate results.

CHAPTER 6 CONCLUSION

As indicated in the literature review (Chapter 2) ship emissions reduce air quality of coastal cities and maritime regions causing adverse effects on health and the environment. For this reason, it was valuable to conduct this source apportionment study in one of the largest eastern port cities in North America. Another impetus for the study was that IMO regulations governing the sulfur content of maritime fuels changed from 3.5% to 1%. Therefore, it is important to determine if the reduction in S_F improved air quality in coastal port cities such as Halifax.

The main aim of this study was to identify the source contribution of ship emissions and other sources to $PM_{2.5}$ before the new IMO regulations came into force on August 1, 2012. To achieve that goal several steps were undertaken during 2-year period of study. Initially, 1-year monitoring was conducted on Sir James Dunn Building roof using 2025-dichot, ChemComb cartridges, and BC monitor. Following that, data analysis was accomplished and by means of SAS (v 4.3), SigmaPlot (12.0), IgorPro (v 6.2.2.2), Excel (v 2010), and HYSPLIT data for the model interpretation were generated and prepared. Finally, PMF was applied to identify sources in Halifax region.

The statistical analysis found that there is no significant seasonal difference in total $PM_{2.5}$ concentration with the highest value in summer (3.85 μg m^{-3}) and the lowest in winter (2.67 μg m^{-3}). Seasonal variation of BC showed high values in fall and winter with a mean value of 0.283 μg m^{-3}. During the research there was not observed significant seasonal changes in nitrate levels indicating similar results with the previous studies (mean 0.191 μg m^{-3}). The concentration of sulfate reached a peak in summertime with an annual mean value (0.916 μg m^{-3}) 2.5 times smaller than reported by Jeong et al. (2011). The results revealed that the decrease of the amount of sulfate might be due to the new IMO regulations on S_F and switching the Tufts Cove Power Plant from oil to natural gas.

The PMF model was successfully applied to the $PM_{2.5}$ mass and $PM_{2.5}$ chemical species data to apportion $PM_{2.5}$ sources in Halifax. Meteorological parameters and air mass back trajectories helped to identify and confirm the $PM_{2.5}$ sources "factors" within PMF. The PMF modelling found a six-factor (six-source) solution for Halifax. The following sources were

identified: Sea salt, Surface dust, LRT Secondary (ammonium sulfate), LRT Secondary (nitrate and sulfate), Ship emissions, and the mixed sources of Vehicles and re-suspended gypsum.

The first factor, Sea salt, contributed 0.147 μg m^{-3} (5.3%) to the total $PM_{2.5}$ mainly in spring, winter, and fall. The source contribution rose indicates on a potential source direction from sea breeze. Surface dust factor was highly contributing in summer and spring with a magnitude of 0.23 μg m^{-3} (8.3%). The high % contribution of this source was explained by the building reconstruction at Sir James Dunn building. The direction of the source was in agreement with the location of the construction works. LRT Secondary (ammonium sulfate) plots indicated high values in summer with 0.085 μg m^{-3} (3.1%) contributions to the total $PM_{2.5}$ mass. The direction coincided with the largest sources of sulfur, e.g. Eastern Canada, the NE US. The study reports that LRT Secondary (nitrate and sulfate) source was mainly prevalent in wintertime with the air mass flow from Eastern Canada (New Brunswick) and the NE US. The contribution estimated by the model was 0.107 μg m^{-3} (3.9%). The third largest contributor to the total $PM_{2.5}$ mass according to the work is Ship emissions source. V/Ni ratio (2.7) as well as the direction that was strongly aligned with the harbour indicated that the source was chosen correctly. The calculated mass concentration was 0.182 μg m^{-3} (6.6%). The last and the largest (by mass concentration and %) source is Vehicles and re-suspended gypsum with a contribution 2.015 μg m^{-3} (72.8%). During the current study reconstruction (repointing) works were noticed at the sampling site which resulted in increased concentration of re-suspended gypsum.

Air mass back trajectories and meteorological data were useful to explain the variation of the contribution of each source to the total $PM_{2.5}$ mass. Also, they helped to understand the reason of high peak events during the sampling period. Pollution roses and source contribution roses were utilized to identify the direction of local sources, while backward trajectories to identify long range. Pollution roses indicate that Halifax region was mainly influenced by western and south-western winds during one year sampling campaign.

Comparison of the predicted $PM_{2.5}$ mass with observed (R^2 = 0.83, bias = -0.23, RMSE = 0.09 μg m^{-3}) indicated on a good correlation. The PMF model was proved to be robust and accurate at predicting the ship emissions contribution (and other major sources) to $PM_{2.5}$ mass concentration in Halifax. As a final point, the study estimated a three times (mass concentration) reduction in ship emissions contribution to the total $PM_{2.5}$ mass in comparison with Jeong et al. (2011). Also the comparison between Minguillon et al. (2008), Pandolfi et al. (2011), and Zhao

et al. (2013) showed that the ship contribution to $PM_{2.5}$ in Halifax is lower than other major ports around the world. A 2.5 times reduction in sulfate almost coincided with IMO 3.5 times reduction of S_F. Further analysis should be performed to assess the actual effect of the IMO regulations on air quality in Halifax.

According to the results of the study the Halifax population is mainly exposed to Vehicles and re-suspended gypsum/cement fugitive dust, indicating that careful air quality measurements should be considered on construction sites. For instance, dust should be properly controlled and workers should be provided with adequate protective equipment, e.g. masks. Also, personal exposure monitoring can be conducted to identify the exposure to the variety of species. In addition, the fugitive construction dust could be reduced by water spraying near to cement/curb stone cutting and grinding activity.

The results found in this research thesis will be useful in estimating the reduction of marine emissions in Halifax and other port cities around the world. Moreover, the project data, findings, and results will be valuable for informing air quality management policy in Halifax, Provincially and Nationally in order to develop mitigation strategies. Also the results of this study will be used to compare with, and validate, a parallel dispersion model study that formed part of the greater Health Canada, Halifax Marine Emission Study. In addition, PMF results give an insight into population exposure to various sources of $PM_{2.5}$. The method used in this study can be applied to other receptor studies anywhere in the world for identifying source contributions to $PM_{2.5}$. However, if source apportionment is conducted in such a clean area like Halifax it is recommended to increase the sampling period (> 24-hr) or the volume of the air that passes through the instrument. Thus, the total $PM_{2.5}$ mass will rise and the rate of the negative values will be decreased after the blank correction. A greater $PM_{2.5}$ sample mass will also improve the S/N ratio during PMF modelling which will in turn make the model more robust.

In order to validate the PMF model output and increase the robustness of the results it is recommended to conduct a parallel PMC or CMB analysis, where the latter one will work as a complementary tool. Moreover, dispersion models, e.g. AERMOD, CALPUFF, can be applied in conjunction with PMF to validate the results.

BIBLIOGRAPHY

Air Resources Laboratory. (2012). HYSPLIT model research. Retrieved from http://www.arl.noaa.gov/documents/Summaries/Dispersion_HYSPLIT.pdf

Barn, P., Jackson, P., Suzuki, N., Kosatsky, T., Jennejohn, D., & Henderson, S. (2011). Air Quality Assessment Tools : A Guide for Public Health Practitioners. *Environmental Health*, (December).

Brewer, R., & Belzer, W. (2001). Assessment of metal concentrations in atmospheric particles from Burnaby Lake, British Columbia, Canada. *Atmospheric Environment*, *35*(30), 5223–5233. doi:10.1016/S1352-2310(01)00343-0

Burnett, R. T., Thun, M. J., Calle, E. E., Krewski, D., & Thurston, G. D. (2002). Lung Cancer, Cardiopulmonary Mortality, and Long-term Exposure to Fine Particulate Air Pollution. *American Medical Association*, *287*(9), 1132–1141.

Carlsten, C., & Kaufman, J. D. (n.d.). Air pollution. *Occupational and environmental lung disease* (pp. 843–851).

Chen, L. W. A., Watson, J. G., Chow, J. C., & Magliano, K. L. (2007). Quantifying PM2.5 source contributions for the San Joaquin Valley with multivariate receptor models. *Environmental science & technology*, *41*(8), 2818–26. Retrieved from http://www.ncbi.nlm.nih.gov/pubmed/17533844

Cooper, J. A. (2011). Chemical Mass Balance approach to quantitative source apportionment of environmental pollutants. Portland,OR.

Corbett, J. J., Winebrake, J. J., Green, E. H., Kasibhatla, P., Eyring, V., & Lauer, A. (2007). Mortality from ship emissions: a global assessment. *Environmental science & technology*, *41*(24), 8512–8. Retrieved from http://www.ncbi.nlm.nih.gov/pubmed/18200887

Dabek-Zlotorzynska, E., Dann, T. F., Kalyani Martinelango, P., Celo, V., Brook, J. R., Mathieu, D., Ding, L., et al. (2011). Canadian National Air Pollution Surveillance (NAPS) PM2.5 speciation program: Methodology and PM2.5 chemical composition for the years 2003–2008. *Atmospheric Environment*, *45*(3), 673–686. doi:10.1016/j.atmosenv.2010.10.024

Dabek-zlotorzynska, E., Dann, T. F., Martinelango, P. K., Celo, V., Brook, J. R., Mathieu, D., Ding, L., et al. (n.d.). Author ' s personal copy Canadian National Air Pollution Surveillance (NAPS) PM 2 . 5 speciation program : Methodology and PM 2 . 5 chemical composition for the years 2003e2008. *Atmospheric Environment*. doi:10.1016/j.atmosenv.2010.10.024

Davis, R. E., Normile, C. P., Sitka, L., Hondula, D. M., Knight, D. B., Gawtry, S. P., & Stenger, P. J. (2009). A comparison of trajectory and air mass approaches to examine ozone variability. *Atmospheric Environment*, 1–11. doi:10.1016/j.atmosenv.2009.09.038

Davy, P. K., Gunchin, G., Markwitz, A., Trompetter, W. J., Barry, B. J., Shagjjamba, D., & Lodoysamba, S. (2011). Air particulate matter pollution in Ulaanbaatar, Mongolia: Determination of composition, source contributions and source locations. *Atmospheric Pollution Research*, *2*(2), 126–137. doi:10.5094/APR.2011.017

Dockery, D. W., Pope III ,C. A., Xu, X., Spengler, J.D., Ware, J.H., Fay, M.E., Ferris, B.G., and Speizer, F. E. (1993). An association between air pollution and mortality in six U.S. cities. *The New England Journal of Medicine*, *329*, 1753–1759.

Dowd, C. D. O., Facchini, M. C., Cavalli, F., Ceburnis, D., Mircea, M., Decesari, S., Fuzzi, S., et al. (2004). Biogenically driven organic contribution to marine aerosol. *Nature*, *431*, 676–680. doi:10.1038/nature02970.1.

Facchini, M. C., Decesari, S., Rinaldi, M., Carbone, C., Finessi, E., Mircea, M., Fuzzi, S., et al. (2008). Important source of marine secondary organic aerosol from biogenic amines. *Environmental science & technology*, *42*(24), 9116–21. Retrieved from http://www.ncbi.nlm.nih.gov/pubmed/19174880

Fritz James S., G. D. T. (2000). *Ion Chromatography* (third., p. 254). Wiley-VCH.

Gibson CMOS Presentaion. (n.d.).

Gibson, M. D. (2003). Source apportionment of PM10 in Glasgow. Glasgow: Department of Civil Engineering, University of Strathclyde.

Gibson, M. D., Heal, M. R., Bache, D. H., Hursthouse, A. S., Beverland, I. J., Craig, S. E., Clark, C. F., et al. (2009a). Using Mass Reconstruction along a Four-Site Transect as a Method to Interpret PM 10 in West-Central Scotland,United Kingdom. *Journal of the Air & Waste Management Association*, *59*(12), 1429–1436. doi:10.3155/1047-3289.59.12.1429

Gibson, M. D., Heal, M. R., Bache, D. H., Hursthouse, A. S., Beverland, I. J., Craig, S. E., Clark, C. F., et al. (2009b). Using Mass Reconstruction along a Four-Site Transect as a Method to Interpret PM 10 in West-Central Scotland,United Kingdom. *Journal of the Air & Waste Management Association*, *59*(12), 1429–1436. doi:10.3155/1047-3289.59.12.1429

Gibson, M. D., Pierce, J.R., Waugh, D., Kuchta, J., Chisholm , L., Duck, T.,, Hopper, J., Beauchamp , S., , King, G., Franklin, J.E., Leaitch , R., Wheeler, A., Li, Z., Gagnon, G., Palmer, P. I. (2013). Identifying the sources driving observed PM2.5 variability over Halifax, Nova Scotia, during BORTAS-B. *Journal of Atmospheric Chemistry and Physics*.

Gibson, M.D., Jackson, M.H., Murdoch, F. (1997). Relationship between the concentration of atmospheric aromatic hydrocarbons and traffic density in an urban street (Hope street, Glasgow). *International Environmental Technology*, 25–27.

Godish, T. (2004). *Air quality* (4th ed., p. 460). Lewis Publishers, New York.

Guo, H., Wang, T., & Louie, P. K. K. (2004a). Source apportionment of ambient non-methane hydrocarbons in Hong Kong: application of a principal component analysis/absolute principal component scores (PCA/APCS) receptor model. *Environmental pollution (Barking, Essex : 1987)*, *129*(3), 489–98. doi:10.1016/j.envpol.2003.11.006

Guo, H., Wang, T., & Louie, P. K. K. (2004b). Source apportionment of ambient non-methane hydrocarbons in Hong Kong: application of a principal component analysis/absolute principal component scores (PCA/APCS) receptor model. *Environmental pollution (Barking, Essex : 1987)*, *129*(3), 489–98. doi:10.1016/j.envpol.2003.11.006

Harrison, R. M. (1997). Sources and processes affecting concentrations of PM10 and PM2.5 particulate matter in Birmingham (U.K.). *Atmospheric Environment*, *31*(24), 4103–4117.

Harrison, R. M., Beddows, D. C. S., & Dall'Osto, M. (2011). PMF analysis of wide-range particle size spectra collected on a major highway. *Environmental science & technology*, *45*(13), 5522–8. doi:10.1021/es2006622

Harrison, R. M., Jones, A. M., & Lawrence, R. G. (2003). A pragmatic mass closure model for airborne particulate matter at urban background and roadside sites. *Atmospheric Environment*, *37*(35), 4927–4933. doi:10.1016/j.atmosenv.2003.08.025

Harrison, R. M., & Yin, J. (2008a). Sources and processes affecting carbonaceous aerosol in central England. *Atmospheric Environment*, *42*(7), 1413–1423. doi:10.1016/j.atmosenv.2007.11.004

Harrison, R. M., & Yin, J. (2008b). Sources and processes affecting carbonaceous aerosol in central England. *Atmospheric Environment*, *42*(7), 1413–1423. doi:10.1016/j.atmosenv.2007.11.004

Hien, P. D., Bac, V. T., Tham, H. C., Nhan, D. D., & Vinh, L. D. (2002). Concentrations during the monsoon season in Hanoi , Vietnam. *East Asia*, *36*, 3473–3484.

Hinds, W. C. (1999). *Aerosol technology: Properties, behavior, and measurement of airborne particles*. New York: New York: Wiley.

Isakson, J., Persson, T. A., & Lindgren, E. S. (2001). Identification and assessment of ship emissions and their effects in the harbour of Goteborg , Sweden. *Atmospheric Environment*, *35*, 3659–3666.

Jantunen, M., Hänninen, O., Koistinen, K., & Hashim, J. H. (2002). Fine PM measurements: personal and indoor air monitoring. *Chemosphere*, *49*(9), 993–1007. Retrieved from http://www.ncbi.nlm.nih.gov/pubmed/12492162

Jeong, C.-H., Evans, G. J., Dann, T., Graham, M., Herod, D., Dabek-Zlotorzynska, E., Mathieu, D., et al. (2008a). Influence of biomass burning on wintertime fine particulate matter:

Source contribution at a valley site in rural British Columbia. *Atmospheric Environment*, *42*(16), 3684–3699. doi:10.1016/j.atmosenv.2008.01.006

Jeong, C.-H., Evans, G. J., Dann, T., Graham, M., Herod, D., Dabek-Zlotorzynska, E., Mathieu, D., et al. (2008b). Influence of biomass burning on wintertime fine particulate matter: Source contribution at a valley site in rural British Columbia. *Atmospheric Environment*, *42*(16), 3684–3699. doi:10.1016/j.atmosenv.2008.01.006

Jeong, C.-H., Evans, G. J., Dann, T., Graham, M., Herod, D., Dabek-Zlotorzynska, E., Mathieu, D., et al. (2008c). Influence of biomass burning on wintertime fine particulate matter: Source contribution at a valley site in rural British Columbia. *Atmospheric Environment*, *42*(16), 3684–3699. doi:10.1016/j.atmosenv.2008.01.006

Jeong, C.-H., McGuire, M. L., Herod, D., Dann, T., Dabek-Zlotorzynska, E., Wang, D., Ding, L., et al. (2011a). Receptor model based identification of PM2.5 sources in Canadian cities. *Atmospheric Pollution Research*, *2*(2), 158–171. doi:10.5094/APR.2011.021

Jeong, C.-H., McGuire, M. L., Herod, D., Dann, T., Dabek-Zlotorzynska, E., Wang, D., Ding, L., et al. (2011b). Receptor model based identification of PM2.5 sources in Canadian cities. *Atmospheric Pollution Research*, *2*(2), 158–171. doi:10.5094/APR.2011.021

Jeong, C.-H., McGuire, M. L., Herod, D., Dann, T., Dabek-Zlotorzynska, E., Wang, D., Ding, L., et al. (2011c). Receptor model based identification of PM2.5 sources in Canadian cities. *Atmospheric Pollution Research*, *2*(2), 158–171. doi:10.5094/APR.2011.021

Jeong, C.-H., McGuire, M. L., Herod, D., Dann, T., Dabek-Zlotorzynska, E., Wang, D., Ding, L., et al. (2011d). Receptor model based identification of PM2.5 sources in Canadian cities. *Atmospheric Pollution Research*, *2*(2), 158–171. doi:10.5094/APR.2011.021

John Watt, Johan Tidblad, Vladimir Kucera, R. H. (2009). *The effects of air pollution on cultural heritage* (p. 306). Springer Science, NY.

Khoder, M. I. (2002). Atmospheric conversion of sulfur dioxide to particulate sulfate and nitrogen dioxide to particulate nitrate and gaseous nitric acid in an urban area. *Chemosphere*, *49*(6), 675–84. Retrieved from http://www.ncbi.nlm.nih.gov/pubmed/12430655

Kim Oanh, N. T., Pongkiatkul, P., Upadhyay, N., & Hopke, P. P. (2009). Designing ambient particulate matter monitoring program for source apportionment study by receptor modeling. *Atmospheric Environment*, *43*(21), 3334–3344. doi:10.1016/j.atmosenv.2009.04.016

Korea, S., Lee, H. S., & Kang, B. (2001). Chemical characteristics of principal PM species in, *35*(October 1995).

Kotchenruther, R. a. (2013). A regional assessment of marine vessel PM2.5 impacts in the U.S. Pacific Northwest using a receptor-based source apportionment method. *Atmospheric Environment*, *68*, 103–111. doi:10.1016/j.atmosenv.2012.11.067

Lack, D. a, Cappa, C. D., Langridge, J., Bahreini, R., Buffaloe, G., Brock, C., Cerully, K., et al. (2011). Impact of fuel quality regulation and speed reductions on shipping emissions: implications for climate and air quality. *Environmental science & technology*, *45*(20), 9052–60. doi:10.1021/es2013424

Larson, T., Gould, T., Simpson, C., Liu, L. J. S., Claiborn, C., & Lewtas, J. (2004a). Source apportionment of indoor, outdoor, and personal PM2.5 in Seattle, Washington, using positive matrix factorization. *Journal of the Air & Waste Management Association (1995)*, *54*(9), 1175–87. Retrieved from http://www.ncbi.nlm.nih.gov/pubmed/15468670

Larson, T., Gould, T., Simpson, C., Liu, L. J. S., Claiborn, C., & Lewtas, J. (2004b). Source apportionment of indoor, outdoor, and personal PM2.5 in Seattle, Washington, using positive matrix factorization. *Journal of the Air & Waste Management Association (1995)*, *54*(9), 1175–87. Retrieved from http://www.ncbi.nlm.nih.gov/pubmed/15468670

Lonati, G, Giugliano, M., Butelli, P., Romele, L., & Tardivo, R. (2005). Major chemical components of PM2.5 in Milan (Italy). *Atmospheric Environment*, *39*(10), 1925–1934. doi:10.1016/j.atmosenv.2004.12.012

Lonati, Giovanni, Cernuschi, S., & Sidi, S. (2010). Air quality impact assessment of at-berth ship emissions: Case-study for the project of a new freight port. *The Science of the total environment*, *409*(1), 192–200. doi:10.1016/j.scitotenv.2010.08.029

Maliszewska-Kordybach, B. (1999). Sources , Concentrations , Fate and Effects of Polycyclic Aromatic Hydrocarbons (PAHs) in the Environment . Part A : PAHs in Air. *Polish Journal of Environmental Studies*, *8*(3), 131–136.

Mark Gibson. (2010). Mark Gibson 103rd AWMA Calgary 2010.

Marmur, A., Park, S.-K., Mulholland, J. a., Tolbert, P. E., & Russell, A. G. (2006). Source apportionment of PM2.5 in the southeastern United States using receptor and emissions-based models: Conceptual differences and implications for time-series health studies. *Atmospheric Environment*, *40*(14), 2533–2551. doi:10.1016/j.atmosenv.2005.12.019

Minguillon, M.C., Arhami, M., Schauer, J.J., Sioutas, C.. (2008). Seasonal and spatial variations of sources of fine and quasi-ultrafine particulate matter in neighborhoods near the Los Angeles–Long Beach harbor. *Atmospheric Environment*, *42*, 7317–7328. doi: 10.1016/j.atmosenv.2008.07.036

Norris, G. and Vedantham, R. (2008). EPA Positive Matrix Factorization (PMF) 3.0 Fundamentals & User Guide.

Norris, G. ; Vedantham, R. (2008). EPA Positive Matrix Factorization (PMF) 3.0. Washington, DC: USEPA. Retrieved from www.epa.gov

O'Dowd, C. D., & De Leeuw, G. (2007). Marine aerosol production: a review of the current knowledge. *Philosophical transactions. Series A, Mathematical, physical, and engineering sciences*, *365*(1856), 1753–74. doi:10.1098/rsta.2007.2043

Paatero, P; Hopke, P. (2003). Discarding or downweighting high-noise variables in factor analytic models. *Analytica Chimica Acta*, *490*(1-2), 277–289. doi:10.1016/S0003-2670(02)01643-4

Pandolfi, M., Gonzalez-Castanedo, Y., Alastuey, A., De la Rosa, J. D., Mantilla, E., De la Campa, a S., Querol, X., et al. (2011). Source apportionment of PM(10) and PM(2.5) at multiple sites in the strait of Gibraltar by PMF: impact of shipping emissions. *Environmental science and pollution research international*, *18*(2), 260–9. doi:10.1007/s11356-010-0373-4

Particulates. (n.d.). No Title. Retrieved from http://www.ecotech.com/particulates-categories/particulates

Pekney, N. J., Davidson, C. I., Bein, K. J., Wexler, A. S., & Johnston, M. V. (2006). Identification of sources of atmospheric PM at the Pittsburgh Supersite, Part I: Single particle analysis and filter-based positive matrix factorization. *Atmospheric Environment*, *40*, 411–423. doi:10.1016/j.atmosenv.2005.12.072

Pesticides and health. (2007). Retrieved from http://www.hc-sc.gc.ca/ewh-semt/pubs/contaminants/pesticides-eng.php#a2

Phinney, L. (2008). Report on the Feasibility of extending the Contribution of Marine Activities to Ambient Air Chemistry study to Saint John, NB, and St John's, NL. Darmouth. Retrieved from http://publications.gc.ca/collections/collection_2009/ec/En57-36-2008-3E.pdf

Pope III, C. A., Muhlestein, J. B., May, H. T., Renlund, D. G., Anderson, J. L., & Horne, B. D. (2006). Ischemic heart disease events triggered by short-term exposure to fine particulate air pollution. *Circulation*, *114*(23), 2443–8. doi:10.1161/CIRCULATIONAHA.106.636977

Poplawski, K., Setton, E., McEwen, B., Hrebenyk, D., Graham, M., & Keller, P. (2011). Impact of cruise ship emissions in Victoria, BC, Canada. *Atmospheric Environment*, *45*(4), 824–833. doi:10.1016/j.atmosenv.2010.11.029

Port of Halifax. (2012). Halifax. Retrieved from http://www.portofhalifax.ca/english/about-us/index.html

Querol, X., Alastuey, a., Ruiz, C. R., Artiñano, B., Hansson, H. C., Harrison, R. M., Buringh, E., et al. (2004). Speciation and origin of PM10 and PM2.5 in selected European cities. *Atmospheric Environment*, *38*(38), 6547–6555. doi:10.1016/j.atmosenv.2004.08.037

Rattigan, O. V., Hogrefe, O., Felton, H. D., Schwab, J. J., Roychowdhury, U. K., Husain, L., Dutkiewicz, V. a., et al. (2006). Multi-year urban and rural semi-continuous PM2.5 sulfate and nitrate measurements in New York state: Evaluation and comparison with filter based measurements. *Atmospheric Environment*, *40*, 192–205. doi:10.1016/j.atmosenv.2005.12.071

Reff, A., Eberly, S. I., & Bhave, P. V. (2007). Receptor modeling of ambient particulate matter data using positive matrix factorization: review of existing methods. *Journal of the Air & Waste Management Association (1995)*, *57*(2), 146–54. Retrieved from http://www.ncbi.nlm.nih.gov/pubmed/17355075

Schembari, C., Cavalli, F., Cuccia, E., Hjorth, J., Calzolai, G., Pérez, N., Pey, J., et al. (2012). Impact of a European directive on ship emissions on air quality in Mediterranean harbours. *Atmospheric Environment*, *61*, 661–669. doi:10.1016/j.atmosenv.2012.06.047

Seinfeld, J. H., & Pandis, S. N. (2006). *Atmospheric Chemistry and Physics: From Air Pollution to Climate Change*. *Atmospheric Chemistry and Physics* (2nd ed.). John Wiley&Sons, New Jersey.

Song, S.-K., Shon, Z.-H., Kim, Y.-K., Kang, Y.-H., Oh, I.-B., & Jung, C.-H. (2010). Influence of ship emissions on ozone concentrations around coastal areas during summer season. *Atmospheric Environment*, *44*(5), 713–723. doi:10.1016/j.atmosenv.2009.11.010

Song, X., Polissar, A. V, & Hopke, P. K. (2001). Sources of fine particle composition in the northeastern US, *35*(January), 5277–5286.

Stohl, A. (1998). Computation, accuracy and applications of trajectories—A review and bibliography. *Atmospheric Environment*, *32*(6), 947–966. doi:10.1016/S1352-2310(97)00457-3

Teom FDMS Equipment. (2008). Site operational procedures for TEOM FDMS analysers.

Theodore, L. (2008). *Air pollution control equipment calculations* (p. 574). John Wiley&Sons, New Jersey.

Thurston, G.D. and Spengler, J. D. (1985). A Quantitative Assessment of source contributions to Inhalable Particulate Matter pollution in Metropolitan Boston. *Atmospheric Environment*, *19*, 9–25.

Tiwary, A., & Colls, J. (2010). *Air Pollution: Measurement, modelling and mitigation*. *Atmospheric Environment* (3d ed., p. 501). Routledge, NY.

Tzannatos, E. (2010). Ship emissions and their externalities for the port of Piraeus – Greece. *Atmospheric Environment*, *44*(3), 400–407. doi:10.1016/j.atmosenv.2009.10.024

U.S. Environmental Protection. (1997). National Ambient Air Quality Standard (NAAQS) for Particulate Matter.

USEPA. (1998). PM2.5 Mass Weighing Laboratory Standard Operating Procedures for the Performance Evaluatio Program. *Quality Assurance Guidance Document*, 1–165.

Vaattovaara, P., Huttunen, P. E., Yoon, Y. J., Joutsensaari, J., Lehtinen, K. E. J., O'Dowd, C. D., & Laaksonen, a. (2006). The composition of nucleation and Aitken modes particles during coastal nucleation events: evidence for marine secondary organic contribution. *Atmospheric Chemistry and Physics Discussions*, *6*(2), 3337–3379. doi:10.5194/acpd-6-3337-2006

Viana, M., Querol, X., Alastuey, a, Gil, J. I., & Menéndez, M. (2006). Identification of PM sources by principal component analysis (PCA) coupled with wind direction data. *Chemosphere*, *65*(11), 2411–8. doi:10.1016/j.chemosphere.2006.04.060

Ward, T. J., Hamilton, R. F., & Smith, G. C. (2004). The Missoula, Montana PM2.5 speciation study—seasonal average concentrations. *Atmospheric Environment*, *38*(37), 6371–6379. doi:10.1016/j.atmosenv.2004.07.012

Ward, T. J., Rinehart, L. R., & Lange, T. (2006). The 2003/2004 Libby, Montana PM 2.5 Source Apportionment Research Study. *Aerosol Science and Technology*, *40*(3), 166–177. doi:10.1080/02786820500494536

Ward, T. J; Raymond, F. ; Hamilton, Jr; Garon, C. (2007). The Missoula, Montana PM2.5 Source Apportionment Research Study. The university of Montana, Missoula.

Wrobel, A. (1999). The influence of meteorological parameters on short range transport of aerosols. *Nuclear Instruments and Methods in Physics Research*, *150*, 403–408.

Yin, J., Allen, a. G., Harrison, R. M., Jennings, S. G., Wright, E., Fitzpatrick, M., Healy, T., et al. (2005). Major component composition of urban PM10 and PM2.5 in Ireland. *Atmospheric Research*, *78*(3-4), 149–165. doi:10.1016/j.atmosres.2005.03.006

Yin, Jianxin, & Harrison, R. M. (2008). Pragmatic mass closure study for PM1.0, PM2.5 and PM10 at roadside, urban background and rural sites. *Atmospheric Environment*, *42*(5), 980–988. doi:10.1016/j.atmosenv.2007.10.005

Zhao, M., Zhang, Y., Ma, W., Fu, Q., Yang, X., Li, C., Zhou, B., et al. (2013). Characteristics and ship traffic source identification of air pollutants in China's largest port. *Atmospheric Environment*, *64*(x), 277–286. doi:10.1016/j.atmosenv.2012.10.007

APPENDIX

Table 15 Descriptive statistics of the meteorological variables obtained at sampling site during the $PM_{2.5}$ sampling period.

	n	Mean	Std	Min	25th Pctl	Median	75th Pctl	Max
Wind Speed (m/sec)	115	2.27	1.33	0.19	1.25	1.93	3.16	6.47
Temperature (ºC)	115	9.52	8.45	-9.12	2.78	9.97	17.78	22.67
Relative Humidity	115	77.12	12.64	49.20	68.39	79.83	86.72	97.38
Pressure (kPa)	115	93.41	24.79	3.96*	100.04	101.05	101.74	103.07
Average Wind Vector: 199º ~ SSW								

*considered an outlier (instrument malfunction)

One Way Analysis of Variance

Normality Test (Shapiro-Wilk) Failed (P < 0.050)
Kruskal-Wallis One Way Analysis of Variance on Ranks

Group	**N**	**Missing**	**Median**	**25%**	**75%**
winter	28	0	2.673	2.083	4.146
spring	30	3	3.367	1.936	4.588
summer	31	0	3.846	1.179	5.892
fall	26	0	3.715	1.882	5.790

H = 1.602 with 3 degrees of freedom. (P = 0.659)

The differences in the median values among the treatment groups are not great enough to exclude the possibility that the difference is due to random sampling variability; there is not a statistically significant difference (P = 0.659).

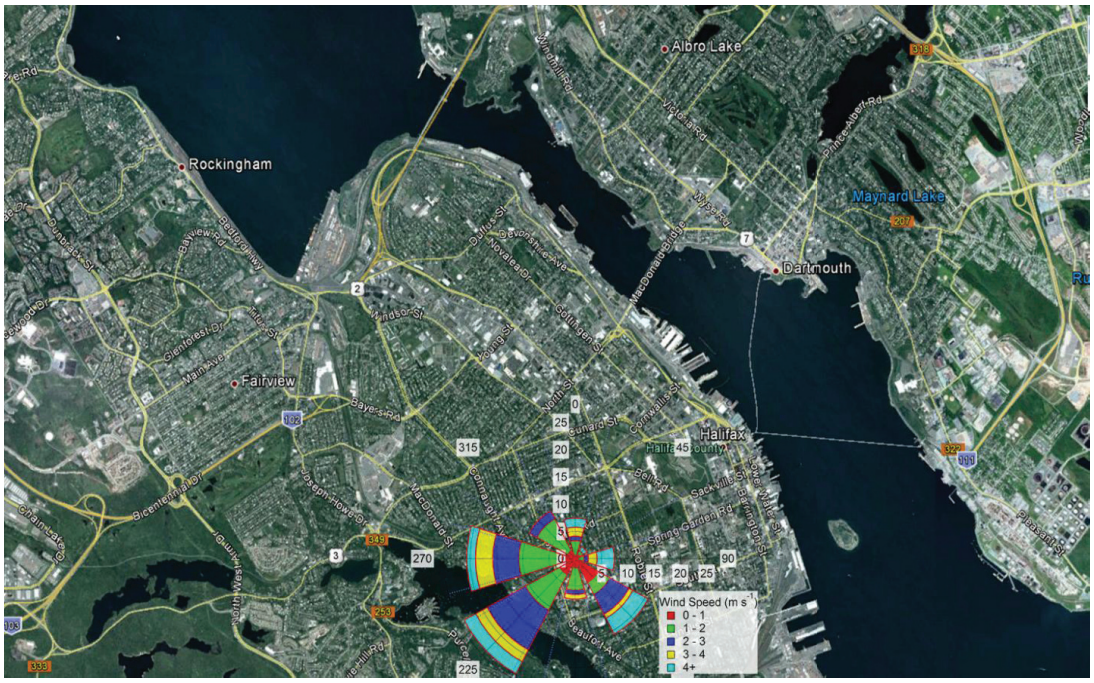

Figure 45 Wind rose showing wind direction and wind speed frequency for the period of August 20, 2011 to August 20, 2012.

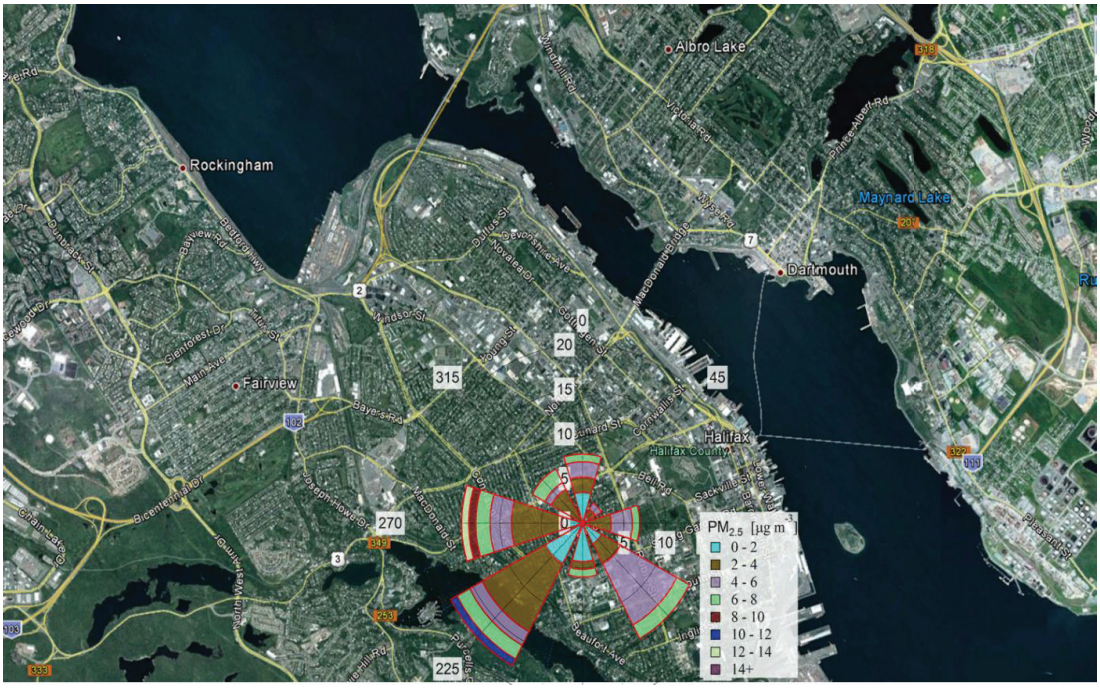

Figure 46 $PM_{2.5}$ pollution rose for the period of August 20, 2011 to August 20, 2012.

Figure 47 BC pollution rose for the period of August 20, 2011 to August 20, 2012.

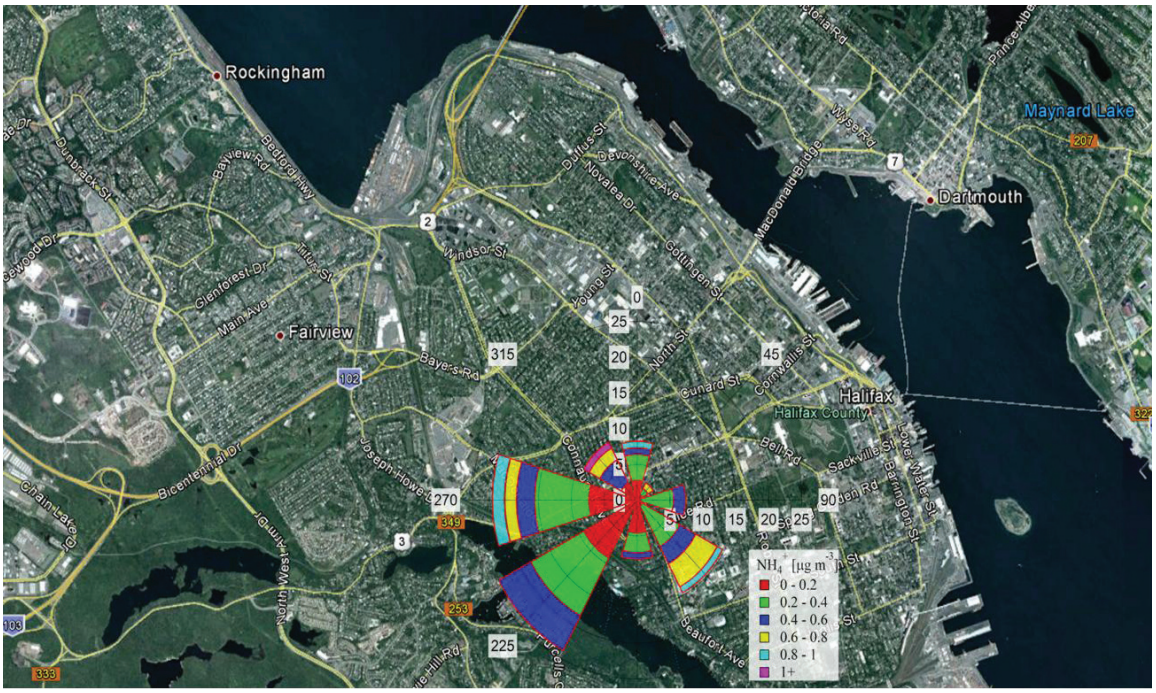

Figure 48 NH_4^+ pollution rose for the period of August 20, 2011 to August 20, 2012.

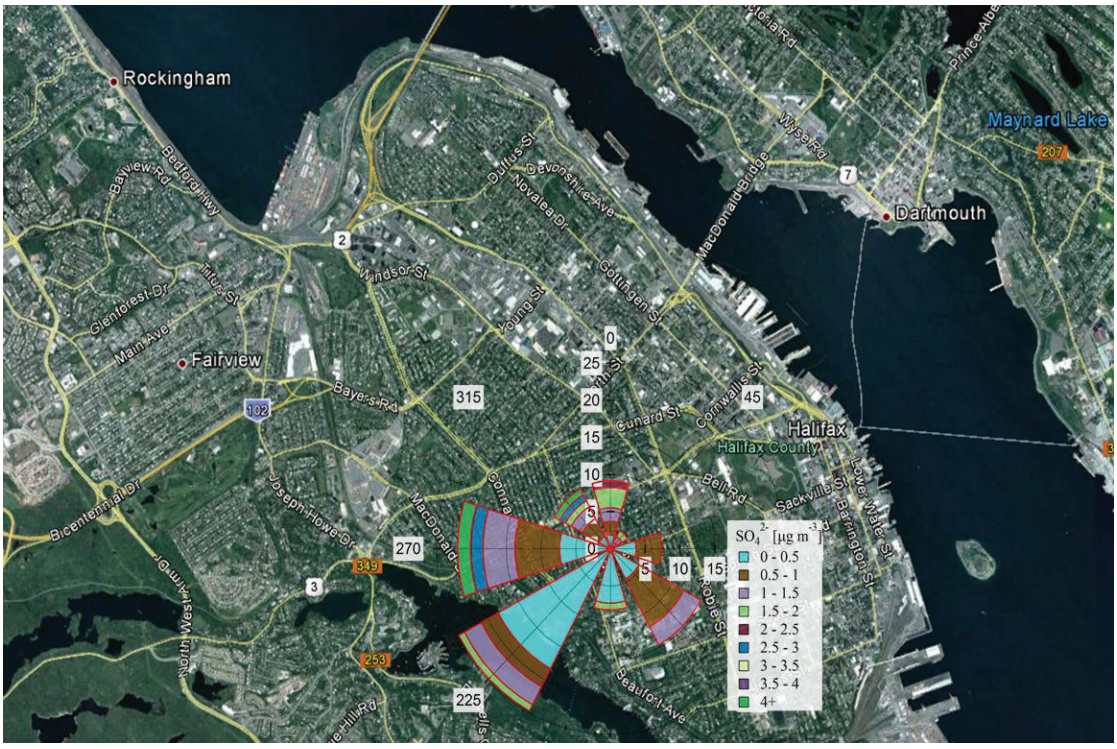

Figure 49 SO_4^{2-} pollution rose for the period of August 20, 2011 to August 20, 2012.

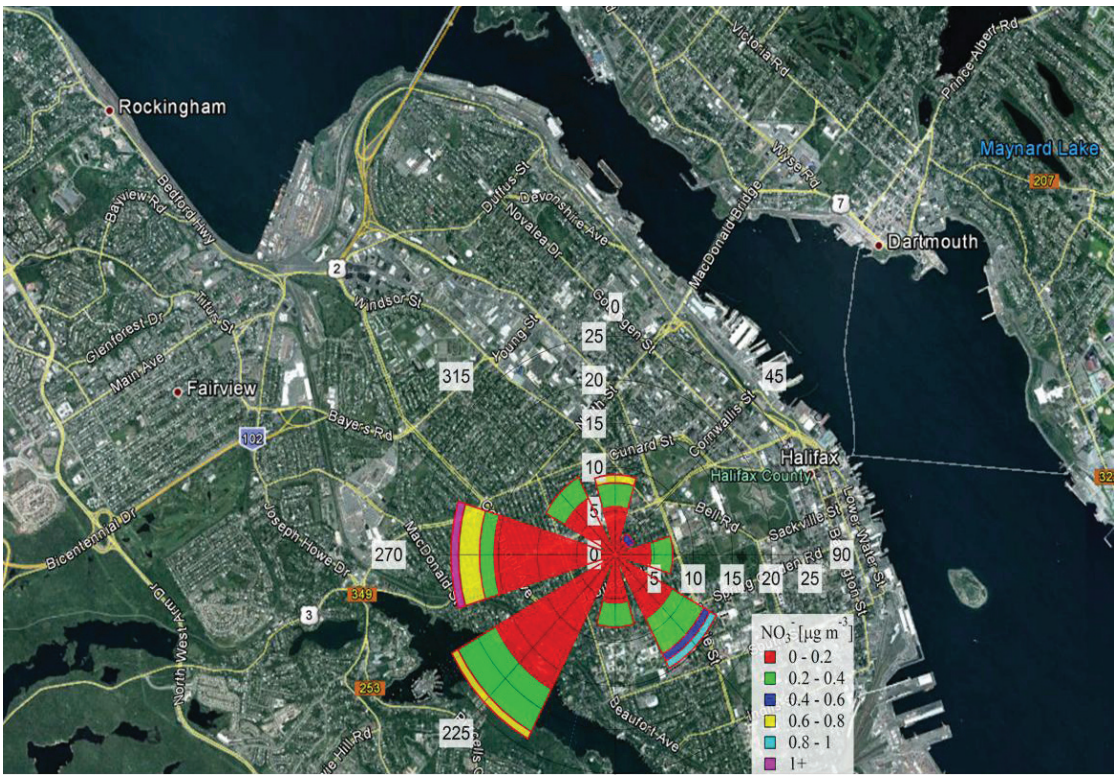

Figure 50 NO_3^- pollution rose for the period of August 20, 2011 to August 20, 2012.

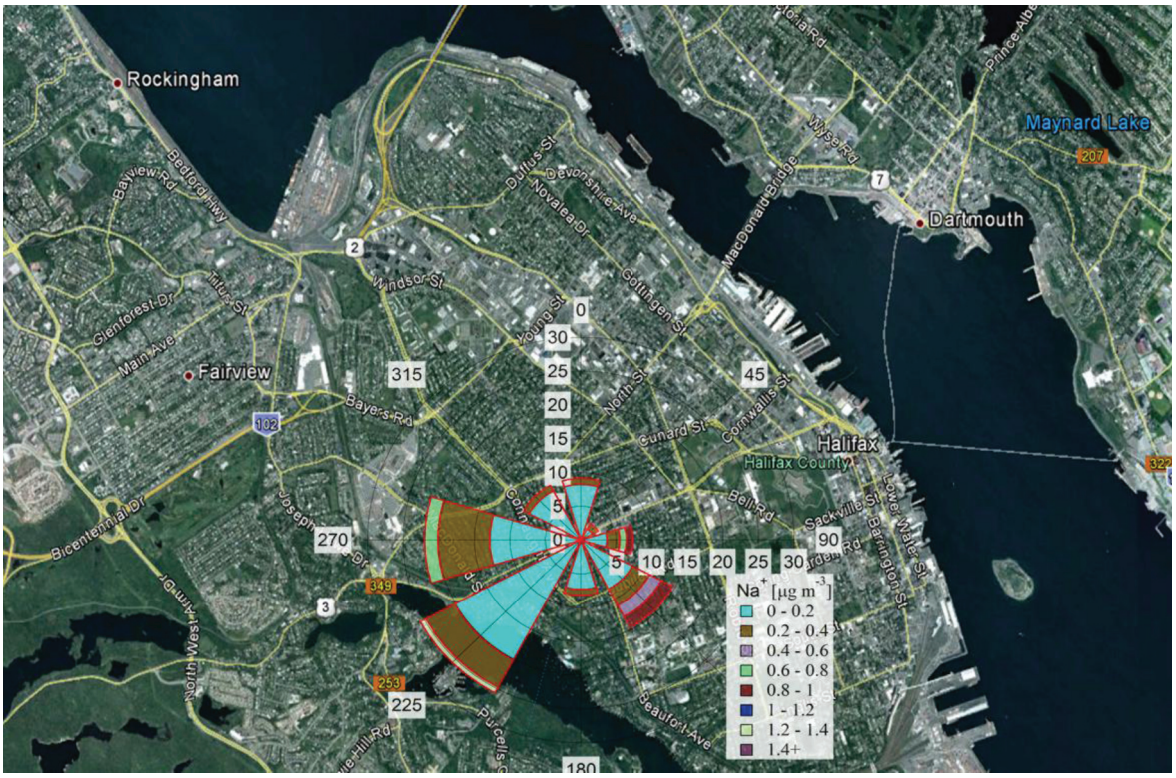

Figure 51 Na^{+} pollution rose for the period of August 20, 2011 to August 20, 2012.

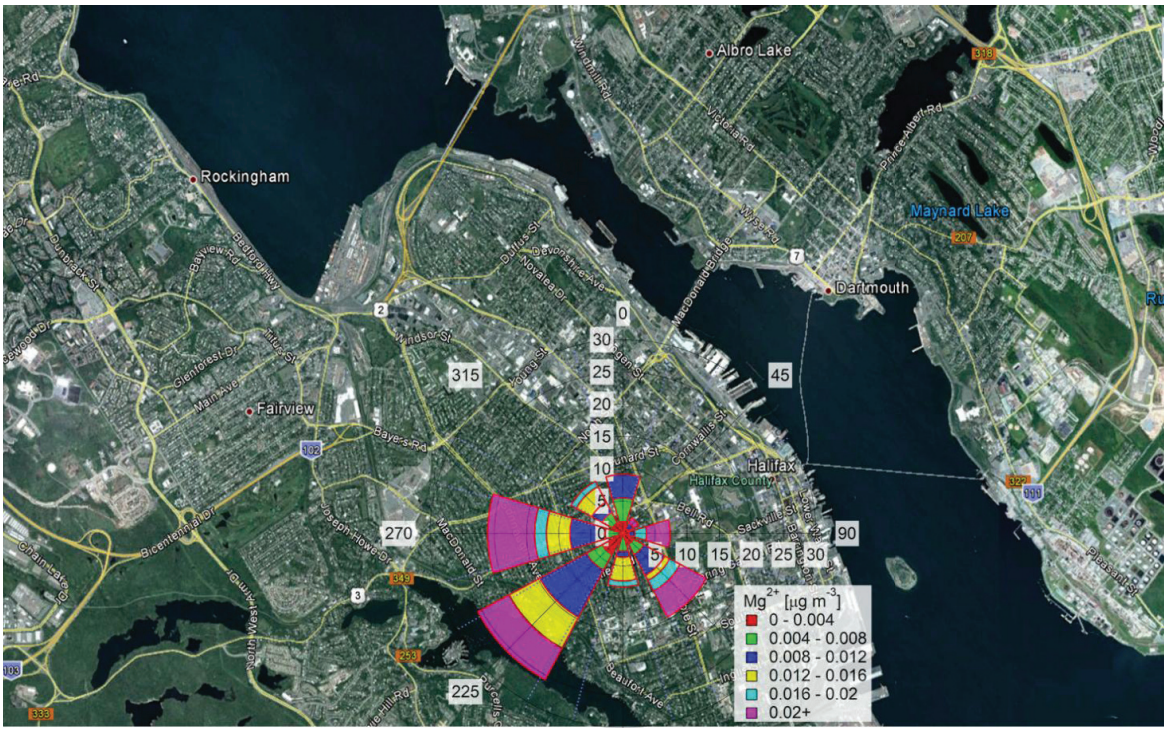

Figure 52 Mg^{2+} pollution rose for the period of August 20, 2011 to August 20, 2012.

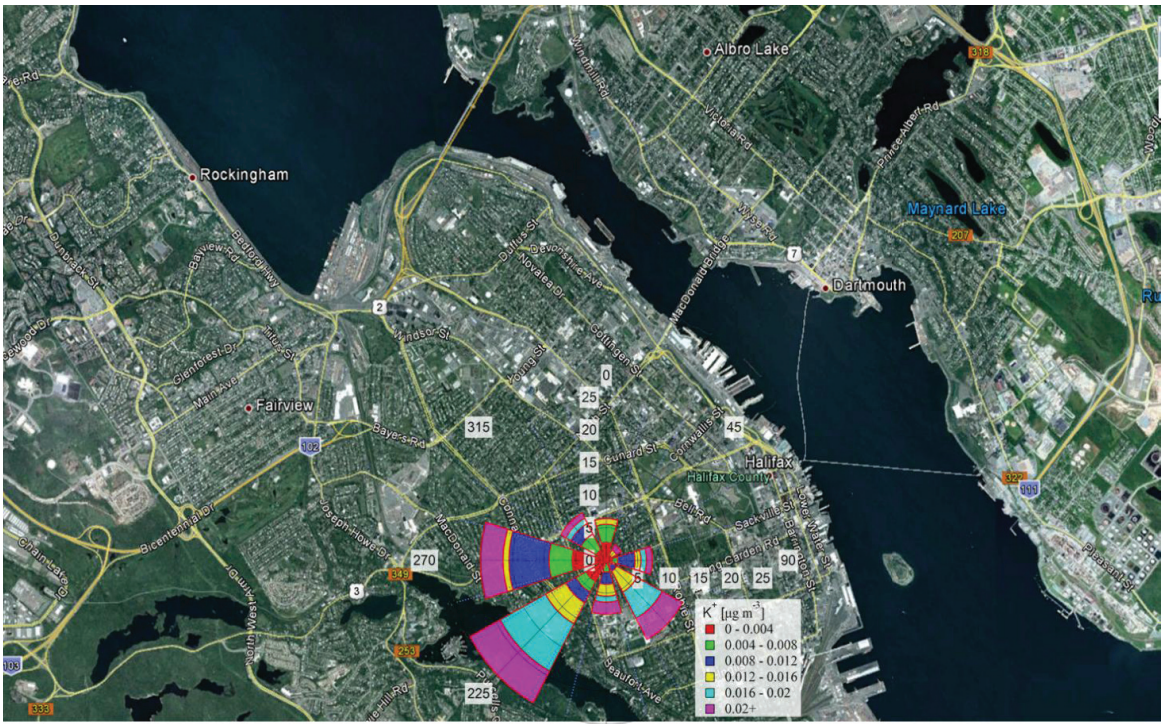

Figure 53 K^+ pollution rose for the period of August 20, 2011 to August 20, 2012.

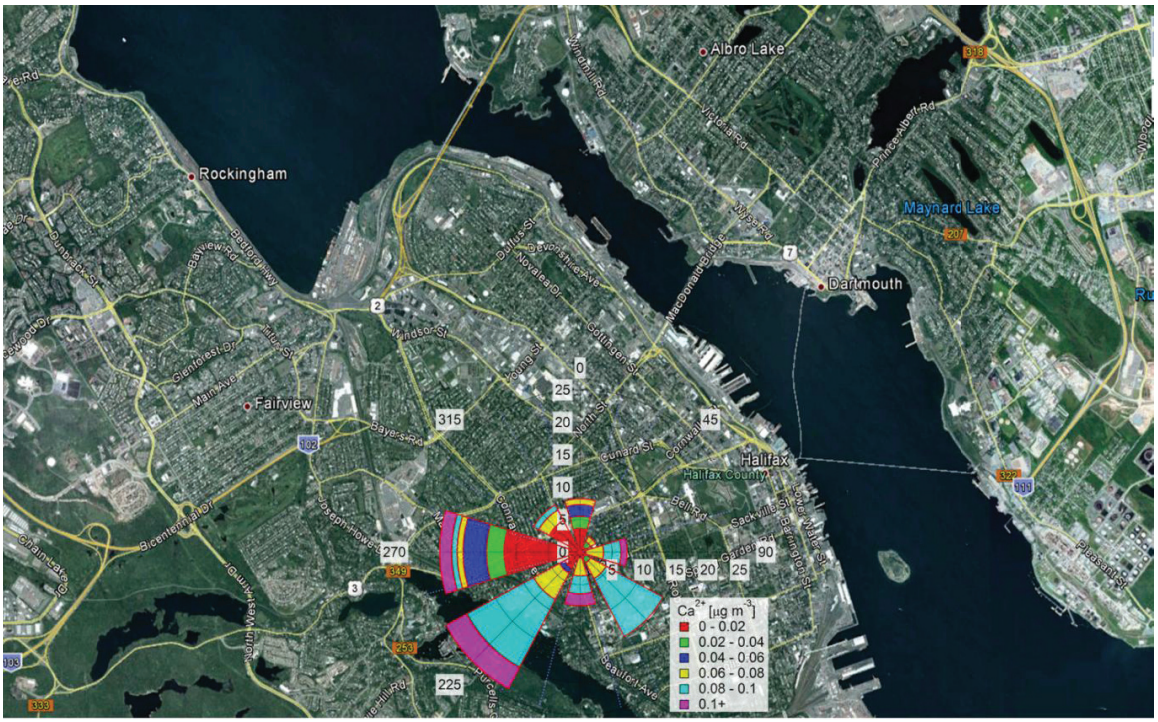

Figure 54 Ca^{2+} pollution rose for the period of August 20, 2011 to August 20, 2012.

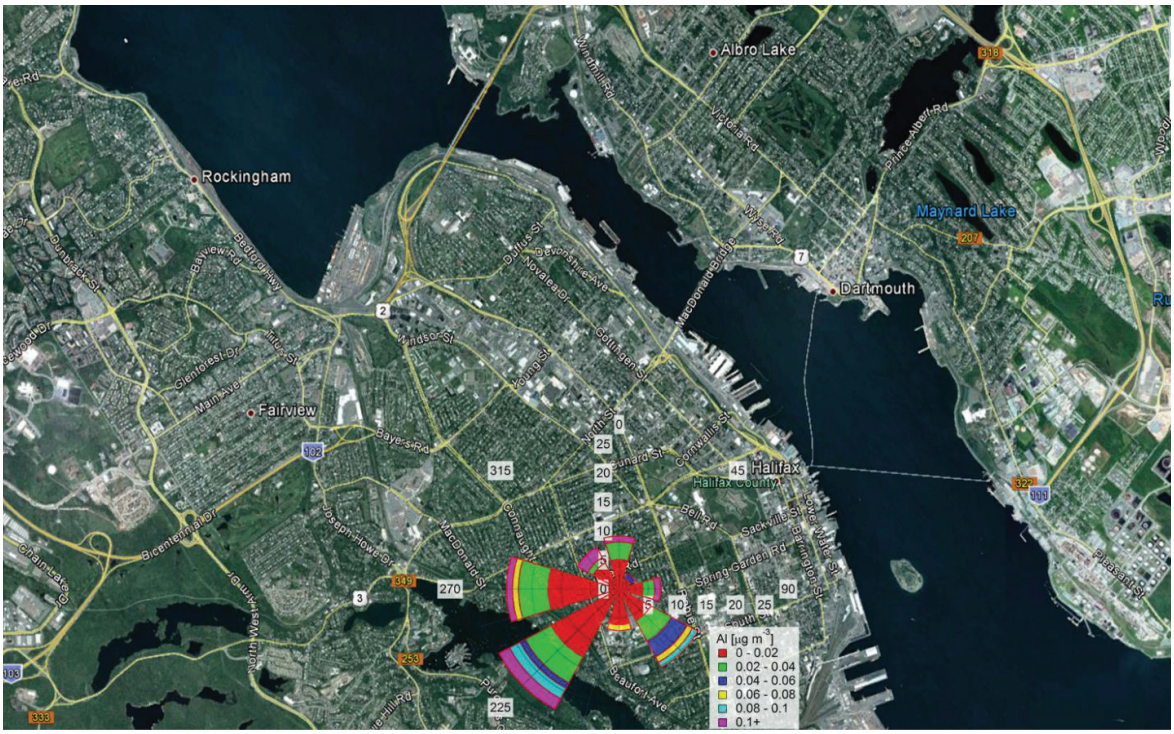

Figure 55 Al pollution rose for the period of August 20, 2011 to August 20, 2012.

Figure 56 Ba pollution rose for the period of August 20, 2011 to August 20, 2012.

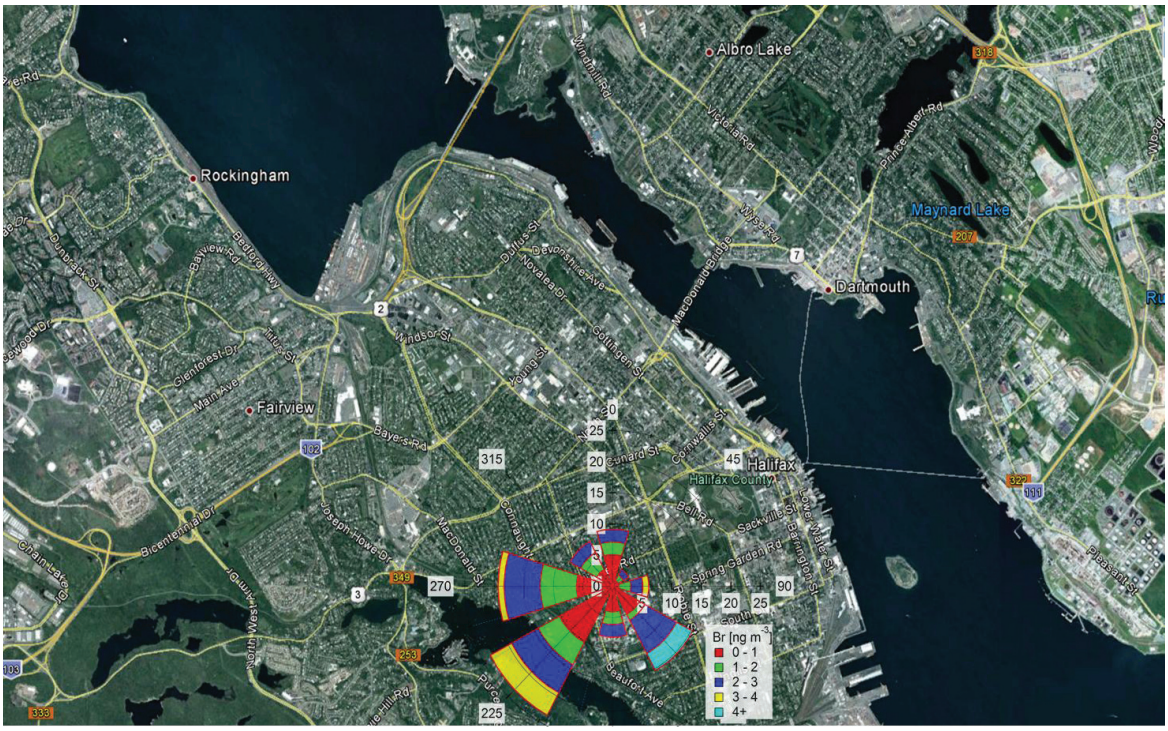

Figure 57 Br pollution rose for the period of August 20, 2011 to August 20, 2012.

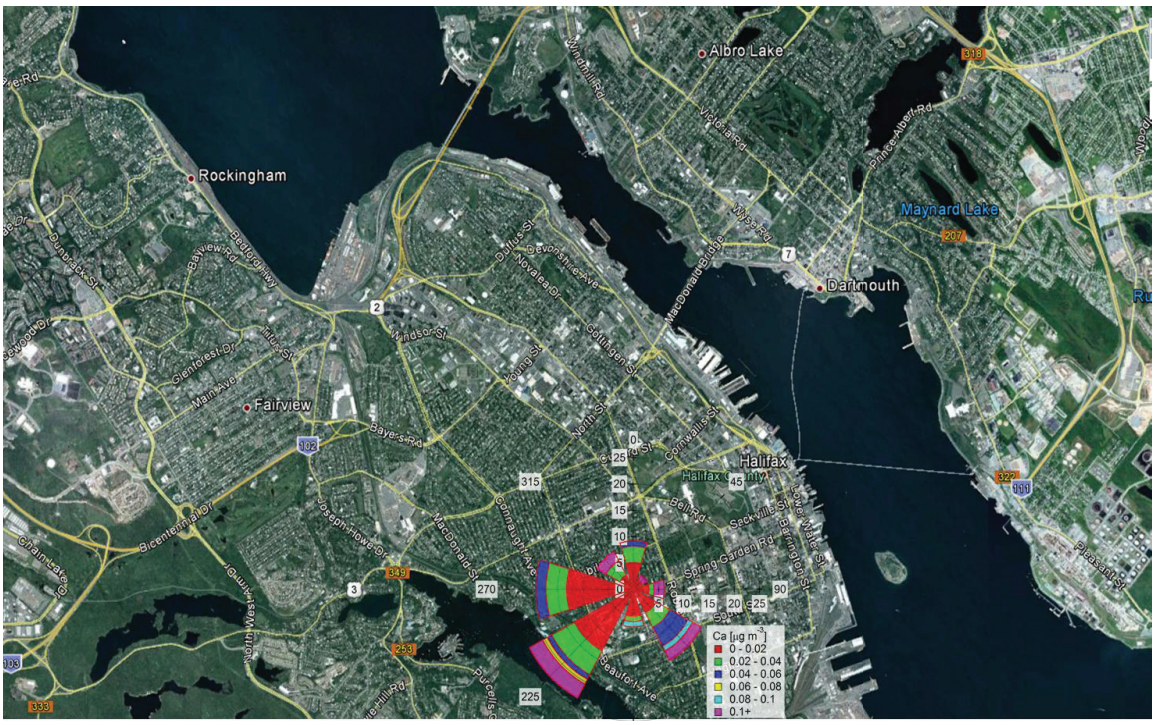

Figure 58 Ca pollution rose for the period of August 20, 2011 to August 20, 2012.

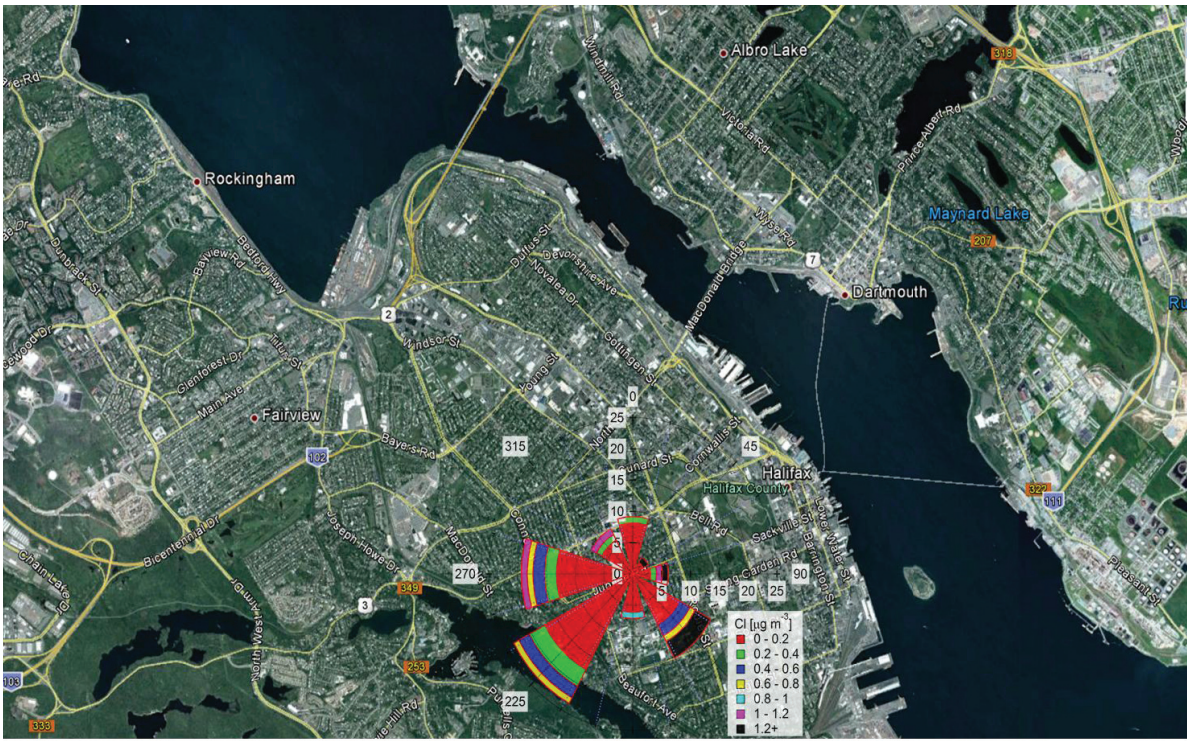

Figure 59 Cl pollution rose for the period of August 20, 2011 to August 20, 2012.

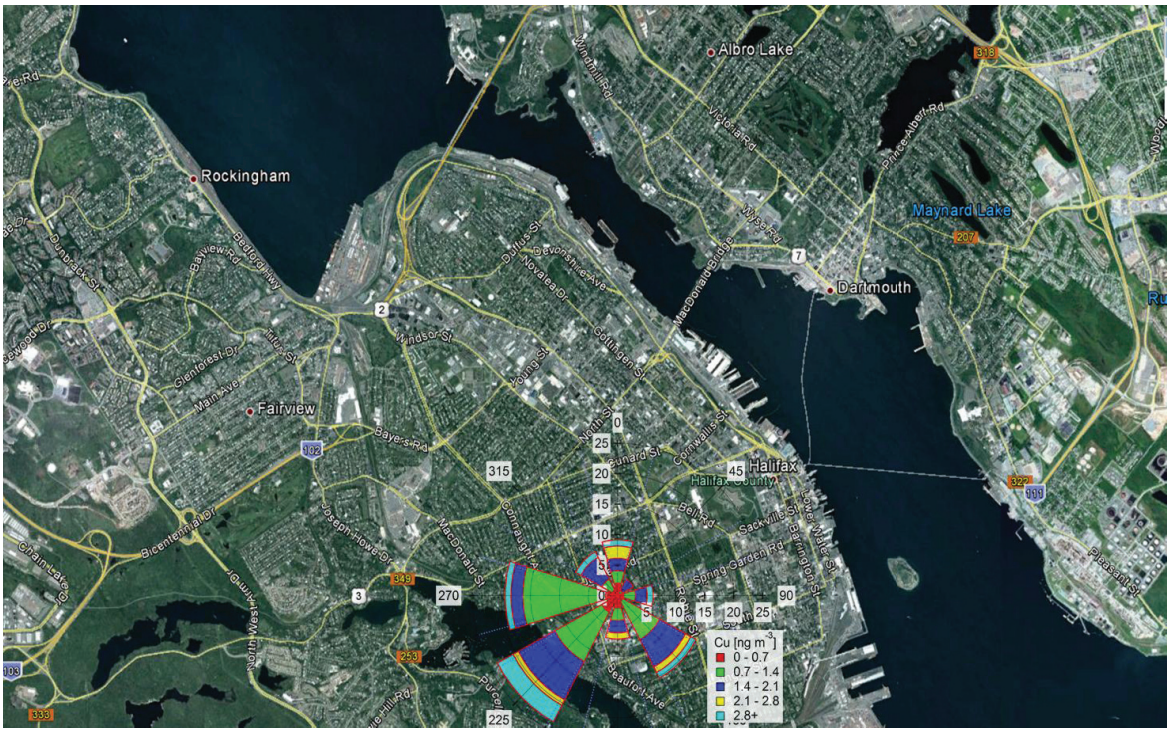

Figure 60 Cu pollution rose for the period of August 20, 2011 to August 20, 2012.

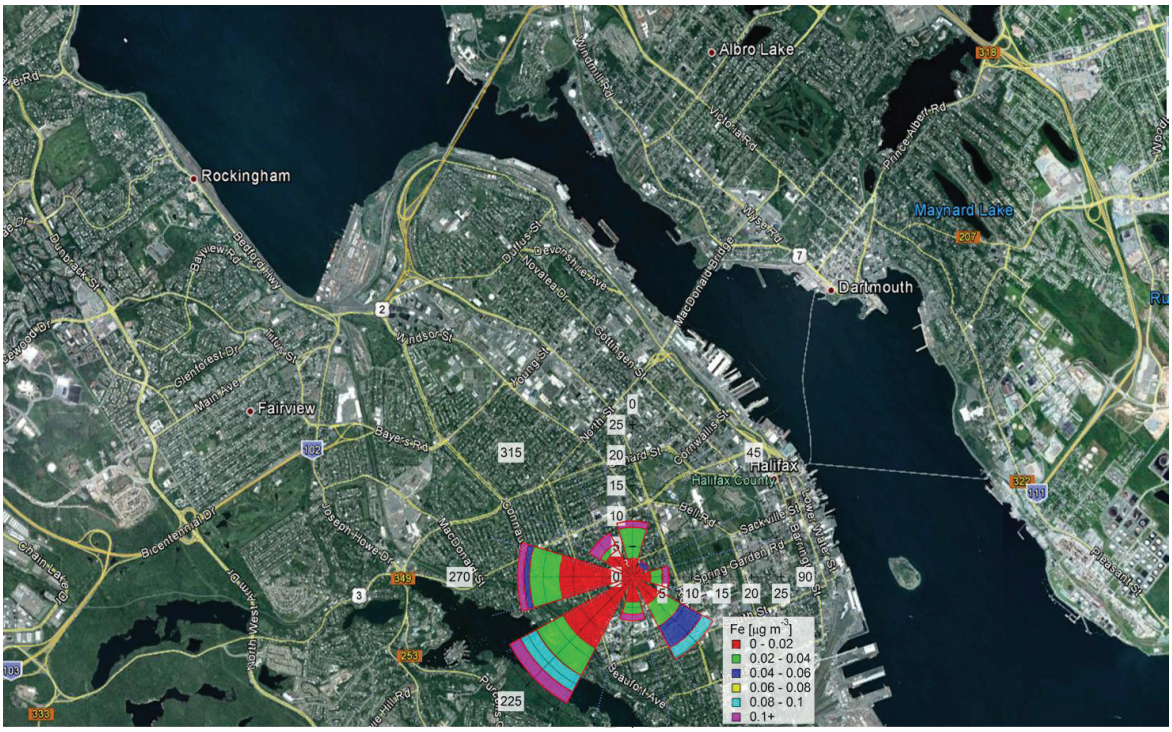

Figure 61 Fe pollution rose for the period of August 20, 2011 to August 20, 2012.

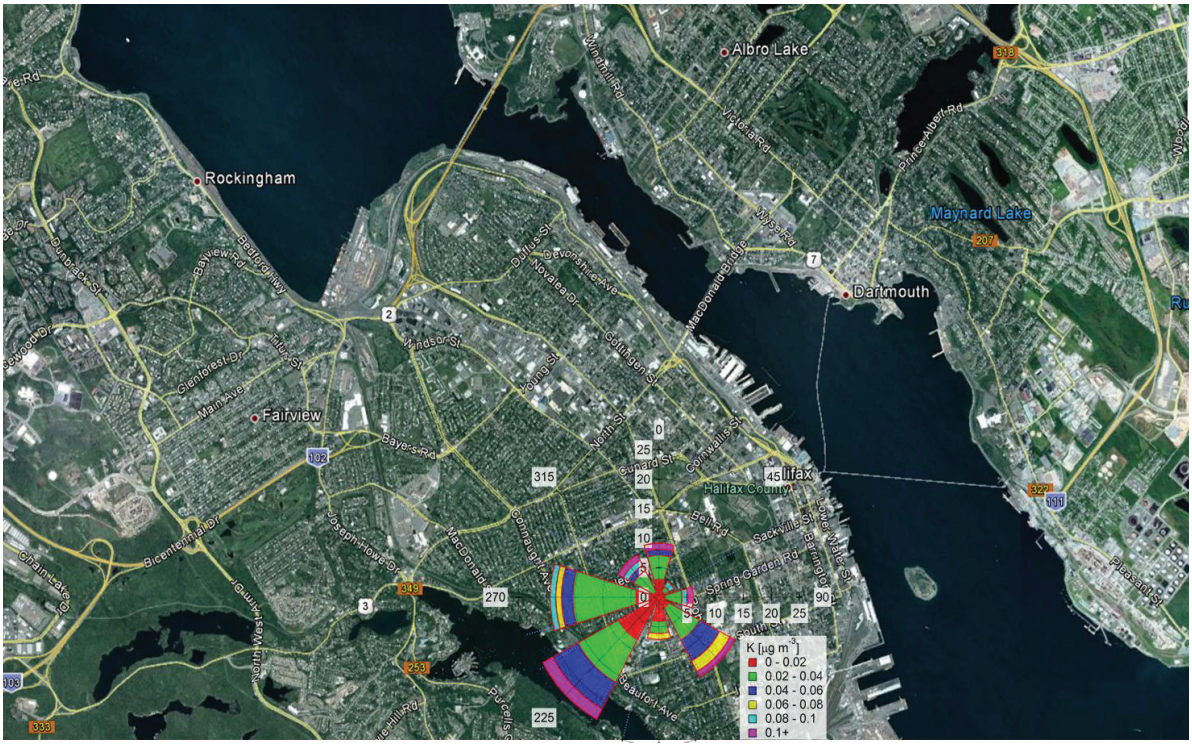

Figure 62 K pollution rose for the period of August 20, 2011 to August 20, 2012.

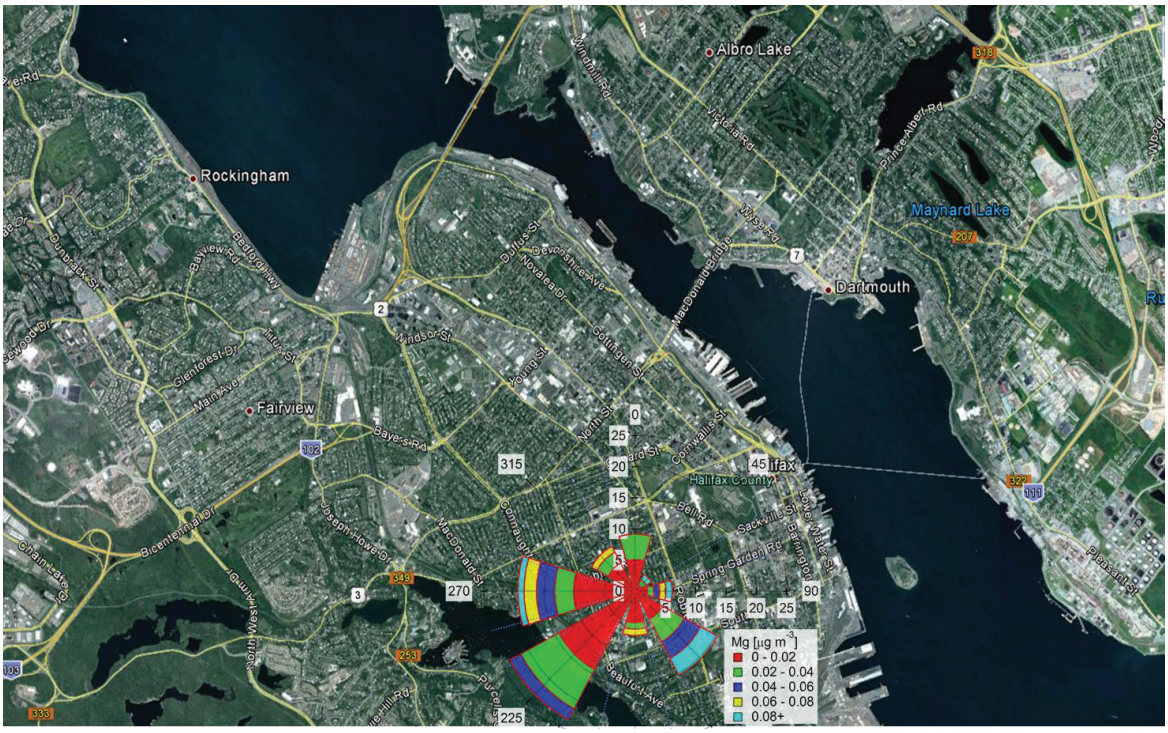

Figure 63 Mg pollution rose for the period of August 20, 2011 to August 20, 2012.

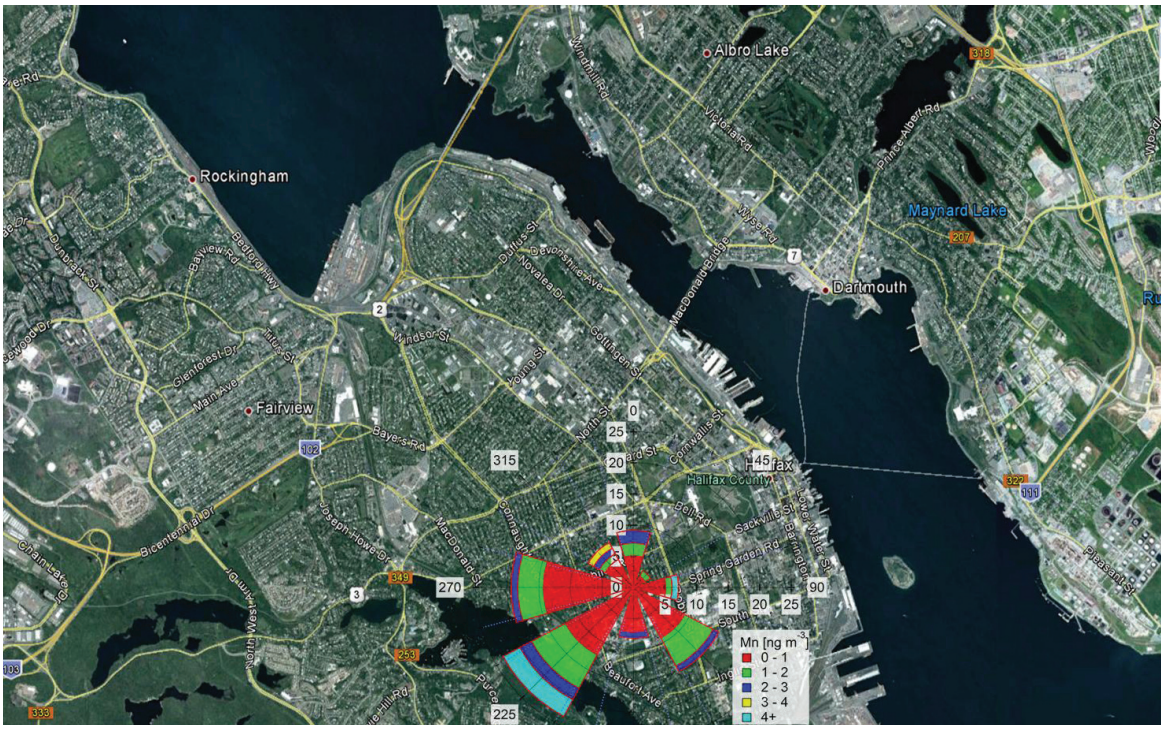

Figure 64 Mn pollution rose for the period of August 20, 2011 to August 20, 2012.

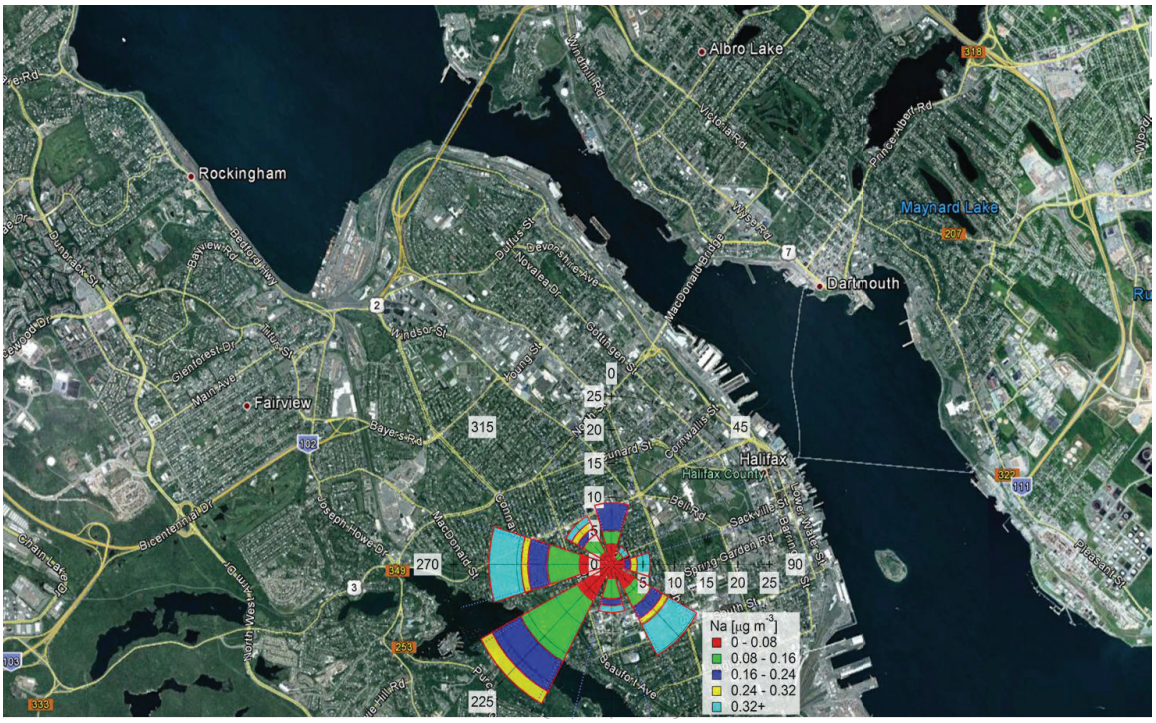

Figure 65 Na pollution rose for the period of August 20, 2011 to August 20, 2012.

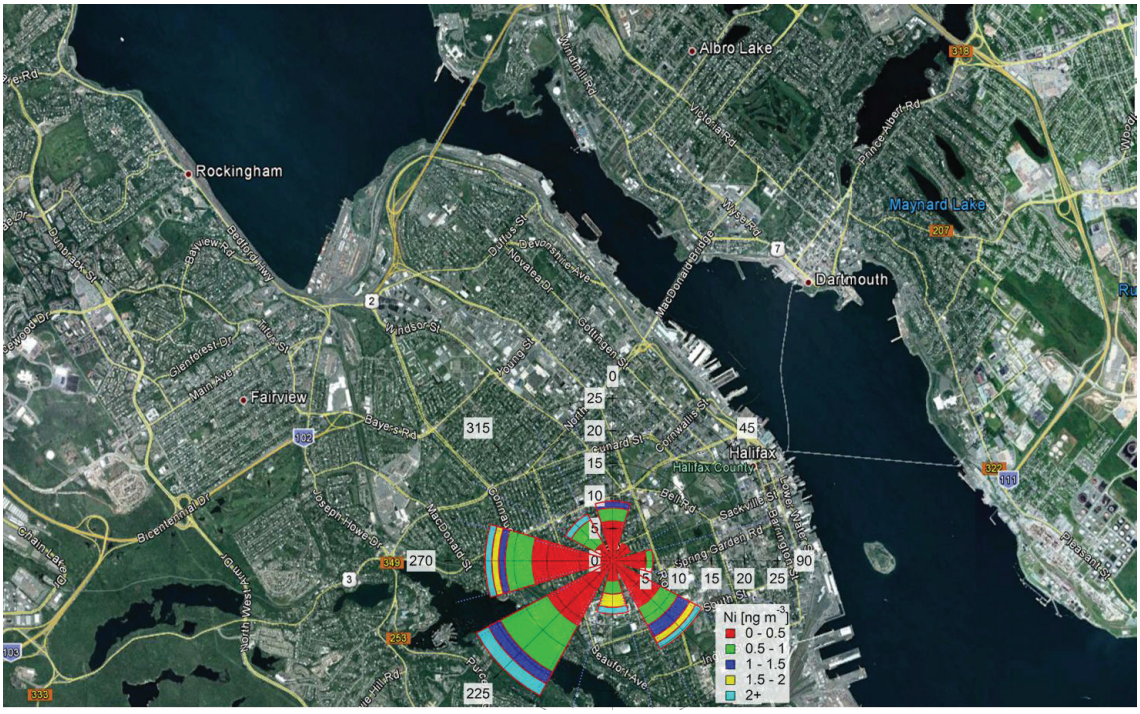

Figure 66 Ni pollution rose for the period of August 20, 2011 to August 20, 2012.

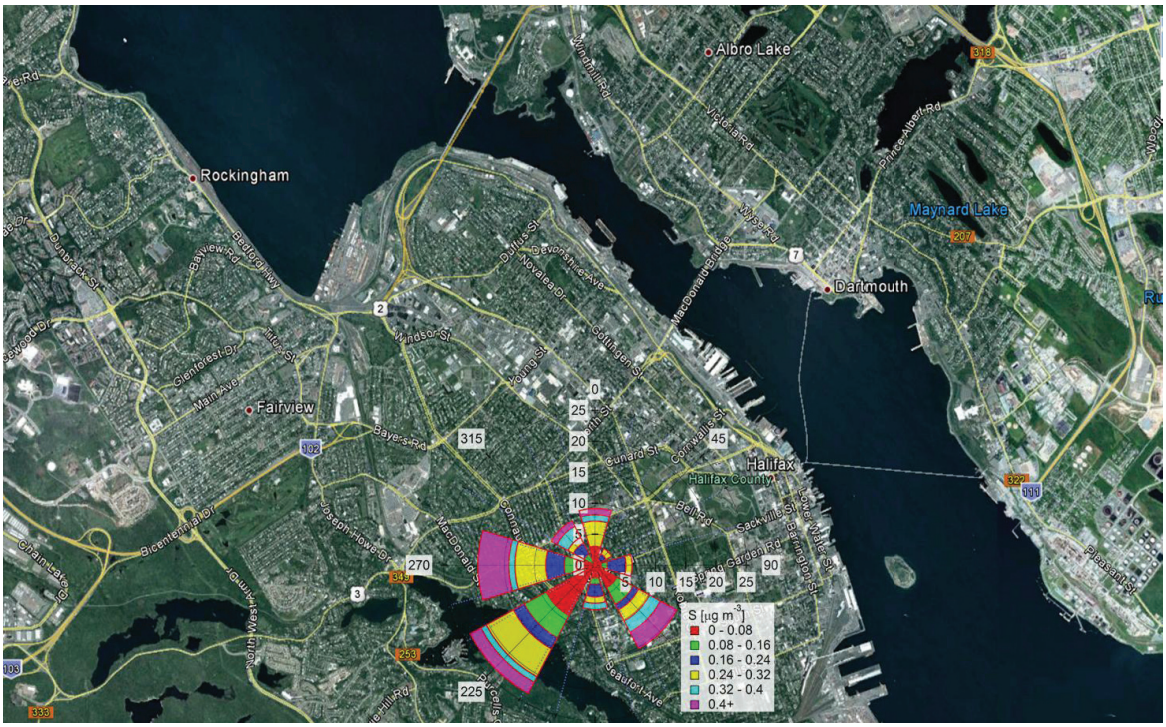

Figure 67 S pollution rose for the period of August 20, 2011 to August 20, 2012.

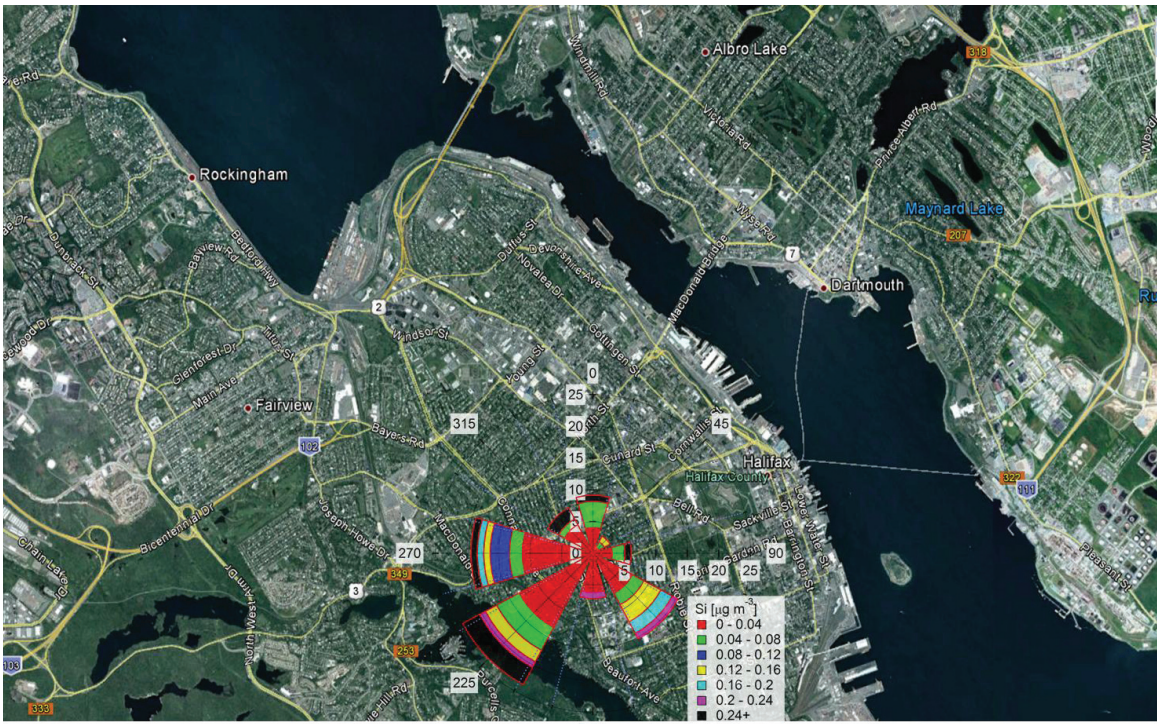

Figure 68 Si pollution rose for the period of August 20, 2011 to August 20, 2012.

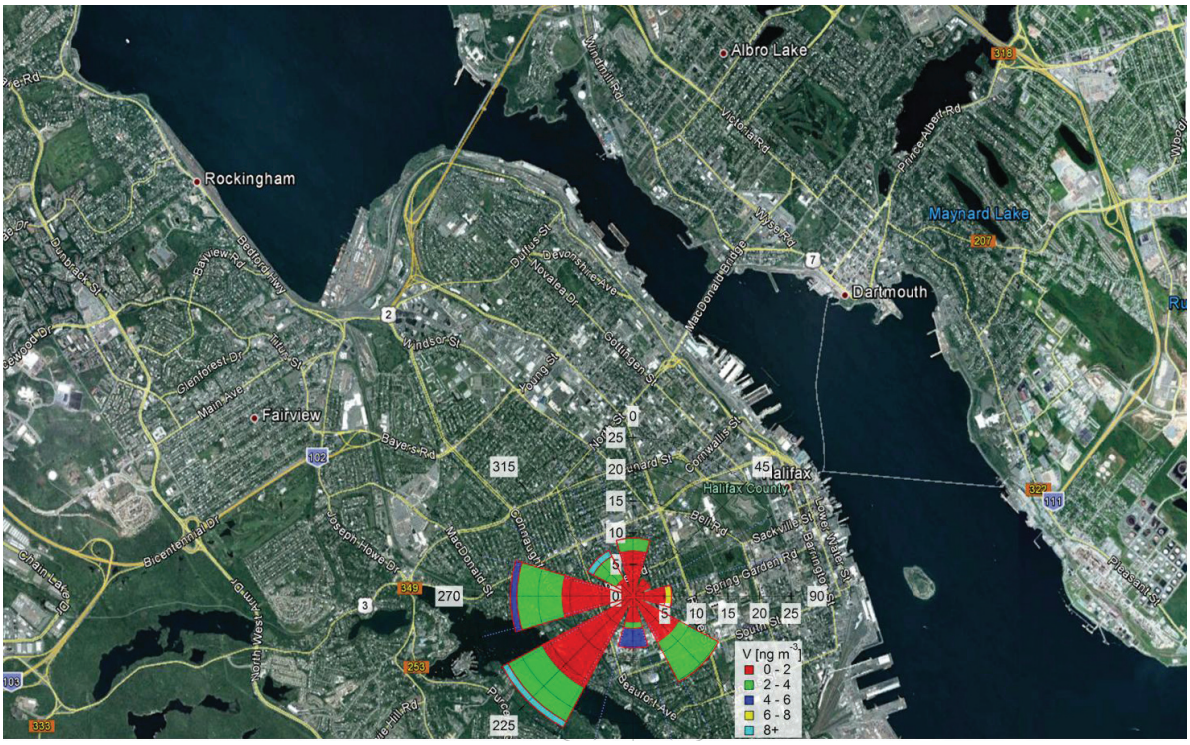

Figure 69 V pollution rose for the period of August 20, 2011 to August 20, 2012.

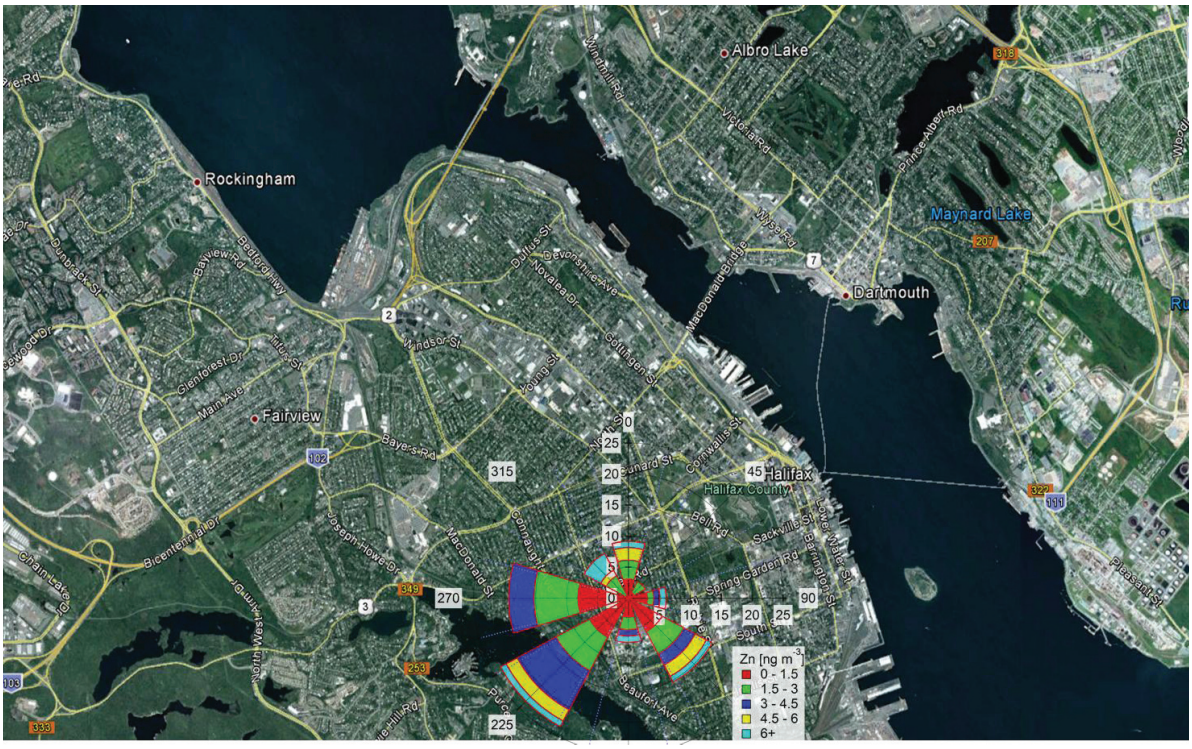

Figure 70 Zn pollution rose for the period of August 20, 2011 to August 20, 2012.

Figure 71 $PM_{2.5}$ AQI level of Michigan-Indiana-Ohio area (source: http://airnow.gov/index.cfm?action=airnow.mapsarchivecalendar).

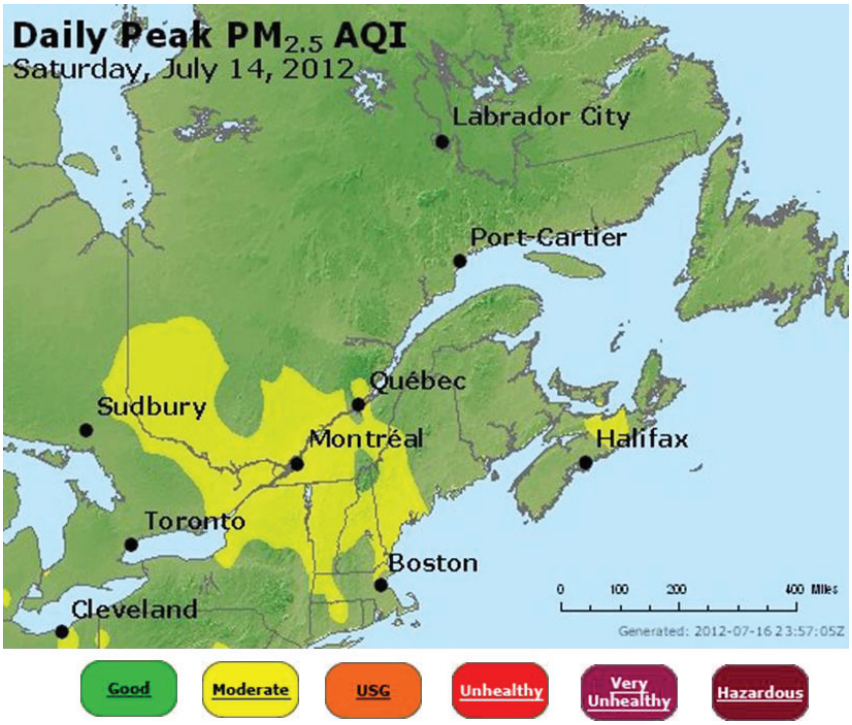

Figure 72 $PM_{2.5}$ AQI level of Eastern Canada (source: http://airnow.gov/index.cfm?action=airnow.mapsarchivecalendar).

Environment Canada kindly supplied weather data from a number of weather stations (Shearwater RCS, Nova Scotia, Halifax, Stanfield Airport, Queen Square, Dartmouth) in order to create a daily weather summary covering the entire duration of the study. The daily weather summary data was provided on February 13, 2013. Table 16 contains the weather summary from August 1, 2011 to August 31, 2012.

Table 16 Weather Data for Halifax Ship Emissions Study - Weather Summary.

Date (dd-mm-yyyy)	Tmax (°C)	Tmin (°C)	Tmean (°C)	RH min (%)	RH max (%)	Total Snow (cm)	Total Pcpn (mm)	Average Wind Spd (m s-1)	Gust Direction (10s Deg True)	Gust Spd (km h-1)	Gust Spd (m s-1)	Total of Avg Hourly Solar Radiation (W m-2)	Day with Thunder 1=thunder observed	Date (dd-mm-yyyy)
11-08-01	20.9	13.5	17.2	68	100		0	2	0	0	0	6900		11-08-01
11-08-02	21.3	14.9	18.1	83	100		40.9	3	9	35	9.7	2222	1 (7hrs)	11-08-02
11-08-03	17.9	16.3	17.1	89	97		15.6	5	7	48	13.3	1649	1 (1 hr)	11-08-03
11-08-04	19.1	13.5	16.3	81	96		0.3	4	5	32	8.9	2143		11-08-04
11-08-05	21.3	12.1	16.7	59	92		0	4	36	33	9.2	3753		11-08-05
11-08-06	23.7	11.7	17.7	58	98		0	2	0	0	0	6286		11-08-06
11-08-07	22.6	16.5	19.6	80	97		1.7	2	0	0	0	3705		11-08-07
11-08-08	18.7	16.7	17.7	89	99		95.9	3	11	35	9.7	1167		11-08-08
11-08-09	21.3	15.2	18.3	72	97		0.4	4	34	44	12.2	2848		11-08-09
11-08-10	16.1	14.1	15.1	88	97		5.3	4	11	39	10.8	1499		11-08-10
11-08-11	19.9	14.5	17.2	87	99		0.6	3	0	0	0	2409		11-08-11
11-08-12	20	13.9	17	78	100		0	2	0	0	0	6069		11-08-12
11-08-13	26.7	12.3	19.5	48	100		0	1	0	0	0	6692		11-08-13
11-08-14	26.4	14.4	20.4	48	95		0	2	0	0	0	6331		11-08-14
11-08-15	22.7	16.9	19.8	58	98		1.4	2	7	37	10.3	3917		11-08-15
11-08-16	22.7	15.7	19.2	72	100		2.7	4	22	39	10.8	5894		11-08-16
11-08-17	26.6	13.6	20.1	37	93		0	3	30	37	10.3	6593		11-08-17
11-08-18	24.2	13.6	18.9	48	95		0	3	22	35	9.7	7003		11-08-18
11-08-19	25.1	18	21.6	72	96		0	3	22	33	9.2	4486		11-08-19
11-08-20	23.7	16.7	20.2	62	97		0	3	0	0	0	4830		11-08-20
11-08-21	25.9	17.5	21.7	67	96		0	3	0	0	0	6134		11-08-21
11-08-22	21.9	17.8	19.9	82	99		2.6	5	15	46	12.8	2987		11-08-22
11-08-23	23.7	14.4	19.1	38	95		0	3	0	0	0	6540		11-08-23
11-08-24	24	12.8	18.4	44	91		0	3	22	35	9.7	6527		11-08-24
11-08-25	24.2	13.7	19	63	100		0	4	19	37	10.3	5448		11-08-25
11-08-26	27	16.2	21.6	67	100		1.2	4	21	37	10.3	4752		11-08-26
11-08-27	24.7	14.6	19.7	60	99		0	2	0	0	0	6039		11-08-27
11-08-28	21.3	18.1	19.7	94	98		5.9	4	18	61	17	1210		11-08-28
11-08-29	22.9	13	18	59	93		0	6	21	65	18.1	6205		11-08-29
11-08-30	21.2	11.6	16.4	60	95		0	2	0	0	0	5069		11-08-30
11-08-31	25.5	12.3	18.9	35	92		0	2	0	0	0	6317		11-08-31
11-09-01	20.7	12.7	16.7	63	93		0	2	0	0	0	4777		11-09-01
11-09-02	21.2	13.3	17.3	62	96		0	3	8	35	9.7	5731		11-09-02
11-09-03	23.3	13.9	18.6	61	96		0	2	0	0	0	5448		11-09-03
11-09-04	24	17	20.5	66	89		0	3	0	0	0	3893		11-09-04
11-09-05	24.7	17.9	21.3	69	97		0	5	20	43	12	4646		11-09-05
11-09-06	22.8	12.2	17.5	82	100		5.5	4	30	39	10.8	1540		11-09-06
11-09-07	16.4	10.7	13.6	66	95		0	2	0	0	0	2334		11-09-07
11-09-08	21.3	14.7	18	82	98		5.7	2	0	0	0	1617		11-09-08
11-09-09	21.5	13	17.3	69	100		0.3	2	0	0	0	3996		11-09-09
11-09-10	18.8	8.8	13.8	43	92		0	4	32	41	11.4	6006		11-09-10
11-09-11	18.5	7.1	12.8	56	95		0	3	17	33	9.2	6074		11-09-11
11-09-12	24	12.3	18.2	57	94		0	3	22	33	9.2	5584		11-09-12
11-09-13	18.9	14.1	16.5	86	98		0	2	0	0	0	2185		11-09-13
11-09-14	24.1	15.7	19.9	71	97		0	3	21	33	9.2	5098		11-09-14
11-09-15	20	16.9	18.5	96	100		4.8	2	0	0	0	1377		11-09-15
11-09-16	18.4	9.1	13.8	44	100		0	4	31	52	14.5	4720		11-09-16
11-09-17	18.1	7.4	12.8	35	85		0	4	32	37	10.3	5773		11-09-17
11-09-18	17.2	6.5	11.9	56	92		0	1	0	0	0	3735		11-09-18
11-09-19		11						3	0	0	0	887		11-09-19
11-09-20								4	0	0	0			11-09-20
11-09-21	22.7	11.4	17.1	56	94		0	2	0	0	0			11-09-21
11-09-22	19	8.8	13.9	74	99		9.6	2	0	0	0			11-09-22
11-09-23	21.9	16.1	19	83	100		0	1	0	0	0	1861		11-09-23
11-09-24	18.1	17	17.6	98	100		15.8	1	0	0	0	714		11-09-24

11-09-25	26.6	17.1	21.9	46	100		0	2	0	0	0	4615		11-09-25
11-09-26	26.3	15.8	21.1	44	88		0	3	0	0	0	4557		11-09-26
11-09-27	21.1	7.6	14.4	40	89		0	4	35	39	10.8	5155		11-09-27
11-09-28	15.1	5.4	10.3	59	90		0	2	0	0	0	5074		11-09-28
11-09-29	19.1	8.9	14	73	100		2.1	3	20	39	10.8	3405		11-09-29
11-09-30	22.1	15.4	18.8	61	100		1.1	5	20	44	12.2	3787		11-09-30
11-10-01	19.2	15.4	17.3	95	100		14.7	3	14	32	8.9	522		11-10-01
11-10-02	19.2	16.4	17.8	94	100		23.4	3	4	32	8.9	582		11-10-02
11-10-03	22.1	15.4	18.8	77	100		4.2	2	0	0	0	2679		11-10-03
11-10-04	16.3	11.6	14	85	96		46.6	4	1	43	12	755		11-10-04
11-10-05	12.8	3.8	8.3	74	95		36.5	8	32	59	16.4	1167		11-10-05
11-10-06	6.9	2.7	4.8	58	85		0	6	31	57	15.8	2955		11-10-06
11-10-07	9.7	1.6	5.7	39	82		0	3	34	37	10.3	4564		11-10-07
11-10-08	24	6.4	15.2	46	82		0	3	27	32	8.9	4182		11-10-08
11-10-09	27.3	14.1	20.7	38	81		0	3	30	32	8.9	4253		11-10-09
11-10-10	24	9	16.5	35	77		0	4	32	46	12.8	3967	1 (1 hr)	11-10-10
11-10-11	14.4	4.3	9.4	54	92		0	3	1	32	8.9	3538		11-10-11
11-10-12	13	5.5	9.3	59	88		0	3	0	0	0	4184		11-10-12
11-10-13	15.5	12.3	13.9	81	97		15.5	4	10	33	9.2	1377		11-10-13
11-10-14	16.7	14.4	15.6	97	100		26.5	4	10	39	10.8	610		11-10-14
11-10-15	18.2	14.4	16.3	63	100		1.2	7	21	54	15	3844		11-10-15
11-10-16	17.5	10.2	13.9	53	85		0	6	21	54	15	3134		11-10-16
11-10-17	16.2	8.6	12.4	67	92		3.7	4	18	67	18.6	855		11-10-17
11-10-18	17.8	9.4	13.6	59	90		0	4	23	48	13.3	2949		11-10-18
11-10-19	14.5	9.3	11.9	64	96		12.1	2	6	48	13.3	1418		11-10-19
11-10-20	20.3	11.3	15.8	94	100		71.2	5	22	61	17	197		11-10-20
11-10-21	17.9	9.6	13.8	65	96		0	4	21	44	12.2	3195		11-10-21
11-10-22	16	8.1	12.1	58	94		0	2	0	0	0	3174		11-10-22
11-10-23	16.1	5.6	10.9	55	93		0	2	0	0	0	2521		11-10-23
11-10-24	14.5	4.4	9.5	68	97		0	1	0	0	0	2499		11-10-24
11-10-25	12.3	7.3	9.8	80	94		0.6	2	30	39	10.8	855		11-10-25
11-10-26	11.3	4.3	7.8	53	79		0	7	31	59	16.4	2278		11-10-26
11-10-27	6.7	2.2	4.5	60	94		2.3	2	0	0	0	1106		11-10-27
11-10-28	7.8	2.1	5	47	95		2.9	4	32	44	12.2	2676		11-10-28
11-10-29	9.3	1.6	5.5	37	95		6.2	3	9	41	11.4	3441		11-10-29
11-10-30	6.6	1.8	4.2	79	95		42.8	9	33	82	22.8	391		11-10-30
11-10-31	6.9	0.1	3.5	51	90		0	5	33	44	12.2	2599		11-10-31
11-11-01	9.6	0.5	5.1	49	90		0.3	1	0	0	0	3021		11-11-01
11-11-02	10.7	-0.5	5.1	55	96		0	1	0	0	0	3186		11-11-02
11-11-03	11.8	-0.3	5.8	62	99		0	2	0	0	0	2833		11-11-03
11-11-04	9.7	1.3	5.5	59	92		0.3	3	36	41	11.4	1319		11-11-04
11-11-05	4.7	-1.9	1.4	49	83		0	5	35	44	12.2	1834		11-11-05
11-11-06	12.2	-0.3	6	42	86		0	3	25	35	9.7	3038		11-11-06
11-11-07	14.2	3.4	8.8	36	93		0	2	0	0	0	2984		11-11-07
11-11-08	16.6	4.3	10.5	32	90		0	3	29	32	8.9	2759		11-11-08
11-11-09	15.5	2	8.8					1	0	0	0	2465		11-11-09
11-11-10	13.2	5.3	9.3	79	98		0	3	12	44	12.2	2142		11-11-10
11-11-11	15.5	4.7	10.1	81	100		99.9	9	15	70	19.5	111		11-11-11
11-11-12	7.7	3.4	5.6	49	83		0	5	28	46	12.8	2144		11-11-12
11-11-13	12.6	5.2	8.9	55	96		0	3	0	0	0	2572		11-11-13
11-11-14	14.1	10.6	12.4	82	95		0	7	22	54	15	871		11-11-14
11-11-15	16	9.7	12.9	70	96		1.4	4	22	48	13.3	991		11-11-15
11-11-16	13.1	2.9	8	52	98		13.1	2	9	41	11.4	2305		11-11-16
11-11-17	12.8	3.6	8.2	77	99		9.9	4	36	41	11.4	960		11-11-17
11-11-18	4.2	0.8	2.5	55	95		1.4	5	30	50	13.9	2099		11-11-18
11-11-19	9.4	-1.3	4.1	56	87		0	5	23	65	18.1	2164		11-11-19
11-11-20	13.5	8.9	11.2	75	88		0	7	23	72	20	1384		11-11-20
11-11-21	8.9	-4.1	2.4	45	78		0	4	36	39	10.8	2244		11-11-21
11-11-22	3	-5.2	-1.1	37	88		0	2	0	0	0	2265		11-11-22
11-11-23	0.6	-2.2	-0.8	68	100	16	41	4	3	57	15.8	44		11-11-23
11-11-24	2.5	-1.4	0.6	67	97		0.5	6	1	50	13.9	1491		11-11-24
11-11-25	8.5	-0.5	4	74	91		0	3	21	37	10.3	938		11-11-25
11-11-26	11.5	1.5	6.5	63	94		0	2	0	0	0	1400		11-11-26
11-11-27	7.2	1.4	4.3	58	86		0	2	0	0	0	1819		11-11-27
11-11-28	13.4	7.2	10.3	76	95		0	5	22	48	13.3	1447		11-11-28
11-11-29	8.5	1.7	5.1	75	100		0	2	0	0	0	899		11-11-29
11-11-30	13.1	6.8	10	92	100		4	5	16	54	15			11-11-30
11-12-01	10.8	2.1	6.5	73	99		0	3	1	32	8.9	1249		11-12-01
11-12-02	5.4	-0.8	2.3	62	95		0	2	0	0	0	1756		11-12-02
11-12-03	4	-0.1	2	69	96		0	2	0	0	0	795		11-12-03
11-12-04	6.9	-0.5	3.2	63	87		0	3	22	33	9.2	1423		11-12-04
11-12-05	11.2	6.4	8.8	81	97		0	3	0	0	0	1136		11-12-05
11-12-06	12.2	7.2	9.7	84	100		9.3	4	24	41	11.4	703		11-12-06
11-12-07	11	7.7	9.4	98	100		13.8	2	0	0	0	348		11-12-07
11-12-08	13.5	0.6	7.1	57	100		18	8	23	89	24.7	684		11-12-08
11-12-09	7.9	-1.2	3.4	52	81		0	4	20	35	9.7	927		11-12-09

11-12-10	9.3	-0.1	4.6	78	95		4.6	4	34	39	10.8	440	11-12-10
11-12-11	0.3	-5.4	-2.6	44	74		0	4	34	39	10.8	1357	11-12-11
11-12-12	8.2	-5.7	1.3	67	97		0	3	24	48	13.3	1322	11-12-12
11-12-13	9.3	-0.5	4.4	78	100		0	2	36	32	8.9	692	11-12-13
11-12-14	3.3	-2.8	0.3	60	89		0	5	1	41	11.4	780	11-12-14
11-12-15	9.2	-2	3.6	69	98		15.2	5	20	59	16.4	268	11-12-15
11-12-16	10.4	1.1	5.8	72	98		5.8	6	20	63	17.5	591	11-12-16
11-12-17	1.5	-3.5	-1	51	80		0	3	0	0	0	1229	11-12-17
11-12-18	-0.8	-4.7	-2.8	61	87		0	5	2	39	10.8	619	11-12-18
11-12-19	5.6	-6.7	-0.6	42	93		0.9	4	25	46	12.8	1294	11-12-19
11-12-20	5.1	-8	-1.5	49	92		1.2	5	31	57	15.8	1344	11-12-20
11-12-21	8.8	-7.8	0.5	62	99		21.4	4	18	56	15.6	840	11-12-21
11-12-22	10.2	1.1	5.7	83	100		6.7	4	18	50	13.9	390	11-12-22
11-12-23	1.1	-0.5	0.3			11		2	0	0	0	73	11-12-23
11-12-24	0	-12.6	-6.3	70	91		0	5	36	43	12	1010	11-12-24
11-12-25	-1.1	-12.6	-6.9	60	89		0	2	0	0	0	1310	11-12-25
11-12-26	4.4	-1.5	1.5	77	96		0	4	18	35	9.7	523	11-12-26
11-12-27	5.1	-2.3	1.4	69	91		0	4	22	32	8.9	1249	11-12-27
11-12-28	9.4	3.6	6.5	84	99		16.4	6	14	63	17.5	92	11-12-28
11-12-29	3.6	-2.7	0.5					8	0	0	0	1297	11-12-29
11-12-30	1.6	-4	-1.2	43	68		0	5	26	54	15	1368	11-12-30
11-12-31	9.5	-3.1	3.2	68	100	1	33.6	4	17	39	10.8	167	11-12-31
12-01-01	8.5	0.2	4.4	80	100		2	5	33	56	15.6	823	12-01-01
12-01-02	10.3	1.9	6.1	73	100		11.3	6	18	67	18.6	121	12-01-02
12-01-03	5.1	-4.8	0.2	58	81		0	3	36	37	10.3	1119	12-01-03
12-01-04	-4.8	-10.7	-7.8	68	82	1	0	6	2	46	12.8	1029	12-01-04
12-01-05	1.4	-7.4	-3	65	98		1.5	3	16	39	10.8	337	12-01-05
12-01-06	-2.6	-7.3	-5	55	93	1	0.3	3	32	35	9.7	1420	12-01-06
12-01-07	5.6	-3.9	0.9	94	100		1	2	0	0	0	361	12-01-07
12-01-08	5.2	-1.8	1.7	60	95		0	3	30	32	8.9	1429	12-01-08
12-01-09	-1.1	-6.9	-4	46	91	1	0	3	34	33	9.2	1042	12-01-09
12-01-10	3.8	-6.6	-1.4					3	0	0	0	674	12-01-10
12-01-11	0.8	-11.9	-5.6	51	83	1	0	5	33	48	13.3	1481	12-01-11
12-01-17	4.5	-1.7	1.4	79	100		0.9	4	23	46	12.8	293	12-01-17
12-01-18	8.6	-6.7	1	56	100		2	6	22	48	13.3	1193	12-01-18
12-01-19	-5	-9.8	-7.4	39	82		0	5	31	48	13.3	1107	12-01-19
12-01-20	1.7	-9	-3.7	81	100	4	11.2	4	27	43	12	345	12-01-20
12-01-21	-4.7	-10	-7.4	72	92		0.3	3	26	33	9.2	1002	12-01-21
12-01-22	-7	-13.6	-10.3	49	80		0	4	35	35	9.7	1636	12-01-22
12-01-23	3.9	-12.1	-4.1	63	93		0.3	2	0	0	0	1478	12-01-23
12-01-24	9.8	3.2	6.5	95	100	1	26.4	5	21	52	14.5	167	12-01-24
12-01-25	5.3	0.5	2.9	64	100		0	3	28	35	9.7	1327	12-01-25
12-01-26	0.7	-5.8	-2.6	48	78		0	4	32	37	10.3	1754	12-01-26
12-01-27	7.7	-5.4	1.2	65	99		39.4	4	7	59	16.4	523	12-01-27
12-01-28	7.1	-4	1.6	66	100	1	0.3	6	29	65	18.1	958	12-01-28
12-01-29	6.4	-1.4	2.5	43	93		0.3	5	24	50	13.9		12-01-29
12-01-30	6.1	-7.3	-0.6	62	100	3	0.9	4	24	46	12.8		12-01-30
12-01-31	-4.1	-9.4	-6.8	62	81		0	3	0	0	0		12-01-31
12-02-01	4.2	-5.1	-0.5	70	100		4	4	11	39	10.8	160	12-02-01
12-02-02	0.3	-7.5	-3.6	82	99		0.6	4	1	35	9.7	587	12-02-02
12-02-03	-4.2	-9.8	-7	61	83		0	5	35	41	11.4	2136	12-02-03
12-02-04	-3.9	-10.7	-7.3	60	88		0	3	34	35	9.7	1787	12-02-04
12-02-05	-6.6	-12.3	-9.5	59	82		0	3	33	35	9.7	1993	12-02-05
12-02-06	4.7	-8.9	-2.1	65	85		0	4	23	48	13.3	1126	12-02-06
12-02-07	4.5	-6.1	-0.8	57	93	1	0	3	0	0	0	1055	12-02-07
12-02-08	-1.3	-10.1	-5.7	30	76		0	3	33	33	9.2	2189	12-02-08
12-02-09	1	-2.6	-0.8	71	86		0	2	0	0	0	788	12-02-09
12-02-10	4.1	-5.1	-0.5	43	94		0	3	0	0	0	2214	12-02-10
12-02-11	4.5	0	2.3	92	99	1	53.2	4	34	74	20.6	334	12-02-11
12-02-12	0.2	-13.1	-6.5	67	96	2	1.2	7	34	74	20.6	831	12-02-12
12-02-13	-4.5	-15	-9.8	61	84		0	5	24	43	12	1754	12-02-13
12-02-14	2.7	-9	-3.2	56	92		0	3	0	0	0	2074	12-02-14
12-02-15	6.8	-0.3	3.3	74	98		0	2	0	0	0	2243	12-02-15
12-02-16	5.3	-2.4	1.5	75	99		0	3	0	0	0	1336	12-02-16
12-02-17	2.7	-4.5	-0.9	75	99		3.6	2	0	0	0	1270	12-02-17
12-02-18	3.6	0.1	1.9	68	99	1	8.7	4	32	50	13.9	1910	12-02-18
12-02-19	2	-3.8	-0.9	51	71		0	5	30	44	12.2	2449	12-02-19
12-02-20	0.2	-7.9	-3.9	46	74		0	4	34	33	9.2	2564	12-02-20
12-02-21	3.8	-9.1	-2.7	29	85		0	3	34	33	9.2	2576	12-02-21
12-02-22	7.6	-1.7	3	78	100		12.7	4	21	57	15.8	900	12-02-22
12-02-23	5.4	0.5	3	80	100	1	7.5	3	27	56	15.6	650	12-02-23

12-02-24	6.8	0.7	3.8	47	94		0	4	27	61	17	1708	12-02-24
12-02-25	6.8	0.4	3.6	63	99		22.5	9	23	83	23.1	1883	12-02-25
12-02-26	2.6	-5	-1.2	54	89		0.3	6	31	52	14.5	2267	12-02-26
12-02-27	-0.4	-7.6	-4	32	99	2	2.4	4	33	39	10.8	2174	12-02-27
12-02-28	4	-6.4	-1.2	81	100		5	5	35	52	14.5	1161	12-02-28
12-02-29	0.2	-8.6	-4.2					3	0	0	0		12-02-29
12-03-01	-5	-9.4	-7.2	64	94	1	1.2	6	5	46	12.8	1377	12-03-01
12-03-02	-0.6	-7.3	-4	67	95	3	2.3	5	6	37	10.3	1432	12-03-02
12-03-03	8.1	-3.4	2.4	78	100		11.1	5	16	63	17.5	584	12-03-03
12-03-04	5.5	0.4	3	64	99	1	2.6	3	26	32	8.9	1081	12-03-04
12-03-05	3.8	-1.8	1	76	97	3	2.7	3	24	37	10.3	1829	12-03-05
12-03-06	-1.8	-6.7	-4.3	71	94		0	5	33	46	12.8	1137	12-03-06
12-03-07	4	-8.8	-2.4	56	93		0	4	19	39	10.8	1804	12-03-07
12-03-08	11.9	2.5	7.2	68	97		0	6	24	70	19.5	2435	12-03-08
12-03-09	9.3	-2.6	3.4	66	93	1	2.2	7	22	80	22.2	605	12-03-09
12-03-10	3.4	-5.8	-1.2	32	81		0	3	0	0	0	3352	12-03-10
12-03-11	3.6	-6.5	-1.5	48	92		0	4	22	44	12.2	2641	12-03-11
12-03-12	13.9	1	7.5	28	96		0	2	32	32	8.9	3483	12-03-12
12-03-13	5.8	-0.1	2.9	42	96		5.3	4	10	50	13.9	1940	12-03-13
12-03-14	1.1	-0.5	0.3	91	98	1	11.8	5	8	54	15	537	12-03-14
12-03-15	0.5	-1.5	-0.5	93	100	2	10.4	3	2	33	9.2	892	12-03-15
12-03-16	3.2	-1.8	0.7	77	99	2	8.1	2	0	0	0	1930	12-03-16
12-03-17	8.4	0.3	4.4	59	99		1.2	3	33	37	10.3	3824	12-03-17
12-03-18	12.2	2	7.1	54	86		0	3	24	35	9.7	3080	12-03-18
12-03-19	13	-0.1	6.5	37	91		0	3	3	35	9.7	3776	12-03-19
12-03-20	17.2	-0.4	8.4	55	94		0	2	0	0	0	3479	12-03-20
12-03-21	26	8.6	17.3	26	83		0	3	32	32	8.9	3531	12-03-21
12-03-22	28.3	11.8	20.1	32	78		0	3	35	50	13.9	3546	12-03-22
12-03-23	13.5	-2.3	5.6	20	70		0	6	33	69	19.2	3866	12-03-23
12-03-24	6.3	-2.8	1.8	23	63		0	5	34	48	13.3	3689	12-03-24
12-03-25	5.7	-2	1.9	25	97		0.6	3	18	33	9.2	2130	12-03-25
12-03-26	6.7	-2.7	2	70	99		2.3	5	34	44	12.2	1275	12-03-26
12-03-27	-2.2	-4.7	-3.5	53	87		0	7	33	65	18.1	1943	12-03-27
12-03-28	4	-5.2	-0.6	39	77		0	4	31	37	10.3	3457	12-03-28
12-03-29	3.5	-2.9	0.3	62	87		0	2	0	0	0	2792	12-03-29
12-03-30	6.1	-0.8	2.7	34	84		0	3	34	35	9.7	3244	12-03-30
12-03-31	9.6	-2.7	3.5	30	78		0	3	21	33	9.2	6133	12-03-31
12-04-01	6.3	-3.9	1.2	59	92		0	3	16	32	8.9	6473	12-04-01
12-04-02	7.5	-1.5	3	53	93		0	2	0	0	0	3479	12-04-02
12-04-03	4.7	-2.3	1.2	43	75		0	6	34	59	16.4	4926	12-04-03
12-04-04	9.7	-0.4	4.7	38	90		0	5	30	35	9.7	4428	12-04-04
12-04-05	8.7	1.1	4.9	34	91		0	4	30	37	10.3	3127	12-04-05
12-04-06	8.4	-0.5	4	38	86		0	3	21	33	9.2	4853	12-04-06
12-04-07	8.6	-0.7	4	37	98	9	1.4	4	33	57	15.8	2790	12-04-07
12-04-08	3.7	-1.6	1.1	74	100		4.1	7	30	57	15.8	3455	12-04-08
12-04-09	7.5	1.7	4.6	77	94		0	5	21	43	12	2560	12-04-09
12-04-10	11.5	1.3	6.4	51	94		0	5	21	39	10.8	6522	12-04-10
12-04-11	12	1.2	6.6	68	95		1.9	2	4	32	8.9	5782	12-04-11
12-04-12	10.2	2.1	6.2	64	91		3.1	5	2	46	12.8	2888	12-04-12
12-04-13	9.8	1	5.4	45	88	1	0	5	34	43	12	3589	12-04-13
12-04-14	15	2.7	8.9	21	83	1	0	3	31	44	12.2	6832	12-04-14
12-04-15	11.4	2	6.7	48	97		0	3	0	0	0	6362	12-04-15
12-04-16	14.2	3.3	8.8	74	100		0	3	0	0	0	5379	12-04-16
12-04-17	9.8	6.6	8.2	96	100		0	3	0	0	0	1669	12-04-17
12-04-18								3	0	0	0	5366	12-04-18
12-04-19	8.2	0.3	4.3	55	94		0	3	0	0	0	5758	12-04-19
12-04-20	14.4	0	7.2	42	97		0	2	21	39	10.8	7014	12-04-20
12-04-21	11.2	4	7.6	72	99		0	4	17	32	8.9	6635	12-04-21
12-04-22	14.3	4.1	9.2	98	100		2.3	3	18	33	9.2	1900	12-04-22
12-04-23	12.4	3.9	8.2	95	100		1.4	4	8	46	12.8	1307	12-04-23
12-04-24	11.5	6.9	9.2	94	100		16.5	5	12	52	14.5	1121	12-04-24
12-04-25	14.1	5	9.6	88	100		5.2	2	0	0	0	3268	12-04-25
12-04-26	14.1	4.3	9.2	50	95		0	4	23	44	12.2	7284	12-04-26
12-04-27	11.8	4.7	8.3	76	100		25.3	5	21	56	15.6	1676	12-04-27
12-04-28	5.3	2	3.7	43	81		0	5	28	48	13.3	2572	12-04-28
12-04-29	9.6	0.6	5.1	26	79		0	4	21	37	10.3	7441	12-04-29
12-04-30	8.7	-1.1	3.8	35	89		0	3	35	35	9.7	5575	12-04-30
12-05-01	9.8	0.6	5.2	48	83		0	3	16	32	8.9		12-05-01
12-05-02	11.7	3.7	7.7	53	83		0	2	0	0	0		12-05-02
12-05-03	17.2	2	9.6	24	82		0	4	35	43	12		12-05-03
12-05-04	10.7	3.4	7.1	66	92		0	3	0	0	0		12-05-04
12-05-05	18.4	3.2	10.8	42	96		0	2	0	0	0		12-05-05
12-05-06	16	5.8	10.9	48	89		0	5	36	41	11.4	6885	12-05-06
12-05-07	12.9	4.1	8.5	68	95		1	4	0	0	0	2865	12-05-07
12-05-08	9.4	2.1	5.8	83	99		0.6	3	0	0	0	6463	12-05-08
12-05-09	11.3	6.4	8.9	93	99		9.2	5	21	41	11.4	890	12-05-09

12-05-10	12.6	8.7	10.7	86	100	7	6	16	59	16.4	2235		12-05-10
12-05-11	12.1	6.6	9.4	75	100	0	4	19	33	9.2	5592		12-05-11
12-05-12	14.9	5.9	10.4	47	97	0.2	3	23	44	12.2	7315		12-05-12
12-05-13	17.3	5.1	11.2	43	90	0	3	0	0	0	7089		12-05-13
12-05-14	14.6	7.8	11.2	79	99	0	3	0	0	0			12-05-14
12-05-15	20.7	9.7	15.2	60	96	0	3	15	32	8.9	6062		12-05-15
12-05-16	15.6	11.1	13.4	86	99	6.4	4	20	35	9.7	4014		12-05-16
12-05-17	15.2	7.9	11.6	59	100	10.2	3	22	32	8.9	2523		12-05-17
12-05-18	18.4	4.3	11.4	37	91	0.2	3	21	37	10.3	7722		12-05-18
12-05-19	19.7	7.8	13.8	34	76	0	2	0	0	0	7270		12-05-19
12-05-20	19.1	9.8	14.5	30	74	0	3	0	0	0	7604		12-05-20
12-05-21	21.7	8.9	15.3	30	95	0	3	21	35	9.7	7482		12-05-21
12-05-22	18.1	9.5	13.8	93	99	28	2	16	32	8.9	1909		12-05-22
12-05-23	21.3	10.1	15.7	70	100	0.6	2	36	33	9.2	3183		12-05-23
12-05-24	18	8	13	50	95	0	3	0	0	0	7641		12-05-24
12-05-25	12.1	8.5	10.3	83	99	0	3	0	0	0	5833		12-05-25
12-05-26	19.7	10.7	15.2	60	99	0	3	0	0	0	2346		12-05-26
12-05-27	18.5	7.9	13.2	36	83	0	3	0	0	0	7865		12-05-27
12-05-28	20.3	6.5	13.4	35	85	0.8	2	0	0	0	3901		12-05-28
12-05-29	8.9	6.7	7.8	67	91	6.6	3	11	32	8.9	1616		12-05-29
12-05-30	12	6.9	9.5	93	100	6.6	3	11	32	8.9	1227		12-05-30
12-05-31	12.4	8.4	10.4	86	100	0	2	0	0	0	3080		12-05-31
12-06-01	19.1	8.5	13.8	50	99	0.2	3	1	37	10.3	4636		12-06-01
12-06-02	17.5	7.2	12.4	57	95	0	2	0	0	0	7357		12-06-02
12-06-03	14.7	9.3	12	67	97	0	4	10	39	10.8	4897		12-06-03
12-06-04	13.1	8.9	11	67	94	7.2	4	36	35	9.7	1665		12-06-04
12-06-05	12	8.8	10.4	80	95	3	5	4	39	10.8	2058		12-06-05
12-06-06	14.1	7.9	11	66	95	2.8	5	33	39	10.8	3166		12-06-06
12-06-07	16.2	7.9	12.1	52	95	0	4	31	33	9.2	4338		12-06-07
12-06-08	19.9	9	14.5	42	97	0	3	22	41	11.4	5369		12-06-08
12-06-09	15.6	9.3	12.5			22.2	3	17	33	9.2	2285		12-06-09
12-06-10	19	9	14			1.2	2	0	0	0	3155		12-06-10
12-06-11	17.2	8.5	12.9	52	99	0	3	0	0	0	7472		12-06-11
12-06-12	14.7	8.2	11.5	66	98	0	3	0	0	0	7712		12-06-12
12-06-13	16.1	7.4	11.8	74	100	0.2	2	0	0	0	6658		12-06-13
12-06-14	23.3	9.7	16.5	61	100	0	2	0	0	0	5609		12-06-14
12-06-15	21.3	11.7	16.5	64	92	0	4	1	39	10.8	5113		12-06-15
12-06-16	16.6	8.2	12.4	57	88	0	4	13	39	10.8	5136		12-06-16
12-06-17	14.8	7.5	11.2	70	88	0	3	0	0	0	7500		12-06-17
12-06-18	13.8	9.1	11.5	72	94	0	2	0	0	0	6530		12-06-18
12-06-19	16.6	9.6	13.1	76	97	0	2	0	0	0	6234		12-06-19
12-06-20	21.8	12.2	17	72	94	0	2	0	0	0	4002		12-06-20
12-06-21	26.4	12.9	19.7	48	97	0	4	36	39	10.8			12-06-21
12-06-22	16.9	12.9	14.9	84	94	0	3	0	0	0			12-06-22
12-06-23	14.7	12.4	13.6	90	99	17.8	4	10	35	9.7			12-06-23
12-06-24	16.8	13.5	15.2	94	99	0	3	0	0	0			12-06-24
12-06-25	21.5	13.2	17.4	68	99	0.2	3	0	0	0			12-06-25
12-06-26	17.2	14.6	15.9	94	99	33.8	5	12	65	18.1			12-06-26
12-06-27	17.7	13.9	15.8	84	99	0	5	17	35	9.7			12-06-27
12-06-28	20.3	14.2	17.3	77	96	0	4	22	32	8.9		1 (1hr)	12-06-28
12-06-29	22.6	14.2	18.4	66	98	0	3	19	41	11.4			12-06-29
12-06-30	27.9	16.1	22	58	99	0	3	22	41	11.4			12-06-30
12-07-01	28.4	15.3	21.9	51	94	0	2	0	0	0	7288		12-07-01
12-07-02	24.5	14.8	19.7	67	96	0	2	30	37	10.3	4450	1 (3hr)	12-07-02
12-07-03	26.2	14.4	20.3	53	97	0	2	0	0	0	6347		12-07-03
12-07-04	20.7	13.4	17.1	75	97	0	3	0	0	0	7576		12-07-04
12-07-05	18.9	16.5	17.7	91	99	7.6	3	0	0	0	1450		12-07-05
12-07-06	25.1	16.2	20.7	72	99	2.6	3	0	0	0	5622		12-07-06
12-07-07	21.5	16.5	19	83	99	0	2	0	0	0	2947	1 (1 hr)	12-07-07
12-07-08	26.4	16	21.2	40	99	0	3	32	35	9.7	6848		12-07-08
12-07-09	25	13.5	19.3	29	82	0	3	24	37	10.3	7428		12-07-09
12-07-10	26.3	12.4	19.4	34	84	0	3	23	35	9.7	7701		12-07-10
12-07-11	26.8	14.6	20.7	32	90	0	3	24	32	8.9	7112		12-07-11
12-07-12	23.7	12.9	18.3	53	96	0	3	0	0	0	6861		12-07-12
12-07-13	29.9	13.9	21.9	50	97	0	2	0	0	0	7358		12-07-13
12-07-14	27.3	15.3	21.3	64	88	0	3	22	35	9.7	7206	1 (2 hr)	12-07-14
12-07-15	20.7	15.4	18.1	76	98	0	3	0	0	0	5364		12-07-15
12-07-16	18.3	15.3	16.8	89	97	0.8	2	0	0	0	1665		12-07-16
12-07-17	22.7	17.1	19.9	78	98	0.2	2	0	0	0	4489		12-07-17
12-07-18	28.4	17.3	22.9	49	99	1	3	31	32	8.9	6207		12-07-18
12-07-19	25.7	15.5	20.6	38	84	0	3	31	35	9.7	7122		12-07-19
12-07-20	23.4	12.2	17.8	42	85	0	4	34	37	10.3	6812		12-07-20
12-07-21	21	10.8	15.9	65	95	0	3	17	32	8.9	7430		12-07-21
12-07-22	25.3	12.3	18.8	44	96	0	2	20	33	9.2	7078		12-07-22
12-07-23	25.2	14.6	19.9				4	0	0	0	6894		12-07-23
12-07-24	19.5	15.5	17.5	88	99	20	4	17	41	11.4	1641		12-07-24

12-07-25	24.7	14.6	19.7	52	98	16	4	2	37	10.3	5012	1 (3 hr)	12-07-25
12-07-26	26.2	13.3	19.8	43	98	0	3	23	33	9.2	5186		12-07-26
12-07-27	19.5	16.8	18.2	94	98	7.4	2	0	0	0	1218		12-07-27
12-07-28	22	15.9	19	74	97	0.2	2	0	0	0	6658		12-07-28
12-07-29	20.1	15.5	17.8	73	98	7	2	0	0	0	2035		12-07-29
12-07-30	24.8	14	19.4	43	95	0.4	3	0	0	0	5488		12-07-30
12-07-31	28.1	13.5	20.8	49	96	0	2	20	33	9.2	7165		12-07-31
12-08-01	20.7	16.4	18.6	89	96	6.6	4	23	44	12.2	1434		12-08-01
12-08-02	20.3	17.3	18.8	91	98	7.2	2	0	0	0	1687		12-08-02
12-08-03	24.9	17.8	21.4	74	99	0.2	2	0	0	0	5540		12-08-03
12-08-04	26.8	17.1	22	64	98	0	2	0	0	0	6536		12-08-04
12-08-05	21.8	17.5	19.7	85	99	0	2	19	32	8.9	5047		12-08-05
12-08-06	24.4	18.2	21.3	83	99	1	4	21	41	11.4	2957		12-08-06
12-08-07	23.4	16	19.7	83	99	4.4	2	0	0	0	1906		12-08-07
12-08-08	25.7	15.7	20.7	57	97	0	2	0	0	0	7108		12-08-08
12-08-09	26.2	16.7	21.5	50	97	0	2	0	0	0	6848		12-08-09
12-08-10	27.1	15	21.1	57	98	0	2	0	0	0	6738		12-08-10
12-08-11	21.4	18.7	20.1	91	99	6.2	3	0	0	0	1616		12-08-11
12-08-12	25.6	19	22.3	81	99	0.2	2	0	0	0	3601		12-08-12
12-08-13	24.3	18.9	21.6	85	99	2.2	3	0	0	0	3559		12-08-13
12-08-14	26	17.6	21.8	72	99	0	2	0	0	0	5720		12-08-14
12-08-15	24.1	16.8	20.5	74	97	0	2	0	0	0	6081		12-08-15
12-08-16	23.2	17.8	20.5	85	99	10.2	3	7	41	11.4	2572		12-08-16
12-08-17	26.2	17.7	22	58	96	0.6	3	0	0	0	4333		12-08-17
12-08-18	24.2	16.4	20.3	75	98	0	2	0	0	0	5874		12-08-18
12-08-19	23.9	18.1	21	72	99	4.2	2	0	0	0	3787		12-08-19
12-08-20	25.5	19.8	22.7	69	98	3.4	2	0	0	0	3098		12-08-20
12-08-21	27.6	17.8	22.7	41	93	0	2	0	0	0	5736		12-08-21
12-08-22	23.8	15.8	19.8	56	94	0	2	0	0	0	6073		12-08-22
12-08-23	26	16.8	21.4	37	96	0	2	0	0	0	6554		12-08-23
12-08-24	26.6	13.8	20.2	31	94	0	3	0	0	0	6705		12-08-24
12-08-25	23.1	14.2	18.7	56	96	0	2	0	0	0	6170		12-08-25
12-08-26	22.5	13.5	18	67	97	0	2	0	0	0	6496		12-08-26
12-08-27	27.1	15.4	21.3	44	93	0	3	22	32	8.6	6264		12-08-27
12-08-28	20.9	15.7	18.3	83	97	2.4	4	21	44	11.9	1216		12-08-28
12-08-29	20.6	13.4	17	39	84	0.2	4	32	43	11.6	6640		12-08-29
12-08-30	26	13.7	19.9	36	87	0	3	23	44	11.9	6310		12-08-30
12-08-31	25.5	14.5	20	59	95	0	3	23	33	8.9	2614		12-08-31

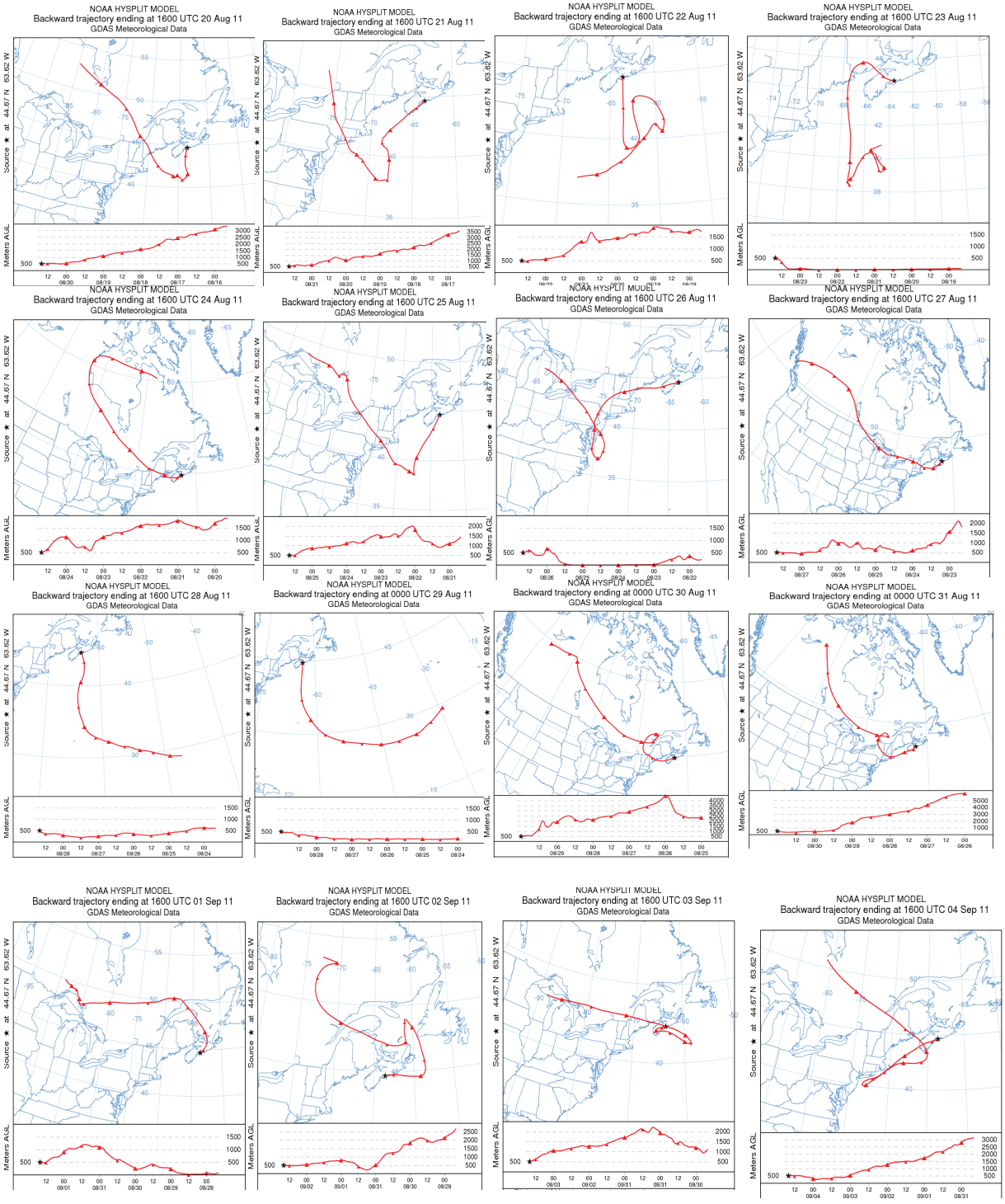
NOAA HYSPLIT MODEL
Backward trajectory ending at 1600 UTC 20 Aug 11
GDAS Meteorological Data
NOAA HYSPLIT MODEL
Backward trajectory ending at 1600 UTC 21 Aug 11
GDAS Meteorological Data
NOAA HYSPLIT MODEL
Backward trajectory ending at 1600 UTC 22 Aug 11
GDAS Meteorological Data
NOAA HYSPLIT MODEL
Backward trajectory ending at 1600 UTC 23 Aug 11
GDAS Meteorological Data
NOAA HYSPLIT MODEL
Backward trajectory ending at 1600 UTC 24 Aug 11
GDAS Meteorological Data
NOAA HYSPLIT MODEL
Backward trajectory ending at 1600 UTC 25 Aug 11
GDAS Meteorological Data
NOAA HYSPLIT MODEL
Backward trajectory ending at 1600 UTC 26 Aug 11
GDAS Meteorological Data
NOAA HYSPLIT MODEL
Backward trajectory ending at 1600 UTC 27 Aug 11
GDAS Meteorological Data
NOAA HYSPLIT MODEL
Backward trajectory ending at 1600 UTC 28 Aug 11
GDAS Meteorological Data
NOAA HYSPLIT MODEL
Backward trajectory ending at 0000 UTC 29 Aug 11
GDAS Meteorological Data
NOAA HYSPLIT MODEL
Backward trajectory ending at 0000 UTC 30 Aug 11
GDAS Meteorological Data
NOAA HYSPLIT MODEL
Backward trajectory ending at 0000 UTC 31 Aug 11
GDAS Meteorological Data
NOAA HYSPLIT MODEL
Backward trajectory ending at 1600 UTC 01 Sep 11
GDAS Meteorological Data
NOAA HYSPLIT MODEL
Backward trajectory ending at 1600 UTC 02 Sep 11
GDAS Meteorological Data
NOAA HYSPLIT MODEL
Backward trajectory ending at 1600 UTC 03 Sep 11
GDAS Meteorological Data
NOAA HYSPLIT MODEL
Backward trajectory ending at 1600 UTC 04 Sep 11
GDAS Meteorological Data

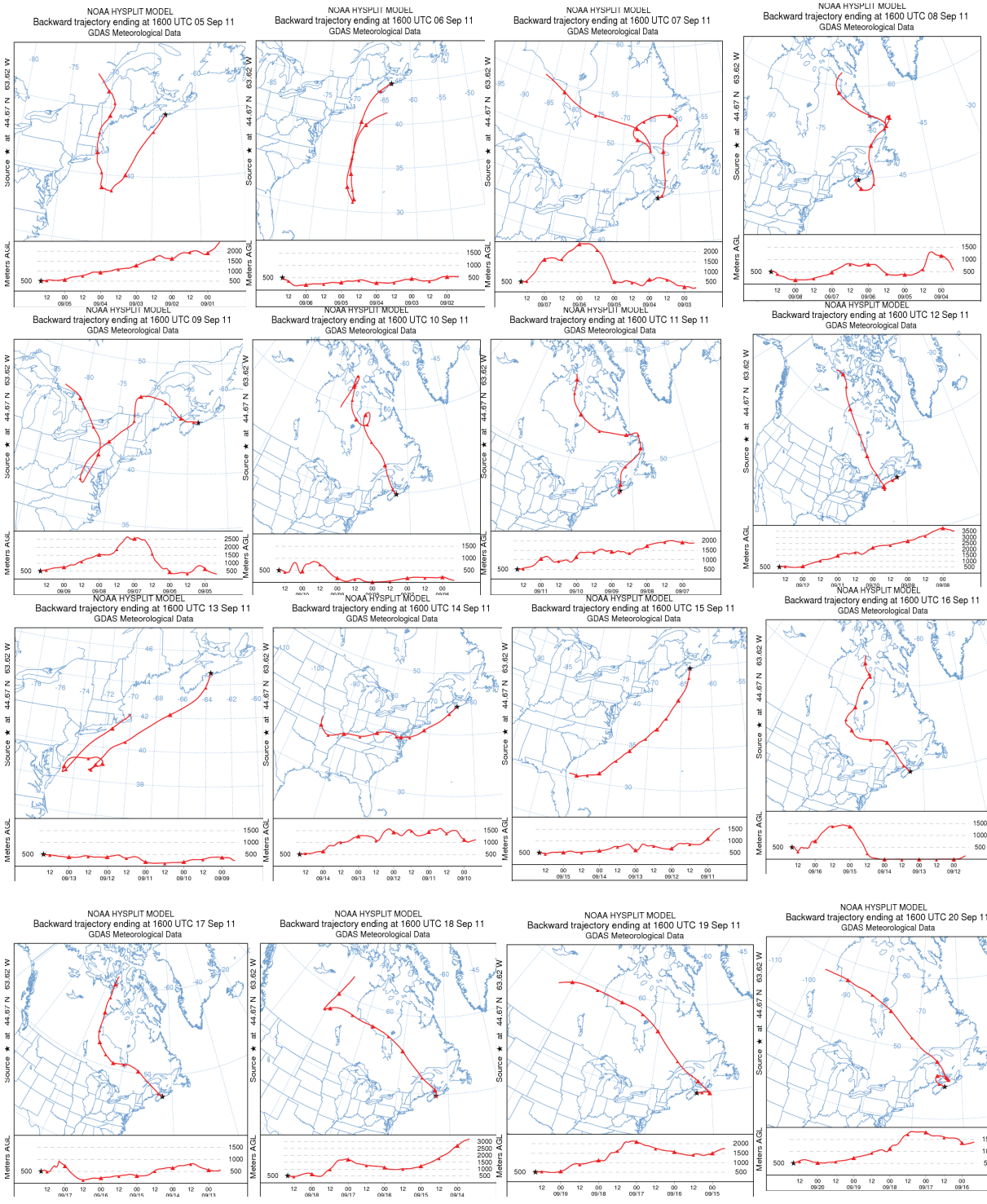
NOAA HYSPLIT MODEL
Backward trajectory ending at 1600 UTC 05 Sep 11
GDAS Meteorological Data
NOAA HYSPLIT MODEL
Backward trajectory ending at 1600 UTC 06 Sep 11
GDAS Meteorological Data
NOAA HYSPLIT MODEL
Backward trajectory ending at 1600 UTC 07 Sep 11
GDAS Meteorological Data
NOAA HYSPLIT MODEL
Backward trajectory ending at 1600 UTC 08 Sep 11
GDAS Meteorological Data
NOAA HYSPLIT MODEL
Backward trajectory ending at 1600 UTC 09 Sep 11
GDAS Meteorological Data
NOAA HYSPLIT MODEL
Backward trajectory ending at 1600 UTC 10 Sep 11
GDAS Meteorological Data
NOAA HYSPLIT MODEL
Backward trajectory ending at 1600 UTC 11 Sep 11
GDAS Meteorological Data
NOAA HYSPLIT MODEL
Backward trajectory ending at 1600 UTC 12 Sep 11
GDAS Meteorological Data
NOAA HYSPLIT MODEL
Backward trajectory ending at 1600 UTC 13 Sep 11
GDAS Meteorological Data
NOAA HYSPLIT MODEL
Backward trajectory ending at 1600 UTC 14 Sep 11
GDAS Meteorological Data
NOAA HYSPLIT MODEL
Backward trajectory ending at 1600 UTC 15 Sep 11
GDAS Meteorological Data
NOAA HYSPLIT MODEL
Backward trajectory ending at 1600 UTC 16 Sep 11
GDAS Meteorological Data
NOAA HYSPLIT MODEL
Backward trajectory ending at 1600 UTC 17 Sep 11
GDAS Meteorological Data
NOAA HYSPLIT MODEL
Backward trajectory ending at 1600 UTC 18 Sep 11
GDAS Meteorological Data
NOAA HYSPLIT MODEL
Backward trajectory ending at 1600 UTC 19 Sep 11
GDAS Meteorological Data
NOAA HYSPLIT MODEL
Backward trajectory ending at 1600 UTC 20 Sep 11
GDAS Meteorological Data

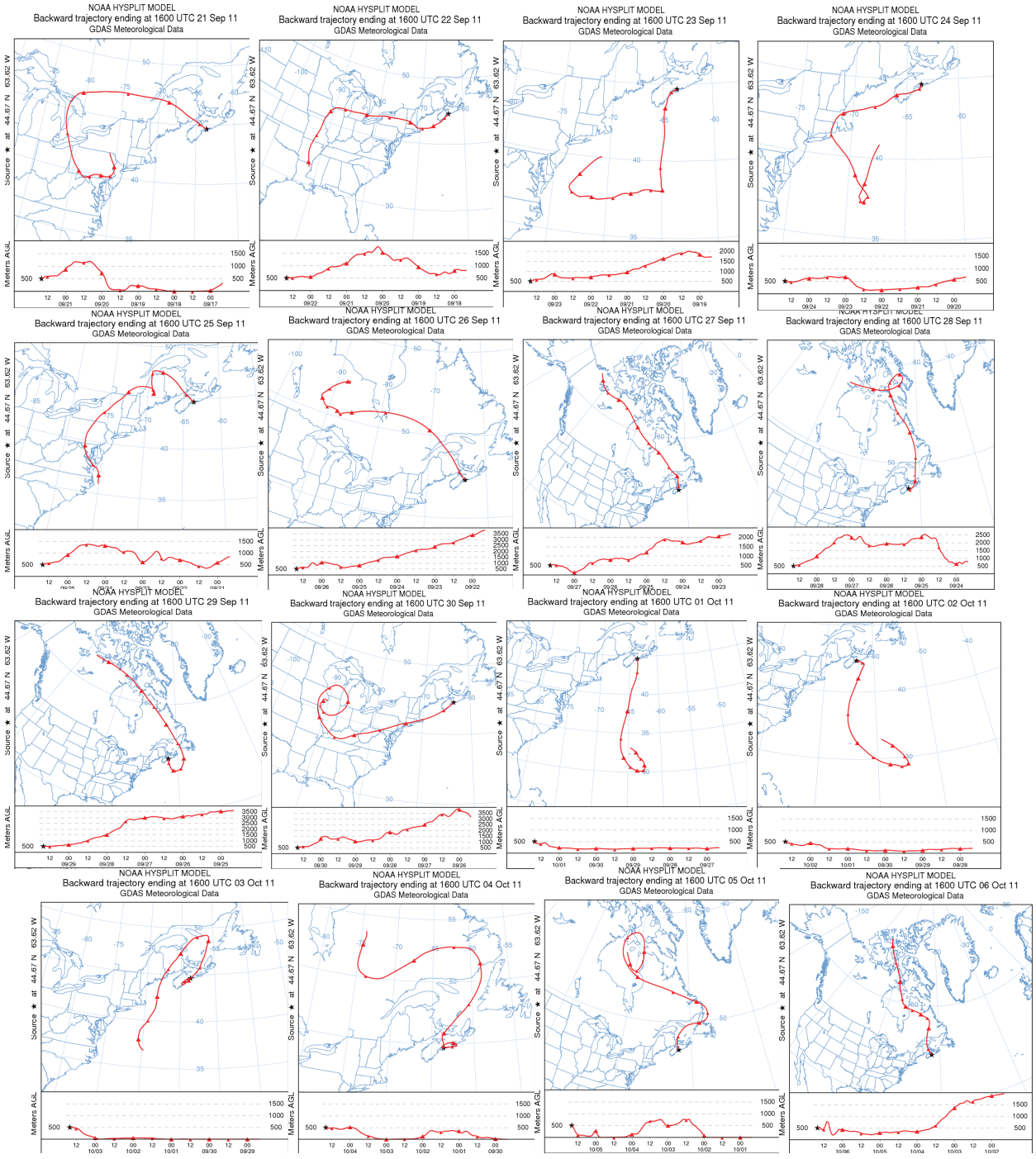
NOAA HYSPLIT MODEL
Backward trajectory ending at 1600 UTC 21 Sep 11
GDAS Meteorological Data
NOAA HYSPLIT MODEL
Backward trajectory ending at 1600 UTC 22 Sep 11
GDAS Meteorological Data
NOAA HYSPLIT MODEL
Backward trajectory ending at 1600 UTC 23 Sep 11
GDAS Meteorological Data
NOAA HYSPLIT MODEL
Backward trajectory ending at 1600 UTC 24 Sep 11
GDAS Meteorological Data
NOAA HYSPLIT MODEL
Backward trajectory ending at 1600 UTC 25 Sep 11
GDAS Meteorological Data
NOAA HYSPLIT MODEL
Backward trajectory ending at 1600 UTC 26 Sep 11
GDAS Meteorological Data
NOAA HYSPLIT MODEL
Backward trajectory ending at 1600 UTC 27 Sep 11
GDAS Meteorological Data
NOAA HYSPLIT MODEL
Backward trajectory ending at 1600 UTC 28 Sep 11
GDAS Meteorological Data
NOAA HYSPLIT MODEL
Backward trajectory ending at 1600 UTC 29 Sep 11
GDAS Meteorological Data
NOAA HYSPLIT MODEL
Backward trajectory ending at 1600 UTC 30 Sep 11
GDAS Meteorological Data
NOAA HYSPLIT MODEL
Backward trajectory ending at 1600 UTC 01 Oct 11
GDAS Meteorological Data
NOAA HYSPLIT MODEL
Backward trajectory ending at 1600 UTC 02 Oct 11
GDAS Meteorological Data
NOAA HYSPLIT MODEL
Backward trajectory ending at 1600 UTC 03 Oct 11
GDAS Meteorological Data
NOAA HYSPLIT MODEL
Backward trajectory ending at 1600 UTC 04 Oct 11
GDAS Meteorological Data
NOAA HYSPLIT MODEL
Backward trajectory ending at 1600 UTC 05 Oct 11
GDAS Meteorological Data
NOAA HYSPLIT MODEL
Backward trajectory ending at 1600 UTC 06 Oct 11
GDAS Meteorological Data
Source ★ at 44.67 N 63.62 W
Meters AGL

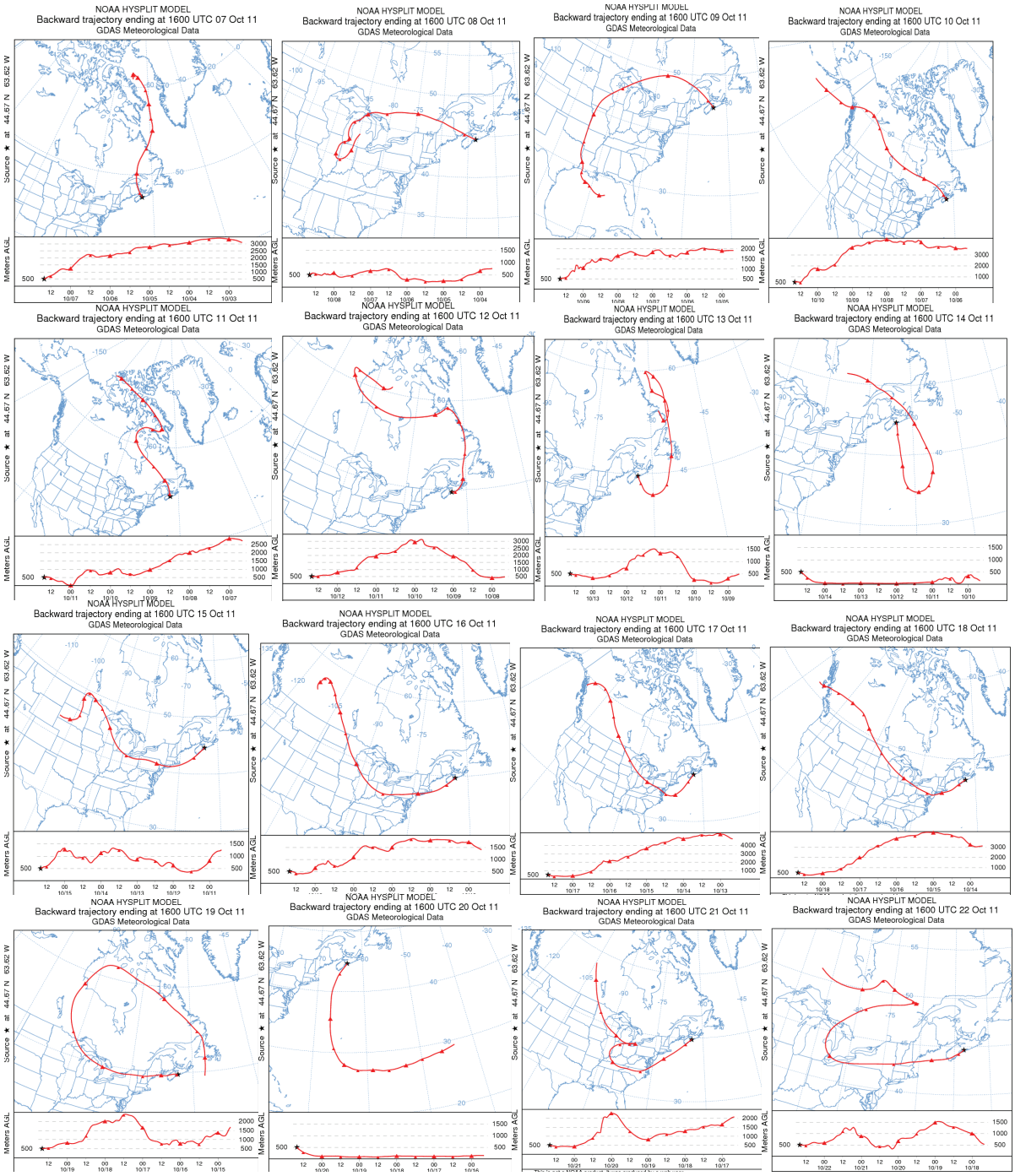
NOAA HYSPLIT MODEL
Backward trajectory ending at 1600 UTC 07 Oct 11
GDAS Meteorological Data
NOAA HYSPLIT MODEL
Backward trajectory ending at 1600 UTC 08 Oct 11
GDAS Meteorological Data
NOAA HYSPLIT MODEL
Backward trajectory ending at 1600 UTC 09 Oct 11
GDAS Meteorological Data
NOAA HYSPLIT MODEL
Backward trajectory ending at 1600 UTC 10 Oct 11
GDAS Meteorological Data
NOAA HYSPLIT MODEL
Backward trajectory ending at 1600 UTC 11 Oct 11
GDAS Meteorological Data
NOAA HYSPLIT MODEL
Backward trajectory ending at 1600 UTC 12 Oct 11
GDAS Meteorological Data
NOAA HYSPLIT MODEL
Backward trajectory ending at 1600 UTC 13 Oct 11
GDAS Meteorological Data
NOAA HYSPLIT MODEL
Backward trajectory ending at 1600 UTC 14 Oct 11
GDAS Meteorological Data
NOAA HYSPLIT MODEL
Backward trajectory ending at 1600 UTC 15 Oct 11
GDAS Meteorological Data
NOAA HYSPLIT MODEL
Backward trajectory ending at 1600 UTC 16 Oct 11
GDAS Meteorological Data
NOAA HYSPLIT MODEL
Backward trajectory ending at 1600 UTC 17 Oct 11
GDAS Meteorological Data
NOAA HYSPLIT MODEL
Backward trajectory ending at 1600 UTC 18 Oct 11
GDAS Meteorological Data
NOAA HYSPLIT MODEL
Backward trajectory ending at 1600 UTC 19 Oct 11
GDAS Meteorological Data
NOAA HYSPLIT MODEL
Backward trajectory ending at 1600 UTC 20 Oct 11
GDAS Meteorological Data
NOAA HYSPLIT MODEL
Backward trajectory ending at 1600 UTC 21 Oct 11
GDAS Meteorological Data
NOAA HYSPLIT MODEL
Backward trajectory ending at 1600 UTC 22 Oct 11
GDAS Meteorological Data
Source ★ at 44.67 N 63.62 W
Meters AGL

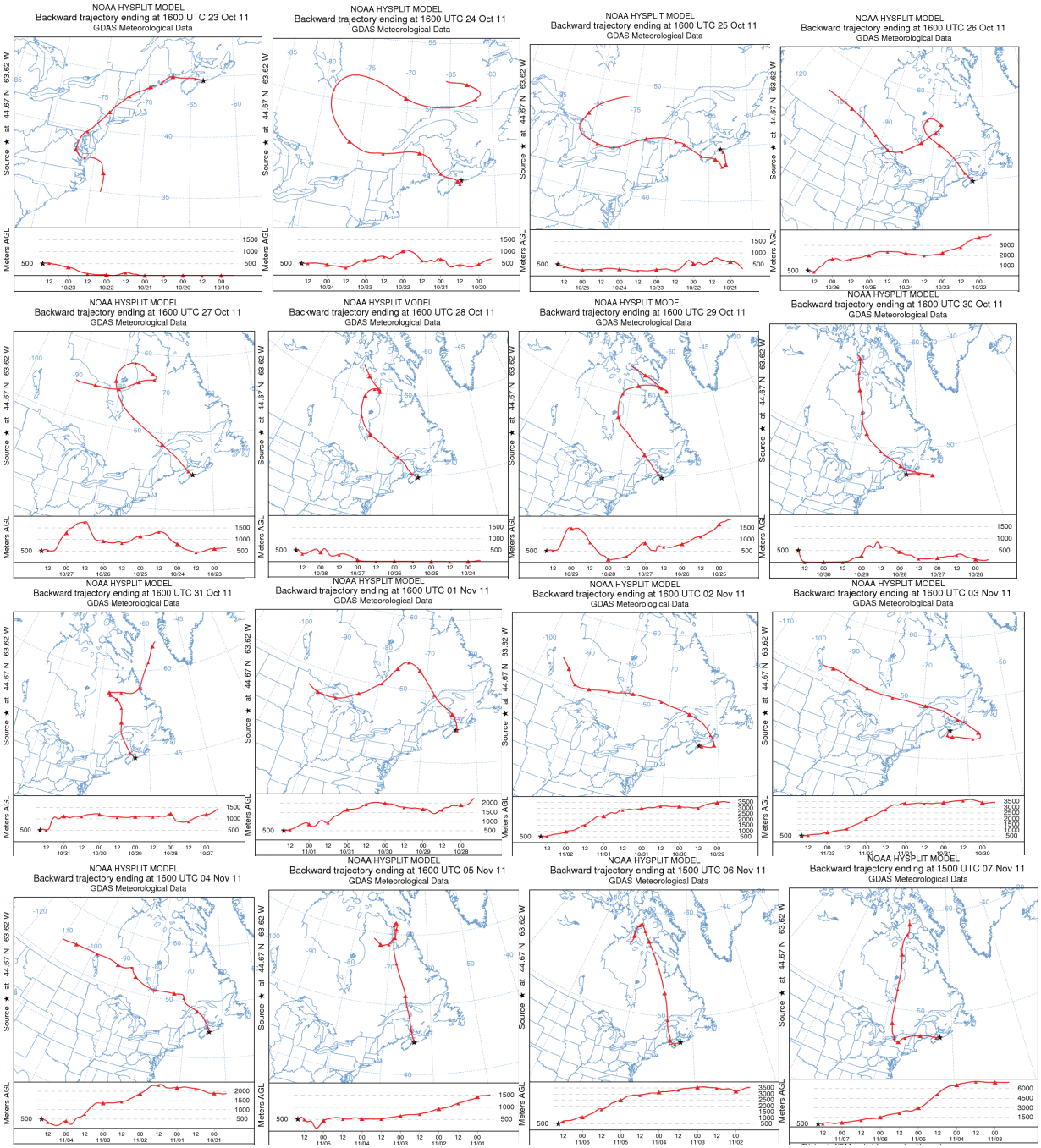
NOAA HYSPLIT MODEL
Backward trajectory ending at 1600 UTC 23 Oct 11
GDAS Meteorological Data
NOAA HYSPLIT MODEL
Backward trajectory ending at 1600 UTC 24 Oct 11
GDAS Meteorological Data
NOAA HYSPLIT MODEL
Backward trajectory ending at 1600 UTC 25 Oct 11
GDAS Meteorological Data
NOAA HYSPLIT MODEL
Backward trajectory ending at 1600 UTC 26 Oct 11
GDAS Meteorological Data
NOAA HYSPLIT MODEL
Backward trajectory ending at 1600 UTC 27 Oct 11
GDAS Meteorological Data
NOAA HYSPLIT MODEL
Backward trajectory ending at 1600 UTC 28 Oct 11
GDAS Meteorological Data
NOAA HYSPLIT MODEL
Backward trajectory ending at 1600 UTC 29 Oct 11
GDAS Meteorological Data
NOAA HYSPLIT MODEL
Backward trajectory ending at 1600 UTC 30 Oct 11
GDAS Meteorological Data
NOAA HYSPLIT MODEL
Backward trajectory ending at 1600 UTC 31 Oct 11
GDAS Meteorological Data
NOAA HYSPLIT MODEL
Backward trajectory ending at 1600 UTC 01 Nov 11
GDAS Meteorological Data
NOAA HYSPLIT MODEL
Backward trajectory ending at 1600 UTC 02 Nov 11
GDAS Meteorological Data
NOAA HYSPLIT MODEL
Backward trajectory ending at 1600 UTC 03 Nov 11
GDAS Meteorological Data
NOAA HYSPLIT MODEL
Backward trajectory ending at 1600 UTC 04 Nov 11
GDAS Meteorological Data
NOAA HYSPLIT MODEL
Backward trajectory ending at 1600 UTC 05 Nov 11
GDAS Meteorological Data
NOAA HYSPLIT MODEL
Backward trajectory ending at 1500 UTC 06 Nov 11
GDAS Meteorological Data
NOAA HYSPLIT MODEL
Backward trajectory ending at 1500 UTC 07 Nov 11
GDAS Meteorological Data

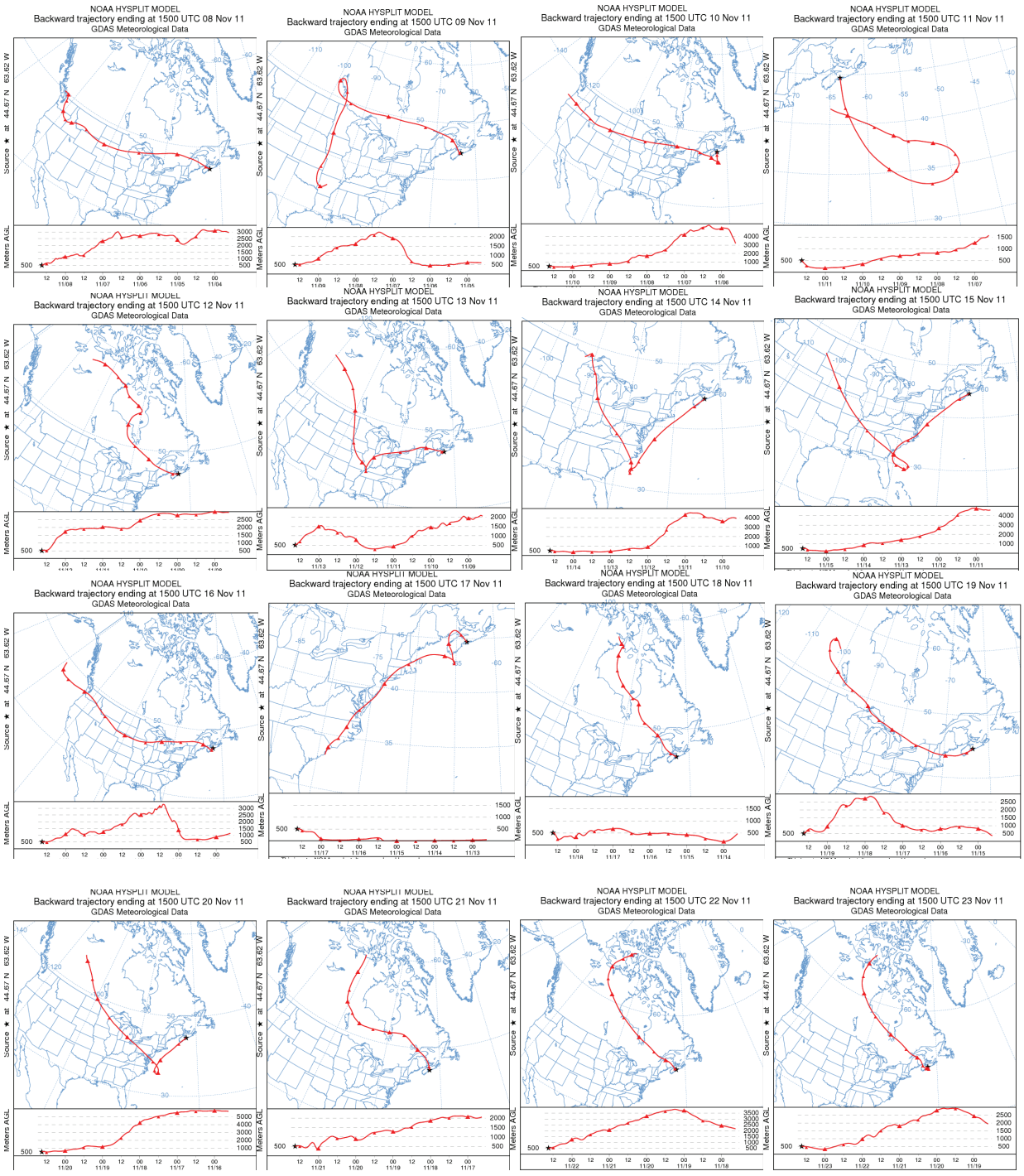
NOAA HYSPLIT MODEL
Backward trajectory ending at 1500 UTC 08 Nov 11
GDAS Meteorological Data
NOAA HYSPLIT MODEL
Backward trajectory ending at 1500 UTC 09 Nov 11
GDAS Meteorological Data
NOAA HYSPLIT MODEL
Backward trajectory ending at 1500 UTC 10 Nov 11
GDAS Meteorological Data
NOAA HYSPLIT MODEL
Backward trajectory ending at 1500 UTC 11 Nov 11
GDAS Meteorological Data
NOAA HYSPLIT MODEL
Backward trajectory ending at 1500 UTC 12 Nov 11
GDAS Meteorological Data
NOAA HYSPLIT MODEL
Backward trajectory ending at 1500 UTC 13 Nov 11
GDAS Meteorological Data
NOAA HYSPLIT MODEL
Backward trajectory ending at 1500 UTC 14 Nov 11
GDAS Meteorological Data
NOAA HYSPLIT MODEL
Backward trajectory ending at 1500 UTC 15 Nov 11
GDAS Meteorological Data
NOAA HYSPLIT MODEL
Backward trajectory ending at 1500 UTC 16 Nov 11
GDAS Meteorological Data
NOAA HYSPLIT MODEL
Backward trajectory ending at 1500 UTC 17 Nov 11
GDAS Meteorological Data
NOAA HYSPLIT MODEL
Backward trajectory ending at 1500 UTC 18 Nov 11
GDAS Meteorological Data
NOAA HYSPLIT MODEL
Backward trajectory ending at 1500 UTC 19 Nov 11
GDAS Meteorological Data
NOAA HYSPLIT MODEL
Backward trajectory ending at 1500 UTC 20 Nov 11
GDAS Meteorological Data
NOAA HYSPLIT MODEL
Backward trajectory ending at 1500 UTC 21 Nov 11
GDAS Meteorological Data
NOAA HYSPLIT MODEL
Backward trajectory ending at 1500 UTC 22 Nov 11
GDAS Meteorological Data
NOAA HYSPLIT MODEL
Backward trajectory ending at 1500 UTC 23 Nov 11
GDAS Meteorological Data

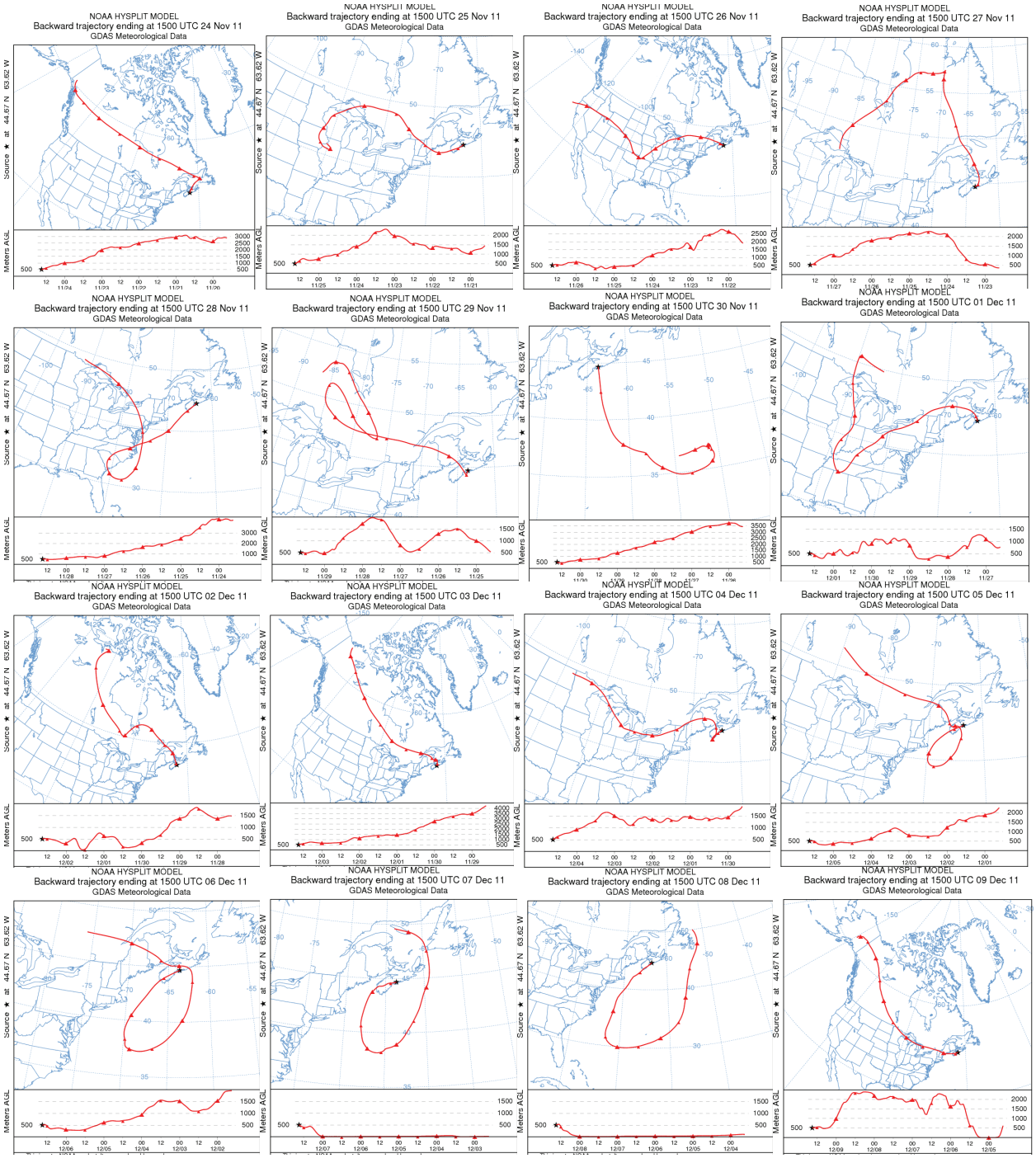
NOAA HYSPLIT MODEL
Backward trajectory ending at 1500 UTC 24 Nov 11
GDAS Meteorological Data
NOAA HYSPLIT MODEL
Backward trajectory ending at 1500 UTC 25 Nov 11
GDAS Meteorological Data
NOAA HYSPLIT MODEL
Backward trajectory ending at 1500 UTC 26 Nov 11
GDAS Meteorological Data
NOAA HYSPLIT MODEL
Backward trajectory ending at 1500 UTC 27 Nov 11
GDAS Meteorological Data
NOAA HYSPLIT MODEL
Backward trajectory ending at 1500 UTC 28 Nov 11
GDAS Meteorological Data
NOAA HYSPLIT MODEL
Backward trajectory ending at 1500 UTC 29 Nov 11
GDAS Meteorological Data
NOAA HYSPLIT MODEL
Backward trajectory ending at 1500 UTC 30 Nov 11
GDAS Meteorological Data
NOAA HYSPLIT MODEL
Backward trajectory ending at 1500 UTC 01 Dec 11
GDAS Meteorological Data
NOAA HYSPLIT MODEL
Backward trajectory ending at 1500 UTC 02 Dec 11
GDAS Meteorological Data
NOAA HYSPLIT MODEL
Backward trajectory ending at 1500 UTC 03 Dec 11
GDAS Meteorological Data
NOAA HYSPLIT MODEL
Backward trajectory ending at 1500 UTC 04 Dec 11
GDAS Meteorological Data
NOAA HYSPLIT MODEL
Backward trajectory ending at 1500 UTC 05 Dec 11
GDAS Meteorological Data
NOAA HYSPLIT MODEL
Backward trajectory ending at 1500 UTC 06 Dec 11
GDAS Meteorological Data
NOAA HYSPLIT MODEL
Backward trajectory ending at 1500 UTC 07 Dec 11
GDAS Meteorological Data
NOAA HYSPLIT MODEL
Backward trajectory ending at 1500 UTC 08 Dec 11
GDAS Meteorological Data
NOAA HYSPLIT MODEL
Backward trajectory ending at 1500 UTC 09 Dec 11
GDAS Meteorological Data
Source ★ at 44.67 N 63.62 W
Meters AGL

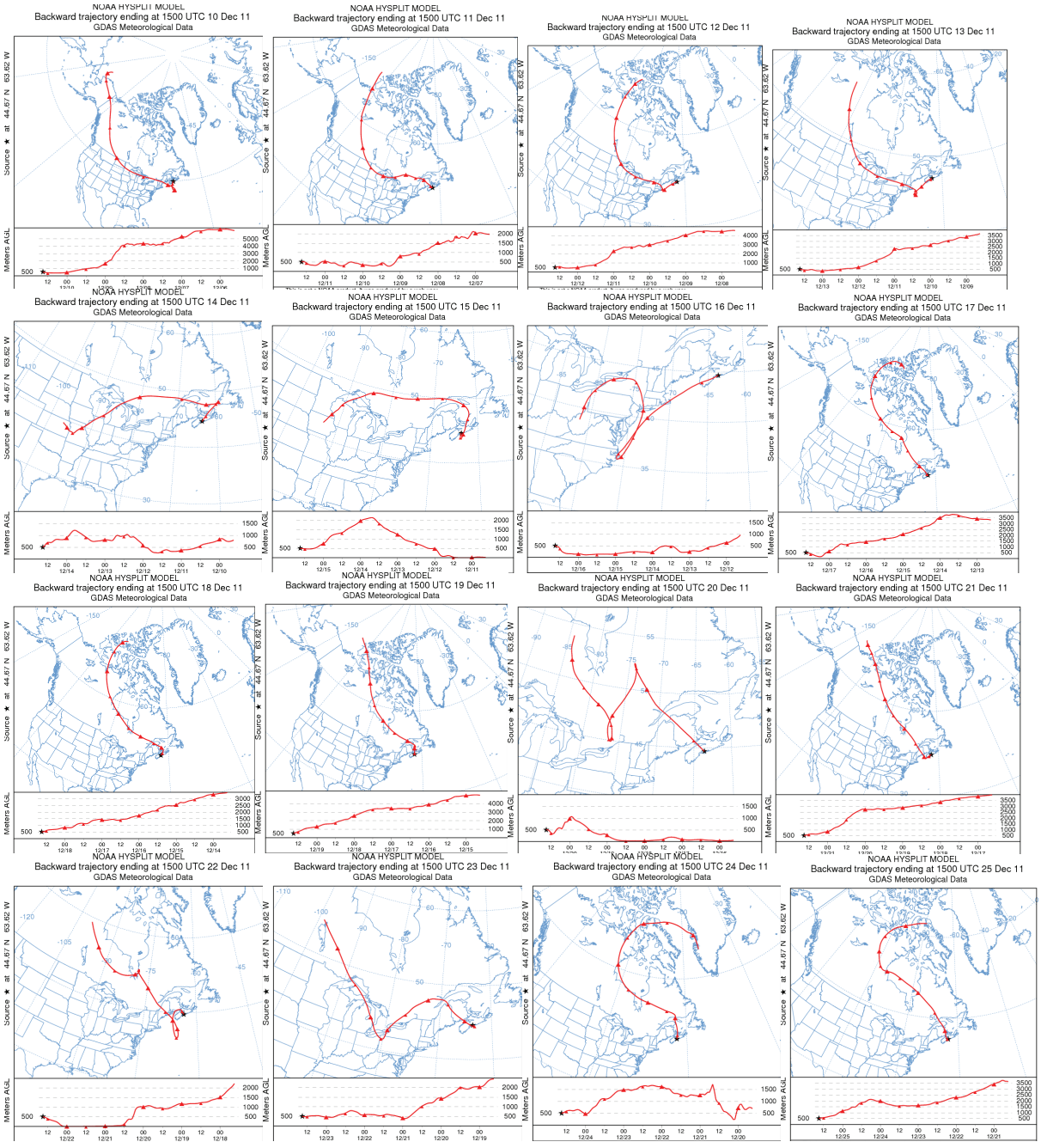
NOAA HYSPLIT MODEL
Backward trajectory ending at 1500 UTC 10 Dec 11
GDAS Meteorological Data
NOAA HYSPLIT MODEL
Backward trajectory ending at 1500 UTC 11 Dec 11
GDAS Meteorological Data
NOAA HYSPLIT MODEL
Backward trajectory ending at 1500 UTC 12 Dec 11
GDAS Meteorological Data
NOAA HYSPLIT MODEL
Backward trajectory ending at 1500 UTC 13 Dec 11
GDAS Meteorological Data
NOAA HYSPLIT MODEL
Backward trajectory ending at 1500 UTC 14 Dec 11
GDAS Meteorological Data
NOAA HYSPLIT MODEL
Backward trajectory ending at 1500 UTC 15 Dec 11
GDAS Meteorological Data
NOAA HYSPLIT MODEL
Backward trajectory ending at 1500 UTC 16 Dec 11
GDAS Meteorological Data
NOAA HYSPLIT MODEL
Backward trajectory ending at 1500 UTC 17 Dec 11
GDAS Meteorological Data
NOAA HYSPLIT MODEL
Backward trajectory ending at 1500 UTC 18 Dec 11
GDAS Meteorological Data
NOAA HYSPLIT MODEL
Backward trajectory ending at 1500 UTC 19 Dec 11
GDAS Meteorological Data
NOAA HYSPLIT MODEL
Backward trajectory ending at 1500 UTC 20 Dec 11
GDAS Meteorological Data
NOAA HYSPLIT MODEL
Backward trajectory ending at 1500 UTC 21 Dec 11
GDAS Meteorological Data
NOAA HYSPLIT MODEL
Backward trajectory ending at 1500 UTC 22 Dec 11
GDAS Meteorological Data
NOAA HYSPLIT MODEL
Backward trajectory ending at 1500 UTC 23 Dec 11
GDAS Meteorological Data
NOAA HYSPLIT MODEL
Backward trajectory ending at 1500 UTC 24 Dec 11
GDAS Meteorological Data
NOAA HYSPLIT MODEL
Backward trajectory ending at 1500 UTC 25 Dec 11
GDAS Meteorological Data
Source ★ at 44.67 N 63.62 W
Meters AGL

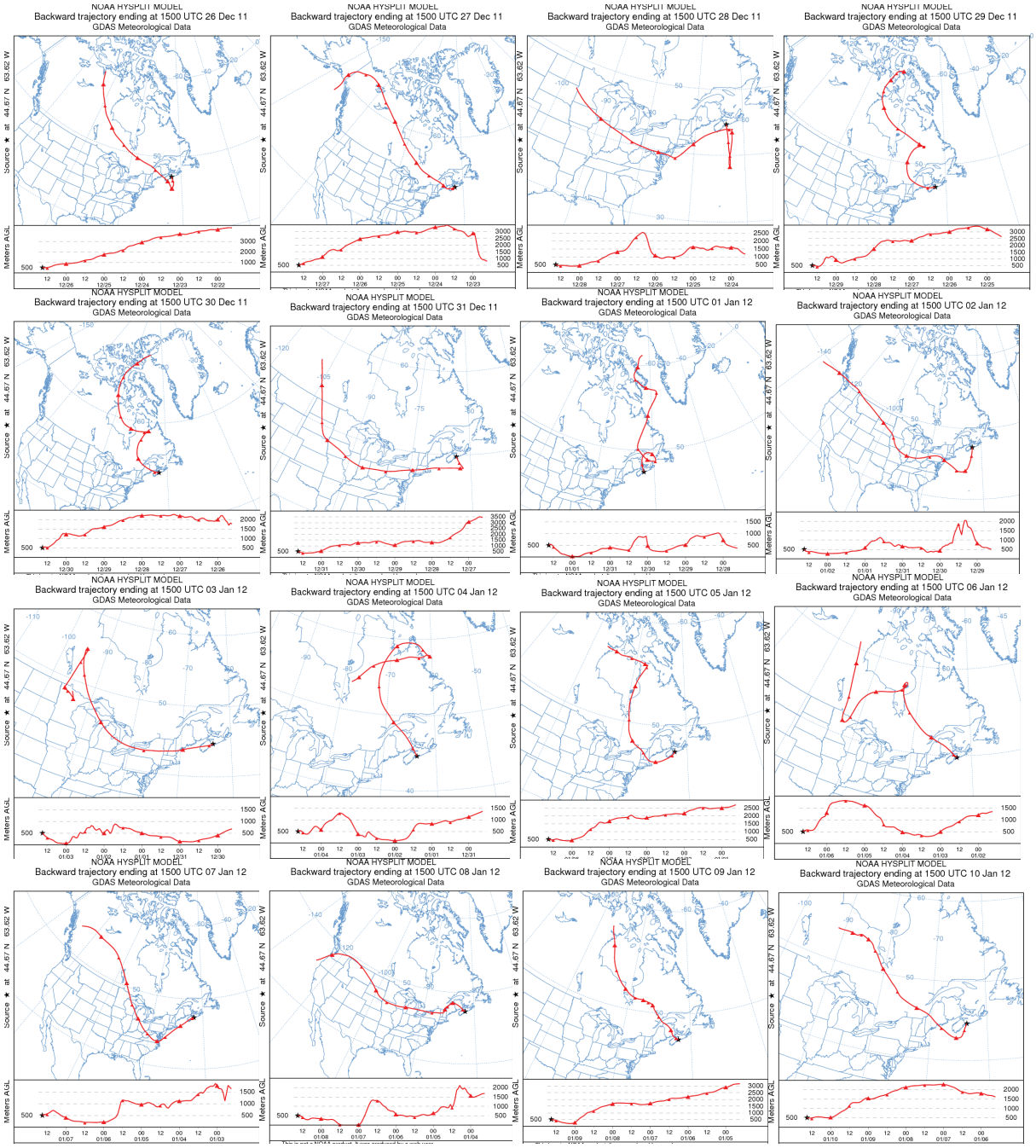
NOAA HYSPLIT MODEL
Backward trajectory ending at 1500 UTC 26 Dec 11
GDAS Meteorological Data
NOAA HYSPLIT MODEL
Backward trajectory ending at 1500 UTC 27 Dec 11
GDAS Meteorological Data
NOAA HYSPLIT MODEL
Backward trajectory ending at 1500 UTC 28 Dec 11
GDAS Meteorological Data
NOAA HYSPLIT MODEL
Backward trajectory ending at 1500 UTC 29 Dec 11
GDAS Meteorological Data
NOAA HYSPLIT MODEL
Backward trajectory ending at 1500 UTC 30 Dec 11
GDAS Meteorological Data
NOAA HYSPLIT MODEL
Backward trajectory ending at 1500 UTC 31 Dec 11
GDAS Meteorological Data
NOAA HYSPLIT MODEL
Backward trajectory ending at 1500 UTC 01 Jan 12
GDAS Meteorological Data
NOAA HYSPLIT MODEL
Backward trajectory ending at 1500 UTC 02 Jan 12
GDAS Meteorological Data
NOAA HYSPLIT MODEL
Backward trajectory ending at 1500 UTC 03 Jan 12
GDAS Meteorological Data
NOAA HYSPLIT MODEL
Backward trajectory ending at 1500 UTC 04 Jan 12
GDAS Meteorological Data
NOAA HYSPLIT MODEL
Backward trajectory ending at 1500 UTC 05 Jan 12
GDAS Meteorological Data
NOAA HYSPLIT MODEL
Backward trajectory ending at 1500 UTC 06 Jan 12
GDAS Meteorological Data
NOAA HYSPLIT MODEL
Backward trajectory ending at 1500 UTC 07 Jan 12
GDAS Meteorological Data
NOAA HYSPLIT MODEL
Backward trajectory ending at 1500 UTC 08 Jan 12
GDAS Meteorological Data
NOAA HYSPLIT MODEL
Backward trajectory ending at 1500 UTC 09 Jan 12
GDAS Meteorological Data
NOAA HYSPLIT MODEL
Backward trajectory ending at 1500 UTC 10 Jan 12
GDAS Meteorological Data
Source ★ at 44.67 N 63.62 W
Meters AGL

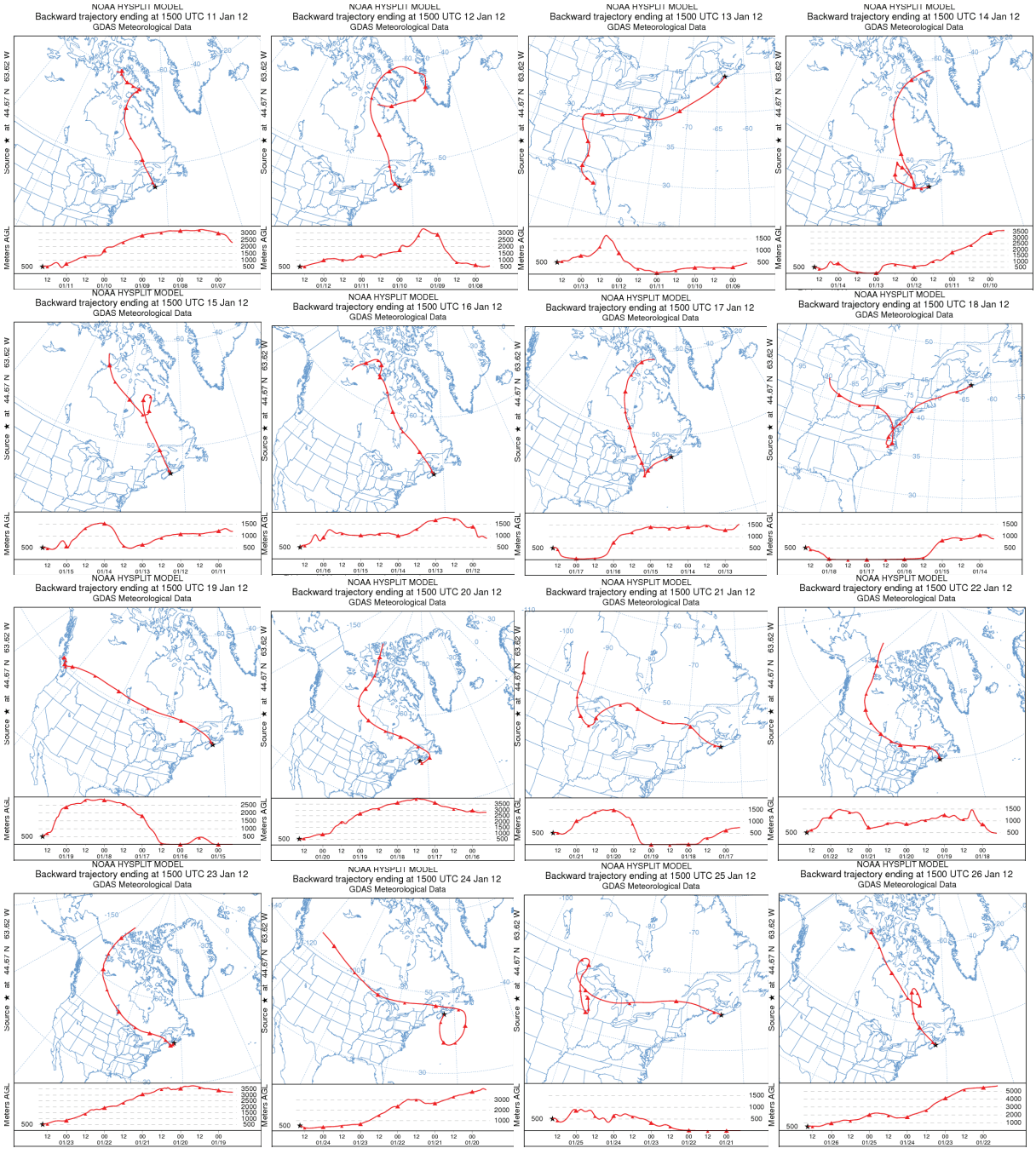
NOAA HYSPLIT MODEL
Backward trajectory ending at 1500 UTC 11 Jan 12
GDAS Meteorological Data
NOAA HYSPLIT MODEL
Backward trajectory ending at 1500 UTC 12 Jan 12
GDAS Meteorological Data
NOAA HYSPLIT MODEL
Backward trajectory ending at 1500 UTC 13 Jan 12
GDAS Meteorological Data
NOAA HYSPLIT MODEL
Backward trajectory ending at 1500 UTC 14 Jan 12
GDAS Meteorological Data
NOAA HYSPLIT MODEL
Backward trajectory ending at 1500 UTC 15 Jan 12
GDAS Meteorological Data
NOAA HYSPLIT MODEL
Backward trajectory ending at 1500 UTC 16 Jan 12
GDAS Meteorological Data
NOAA HYSPLIT MODEL
Backward trajectory ending at 1500 UTC 17 Jan 12
GDAS Meteorological Data
NOAA HYSPLIT MODEL
Backward trajectory ending at 1500 UTC 18 Jan 12
GDAS Meteorological Data
NOAA HYSPLIT MODEL
Backward trajectory ending at 1500 UTC 19 Jan 12
GDAS Meteorological Data
NOAA HYSPLIT MODEL
Backward trajectory ending at 1500 UTC 20 Jan 12
GDAS Meteorological Data
NOAA HYSPLIT MODEL
Backward trajectory ending at 1500 UTC 21 Jan 12
GDAS Meteorological Data
NOAA HYSPLIT MODEL
Backward trajectory ending at 1500 UTC 22 Jan 12
GDAS Meteorological Data
NOAA HYSPLIT MODEL
Backward trajectory ending at 1500 UTC 23 Jan 12
GDAS Meteorological Data
NOAA HYSPLIT MODEL
Backward trajectory ending at 1500 UTC 24 Jan 12
GDAS Meteorological Data
NOAA HYSPLIT MODEL
Backward trajectory ending at 1500 UTC 25 Jan 12
GDAS Meteorological Data
NOAA HYSPLIT MODEL
Backward trajectory ending at 1500 UTC 26 Jan 12
GDAS Meteorological Data
Source ★ at 44.67 N 63.62 W
Meters AGL

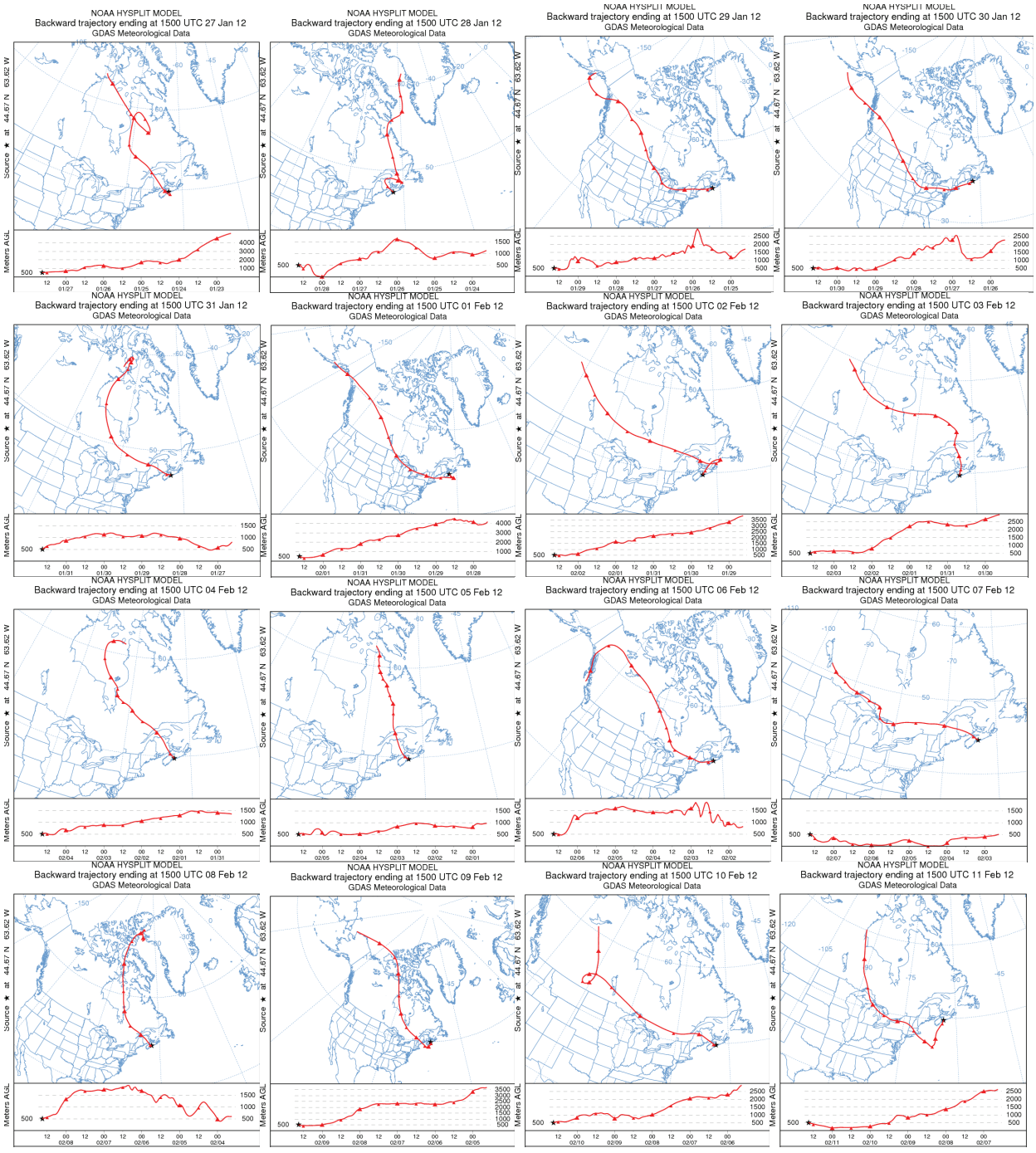
NOAA HYSPLIT MODEL
Backward trajectory ending at 1500 UTC 27 Jan 12
GDAS Meteorological Data
NOAA HYSPLIT MODEL
Backward trajectory ending at 1500 UTC 28 Jan 12
GDAS Meteorological Data
NOAA HYSPLIT MODEL
Backward trajectory ending at 1500 UTC 29 Jan 12
GDAS Meteorological Data
NOAA HYSPLIT MODEL
Backward trajectory ending at 1500 UTC 30 Jan 12
GDAS Meteorological Data
NOAA HYSPLIT MODEL
Backward trajectory ending at 1500 UTC 31 Jan 12
GDAS Meteorological Data
NOAA HYSPLIT MODEL
Backward trajectory ending at 1500 UTC 01 Feb 12
GDAS Meteorological Data
NOAA HYSPLIT MODEL
Backward trajectory ending at 1500 UTC 02 Feb 12
GDAS Meteorological Data
NOAA HYSPLIT MODEL
Backward trajectory ending at 1500 UTC 03 Feb 12
GDAS Meteorological Data
NOAA HYSPLIT MODEL
Backward trajectory ending at 1500 UTC 04 Feb 12
GDAS Meteorological Data
NOAA HYSPLIT MODEL
Backward trajectory ending at 1500 UTC 05 Feb 12
GDAS Meteorological Data
NOAA HYSPLIT MODEL
Backward trajectory ending at 1500 UTC 06 Feb 12
GDAS Meteorological Data
NOAA HYSPLIT MODEL
Backward trajectory ending at 1500 UTC 07 Feb 12
GDAS Meteorological Data
NOAA HYSPLIT MODEL
Backward trajectory ending at 1500 UTC 08 Feb 12
GDAS Meteorological Data
NOAA HYSPLIT MODEL
Backward trajectory ending at 1500 UTC 09 Feb 12
GDAS Meteorological Data
NOAA HYSPLIT MODEL
Backward trajectory ending at 1500 UTC 10 Feb 12
GDAS Meteorological Data
NOAA HYSPLIT MODEL
Backward trajectory ending at 1500 UTC 11 Feb 12
GDAS Meteorological Data
Source ★ at 44.67 N 63.62 W
Meters AGL

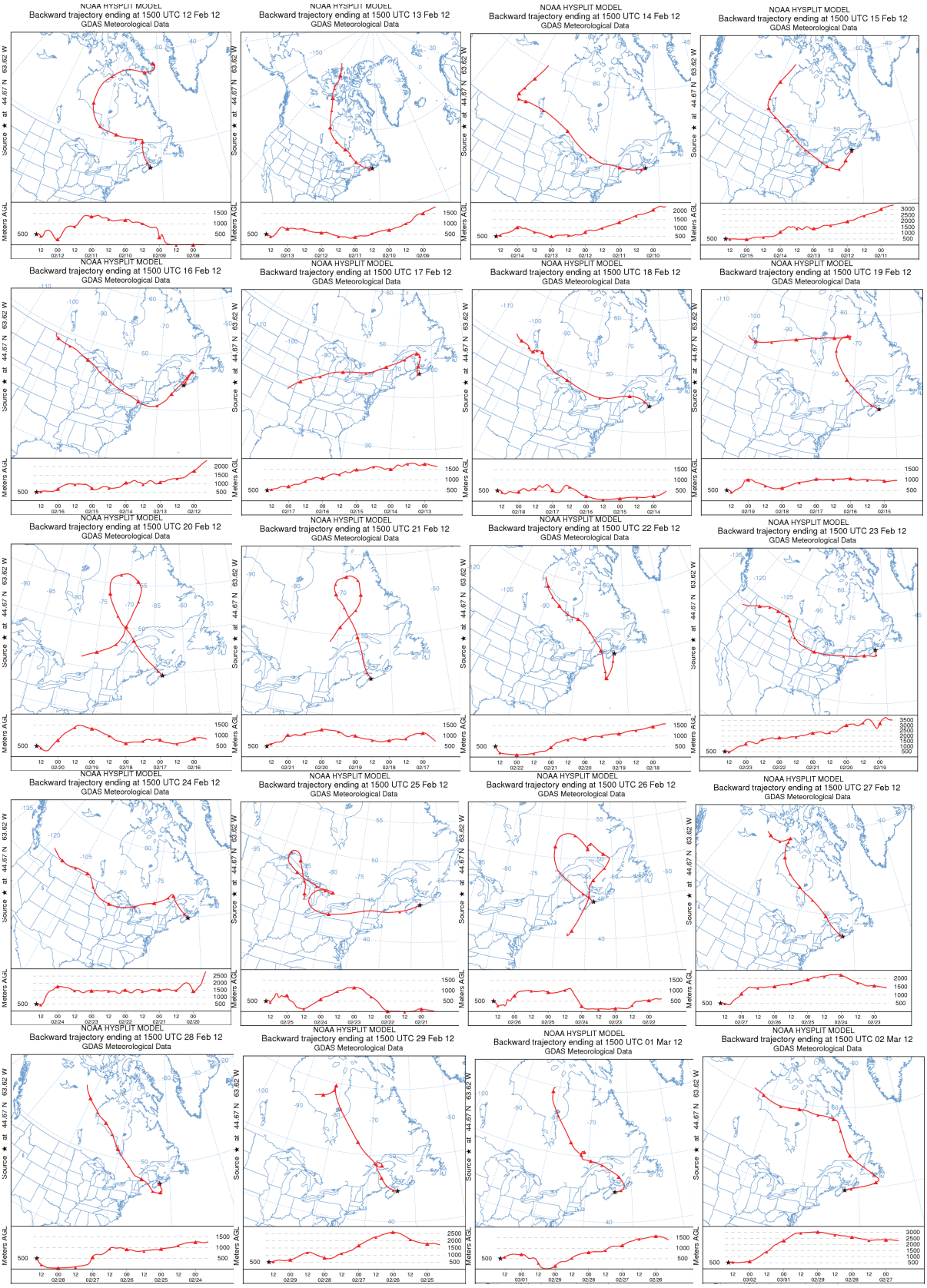
NOAA HYSPLIT MODEL
Backward trajectory ending at 1500 UTC 12 Feb 12
GDAS Meteorological Data
NOAA HYSPLIT MODEL
Backward trajectory ending at 1500 UTC 13 Feb 12
GDAS Meteorological Data
NOAA HYSPLIT MODEL
Backward trajectory ending at 1500 UTC 14 Feb 12
GDAS Meteorological Data
NOAA HYSPLIT MODEL
Backward trajectory ending at 1500 UTC 15 Feb 12
GDAS Meteorological Data
NOAA HYSPLIT MODEL
Backward trajectory ending at 1500 UTC 16 Feb 12
GDAS Meteorological Data
NOAA HYSPLIT MODEL
Backward trajectory ending at 1500 UTC 17 Feb 12
GDAS Meteorological Data
NOAA HYSPLIT MODEL
Backward trajectory ending at 1500 UTC 18 Feb 12
GDAS Meteorological Data
NOAA HYSPLIT MODEL
Backward trajectory ending at 1500 UTC 19 Feb 12
GDAS Meteorological Data
NOAA HYSPLIT MODEL
Backward trajectory ending at 1500 UTC 20 Feb 12
GDAS Meteorological Data
NOAA HYSPLIT MODEL
Backward trajectory ending at 1500 UTC 21 Feb 12
GDAS Meteorological Data
NOAA HYSPLIT MODEL
Backward trajectory ending at 1500 UTC 22 Feb 12
GDAS Meteorological Data
NOAA HYSPLIT MODEL
Backward trajectory ending at 1500 UTC 23 Feb 12
GDAS Meteorological Data
NOAA HYSPLIT MODEL
Backward trajectory ending at 1500 UTC 24 Feb 12
GDAS Meteorological Data
NOAA HYSPLIT MODEL
Backward trajectory ending at 1500 UTC 25 Feb 12
GDAS Meteorological Data
NOAA HYSPLIT MODEL
Backward trajectory ending at 1500 UTC 26 Feb 12
GDAS Meteorological Data
NOAA HYSPLIT MODEL
Backward trajectory ending at 1500 UTC 27 Feb 12
GDAS Meteorological Data
NOAA HYSPLIT MODEL
Backward trajectory ending at 1500 UTC 28 Feb 12
GDAS Meteorological Data
NOAA HYSPLIT MODEL
Backward trajectory ending at 1500 UTC 29 Feb 12
GDAS Meteorological Data
NOAA HYSPLIT MODEL
Backward trajectory ending at 1500 UTC 01 Mar 12
GDAS Meteorological Data
NOAA HYSPLIT MODEL
Backward trajectory ending at 1500 UTC 02 Mar 12
GDAS Meteorological Data

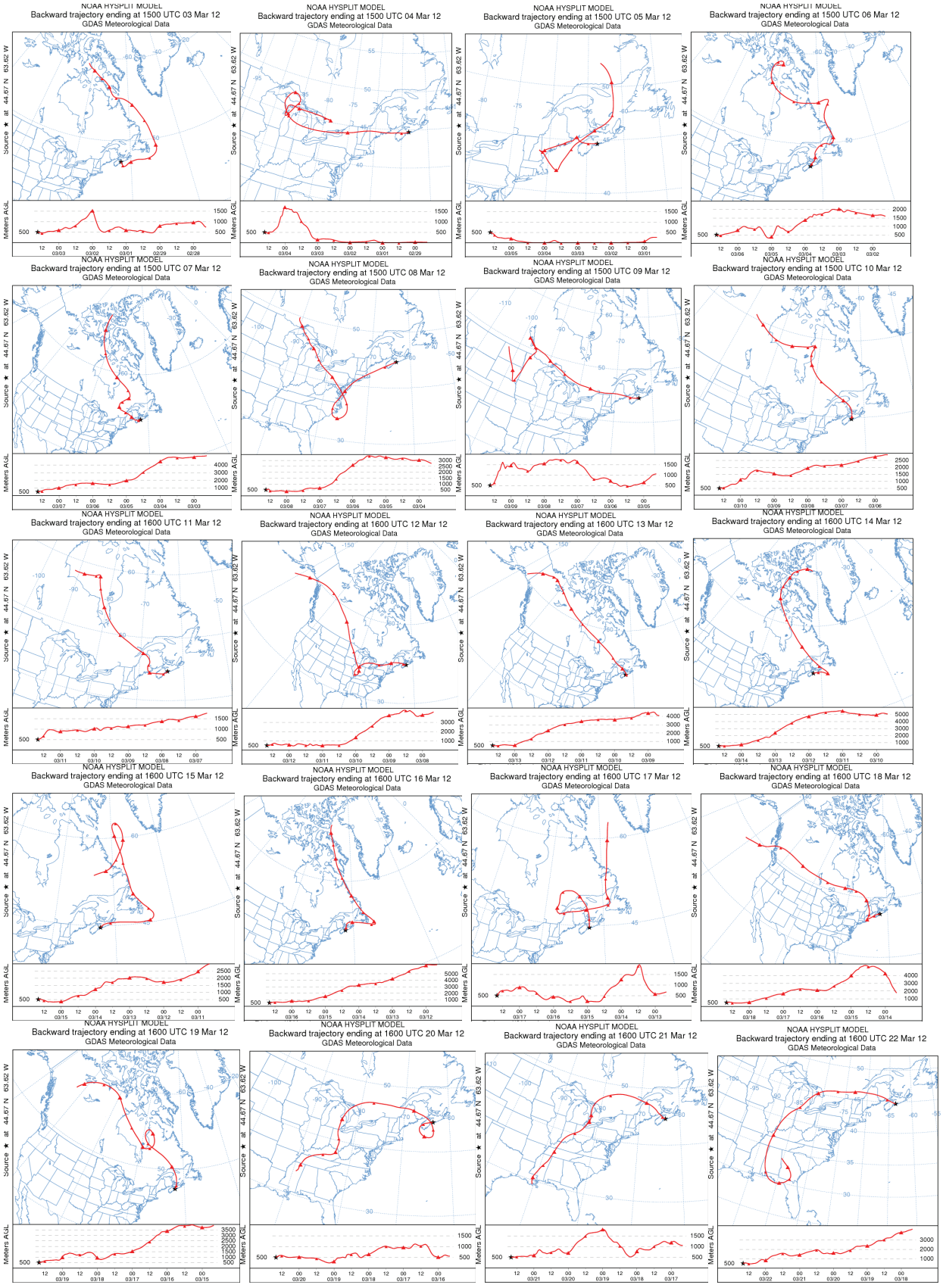
NOAA HYSPLIT MODEL
Backward trajectory ending at 1500 UTC 03 Mar 12
GDAS Meteorological Data
NOAA HYSPLIT MODEL
Backward trajectory ending at 1500 UTC 04 Mar 12
GDAS Meteorological Data
NOAA HYSPLIT MODEL
Backward trajectory ending at 1500 UTC 05 Mar 12
GDAS Meteorological Data
NOAA HYSPLIT MODEL
Backward trajectory ending at 1500 UTC 06 Mar 12
GDAS Meteorological Data
NOAA HYSPLIT MODEL
Backward trajectory ending at 1500 UTC 07 Mar 12
GDAS Meteorological Data
NOAA HYSPLIT MODEL
Backward trajectory ending at 1500 UTC 08 Mar 12
GDAS Meteorological Data
NOAA HYSPLIT MODEL
Backward trajectory ending at 1500 UTC 09 Mar 12
GDAS Meteorological Data
NOAA HYSPLIT MODEL
Backward trajectory ending at 1500 UTC 10 Mar 12
GDAS Meteorological Data
NOAA HYSPLIT MODEL
Backward trajectory ending at 1600 UTC 11 Mar 12
GDAS Meteorological Data
NOAA HYSPLIT MODEL
Backward trajectory ending at 1600 UTC 12 Mar 12
GDAS Meteorological Data
NOAA HYSPLIT MODEL
Backward trajectory ending at 1600 UTC 13 Mar 12
GDAS Meteorological Data
NOAA HYSPLIT MODEL
Backward trajectory ending at 1600 UTC 14 Mar 12
GDAS Meteorological Data
NOAA HYSPLIT MODEL
Backward trajectory ending at 1600 UTC 15 Mar 12
GDAS Meteorological Data
NOAA HYSPLIT MODEL
Backward trajectory ending at 1600 UTC 16 Mar 12
GDAS Meteorological Data
NOAA HYSPLIT MODEL
Backward trajectory ending at 1600 UTC 17 Mar 12
GDAS Meteorological Data
NOAA HYSPLIT MODEL
Backward trajectory ending at 1600 UTC 18 Mar 12
GDAS Meteorological Data
NOAA HYSPLIT MODEL
Backward trajectory ending at 1600 UTC 19 Mar 12
GDAS Meteorological Data
NOAA HYSPLIT MODEL
Backward trajectory ending at 1600 UTC 20 Mar 12
GDAS Meteorological Data
NOAA HYSPLIT MODEL
Backward trajectory ending at 1600 UTC 21 Mar 12
GDAS Meteorological Data
NOAA HYSPLIT MODEL
Backward trajectory ending at 1600 UTC 22 Mar 12
GDAS Meteorological Data

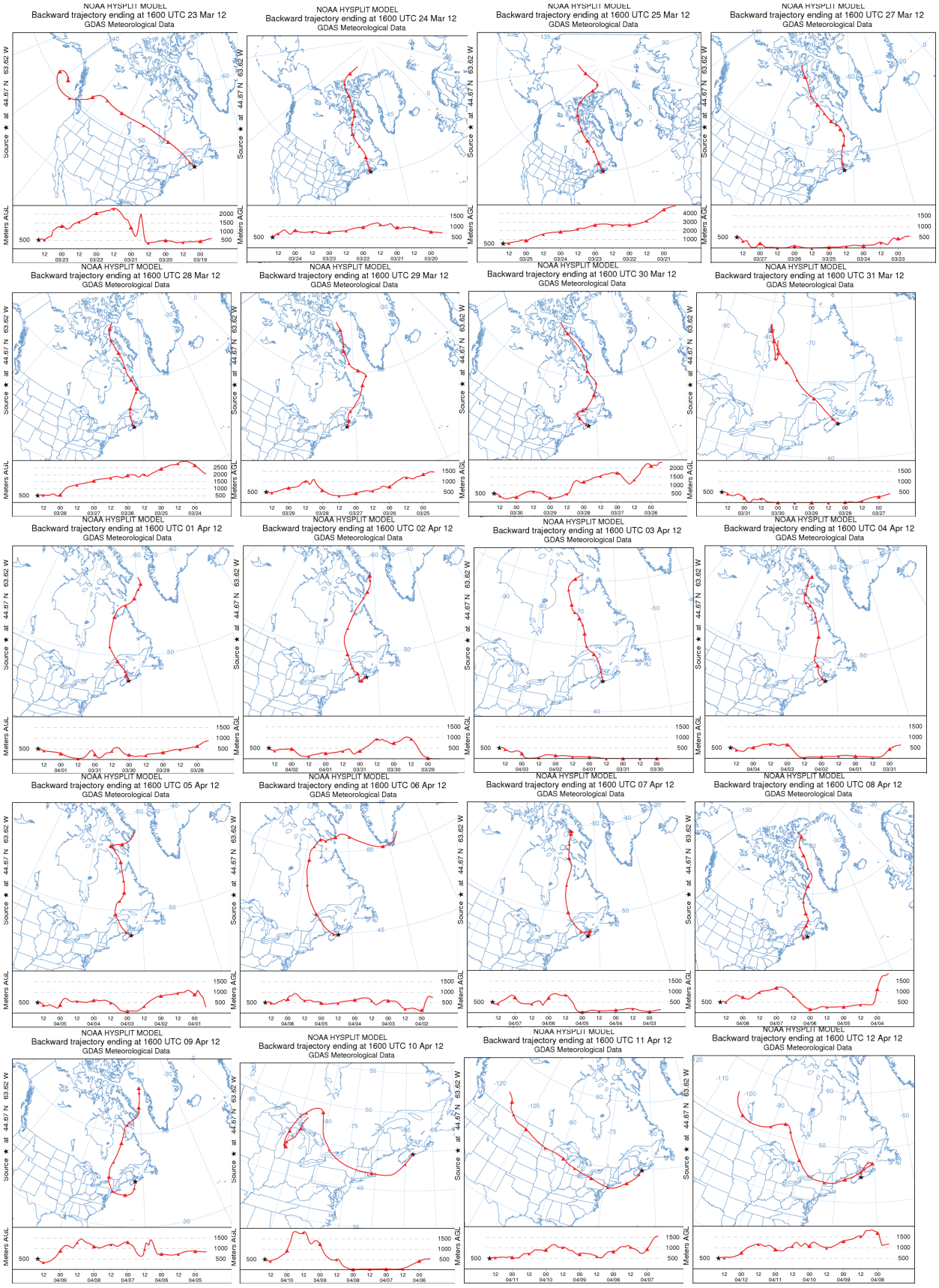
NOAA HYSPLIT MODEL
Backward trajectory ending at 1600 UTC 23 Mar 12
GDAS Meteorological Data
NOAA HYSPLIT MODEL
Backward trajectory ending at 1600 UTC 24 Mar 12
GDAS Meteorological Data
NOAA HYSPLIT MODEL
Backward trajectory ending at 1600 UTC 25 Mar 12
GDAS Meteorological Data
NOAA HYSPLIT MODEL
Backward trajectory ending at 1600 UTC 27 Mar 12
GDAS Meteorological Data
NOAA HYSPLIT MODEL
Backward trajectory ending at 1600 UTC 28 Mar 12
GDAS Meteorological Data
NOAA HYSPLIT MODEL
Backward trajectory ending at 1600 UTC 29 Mar 12
GDAS Meteorological Data
NOAA HYSPLIT MODEL
Backward trajectory ending at 1600 UTC 30 Mar 12
GDAS Meteorological Data
NOAA HYSPLIT MODEL
Backward trajectory ending at 1600 UTC 31 Mar 12
GDAS Meteorological Data
NOAA HYSPLIT MODEL
Backward trajectory ending at 1600 UTC 01 Apr 12
GDAS Meteorological Data
NOAA HYSPLIT MODEL
Backward trajectory ending at 1600 UTC 02 Apr 12
GDAS Meteorological Data
NOAA HYSPLIT MODEL
Backward trajectory ending at 1600 UTC 03 Apr 12
GDAS Meteorological Data
NOAA HYSPLIT MODEL
Backward trajectory ending at 1600 UTC 04 Apr 12
GDAS Meteorological Data
NOAA HYSPLIT MODEL
Backward trajectory ending at 1600 UTC 05 Apr 12
GDAS Meteorological Data
NOAA HYSPLIT MODEL
Backward trajectory ending at 1600 UTC 06 Apr 12
GDAS Meteorological Data
NOAA HYSPLIT MODEL
Backward trajectory ending at 1600 UTC 07 Apr 12
GDAS Meteorological Data
NOAA HYSPLIT MODEL
Backward trajectory ending at 1600 UTC 08 Apr 12
GDAS Meteorological Data
NOAA HYSPLIT MODEL
Backward trajectory ending at 1600 UTC 09 Apr 12
GDAS Meteorological Data
NOAA HYSPLIT MODEL
Backward trajectory ending at 1600 UTC 10 Apr 12
GDAS Meteorological Data
NOAA HYSPLIT MODEL
Backward trajectory ending at 1600 UTC 11 Apr 12
GDAS Meteorological Data
NOAA HYSPLIT MODEL
Backward trajectory ending at 1600 UTC 12 Apr 12
GDAS Meteorological Data
Source ★ at 44.67 N 63.62 W
Meters AGL

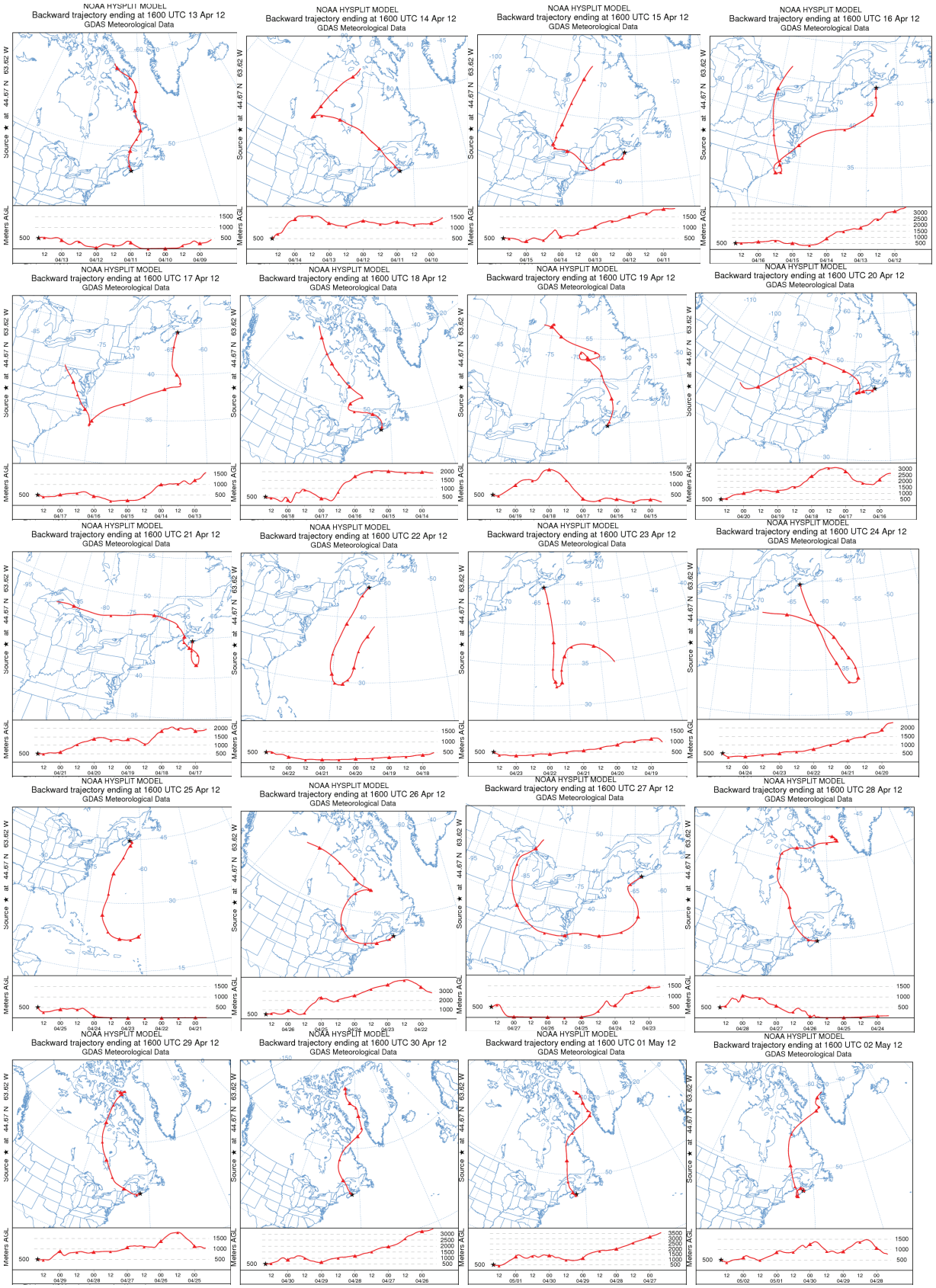
NOAA HYSPLIT MODEL
Backward trajectory ending at 1600 UTC 13 Apr 12
GDAS Meteorological Data
NOAA HYSPLIT MODEL
Backward trajectory ending at 1600 UTC 14 Apr 12
GDAS Meteorological Data
NOAA HYSPLIT MODEL
Backward trajectory ending at 1600 UTC 15 Apr 12
GDAS Meteorological Data
NOAA HYSPLIT MODEL
Backward trajectory ending at 1600 UTC 16 Apr 12
GDAS Meteorological Data
NOAA HYSPLIT MODEL
Backward trajectory ending at 1600 UTC 17 Apr 12
GDAS Meteorological Data
NOAA HYSPLIT MODEL
Backward trajectory ending at 1600 UTC 18 Apr 12
GDAS Meteorological Data
NOAA HYSPLIT MODEL
Backward trajectory ending at 1600 UTC 19 Apr 12
GDAS Meteorological Data
NOAA HYSPLIT MODEL
Backward trajectory ending at 1600 UTC 20 Apr 12
GDAS Meteorological Data
NOAA HYSPLIT MODEL
Backward trajectory ending at 1600 UTC 21 Apr 12
GDAS Meteorological Data
NOAA HYSPLIT MODEL
Backward trajectory ending at 1600 UTC 22 Apr 12
GDAS Meteorological Data
NOAA HYSPLIT MODEL
Backward trajectory ending at 1600 UTC 23 Apr 12
GDAS Meteorological Data
NOAA HYSPLIT MODEL
Backward trajectory ending at 1600 UTC 24 Apr 12
GDAS Meteorological Data
NOAA HYSPLIT MODEL
Backward trajectory ending at 1600 UTC 25 Apr 12
GDAS Meteorological Data
NOAA HYSPLIT MODEL
Backward trajectory ending at 1600 UTC 26 Apr 12
GDAS Meteorological Data
NOAA HYSPLIT MODEL
Backward trajectory ending at 1600 UTC 27 Apr 12
GDAS Meteorological Data
NOAA HYSPLIT MODEL
Backward trajectory ending at 1600 UTC 28 Apr 12
GDAS Meteorological Data
NOAA HYSPLIT MODEL
Backward trajectory ending at 1600 UTC 29 Apr 12
GDAS Meteorological Data
NOAA HYSPLIT MODEL
Backward trajectory ending at 1600 UTC 30 Apr 12
GDAS Meteorological Data
NOAA HYSPLIT MODEL
Backward trajectory ending at 1600 UTC 01 May 12
GDAS Meteorological Data
NOAA HYSPLIT MODEL
Backward trajectory ending at 1600 UTC 02 May 12
GDAS Meteorological Data
Source ★ at 44.67 N 63.62 W
Meters AGL

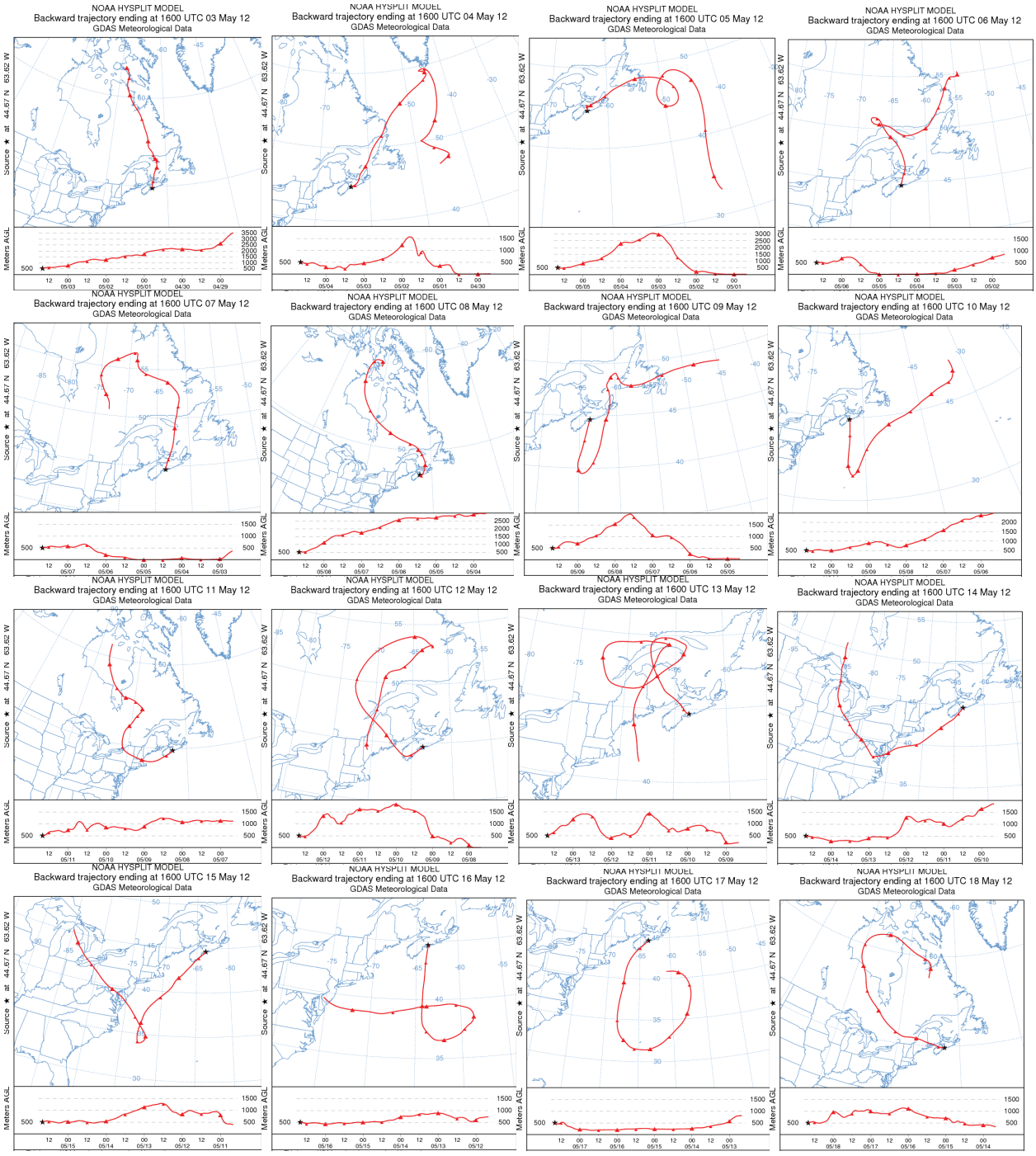
NOAA HYSPLIT MODEL
Backward trajectory ending at 1600 UTC 03 May 12
GDAS Meteorological Data
NOAA HYSPLIT MODEL
Backward trajectory ending at 1600 UTC 04 May 12
GDAS Meteorological Data
NOAA HYSPLIT MODEL
Backward trajectory ending at 1600 UTC 05 May 12
GDAS Meteorological Data
NOAA HYSPLIT MODEL
Backward trajectory ending at 1600 UTC 06 May 12
GDAS Meteorological Data
NOAA HYSPLIT MODEL
Backward trajectory ending at 1600 UTC 07 May 12
GDAS Meteorological Data
NOAA HYSPLIT MODEL
Backward trajectory ending at 1600 UTC 08 May 12
GDAS Meteorological Data
NOAA HYSPLIT MODEL
Backward trajectory ending at 1600 UTC 09 May 12
GDAS Meteorological Data
NOAA HYSPLIT MODEL
Backward trajectory ending at 1600 UTC 10 May 12
GDAS Meteorological Data
NOAA HYSPLIT MODEL
Backward trajectory ending at 1600 UTC 11 May 12
GDAS Meteorological Data
NOAA HYSPLIT MODEL
Backward trajectory ending at 1600 UTC 12 May 12
GDAS Meteorological Data
NOAA HYSPLIT MODEL
Backward trajectory ending at 1600 UTC 13 May 12
GDAS Meteorological Data
NOAA HYSPLIT MODEL
Backward trajectory ending at 1600 UTC 14 May 12
GDAS Meteorological Data
NOAA HYSPLIT MODEL
Backward trajectory ending at 1600 UTC 15 May 12
GDAS Meteorological Data
NOAA HYSPLIT MODEL
Backward trajectory ending at 1600 UTC 16 May 12
GDAS Meteorological Data
NOAA HYSPLIT MODEL
Backward trajectory ending at 1600 UTC 17 May 12
GDAS Meteorological Data
NOAA HYSPLIT MODEL
Backward trajectory ending at 1600 UTC 18 May 12
GDAS Meteorological Data
Source ★ at 44.67 N 63.62 W
Meters AGL

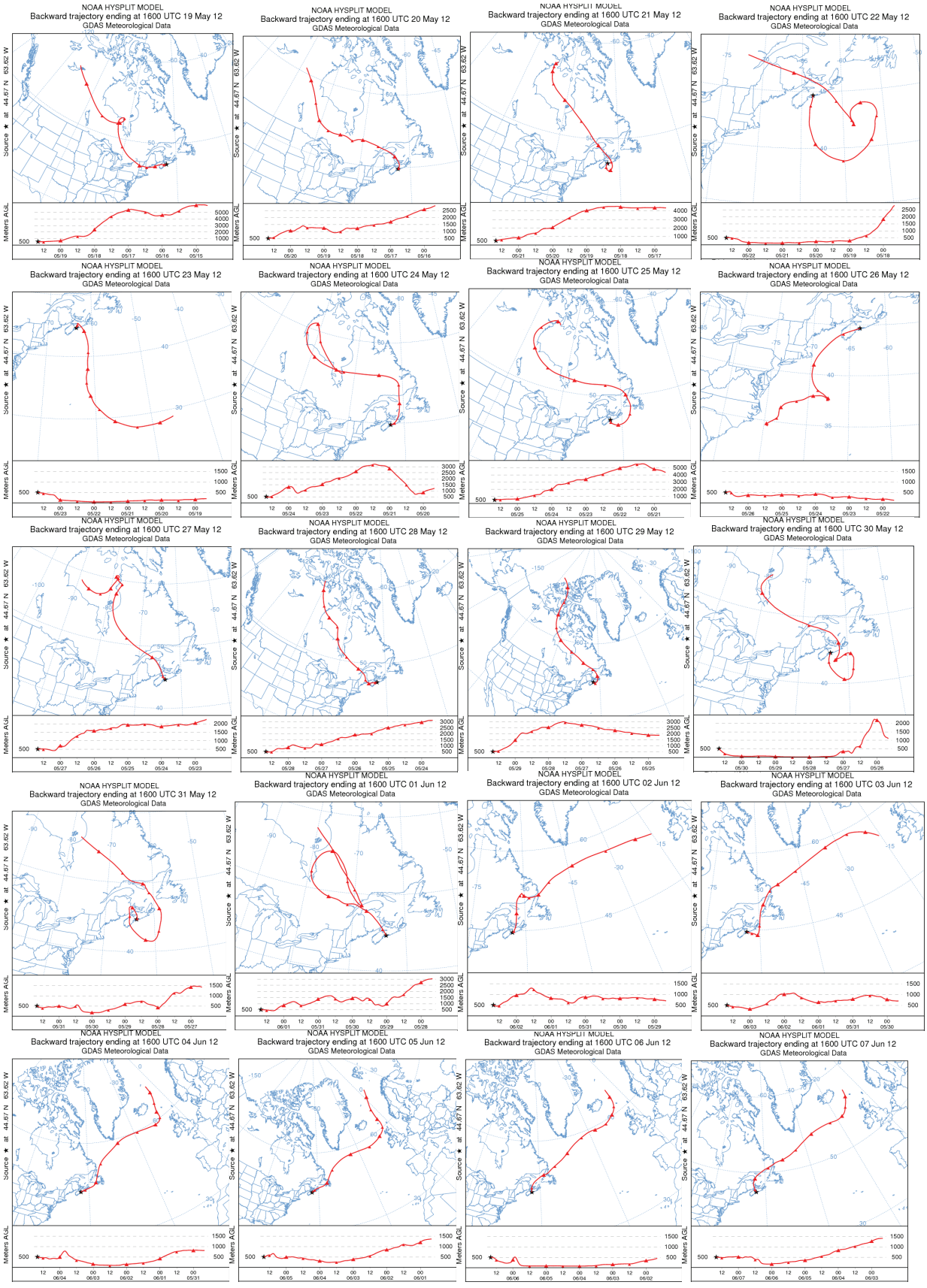
NOAA HYSPLIT MODEL
Backward trajectory ending at 1600 UTC 19 May 12
GDAS Meteorological Data
NOAA HYSPLIT MODEL
Backward trajectory ending at 1600 UTC 20 May 12
GDAS Meteorological Data
NOAA HYSPLIT MODEL
Backward trajectory ending at 1600 UTC 21 May 12
GDAS Meteorological Data
NOAA HYSPLIT MODEL
Backward trajectory ending at 1600 UTC 22 May 12
GDAS Meteorological Data
NOAA HYSPLIT MODEL
Backward trajectory ending at 1600 UTC 23 May 12
GDAS Meteorological Data
NOAA HYSPLIT MODEL
Backward trajectory ending at 1600 UTC 24 May 12
GDAS Meteorological Data
NOAA HYSPLIT MODEL
Backward trajectory ending at 1600 UTC 25 May 12
GDAS Meteorological Data
NOAA HYSPLIT MODEL
Backward trajectory ending at 1600 UTC 26 May 12
GDAS Meteorological Data
NOAA HYSPLIT MODEL
Backward trajectory ending at 1600 UTC 27 May 12
GDAS Meteorological Data
NOAA HYSPLIT MODEL
Backward trajectory ending at 1600 UTC 28 May 12
GDAS Meteorological Data
NOAA HYSPLIT MODEL
Backward trajectory ending at 1600 UTC 29 May 12
GDAS Meteorological Data
NOAA HYSPLIT MODEL
Backward trajectory ending at 1600 UTC 30 May 12
GDAS Meteorological Data
NOAA HYSPLIT MODEL
Backward trajectory ending at 1600 UTC 31 May 12
GDAS Meteorological Data
NOAA HYSPLIT MODEL
Backward trajectory ending at 1600 UTC 01 Jun 12
GDAS Meteorological Data
NOAA HYSPLIT MODEL
Backward trajectory ending at 1600 UTC 02 Jun 12
GDAS Meteorological Data
NOAA HYSPLIT MODEL
Backward trajectory ending at 1600 UTC 03 Jun 12
GDAS Meteorological Data
NOAA HYSPLIT MODEL
Backward trajectory ending at 1600 UTC 04 Jun 12
GDAS Meteorological Data
NOAA HYSPLIT MODEL
Backward trajectory ending at 1600 UTC 05 Jun 12
GDAS Meteorological Data
NOAA HYSPLIT MODEL
Backward trajectory ending at 1600 UTC 06 Jun 12
GDAS Meteorological Data
NOAA HYSPLIT MODEL
Backward trajectory ending at 1600 UTC 07 Jun 12
GDAS Meteorological Data
Source ★ at 44.67 N 63.62 W
Meters AGL

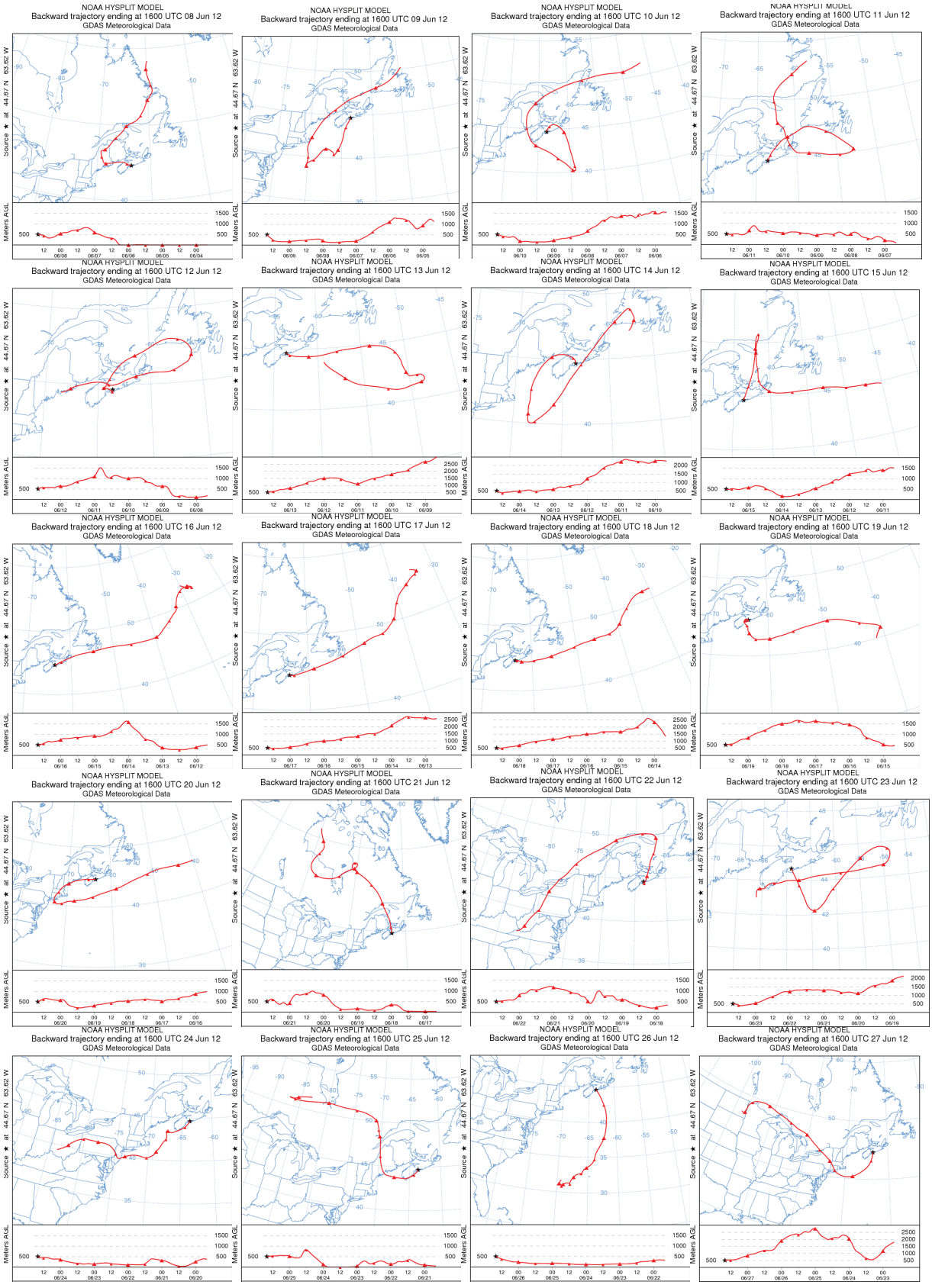
NOAA HYSPLIT MODEL
Backward trajectory ending at 1600 UTC 08 Jun 12
GDAS Meteorological Data
NOAA HYSPLIT MODEL
Backward trajectory ending at 1600 UTC 09 Jun 12
GDAS Meteorological Data
NOAA HYSPLIT MODEL
Backward trajectory ending at 1600 UTC 10 Jun 12
GDAS Meteorological Data
NOAA HYSPLIT MODEL
Backward trajectory ending at 1600 UTC 11 Jun 12
GDAS Meteorological Data
NOAA HYSPLIT MODEL
Backward trajectory ending at 1600 UTC 12 Jun 12
GDAS Meteorological Data
NOAA HYSPLIT MODEL
Backward trajectory ending at 1600 UTC 13 Jun 12
GDAS Meteorological Data
NOAA HYSPLIT MODEL
Backward trajectory ending at 1600 UTC 14 Jun 12
GDAS Meteorological Data
NOAA HYSPLIT MODEL
Backward trajectory ending at 1600 UTC 15 Jun 12
GDAS Meteorological Data
NOAA HYSPLIT MODEL
Backward trajectory ending at 1600 UTC 16 Jun 12
GDAS Meteorological Data
NOAA HYSPLIT MODEL
Backward trajectory ending at 1600 UTC 17 Jun 12
GDAS Meteorological Data
NOAA HYSPLIT MODEL
Backward trajectory ending at 1600 UTC 18 Jun 12
GDAS Meteorological Data
NOAA HYSPLIT MODEL
Backward trajectory ending at 1600 UTC 19 Jun 12
GDAS Meteorological Data
NOAA HYSPLIT MODEL
Backward trajectory ending at 1600 UTC 20 Jun 12
GDAS Meteorological Data
NOAA HYSPLIT MODEL
Backward trajectory ending at 1600 UTC 21 Jun 12
GDAS Meteorological Data
NOAA HYSPLIT MODEL
Backward trajectory ending at 1600 UTC 22 Jun 12
GDAS Meteorological Data
NOAA HYSPLIT MODEL
Backward trajectory ending at 1600 UTC 23 Jun 12
GDAS Meteorological Data
NOAA HYSPLIT MODEL
Backward trajectory ending at 1600 UTC 24 Jun 12
GDAS Meteorological Data
NOAA HYSPLIT MODEL
Backward trajectory ending at 1600 UTC 25 Jun 12
GDAS Meteorological Data
NOAA HYSPLIT MODEL
Backward trajectory ending at 1600 UTC 26 Jun 12
GDAS Meteorological Data
NOAA HYSPLIT MODEL
Backward trajectory ending at 1600 UTC 27 Jun 12
GDAS Meteorological Data

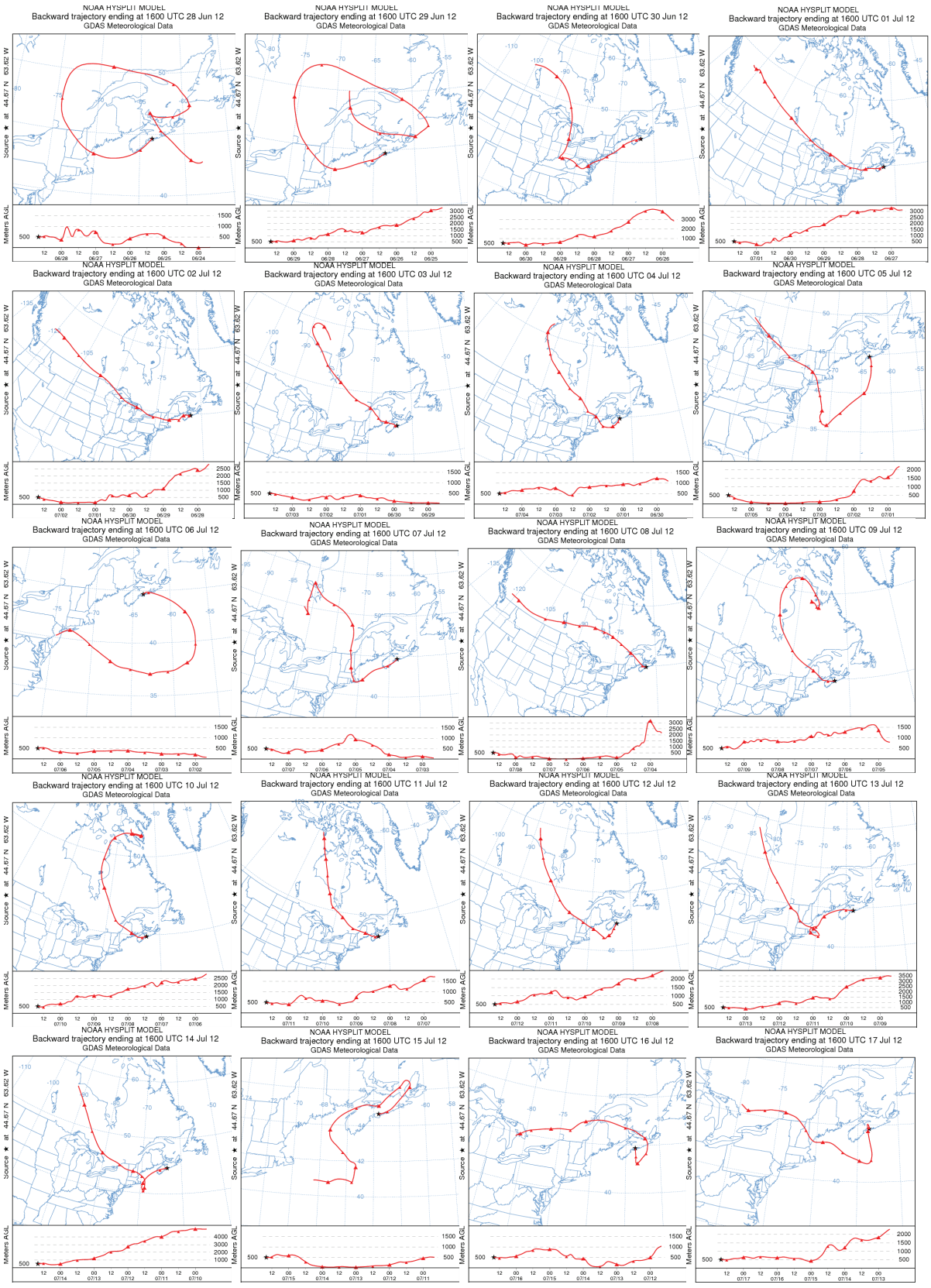
NOAA HYSPLIT MODEL
Backward trajectory ending at 1600 UTC 28 Jun 12
GDAS Meteorological Data
NOAA HYSPLIT MODEL
Backward trajectory ending at 1600 UTC 29 Jun 12
GDAS Meteorological Data
NOAA HYSPLIT MODEL
Backward trajectory ending at 1600 UTC 30 Jun 12
GDAS Meteorological Data
NOAA HYSPLIT MODEL
Backward trajectory ending at 1600 UTC 01 Jul 12
GDAS Meteorological Data
NOAA HYSPLIT MODEL
Backward trajectory ending at 1600 UTC 02 Jul 12
GDAS Meteorological Data
NOAA HYSPLIT MODEL
Backward trajectory ending at 1600 UTC 03 Jul 12
GDAS Meteorological Data
NOAA HYSPLIT MODEL
Backward trajectory ending at 1600 UTC 04 Jul 12
GDAS Meteorological Data
NOAA HYSPLIT MODEL
Backward trajectory ending at 1600 UTC 05 Jul 12
GDAS Meteorological Data
NOAA HYSPLIT MODEL
Backward trajectory ending at 1600 UTC 06 Jul 12
GDAS Meteorological Data
NOAA HYSPLIT MODEL
Backward trajectory ending at 1600 UTC 07 Jul 12
GDAS Meteorological Data
NOAA HYSPLIT MODEL
Backward trajectory ending at 1600 UTC 08 Jul 12
GDAS Meteorological Data
NOAA HYSPLIT MODEL
Backward trajectory ending at 1600 UTC 09 Jul 12
GDAS Meteorological Data
NOAA HYSPLIT MODEL
Backward trajectory ending at 1600 UTC 10 Jul 12
GDAS Meteorological Data
NOAA HYSPLIT MODEL
Backward trajectory ending at 1600 UTC 11 Jul 12
GDAS Meteorological Data
NOAA HYSPLIT MODEL
Backward trajectory ending at 1600 UTC 12 Jul 12
GDAS Meteorological Data
NOAA HYSPLIT MODEL
Backward trajectory ending at 1600 UTC 13 Jul 12
GDAS Meteorological Data
NOAA HYSPLIT MODEL
Backward trajectory ending at 1600 UTC 14 Jul 12
GDAS Meteorological Data
NOAA HYSPLIT MODEL
Backward trajectory ending at 1600 UTC 15 Jul 12
GDAS Meteorological Data
NOAA HYSPLIT MODEL
Backward trajectory ending at 1600 UTC 16 Jul 12
GDAS Meteorological Data
NOAA HYSPLIT MODEL
Backward trajectory ending at 1600 UTC 17 Jul 12
GDAS Meteorological Data
Source ★ at 44.67 N 63.62 W
Meters AGL

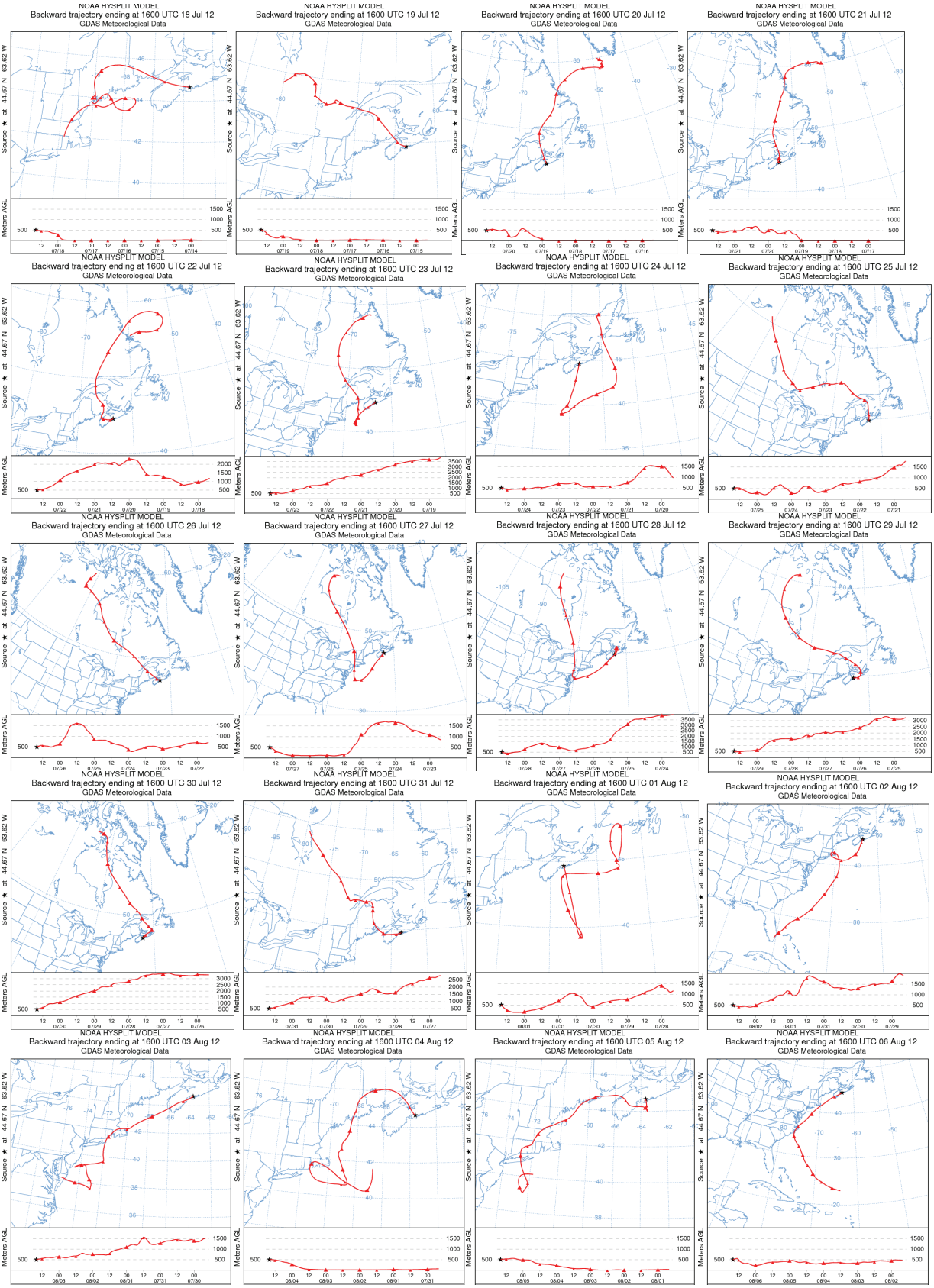
NOAA HYSPLIT MODEL
Backward trajectory ending at 1600 UTC 18 Jul 12
GDAS Meteorological Data
NOAA HYSPLIT MODEL
Backward trajectory ending at 1600 UTC 19 Jul 12
GDAS Meteorological Data
NOAA HYSPLIT MODEL
Backward trajectory ending at 1600 UTC 20 Jul 12
GDAS Meteorological Data
NOAA HYSPLIT MODEL
Backward trajectory ending at 1600 UTC 21 Jul 12
GDAS Meteorological Data
NOAA HYSPLIT MODEL
Backward trajectory ending at 1600 UTC 22 Jul 12
GDAS Meteorological Data
NOAA HYSPLIT MODEL
Backward trajectory ending at 1600 UTC 23 Jul 12
GDAS Meteorological Data
NOAA HYSPLIT MODEL
Backward trajectory ending at 1600 UTC 24 Jul 12
GDAS Meteorological Data
NOAA HYSPLIT MODEL
Backward trajectory ending at 1600 UTC 25 Jul 12
GDAS Meteorological Data
NOAA HYSPLIT MODEL
Backward trajectory ending at 1600 UTC 26 Jul 12
GDAS Meteorological Data
NOAA HYSPLIT MODEL
Backward trajectory ending at 1600 UTC 27 Jul 12
GDAS Meteorological Data
NOAA HYSPLIT MODEL
Backward trajectory ending at 1600 UTC 28 Jul 12
GDAS Meteorological Data
NOAA HYSPLIT MODEL
Backward trajectory ending at 1600 UTC 29 Jul 12
GDAS Meteorological Data
NOAA HYSPLIT MODEL
Backward trajectory ending at 1600 UTC 30 Jul 12
GDAS Meteorological Data
NOAA HYSPLIT MODEL
Backward trajectory ending at 1600 UTC 31 Jul 12
GDAS Meteorological Data
NOAA HYSPLIT MODEL
Backward trajectory ending at 1600 UTC 01 Aug 12
GDAS Meteorological Data
NOAA HYSPLIT MODEL
Backward trajectory ending at 1600 UTC 02 Aug 12
GDAS Meteorological Data
NOAA HYSPLIT MODEL
Backward trajectory ending at 1600 UTC 03 Aug 12
GDAS Meteorological Data
NOAA HYSPLIT MODEL
Backward trajectory ending at 1600 UTC 04 Aug 12
GDAS Meteorological Data
NOAA HYSPLIT MODEL
Backward trajectory ending at 1600 UTC 05 Aug 12
GDAS Meteorological Data
NOAA HYSPLIT MODEL
Backward trajectory ending at 1600 UTC 06 Aug 12
GDAS Meteorological Data
Source ★ at 44.67 N 63.62 W
Meters AGL

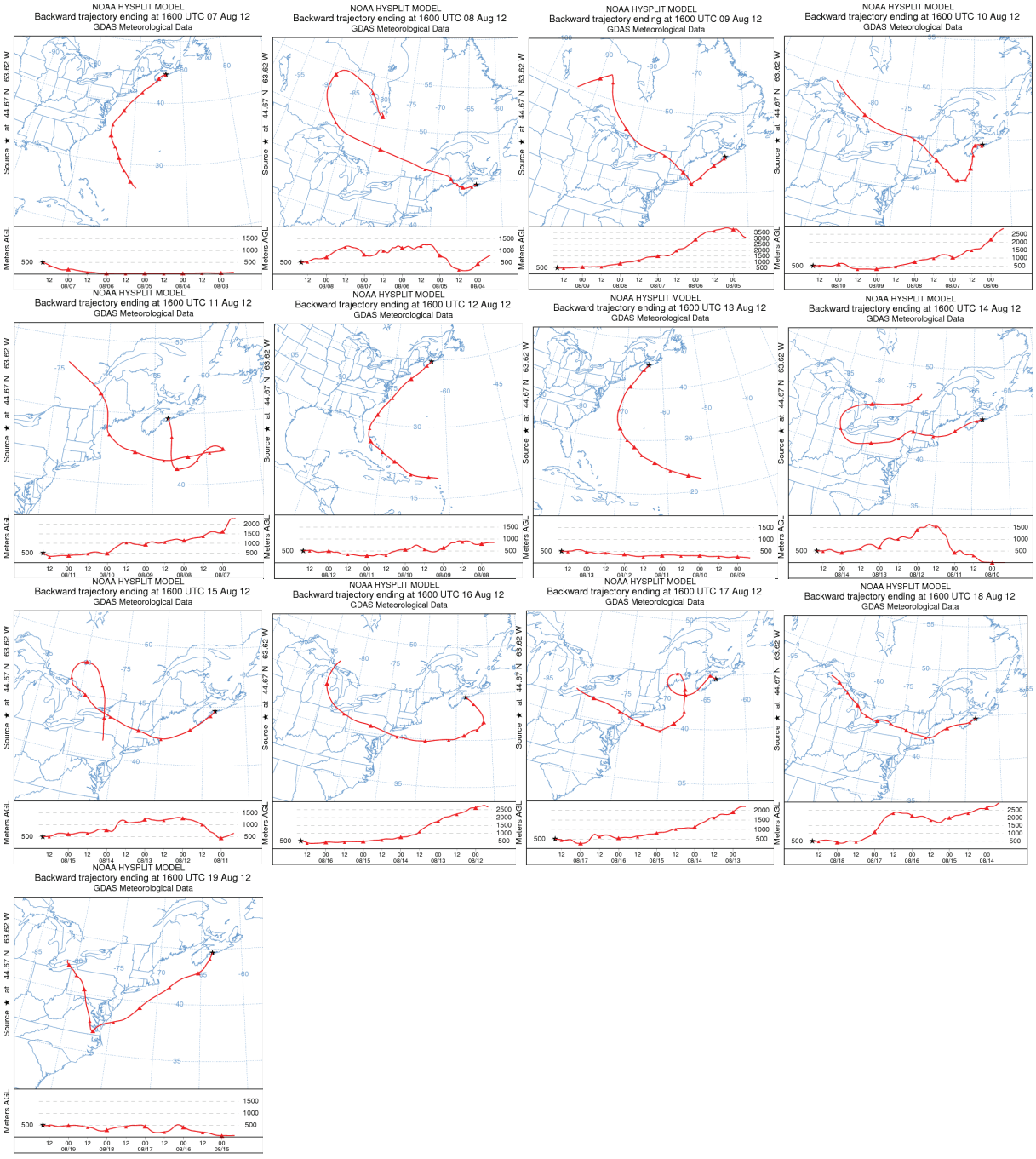

Figure 73 HYSPLIT air mass back trajectories for the whole period of sampling campaign.